UNIVERSITY OF SOUTHAMPTON

FACULTY OF ENGINEERING, SCIENCE & MATHEMATICS

OPTOELECTRONICS RESEARCH CENTRE

Power Scaling of Laser Oscillators and Amplifiers Based on Nd:YVO_4

Michael James Yarrow

Thesis submitted for the degree of Doctor of Philosophy

September 20, 2006

UNIVERSITY OF SOUTHAMPTON

ABSTRACT

FACULTY OF ENGINEERING, SCIENCE AND MATHEMATICS
OPTOELECTRONICS RESEARCH CENTRE

Doctor of Philosophy

POWER SCALING OF LASER OSCILLATORS AND AMPLIFIERS BASED ON Nd:YVO_4

By Michael James Yarrow

This thesis presents a strategy for power and brightness scaling in diode-end-pumped, master-oscillator-power-amplifier laser systems, based on Nd:YVO_4, to achieve mode-locked and single-frequency output powers up to ∼80W with minimal degradation in beam quality due to thermal effects.

Scaling output powers to the tens of watts regime in diode-end-pumped solid-state oscillators and amplifiers, without causing severe degradation in beam quality, is challenging because the large thermal loading density and large thermal gradients in end-pumped gain media cause a number of undesirable thermal effects. In Nd:YVO_4, these thermal effects are particularly severe due to its relatively poor thermal and mechanical properties, however its attractive spectroscopic properties make power scaling of Nd:YVO_4 laser sources an area of much interest.

An actively mode-locked, diode-end-pumped, Nd:YVO_4 oscillator was constructed which produced 360ps pulses at 100MHz repetition rate and an average power of up to 5.3W for 22W of pump power. This source was used to seed a diode-end-pumped, Nd:YVO_4 amplifier chain which was optimised, with the aid of theoretical models, to achieve high gain, high efficiency and low degradation in beam quality. The amplifier yielded a small signal gain of ∼7000 and a maximum output power of 94W for 237W of absorbed pump power. The M^2 values at 79W output power were measured to be 1.7 and 1.9 in orthogonal planes. The amplifier was also operated in long-pulse-train mode by using an acousto-optic modulator to gate the input, thereby achieving higher gains and higher peak powers. In this regime, up to ∼400kW peak powers could be achieved and, by pulse shaping of the seed laser, pulse trains as long as 1μs were achieved with ∼30kW peak powers and >10W average power.

A single-frequency diode-end-pumped Nd:YVO_4 oscillator was also used to seed the amplifier chain. In cw mode, this produced up to 79W of mode-hop-free, single-frequency output with M^2 values of 1.48 and 1.43 in orthogonal planes. Pulse shaping techniques provided output powers of 1kW for long, 1μs , pulses of rectangular shape with ∼10W of average power.

In pulsed (high gain) mode of operation, the beam quality of the two sources was found to be improved significantly due to the effect of gain-guiding in the amplifier.

Issues relating to further power and brightness scaling are discussed as well as the potential applications of these laser sources as pump sources for frequency conversion in optical parametric devices.

Author's Declaration

I, **Michael James Yarrow**, declare that this thesis entitled *Power Scaling of Laser Oscillators and Amplifiers based on Nd:YVO_4* and the work presented in it are my own. I confirm that:

- this work was done wholly while in candidature for a Research degree at the University of Southampton;
- where any part of this thesis has been previously submitted for a degree or any other qualification at this University or any other institution, this has been clearly stated;
- where I have consulted the published work of others, this is always clearly attributed;
- where I have quoted from the work of others; the source is always given. With the exception of such quotations, this thesis is entirely my own work;
- I have acknowledged all main sources of help;
- The derivation of small signal gain in the presence of ETU and setting up of some of the experimental apparatus was based on work done by Dr Ian Musgrave. Chapter 6 of this thesis is based on work done by myself jointly with Dr Ji Won Kim. The single-frequency oscillator in Chapter 6 was built by Dr Ji Won Kim. The rest of this thesis is based on work done wholly by myself;
- parts of this work have been published (see Appendix I for details).

Signed:..... Date: .....

Acknowledgements

I'd like to thank all those who've helped me directly and indirectly over the last few years. First of all, thanks to my supervisor Andy Clarkson for his endless optimism and for bringing everything into focus. Thanks to Ian Musgrave for his time and patience showing me the ropes in the early days and Tim Kendall and Dave Hillier for their tips which probably saved me weeks. Thanks very much to Ji Won Kim for getting things moving in the lab when it really mattered. Thanks to all in the ASSL group for their kindness and support. Thanks to Simon, Tim and Chris for making all the gubbins and keeping the lab in service, the network guys for keeping my work safe and Eve and all the admin. staff for keeping the ORC running smoothly. For useful discussions I'd like to thank Pascal Dupriez. For slightly less useful discussions and distractions, thanks to all my office mates over the years from the legendary P2071 office to the original Porta*cabin-crew* and finally the Porta*village-people*. For always being up for a pint, I'd like to thank Ian, Andy, Steve, Jeff, Gates, Hannah, Corin and Stu (amongst many others) and thanks to my old old mates for not giving a monkey's about lasers. Thanks also to Michaël and the paragliding club for keeping my feet firmly off the ground. For their great support, thanks to my Mum, Dad and family. Finally, thank you Catherine for always being right there beside me.

I would also like to acknowledge financial support from the EPSRC and the ORC and travel bursaries from the IOP and IEEE.

Live as if you were to die tomorrow. Learn as if you were to live forever.

—Mahatma Gandhi

Contents

Frequently Used Symbols and Abbreviations

c	Speed of light in vacuum	[2.998×10^{8}ms^{-1}]
h	Planck constant	[6.626×10^{-34}Js]
l_c	Cavity length	[mm]
l_g	Length of gain medium	[mm]
σ_{21}	Stimulated emission cross section	[m^2]
τ_f	Fluorescence lifetime	[µs]
α_p	Absorption coefficient at pump frequency	[m^{-1}]
B	Brightness	[Wm^{-2}sr^{-1}]
$\Delta\nu$	Linewidth	[Hz]
ν_p	Pump frequency	[Hz]
ν_l	Laser frequency	[Hz]
w_p	Pump beam radius	[µm]
w_l	Laser beam radius	[µm]
L	Round-trip cavity loss	
T	Output coupler transmission	
$E_{sat} = h\nu_l/\sigma_{21}$	Saturation fluence	[Jm^2]
$I_{sat} = h\nu_l/\sigma_{21}\tau_f$	Saturation intensity	[Wm^2]
G_0	Small signal gain	
g_0	Small signal gain coefficient	[m^{-1}]
G	Saturated power gain	
G_B	Brightness gain	
M^2	Beam quality factor	
P_p	Pump power	[W]
cw	continuous-wave	
rf	radio-frequency	
Nd	neodymium	
YVO_4	yttrium orthovanadate	
YAG	($Y_3Al_5O_{12}$) yttrium aluminium garnet	
YLF	($YLiF_4$) yttrium lithium fluoride	
MOPA	Master-oscillator-power-amplifier	
TEM	Transverse electro-magnetic	
FWHM	Full-width-half-maximum	
AOM	Acousto-optic modulator	
ETU	Energy-transfer-upconversion	
ASE	Amplified-spontaneous-emission	

Chapter 1

Introduction

1.1 General Introduction

Lasers are finding their way into a rapidly expanding range of applications. Many of these applications continually demand laser systems with higher output powers, greater efficiency and lower cost. Additionally, many applications require good beam quality and there is often a desire to operate at new wavelengths, with narrow pulses of high peak power or with narrow spectral linewidth. Furthermore, with the availability of lasers with improved performance characteristics, and lower cost, new applications continue to present themselves. Indeed these links between demand and supply of new technology drive the development of high power lasers faster still. The use of lasers is becoming increasingly important in industry. Processes such as welding, drilling, cutting, marking and guiding can now, in many cases, be done with improved quality and greater speed using lasers. More advanced laser processing techniques have emerged in medical fields such as dermatology, dentistry, ophthalmology, and cancer treatment. The entertainment industry has been transformed by lasers since the development of CD and DVD reading and writing technology and lasers could one day revolutionise cinema entertainment with the development of high power red, green and blue (RGB) or white light generating lasers for projection displays [1]. Additionally, many scientific fields continue to benefit from advances in high power laser technology. These include remote sensing and *Li*ght *D*etection *A*nd *R*anging (LIDAR) used for range finding, for example, or for measuring particles or chemicals in

the atmosphere. Spectroscopy benefits from the development of broadband, narrowband or wavelength tunable laser sources. High power laser sources of various wavelengths are also required for writing structures such as waveguides and gratings in materials like germanium doped silica, for example, for use in a growing number of optoelectronic devices. Astrophysicists even hope that laser interferometers will be used to detect gravitational waves for the first time.

Scaling the output power of lasers can be achieved in a number of ways. One method is to use a master-oscillator-power-amplifier (MOPA) configuration, in which a relatively low power laser oscillator is used as a seed for a power-amplifier, or series of amplifiers, which effectively increases the brightness of the output. One of the biggest advantages of this technique is that the problem of power scaling is effectively decoupled from the problem of generating a laser output with desired characteristics like TEM_{00} mode, single-frequency, or mode-locked operation. This implies that a generic amplifier design can be used to scale the power from a range of laser oscillators with different characteristics, or from one oscillator operating in a range of different modes. One of the most challenging aspects of power scaling, however, is the management of the inevitable thermal effects in the laser material caused by optical pumping at high power levels. Minimising these thermal effects and their impact is key to finding an effective amplifier design and choosing the best parameters under which to operate. Furthermore, gaining a better understanding of thermal effects and their impact on laser and amplifier performance will also help others to improve the designs of power scaling systems of the future for a range of laser applications.

The primary goals of the research described in this thesis were to develop a diode-end-pumped mode-locked master-oscillator-power-amplifier (MOPA) using Nd:YVO_4 as the active medium, to formulate a strategy for power scaling in the oscillator and amplifier systems with particular regard to minimising the impact of thermal effects, to investigate the performance characteristics of the system under a range of operating regimes such as continuous wave (cw), mode-locked and pulsed mode and to evaluate the usefulness of the source as a pump for non-linear optical processes such as second harmonic generation and optical parametric oscillation and amplification. An additional goal was

the development of a single-axial-mode oscillator amplifier system for use in cw and pulsed modes using the same amplifier developed for the mode-locked source, thereby taking advantage of the versatility of a MOPA approach and opening up a range of potential applications.

1.2 Background

Just 3 years after Maiman demonstrated the first optical laser in 1960 [2] and 1 year after the first diode-lasers were developed in 1962, Newman *et al.* [3] found that 0.88μm radiation from a GaAs light emitting diode could be used to excite fluorescence near 1.06μm in Nd:$CaWO_4$. In 1964 the first diode-pumped solid-state laser was demonstrated by Keyes *et al.* [4]. Surprisingly, it took until the 1980s for improved fabrication techniques to allow diode lasers to be developed with long enough lifetimes and high enough output powers to become a practical alternative to flash lamps for pumping solid-state lasers. Since then, diode laser output powers have changed magnitude from several milliWatts to several watts, from a single emitter, and furthermore the development of diode bars and diode stacks, which combine many emitters into a single package, are now commercially available with output powers of several kiloWatts. High power diode arrays themselves provide only limited use in most laser applications because, due to the large emitting area, they have relatively poor beam quality and also produce highly elliptical beams. The maximum output power to date of a conventional electrically excited, single-emitter diode laser, with TEM_{00} beam quality, remains less than 6 watts [5], limited by the optical damage threshold of the facets.

The spectral brightness B_s of an optical source is defined by the relation [6]:

$$B_s = \frac{P}{A\Delta\nu\Omega}, \tag{1.1}$$

where P is the power of the beam, A is the emitting area, $\Delta\nu$ is the spectral bandwidth and Ω is the solid angle divergence of the beam. This implies that, while it is possible to scale the output power of a diode source by constructing linear arrays of emitters to form bars and stacks, the maximum brightness of the source is no greater than that of a single emitter. Despite their poor beam

quality however, high power diode arrays are excellent sources for pumping solid-state lasers. Compared to their predecessor, the flash lamp, diode sources have a very narrow bandwidth which means that nearly all the pump light can be concentrated into the absorption band of a given solid-state laser material. This vastly improves the optical efficiency of the laser and reduces the amount of unwanted heat generated in the host material. Importantly, solid-state laser materials have relatively high damage thresholds, compared to diode lasers, so high intensity, diffraction limited beams can be produced by pumping with poor beam quality diode laser sources. In this sense, diode pumped lasers and laser amplifiers provide an effective means of converting low brightness pump light to high brightness laser light.

Power scaling of diode-pumped solid-state lasers and, in particular, Nd^{3+} based solid-state lasers which operate in the 1μm wavelength regime, has attracted much interest over the years. Due to its excellent thermal and mechanical properties, Nd:YAG has been the material of choice for high power 1μm radiation for many years [7]. However, other Nd^{3+} -doped materials have become increasingly popular in recent years, notably Nd:YVO_4 . Although it has relatively poor thermal and mechanical properties, Nd:YVO_4 has a broader absorption bandwidth, a higher absorption coefficient and higher product of stimulated emission cross section and fluorescence lifetime. Furthermore, unlike Nd:YAG, Nd:YVO_4 has natural birefringence so thermally induced birefringence does not cause depolarisation of the output at high pump powers. Various authors have explored the power scaling potential of Nd:YVO_4 lasers in various configurations. In cw Nd:YVO_4 oscillators, side-pumping configurations have produced TEM_{00} output powers as high as 46W [8] and optical efficiencies of around 58% for 23W of output power [9]. In end-pumped configurations, a number of studies, both theoretical and experimental, on the power scaling of Nd:YVO_4 lasers in cw mode, have been published [10–14]. In 1997 Zhang *et al.* [15] produced an end-pumped Nd:YVO_4 laser with 11.6W output and 54% optical to optical efficiency . In 1999 Spectra-Physics Lasers [16] developed a 35W TEM_{00} laser with an optical to optical efficiency of 60% using a dual end-pumped geometry with four laser diodes and two laser rods. In 2003 Shi [17] used an end-pumped configuration to achieve up to 110W output with M^2 factors 1.3 and 1.5 orthogonally and in 2004 Tzuk [18] produced

around 200W output but with a highly multimode output (M^2 = 7 and 35 orthogonally).

In MOPA configurations, whilst a number of authors have reported power scaling of multi-axial mode beams from Nd:YAG, Nd:YLF and Nd:YVO_4 lasers, with TEM_{00} output beams up to average powers of 10-60W [19], the author is not aware of any reports of more than 60W being achieved, without the use of complicated phase conjugate systems. Higher powers (100W) have, however, been achieved with TEM_{00} beam quality, using Nd:$GdVO_4$ as the gain medium, reported by Minassian *et al.* [20] in 2005. Additionally, reports of systems which offer a combination of high peak powers, high average powers and good beam quality, in mode-locked, Q-switched or pulsed mode-locked operation of MOPA systems have generally been limited to average powers below 10W. For example, in 2004, Siebold [21] produced a cw-end-pumped Nd:YVO_4 MOPA with 5.3W average power with 19ps pulses at 40kHz repetition rate and 6.8W, at 41% extraction efficiency, in cw-mode. In 2003 Pearce [22], presented a high repetition rate (>100kHz), cw-end-pumped Nd:YVO_4 , MOPA which produced ∼ns pulses of multi-kW peak powers and >1W average power, as well as up to 50% extraction efficiency. In 1998 Brignon [23] demonstrated an end-pumped Nd:YVO_4 amplifier yielding 100µs output pulses, with extracted energies as high as 3mJ, and around 27% extraction efficiency, using a quasi-cw (∼330W peak power) diode stack. To the author's best knowledge, the highest average powers for pulsed, Nd^{3+} based, MOPA systems with TEM_{00} beam quality, were achieved by Snell *et al.*, who reported a mode-locked, Q-switched MOPA system based on side-pumped Nd:YLF slabs [24] delivering up to ∼27W TEM_{00} average output power and also a Q-switched Nd:YVO_4 MOPA based on a similar architecture [25,26], with up to 53.5W average power. The Nd:YVO_4 mode-locked MOPA described in this thesis, has many attractive characteristics which supersede those of previously reported Nd:YVO_4 systems with regard to the combination of high efficiency, high average power, good beam quality and flexibility of operating regimes. The system also delivers mode-locked pulse trains, with a combination of long pulse envelopes, high peak powers and high average powers to rival many state-of-the-art systems.

As for lasers with single-axial mode and TEM_{00} operation, there have been a

number of reports of high-power MOPA systems based on side-pumped and end-pumped Nd:YAG [27, 28] with up to 195W of output power and based on Nd:YLF [29] with 40W output power. Success in this area, has been partly a result of much interest in such sources for the application of gravitational wave detection. However, Nd:YVO_4 has remained rather less popular for high power single-frequency sources owing to its relatively poor thermal and mechanical properties. In 2005, Xi [30] achieved 18W of single-frequency output from an end-pumped Nd:YVO_4 oscillator and in 2006 Schulz [31] achieved 47.2W with 37% efficiency in an end-pump Nd:YVO_4 MOPA system. This thesis describes the development of a high-power single-frequency source which, in many ways, supersedes other reported systems based on Nd:YVO_4 for its combination of high efficiency and high output power, and which avoids serious detrimental thermal effects, and takes advantage of Nd:YVO_4 's attractive spectroscopic properties. Furthermore, to the authors best knowledge, reports of single-frequency sources, which operate in pulsed mode to achieve long pulse durations and high peak powers, have so far been limited to the $\sim$ns (Q-switched) pulse duration regime or the sub-kW power levels. In this work, by virtue of the high gain and large flexibility in pulse duration and pulse shape, we have exceeded kW power levels for rectangular pulses of $\sim$ µs duration whilst additionally maintaining high average powers $\sim$10W.

1.3 Thesis Overview

In this thesis, the principles of power scaling in diode-pumped solid-state oscillators and amplifiers based on Nd:YVO_4 are described, and applied to the experimental development of a mode-locked MOPA system, and also a single-frequency MOPA system. Chapter 2 discusses the basic principles required for power scaling of solid-state lasers and amplifiers and many of the design considerations are outlined. This starts with a brief description of the four-level laser scheme and optical resonators and the basic equations for threshold pump power and slope efficiency for a laser oscillator. The principle of gain in a laser amplifier is also introduced. The importance of beam quality is discussed and the meaning and use of the M^2 value as a measure of beam quality is described. Having introduced some of the fundamental principles, the chap-

ter goes on to discuss the main processes by which heat is generated in the laser gain medium, the primary one being quantum defect heating but a number of other spectroscopic effects which can add to this heating are also described. The use of Nd:YVO_4 as a gain medium in this work is also justified and its energy level structure and its merits compared with some other popular Nd^{3+} doped materials are discussed. The heat generated in the gain medium remains a primary concern due to a number of detrimental thermal effect which are described. The most significant effects, in the case of Nd:YVO_4 , is aberrated thermal lensing and thermally induced stress fracture, the main features of which are outlined. Several strategies for reducing the thermal effects or their impact on laser performance are then described and some examples of laser architectures which have been adopted for power scaling of solid-state lasers are discussed. These include a number of different pumping geometries as well as gain medium and cooling geometries.

The method of pumping the gain medium using high power diode sources is also an important design consideration for high power solid-state lasers. The chapter goes on to describe the output characteristics and limitations of high power diode bars and diode stacks, and gives examples of some methods for increasing the brightness and reducing the large ellipticity of their output beams. Particular emphasis is given to preparing the beams from diode sources for end-pumping of laser rods, since this is an important requirement for efficient operation of Nd:YVO_4 sources. This includes a discussion of the basic principles of fibre coupling diode sources to produce smooth circular beam profiles.

In Chapter 3, the development of an end-pumped, Nd:YVO_4 , mode-locked oscillator, to be used as a seed laser for a MOPA system, is described. The work follows on from and builds upon the work done by Ian Musgrave from 1999 to 2003 [32]. The main design criteria and the design strategy are described including the choice of Nd^{3+} doping concentration and pumping scheme. The principles of operating an oscillator in mode-locked mode are introduced and different methods of achieving mode-locking are discussed. In particular, the use (as in this oscillator) of a standing-wave acousto-optic modulator as a mode-locker is described. The application of ABCD matrix formalism for calculating the Gaussian modes in resonators is discussed and a strategy for de-

signing the resonator in this system by modelling of the resonator mode and varying relevant parameters is explained. The resonator design used in the oscillator is then described and the sensitivity of its calculated mode size to changes in various parameters such as mirror spacings and thermal lens focal length in the gain medium is shown. The experimental results of the oscillator performance characteristics are then presented and discussed.

In order to formulate an appropriate amplifier design strategy, the theory of laser amplification in end-pumped solid-state amplifiers is reviewed. Chapter 4 builds on the basic principles of amplification, initially in the small-signal limit and then extends this to account for saturation of the amplifier gain. An analytical approach is used to predict the effect of energy-transfer-upconversion on the small signal gain in an amplifier where the population inversion varies longitudinally, as in an end-pumped gain medium with a constant absorption coefficient. An analysis of the saturated gain for a local area of the gain medium is reviewed, initially for a cw and then for a pulsed signal. This saturated gain formula for a pulsed signal is then used in a numerical integration to give the total gain for a Gaussian signal beam passing through an end-pumped gain medium where two simple approximations for the pump beam profile are compared. The effect of varying the ratio of the signal beam size to the pump beam size is explored and the optimisation of this overlap ratio with regard to maximising the gain is discussed. A simplified analysis of the degradation in beam quality, caused by aberrated thermal lensing, follows which is then used to extend the numerical model to make predictions of the brightness scaling potential of an amplifier. Finally the chapter discusses the use of multiple amplifier stages and multiple pass amplifiers as a route for further power scaling

In Chapter 5, many of the principles from Chapter 4 are brought together to form a multi-stage Nd:YVO_4 amplifier design where the seed laser is the mode-locked laser described in Chapter 3. The applications of the MOPA system, particularly for non-linear frequency conversion are discussed. The main issues relevant to the design are explained and strategies for cooling the Nd:YVO_4 crystals and relay-imaging the signal and pump beams from one crystal to the next are discussed. Some of the potential limiting factors on amplifier performance and ways to mitigate their effects are then outlined. Following this, the details of the amplifier design and experimental appara-

tus used, are explained. The method of beam shaping and fibre-coupling of the diode pump sources, used to pump the amplifier chain, is detailed and a generic double-rod amplifier design used in the three amplifier stages is described. An experimental approach for finding the optimum signal beam size for the first amplifier stage is then presented. The results from this are compared to the theory and used to choose the parameters for the subsequent amplifier stages. The final design and experimental set-up of the amplifier chain is then presented and the performance in cw mode, and then mode-locked mode, is discussed. The influence of the non-uniform radial gain profile is found to have a significant effect on the on the signal beam profile, leading to degradation in beam quality. The use of an acousto-optic modulator (AOM) to gate the amplifier input and allow pulsed operation is also described as a means to increase the peak power. The experimental results of the amplifier in pulsed mode are then presented for a range of operating regimes and the performance and potential applications of the source are discussed.

The use of the amplifier system described in Chapter 5 with other seed lasers is then considered. In Chapter 6, the use of the amplifier system to amplify the output from a single-frequency cw Nd:YVO_4 oscillator is described and the applications of such a source are discussed. The principles and methods of achieving single-axial-mode (single-frequency) oscillation are explained and ways to suppress the problematic axial-mode-hopping are described. A single-frequency Nd:YVO_4 oscillator, which was built, is described and its performance characteristics are presented. The experimental results for the single-frequency MOPA system are then presented and discussed, initially in cw mode, and then in pulsed mode applying the same method as used for the mode-locked MOPA. A further development is also presented which uses analogue operation of the AOM to achieve effective pulse shaping of the input pulses to the amplifier, which can compensate for the temporal pulse distortion caused by the amplifier thus achieving a more desirable output pulse shape.

Finally, Chapter 7 concludes the thesis by summarising the main achievements and limitations of the work presented and offers some speculation and directions for future work in this area and potential applications of the systems which have been developed.

1.4 References

[1] **Hollemann, G., Braun, B., Dorsch, F., Hennig, P., Heist, P., Kraus, U., Kutschki, U.** and **Voelckel, H.**, *RGB lasers for projection displays*, Proceedings: SPIE, Vol. 3954, pp. 140–151, 2000.

[2] **Maiman, T. H.**, *Stimulated Optical Radiation in Ruby*, Nature, Vol. 187, No. 4736, pp. 493–494, 1960.

[3] **Newman, R.**, *Excitation of the Nd^{3+} fluorescence in $CaWO_4$ by recombination radiation in GaAs*, Journal of Applied Physics, Vol. 34, No. 2, pp. 437, 1963.

[4] **Keyes, R. J.**, *Injection luminescent pumping of CaF_2:U^{3+} with GaAs diode lasers*, Applied Physics Letters, Vol. 4, No. 3, pp. 50–52, 1964.

[5] **Paschke, K., Sumpf, B., Dittmar, F.** and **Erbert, G.**, *Nearly Diffraction Limited 980-nm Tapered Diode Laser With an Output Power of 7.7 W*, IEEE Journal of Selected Topics in Quantum Electronics, Vol. 11, No. 5, pp. 1223–1227, 2005.

[6] **Koechner, W.**, Solid-State Laser Engineering, Springer, 5th edn., 1999.

[7] **Amano, S.** and **Mochizuki, T.**, *High Average and High Peak Brightness Slab Laser*, IEEE Journal of Quantum Electronics, Vol. 37, No. 2, pp. 296–303, 2001.

[8] **Minassian, A., Thompson, B.** and **Damzen, M. J.**, *Ultrahigh-efficiency TEM_{00} diode-side-pumped Nd:YVO_4 laser*, Applied Physics B: Lasers and Optics, Vol. 76, pp. 341–343, 2003.

[9] **Minassian, A., Thompson, B.** and **Damzen, M. J.**, *High-power TEM_{00} grazing-incidence Nd:YVO_4 oscillators in single and multiple bounce configurations*, Optics Communications, Vol. 245, pp. 295–300, 2005.

[10] **Chen, Y. F.**, *Design criteria for concentration optimization in scaling diode end-pumped lasers to high powers: influence of thermal fracture*, IEEE Journal of Selected Topics in Quantum Electronics, Vol. 35, No. 2, pp. 234–239, 1999.

[11] **Chen, Y. F., Kao, C. F., Huang, T. M., Wang, C. L.** and **Wang, S. C.**, *Influence of Thermal Effect on Output Power Optimization in Fibre-Coupled*

Laser-Diode End-Pumped Lasers, IEEE Journal of Selected Topics in Quantum Electronics, Vol. 3, No. 1, pp. 29–34, 1997.

[12] **Liao, Y., Miller, R. J. D.** and **Armstrong, M. R.**, *Pressure Tuning of Thermal Lensing for High-Power Scaling*, Optics Letters, Vol. 24, No. 19, pp. 1343–1345, 1999.

[13] **Zhang, H., Chao, M., Gao, M., Zhang, L.** and **Yao, J.**, *High Power Diode Single-End-Pumped Nd:YVO_4 Laser*, Optics and Laser Technology, Vol. 35, pp. 445–449, 2003.

[14] **Peng, X., Xu, L.** and **Asundi, A.**, *Power Scaling of Diode Pumped Nd:YVO_4 Lasers*, IEEE Journal of Quantum Electronics, Vol. 38, No. 9, pp. 1291–1299, 2002.

[15] **Zhang, J., Quade, M., Du, K. M., Liao, Y., Falter, S., Baumann, M., Loosen, P.** and **Poprawe, R.**, *Efficient TEM_{00} operation of Nd:YVO_4 laser and end-pumped by fiber-coupled diode laser*, Electronics Letters, Vol. 33, pp. 775–777, 1997.

[16] **Hodgson, N., Griswold, K. D., Jordan, W., Knapp, S. L., Peirce, A. A., Pohalski, C. C., Cheng, E. A., Cole, J., Dudley, D. R., Petersen, A. B.** and **Nighan, W. L.**, *High power TEM_{00} operation of diode-pumped solid state lasers*, Proceedings: SPIE, Vol. 3611, pp. 119–131, 1999.

[17] **Shi, P., Li, D., Zhang, H., Wang, Y.** and **Du, K.**, *An 110W Nd:YVO_4 slab laser with high beam quality output*, Optics Communications, Vol. 229, pp. 349–354, 2003.

[18] **Tzuk, Y., Tal, A., Goldring, S., Glick, Y., Lebiush, E., Kaufman, G.** and **Lavi, R.**, *Diamond cooling of high-power diode-pumped solid-state lasers*, IEEE Journal of Quantum Electronics, Vol. 40, No. 3, pp. 262–269, 2004.

[19] **Forget, S., Balembois, F., Georges, P.** and **Devilder, P. J.**, *A New 3D Multipass amplifier Based on Nd:YAG or Nd:YVO_4 crystals*, Applied Physics B, Vol. 75, pp. 481–485, 2002.

[20] **Minassian, A., Thompson, B., Smith, G.** and **Damzen, M. J.**, *High-power scaling ($>$ 100 W) of a diode-pumped TEM_{00} Nd:$GdVO_4$ laser system*, IEEE

Journal of Selected Topics in Quantum Electronics, Vol. 11, No. 3, pp. 621–625, 2005.

[21] **Siebold, M., Hornung, M., Hein, J., Paunescu, G., Sauerbrey, R., Bergmann, T.** and **Hollemann, G.**, *A high-average-power diode-pumped Nd:YVO_4 regenerative laser amplifier for picosecond-pulses*, Applied Physics B: Lasers and Optics, Vol. 78, pp. 287–290, 2004.

[22] **Pearce, S.** and **Ireland, C. L. M.**, *Performance of a cw pumped Nd:YVO_4 amplifier with kHz pulses*, Optics and Laser Technology, Vol. 35, pp. 375–379, 2003.

[23] **Brignon, A., Feugnet, G., Huignard, J.-P.** and **Pochelle, J.-P.**, *Compact Nd:YAG and Nd:YVO_4 amplifiers end-pumped by a high-brightness stacked array*, IEEE Journal of Quantum Electronics, Vol. 34, No. 3, pp. 577–585, 1998.

[24] **Snell, K., Lee, D.** and **Wall, K.**, *Diode-pumped, High-Power cw and Mode-locked Nd:YLF Lasers*, Advanced Solid State Photonics 2000. Technical Digest.

[25] **Lee, D., Snell, K. J., Manni, J. G.** and **Wall, K. F.**, *Diode-pumped, High-Power Nd:YLF and Nd:YVO4 Lasers*, The Solid State and Diode Laser Technology Review (SSDLTR), 2000.

[26] **Snell, K., Lee, D.** and **Manni, J.**, *High Average Power, High Repetition Rate Nd:YVO_4 MOPA Laser System*, CLEO 1999. Postdeadline Paper, CDP-1.

[27] **Ostermeyer, M., Kappe, P., Menzel, R.** and **Wulfmeyer, V.**, *Diode-pumped Nd:YAG master oscillator power amplifier with high pulse energy, excellent beam quality, and frequency-stabilized master oscillator as a basis for a next-generation lidar system*, Applied Optics, Vol. 44, No. 4, pp. 582–590, 2005.

[28] **Kracht, D., Wilhelm, R., Frede, M., Fallnich, C., Seifert, F., Willke, B.** and **Danzmann, K.**, *High Power Single-Frequency Laser for Gravitational Wave Detection*, Advanced Solid State Photonics 2006. Technical Digest, WE1.

[29] **Wall, K. F., Jaspan, M., Dergachev, A., Szpak, A., Flint, J. H.** and **Moulton, P. F.**, *A 40W single-frequency, Nd:YLF master oscillator/power amplifier*

system, OSA Trends in Optics and Photonics, Vol. 26 Advanced Solid State Photonics, pp. 216–221, 1999.

[30] **Xi, W.-Q., Zhao, J.-Y.** and **Zhang, K.-S.**, *A high-power continuous-wave laser-diode end-pumped Nd:YVO_4 Laser of single-frequency operation*, Chinese Physics Letters, Vol. 22, No. 5, pp. 1144–1147, 2005.

[31] **Schulz, B., Frede, M., Wilhelm, R.** and **Kracht, D.**, *High Power End-Pumped Nd:YVO_4 Amplifier*, Advanced Solid State Photonics 2006. Technical Digest, WB15.

[32] **Musgrave, I. O.**, Study of the Physics of Power Scaling of End-Pumped Solid-State Laser Sources based on Nd:YVO_4 , Ph.D. thesis, Optoelectronics Research Centre, University of Southampton, 2003.

Chapter 2

Power Scaling in Solid-State Lasers and Amplifiers

2.1 Introduction

'Solid-state lasers'describes all lasers in which the host medium for the active laser ion is either a crystal, a glass or a ceramic. Power scaling of solid-state lasers and amplifiers is a field that dates back to the birth of lasers in the 1960s. Kogelnik, 1966 [1] laid down the basic tools required for designing optical systems and resonators. Over the years, as new solid-state materials and new pumping techniques have become available, the average output powers attainable have increased from milliWatts to $\gtrsim$10 kilowatts [2]. This has largely been due to the development of high brightness laser diode bars and stacked diode arrays used to pump the materials. Pump powers of many kilowatts are now attainable in the 780-980nm wavelength region at relatively low cost. The main factors affecting the maximum power output of solid-state lasers are the maximum available power and spectral brightness of the pump source and the efficiency of the laser oscillator which in turn is governed by the losses in the cavity; the choice and quality of the laser crystal used and problems caused by heat generation in the laser crystal. The development of high power pump sources, high quality laser materials and low loss optical components has meant that the main challenges in power scaling today are dominated by management of thermal effects in the gain medium.

This chapter describes the main design considerations for producing high power

solid-state lasers and amplifiers with particular emphasis on end-pumped systems. The relative merits of different laser host materials are discussed with regard to power scaling and the reason for choosing Nd:YVO_4 in our system is explained. Choice of pump source and pumping geometry and detrimental thermal effects in the gain medium are described, and various ways of minimising these effects are discussed.

2.2 The Solid-State Laser

At low power levels, conventional solid-state lasers, which use well known host materials, have been well understood for many years. Their performance can be predicted reasonably successfully using some simple principles and analysis.

2.2.1 The Four-Level Laser Scheme

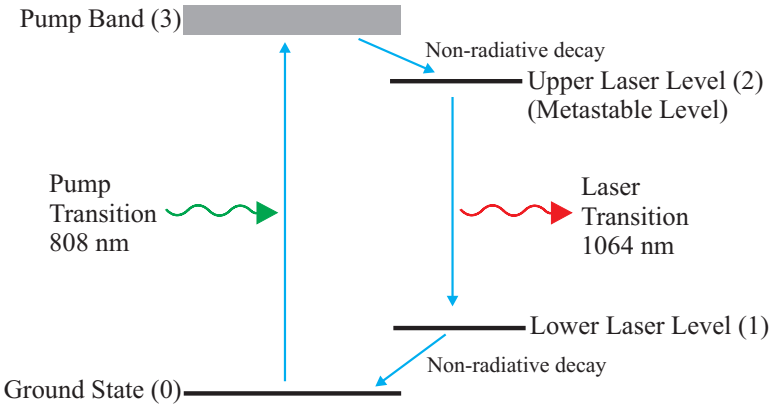

Figure 2.1: Energy level diagram for a four level laser

Most solid-state lasers use rare earth ions as the active laser ion. The energy level structure of these ions is generally characterised by either the three-level or four-level system. The four-level system is shown schematically in Figure 2.1. The absorption of a pump photon by the ion takes place between the ground state (labelled 0) and the pump band (labelled 3) and is followed by a rapid non-radiative decay to the upper laser level with a lifetime represented by τ_{32}. The upper laser level (labelled 2), also called the metastable level, has

a long lifetime, τ_{21}, which means that a population inversion can be achieved and hence laser action can take place. An ion in the metastable level will decay by spontaneous or stimulated emission of a photon to the lower laser level (labelled 1). Unlike in a three-level system, where the lower laser level is the same or close to the ground state, the lower laser level in a four-level system is significantly higher than the ground state and has a fast decay lifetime τ_{10} to the ground state and therefore it remains essentially unpopulated.

2.2.2 The Laser Oscillator

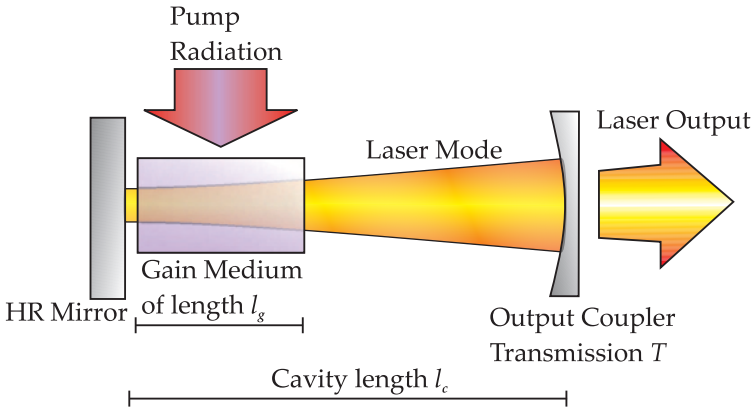

Figure 2.2: A simple solid-state laser oscillator.

Figure 2.2 shows the simple case where a laser oscillator is set-up by placing a gain medium between two mirrors forming a cavity. One with high reflectivity (HR) and the other with partial reflectivity. The cavity shown here uses one plane and one concave mirror but many configurations, using any number of mirrors, are possible. In this example the gain medium is side-pumped but end-pumping is also common. A number of different pumping geometries are discussed later in this chapter. The laser signal builds up from noise in the cavity by bouncing back and forth between the mirrors. On each transit of the gain medium it sees gain and on each reflection, or transit through other optical components, it sees loss. When the pump power reaches threshold, the round-trip gain becomes equal to the round-trip loss. Beyond this pump power, a laser output emerges from the partially reflective mirror at a power proportional to the pump power (above the threshold pump power) with a constant of proportionality known as the slope efficiency. Analytical expres-

sions for the threshold pump power and slope efficiency for a simple oscillator are shown in the next section.

The circulating laser field, within the cavity, is known as the laser mode and in general it contains a number of transverse and longitudinal oscillating modes. The modes which a resonator can support depends on the spacings, curvatures and alignment of the mirrors as well as on the gain distribution in the active medium and aperture effects caused by any of the optical components. It is normally desirable to operate a laser in the fundamental (TEM_{00}) transverse mode, since this offers the lowest possible divergence and hence the highest brightness beam. Indeed, measurement of the beam-size and divergence of a laser beam is used to determine the beam quality as explained in Section 2.2.5. The design of optical resonators based on modelling of Gaussian beam propagation is explained in Chapter 3.

The longitudinal modes of a resonator are present at regular frequency intervals, separated by the axial mode spacing $\Delta\nu$ which is equal to:

$$\Delta\nu = \frac{c}{2l_c}, \tag{2.1}$$

where l_c is the effective cavity length. The number of axial modes that actually oscillate in a laser depends on the cavity configuration, the gain bandwidth of the laser medium and also on the broadening mechanisms of the laser transition. Solid-state laser crystals are generally homogeneously broadened which means that every atom has the same lineshape and frequency response so that they are essentially indistinguishable from one another. This means that each axial mode competes for gain with every other axial mode so it is possible that only the mode with the highest gain oscillates, ie. single-frequency operation. However practical lasers which use standing-wave cavities suffer from an effect called *spatial hole burning* whereby the gain varies in the axial (propagation) direction due to strong saturation of the gain at the antinodes of the standing wave and no saturation at the nodes. This inhomogeneity in the spatial gain distribution means that, generally, many axial modes will oscillate, each one accessing different regions of gain and therefore not competing with one another. In order to achieve single-frequency (single axial mode) operation various techniques have been adopted as will be discussed in Chapter 6.

2.2.3 Threshold and Slope Efficiency

The most important measurable parameters that can be predicted analytically for a laser, are the threshold pump power $P_{p,th}$ and output power P_{out} from which the slope efficiency η_s can be deduced. For the simple case of an end-pumped oscillator, with Gaussian intensity distributions for the pump and laser mode, the approximate expressions for $P_{p,th}$ and η_s can be derived using a simplified rate equation approach [3]. The resulting expressions are [4]:

$$P_{p,th} = \frac{\pi h \nu_P (L+T)({w_p}^2 + {w_l}^2)}{4\sigma_{21}\tau_f \eta_q \eta_{abs}} \tag{2.2}$$

and

$$\eta_s = \left(\frac{T}{L+T}\right)\left(\frac{\nu_l}{\nu_p}\right)\eta_{abs}\eta_q\eta_{PL}, \tag{2.3}$$

where ν_L and ν_P are laser and pump frequencies respectively, w_l and w_p are the average laser and pump spot sizes in the crystal respectively, L is the cavity loss, T the output coupler transmission ($L + T \ll 1$), σ_{21} is the laser transition cross section, τ_f the fluorescence lifetime, η_q is the pumping quantum efficiency (the fraction of pump photons which reach the meta-stable state), $\eta_{abs} \approx 1 - \exp(-\alpha_p l_g)$ is the total fraction of pump power absorbed over the length of gain medium l_g, α_p is the absorption coefficient for the pump and η_{PL} is an effective spatial overlap factor for pump beam and laser mode given by [4] as:

$$\eta_{PL} = \frac{{w_l}^2({w_l}^2 + 2{w_p}^2)}{({w_l}^2 + {w_p}^2)^2}. \tag{2.4}$$

This is valid in the low power regime where $I/I_{sat} \ll 1$, but $\eta_{PL} \to 1$ for the high power regime $I/I_{sat} \gg 1$ where $I_{sat} = h\nu_l/\sigma_{21}\tau_f$ is the saturation intensity. This expression takes into account the spatial and axial distribution of both the laser mode and the pump beam (assuming that the spot sizes are approximately constant over the length of the gain medium) and results in an effective overlap factor of $\eta_{PL} = 0.75$, for matched laser and pump beam sizes ($w_l = w_p$), in contrast to a plane-wave approximation which gives $\eta_{PL} = 1$.

2.2.4 Laser Amplifiers

A popular strategy for power scaling in solid-state lasers is to start with a low or moderate power laser oscillator and then increase the power with a laser

amplifier or chain of amplifiers to form a master-oscillator-power-amplifier (MOPA). The amplifiers may or may not have the same basic geometry as the master-oscillator, but in the simple case of an end-pumped system the amplifier can consist of an end-pumped laser rod through which the laser signal is coupled via a dichroic mirror.

The total gain of a laser signal through an amplifier depends on a number of material, geometrical and optical parameters. However, if we consider the simple case of single-pass amplification of a laser signal passing through an inverted gain medium, the gain for a very small signal can be predicted analytically. The total small signal gain G_0, is the gain through the amplifier for a signal intensity small enough not to significantly deplete the upper state population. It is given by the expression

$$G_0 = \exp(g_0 l), \tag{2.5}$$

where l is the length of active medium traversed and for a 4-level transition, g_0 is the small signal gain per unit length given by

$$g_0 = \sigma_{21} n_2, \tag{2.6}$$

where n_2 is the unsaturated upper state population density. A similar expression to equation (2.5) can also be used for the saturated gain G if n_2 is replaced with the saturated upper state population density.

In the small signal regime, a continuous laser signal passing through a medium with uniform upper state population density, which does not vary in the propagation direction, will grow in power exponentially with distance z through the medium. However, for a larger signal intensity a significant number of excited atoms decay by stimulated emission and, since gain is proportional to the number of excited atoms, the gain is thus reduced and the amplifier is said to be saturated. In the highly saturated regime, the gain becomes low ($g_0 l \ll 1$) and hence

$$\exp(g_0 l) \simeq 1 + g_0 l, \tag{2.7}$$

which implies that the signal intensity grows approximately linearly with distance along the gain medium as all the excited atoms are stimulated. A detailed analysis of the unsaturated and saturated gain in an end-pumped amplifier, in both single and multiple pass configurations, is given in Chapter 4.

2.2.5 The M^2 Parameter

The M^2 parameter is a measure of the beam propagation factor or *beam quality* of a laser beam. Beams with good beam quality can propagate with low divergence when collimated and can also be focused down to small spot-sizes. For a beam propagating though a medium with uniform refractive index and through ideal lenses and mirrors, the M^2 parameter remains an invariant property of the beam. A TEM_{00} beam has the best theoretical beam quality possible and its M^2 parameter is equal to 1. Such beams have pure Gaussian intensity distributions for all propagation distances. All other beams have $M^2 > 1$. The M^2 parameter is commonly referred to as the number of times diffraction-limited a particular beam is.

The M^2 parameter is determined by measuring the beam radius as a function of the propagation distance in the region close to a focal point (beam waist). For a beam propagating along the z-axis, the M^2 value is normally measured in the x and y planes independently to allow for beams which are not cylindrically symmetric. In order to obtain accurate M^2 values the beam radius should be measured using the second moment or variance method [5,6] whereby:

$$\sigma_x^2 = \frac{1}{P}\int_y\int_x x^2 I(x,y)\mathrm{d}x\mathrm{d}y, \tag{2.8}$$

where x is the distance from the optic axis, $I(x,y)$ is local intensity and P is the total power given by:

$$P = \int_y\int_x I(x,y)\mathrm{d}x\mathrm{d}y. \tag{2.9}$$

The beam radius w_x is related to the standard deviation σ_x by the relation:

$$w_x = 2\sigma_x. \tag{2.10}$$

Figure 2.3 shows the beam radius for a beam propagating in the focal region. The the main parameters of interest for a beam waist are labelled. The beam size $w(z)$ and wavefront radius of curvature $R(z)$ as a function of the propagation distance z can be expressed as follows [3]:

$$w(z) = w_0\sqrt{1+\left(\frac{M^2\lambda z}{n\pi w_0^2}\right)^2}, \tag{2.11}$$

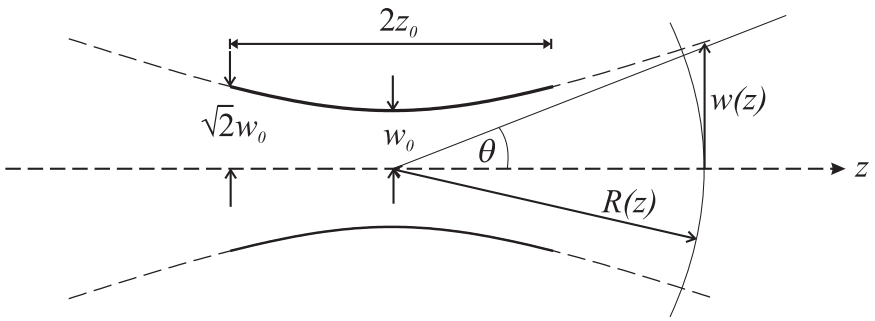

Figure 2.3: Laser beam size versus propagation distance. z_0 is the Rayleigh range over which the beam expands to $\sqrt{2}$ times the minimum waist w_0. $2z_0$ is known as the confocal parameter, θ is the far field divergence angle and $w(z)$ and $R(z)$ are the spot size and wavefront radius of curvature respectively, as a function of propagation distance z.

$$R(z) = z\left[1 + \left(\frac{n\pi w_0^2}{M^2\lambda z}\right)^2\right]. \tag{2.12}$$

These can be reduced to give an expression for the Rayleigh range z_0 over which the beam expands to $\sqrt{2}$ times the minimum waist size:

$$z_0 = \frac{n\pi w_0^2}{M^2\lambda}, \tag{2.13}$$

and the far field divergence angle θ can be given by:

$$\theta = \frac{M^2\lambda}{n\pi w_0}. \tag{2.14}$$

Equations (2.13) and (2.14) are extremely useful for estimating the beam quality and minimum spot sizes of laser beams in many situations.

2.3 Heat Deposition in the Gain Medium

Even when using high quality crystals and narrow linewidth pump sources, the efficiency of solid-state lasers is theoretically limited by the quantum defect of the laser transition. This means that a proportion of the pump power will inevitably be converted to heat in the gain medium. Another problem is that some of the excited ions are lost via concentration quenching processes, so that they cannot contribute to stimulated emission, which leads to additional heating.

2.3.1 The Quantum Defect

The quantum defect is simply the fractional difference in energy between the lasing photons and the pump photon. In terms of energy level transitions, the relaxation from the pump band to the upper laser level and from the lower laser level to the ground state are all thermal in the form of phonon emission. This means that the quantum defect QD can be expressed as:

$$QD = \frac{E_p - E_l}{E_p} = 1 - \frac{\lambda_p}{\lambda_l} = 1 - \frac{\nu_l}{\nu_p}, \tag{2.15}$$

where E_p and E_l are the pump and laser photon energies respectively and λ_p, ν_p and λ_l, ν_l are the pump and laser wavelengths and frequencies respectively, since the photon energy is inversely proportional to the wavelength. It is easy to see why using a laser transition, where the pump wavelength is close to the lasing wavelength is favourable since the quantum defect heating will be lower. Specialised lasers with quantum defects as low as 2.9% have been reported [7]. In general however, other factors such as the energy levels of strongest pump absorption and preferential lasing wavelengths are often more important when high output power and high efficiency is required.

2.3.2 Lifetime Quenching

The behaviour of solid-state laser materials at population inversion densities typical for low pump powers can be understood by simple rate equation analysis. As the pump power density is increased and the population inversion density becomes large, deviations from this well defined behaviour can be observed. Spectroscopic effects that are normally negligible can become significant. At high inversion densities, several different processes, known collectively as lifetime quenching processes, can act to reduce the number of excited ions in the upper laser level and hence effectively reduce the effective lifetime. This leads to a reduction in efficiency of the laser (especially in pulsed mode) and also contributes additional heat loading in the laser material via non-radiative decay. Examples of these processes are energy-transfer-upconversion, excited state absorption and cross relaxation.

2.3.2.1 Energy-Transfer-Upconversion

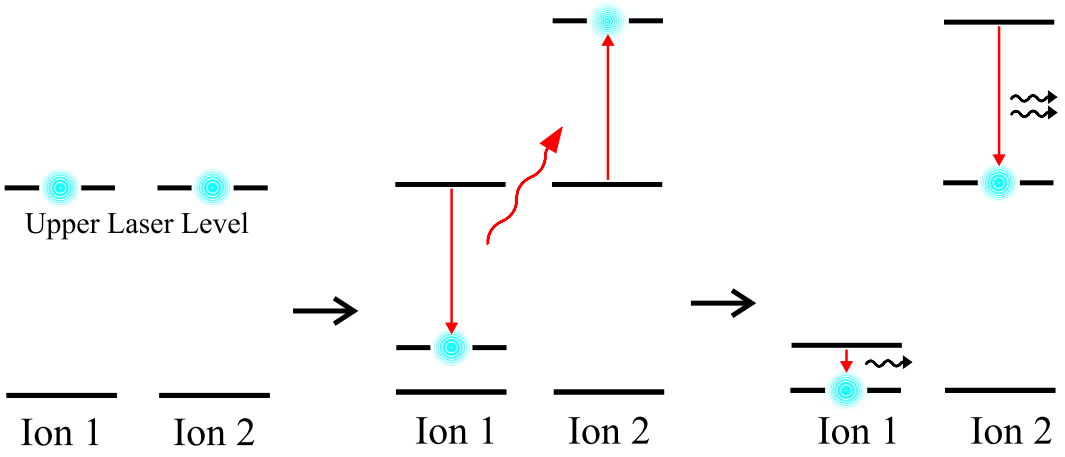

Figure 2.4: Schematic of Energy Transfer Upconversion

Energy-transfer-upconversion (ETU) occurs when two neighboring excited ions, a donor and an acceptor, exchange energy. Energy is transferred from donor to acceptor and consequently the acceptor is excited to a higher energy level whilst the donor ends up in a lower lying level. The particular levels that the donor and acceptor end up in depends on the possible transitions of the material. The result however is generally the same: the acceptor decays back to the upper laser level and the donor decays to the ground state. These decay processes can be radiative or non-radiative, or a combination of both, depending on the material. ETU essentially converts two excited ions into one excited ion and extra heat, as shown in Figure 2.4. The relative influence of ETU on the upper state population depends on the upconversion parameter (W) of the laser material, and the number density (N_2) of excited ions in the laser medium, such that the rate of change of the number density with time is given by [8]:

$$\frac{\mathrm{d}N_2}{\mathrm{d}t} = R - \frac{N_2}{\tau_f} - WN_2^2. \tag{2.16}$$

The two main factors effecting N_2, that can be controlled when designing a laser system are the ion doping concentration in the material which determines the pump absorption length, and the intensity of the pump radiation. Additionally, W usually increases with increasing doping concentration, which adds a further advantage of using low doping concentrations. A more detailed discussion of the influence of ETU on the performance of laser systems will follow in chapter 4.

2.3.2.2 Excited State Absorption

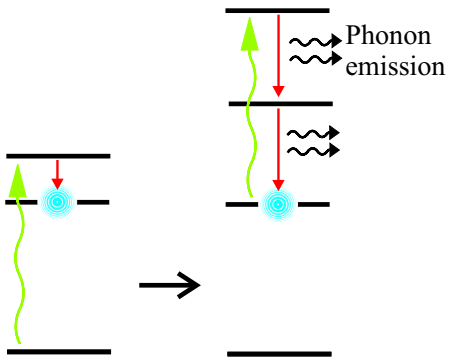

Figure 2.5: Schematic of Excited State Absorption

Excited state absorption is another process which can reduce the efficiency of a laser and lead to additional heating. In this case an ion in the upper laser level absorbs another pump photon, as shown in Figure 2.5, or a laser photon and is raised to a higher energy level before decaying by non-radiative transitions back to the upper laser level. The likelihood of ESA causing an appreciable effect on the performance of the laser depends on the relative cross sections of the ESA transition and stimulated emission [9].

2.3.2.3 Cross Relaxation

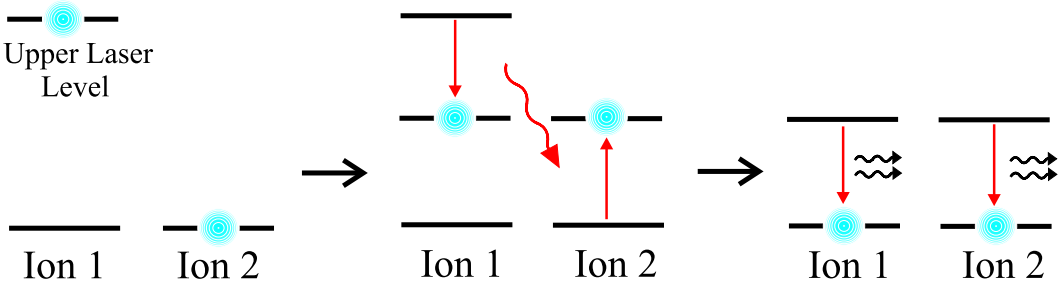

Figure 2.6: Schematic of Cross Relaxation

Cross relaxation, shown schematically in Figure 2.6, occurs when an ion in the metastable level interacts with a ion in the ground state. The ion in the metastable level emits a photon and moves down to an intermediate level and the ion in the ground state absorbs the photon and is moved up to this intermediate level. Both ions then relax down to the ground state via multi-phonon emission or in some cases photon emission.

2.4 Nd:YVO_4 as a Laser Medium

Nd^{3+} was the first trivalent rare earth ion to be used in a laser. The most common host materials are Yttrium Aluminium Garnet ($Y_3Al_5O_{12}$ or YAG), Yttrium Orthovanadate (YVO_4), Yttrium Lithium Fluoride ($YLiF_4$ or YLF) and glass. Nd:YAG was the first to become widely used, and for many years, was one of the most efficient solid-state laser materials. Stimulated emission has since been achieved in over 100 host materials [3]. Nd:YVO_4 was first proposed for use as a laser material by O'Connor in 1966 [10], however it took until 1987 for the optical quality of the crystals to become good enough to be comparable to Nd:YAG for efficiency [11].

The energy level structure of the Nd^{3+} ion allows pumping at around 808 nm to cause excitation to the ${}^4F_{5/2}/{}^2H_{3/2}$ manifold, from where it rapidly relaxes down to the metastable ${}^4F_{3/2}$ level. The dominant lasing transition is from the ${}^4F_{3/2}$ level to the ${}^4I_{11/2}$ level and weaker lasing transitions are also possible from the metastable level to the ${}^4I_{9/2}$ and ${}^4I_{13/2}$ levels. The exact energy or wavelength of these transitions varies a little between host materials but in Nd:YVO_4 these three laser transitions correspond to wavelengths 1064 nm, 914 nm and 1342 nm respectively. Lasers with an output at 1342 or 914 can be made with relative ease [12], however the 1064 line provides potentially the highest yield of photons by stimulated emission due to its higher emission cross section. The 914 transition does, however, have the advantage of a lower quantum defect. The energy level structure for Nd:YVO_4 , including all the important transitions, is shown in Figure 2.7. The cross sections for ESA and cross relaxation in Nd:YVO_4 are relatively low so they can normally be neglected, however ETU can be quite significant in some situations, that are discussed later in this thesis. The energy level structure for Nd^{3+} remains basically the same for different host materials, with small differences in the photon wavelengths for different transitions. The most significant differences between different hosts are in the relative cross sections of the transitions, the spontaneous emission lifetimes, the absorption and emission bandwidths and the thermal and mechanical properties of the material. Table 2.4 outlines some of the basic optical and thermal properties of Nd:YVO_4 , Nd:YAG and Nd:YLF.

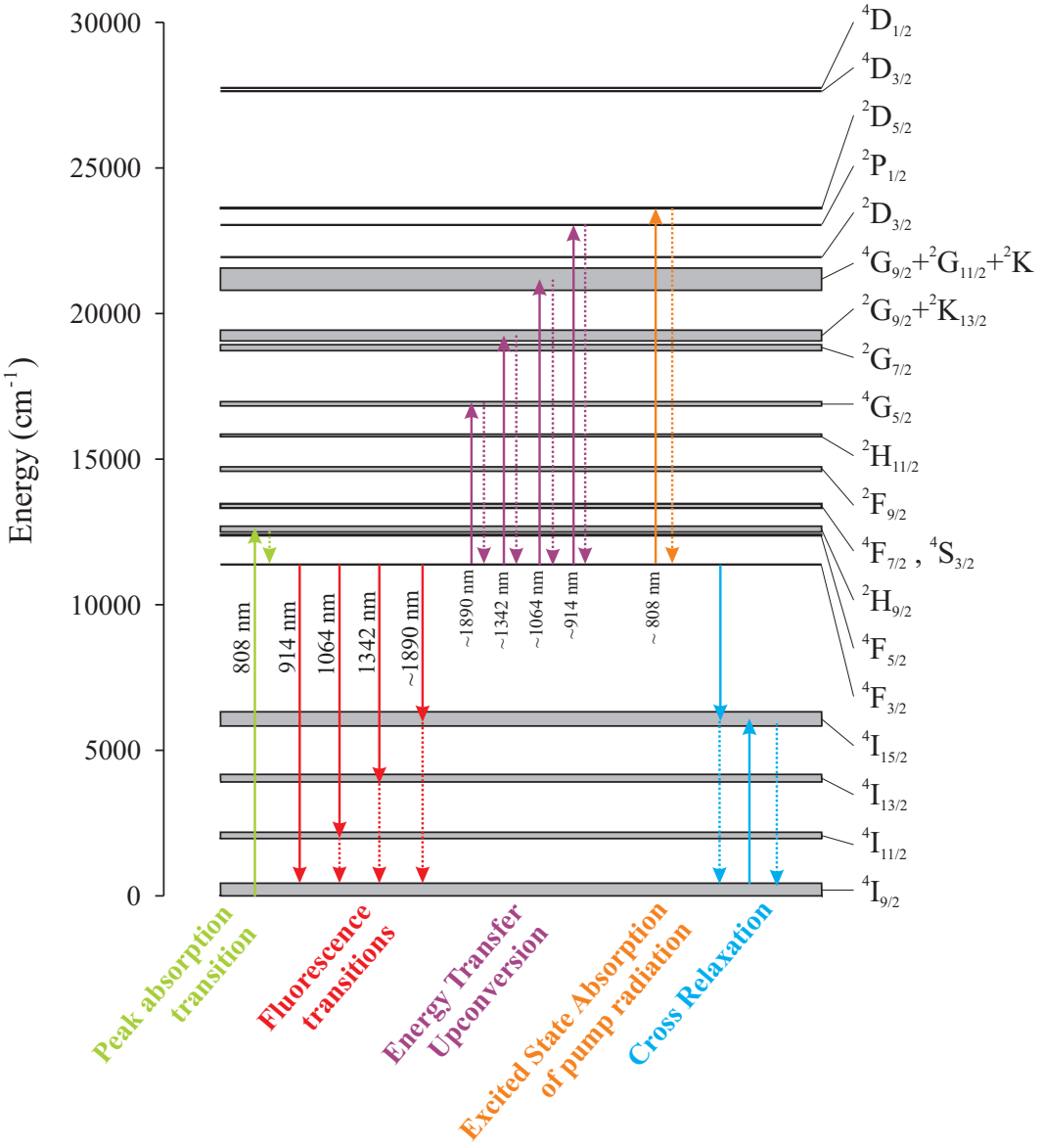

Figure 2.7: Diagram showing (to scale) the energy level structure for Nd^{3+} in a YVO_4 host crystal. The main transitions are shown, including the pump and fluorescence transitions as well as several lifetime quenching mechanisms: ETU, ESA and Cross Relaxation. The dotted lines show heat generating transitions (Data from [13] and [9])

Properties	Nd:YVO_4	Nd:YAG	Nd:YLF
Laser Wavelength (λ_l) (nm)	1064	1064	1047 (π) 1053 (σ)
Peak Absorption Wavelength (λ_p) (nm)	808	808	792 (π) 797 (σ)
Stimulated emission cross section (σ_{21}) ($\times 10^{-19}$ cm^2)	25 (π) 7 (σ)	2.8	1.8 (π) 1.2 (σ)
Fluorescence lifetime (τ_f) (µs)	90	230	485
Linewidth (FWHM) ($\Delta\lambda$) (nm)	0.96	0.51	1.47
Peak absorption coefficient (α_p) (cm^{-1})	31.4 (π) 9.2 (σ)	7	10.8 (π) 3.59 (σ)
Absorption bandwidth † (nm)	15.7	2.5	4.0 (@792nm) 3.2 (@797nm)
Thermal Conductivity (K_c) (W m^{-1}K^{-1})	5	14	6.3
Thermo-optical coefficient (dn/dT) ($\times$ 10^{-6} K^{-1})	8.5 3.0	7.3	-4.3 (π) -2.0 (σ)
Thermal fracture limit (F) (W cm^{-1})	57.6	94.8	22

† Defined as wavelength range where 75% of pump power is absorbed in a 5mm thick crystal

Table 2.1: Optical and thermal properties of Nd:YVO_4 compared to Nd:YAG and Nd:YLF for 1% Nd doping concentration. Data from [3,14,15].

Nd:YVO_4 and Nd:YLF are naturally birefringent so some of the properties differ between the extraordinary (c) axis and the ordinary (a) axis, which correspond to π and σ polarisations respectively. Normally in Nd:YVO_4 , only the c direction is used because σ_{21} is much higher in this direction and therefore the laser output is always π polarised. In Nd:YLF, σ_{21} in the two orientations does not differ by so much so the π polarisation can be used to generate 1047 nm radiation and the σ polarisation can be used to generate 1053nm radiation. Nd:YAG is isotropic so stimulated emission does not favour a particular polarisation. Generating polarised output in a Nd:YAG laser requires the use of polarisation discriminating elements.

As shown in Table 2.4, Nd:YVO_4 has a much higher stimulated emission cross section and consequently a higher $\sigma_{21}\tau_f$ product than Nd:YAG and Nd:YLF. From equations (2.2) and (2.3) we can see that this leads to a relatively low threshold and high slope efficiency assuming all other parameters are the same. Another important feature is that Nd:YVO_4 has a stronger absorption coefficient and a broader absorption bandwidth than the other two. The latter makes it more tolerant to temperature induced variations in the pump diode

wavelength. The pump absorption coefficient in the π direction is more than four times that of Nd:YAG and three times that of Nd:YLF. This means that shorter laser crystals can be used to achieve the same absorption efficiency. This is advantageous when end-pumping with laser diodes because focusing them to small spot sizes implies having a short Rayleigh range due to their relatively poor beam quality. However, the associated high thermal loading density means that it is normally necessary to reduce the Nd^{3+} doping concentration somewhat to increase the absorption length. This can still be advantageous because it reduces the impact of ETU.

While Nd:YVO_4 has very favourable optical properties, its thermal properties can be considered to be a little worse than Nd:YAG and Nd:YLF. While Nd:YLF has the lowest fracture limit and only slightly higher thermal conductivity than Nd:YVO_4 , its resistance to thermal lensing effects are good. Unusually, it has a low and negative thermo-optical coefficient which means that a weak negative thermal lens is produced by intense end-pumping. Both Nd:YVO_4 and Nd:YAG produce positive thermal lenses under intense diode end-pumping. Nd:YAG has the highest thermal conductivity and the highest fracture limit, however it does suffer from thermal stress induced birefringence. Nd:YVO_4 has around one third the thermal conductivity of Nd:YAG and less than two thirds the fracture limit. The additional properties of the thermal expansion coefficient and the stress-optic coefficient are also important when considering the thermal lensing behaviour of these materials but were unavailable to include in Table 2.4. The axial temperature increase, caused by end-pumping, can cause thermal expansion resulting in end-face bulging which forms a positive thermal lens. For Nd:YAG and Nd:YVO_4 this increases the overall thermal lens strength while in Nd:YLF it acts to partially compensate for the negative thermal lens due to its negative thermo-optical coefficient. Thermal expansion also causes an associated stress distribution within the gain medium which leads to further modification of the refractive index. The stress-optic coefficient describes this change in refractive index with respect to the stress in the material. In Nd:YAG this is more important because it suffers from stress induced birefringence, where in Nd:YVO_4 and Nd:YLF their stress induced birefringence is negligible compared to their natural linear birefringence. Its worth noting that, apart from quantum defect heating, ETU is the predominant effect

leading to additional heating in all Nd^{3+} doped materials due to a higher interaction cross section than ESA and cross relaxation. Particular care is needed to avoid fracture under non-lasing or unsaturated conditions when the rate of ETU becomes higher.

2.5 Thermal Effects

There are a number of mechanisms that cause heat deposition in a laser medium under intense optical pumping. In particular, end-pumping laser materials with high power diode sources can lead to large amounts of heat being generated. Active cooling of the gain medium is essential in most high power lasers and amplifiers to remove this unwanted heat. For end-pumped rods, edge-cooling of the gain medium is usually the only option and this can be achieved by mounting the rod in a water-cooled copper heat sink. This means that most of the heat flow is in the radial direction causing radial temperature gradients which generally causes a number of undesirable effects. The temperature distribution in an end-pumped edge-cooled laser rod can be described by an exponential decay in the z-direction in correlation with the exponential decay in absorbed pump power with propagation distance, and an approximately quadratic radial dependence within the pump beam radius [16] and an exponential radial dependence outside the pump beam radius (assuming a 'top-hat' pump beam profile). Figure 2.8 shows, graphically, an estimate of the normalised temperature increase ΔT for a typical rod of dimensions 3mm diameter and 10mm length, caused by end-pumping with a pump beam of radius 0.3mm and a 'top-hat' profile.

2.5.1 Thermal Stress Induced Birefringence

Intense optical pumping and the associated thermal loading in all laser media, causes differential expansion and hence stresses in the material. In general these stresses cause birefringence in the form of differences in refractive indices between the regions under tension and the regions under compression. In end-pumped systems this is particularly problematic since the material be-

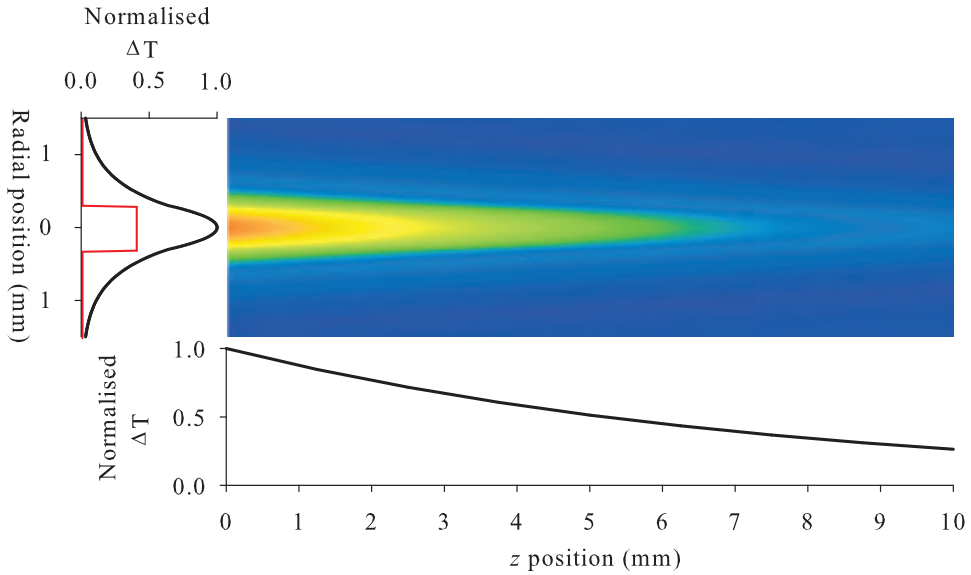

Figure 2.8: Estimated temperature distribution in a typical end-pumped laser rod with a 'top-hat' pump beam profile (shown by red line).

comes compressed in the radial direction and under tension in the tangential direction. The resulting birefringence causes radial and azimuthal dependent retardation for beams passing through the laser rod. A polarised incoming laser beam can therefore become depolarised on transit through the material. Laser materials which have natural linear birefringence, like crystalline Nd:YVO_4 and Nd:YLF, avoid this problem because the stress induced birefringence is usually negligible compared to their natural birefringence. Also, their thermal expansion coefficients are usually different in their a and c-axes, so thermally induced stresses are higher in one direction. In isotropic gain media like Nd:YAG and doped ceramics however, stress induced birefringence is a problem. In laser configurations, a Brewster-angled plate can be used to discriminate between two orthogonal polarisations to produce a linearly polarised output, however the loss due to depolarisation can become large at higher pump powers and additional compensating schemes are often required [17]. This is a another very attractive reason for choosing Nd:YVO_4 as the gain medium in this work.

2.5.2 Aberrated Thermal Lensing

In addition to thermal stress induced changes in refractive index, the temperature change itself causes changes in refractive index. The change in refractive index with respect to temperature change is described by the thermo-optical coefficient $\mathrm{d}n/\mathrm{d}T$, included in Table 2.4. The combination of stress and temperature induced refractive index change leads to the effect of thermal lensing in the gain medium. This lensing is made worse still by the physical distortion of the end-faces of the laser rod caused by thermal expansion in an effect known as end-face bulging. The relative contribution of these three effects on the overall thermal lens depends on the thermo-optical and thermo-mechanical properties of the gain medium but, in Nd:YAG for example, the refractive index variation with temperature accounts for over 80% of the thermal lens contribution [4]. An analytical expression for the temperature distribution in an edge-cooled end-pumped laser rod has been derived by solving the general steady state thermal transport equation, assuming no axial heat flow [18]:

$$\underline{\nabla} \cdot \underline{u}(r,z) = Q(r,z), \tag{2.17}$$

where $\underline{u}(r,z)$ is the heat flux, and $Q(r,z)$ is the power per unit volume deposited as heat in the laser crystal. Considering only the contribution to thermal lensing due to temperature dependence of refractive index this model can be used to predict the thermal lens focal length for an arbitrary pump beam intensity profile $I_p(r)$ [19]:

$$f_{th}(r) = \frac{2\pi K_c r^2}{P_{abs}\gamma(\mathrm{d}n/\mathrm{d}T)s(r)}, \tag{2.18}$$

where K_c is the thermal conductivity, P_{abs} is the total absorbed pump power, γ is the fraction of absorbed pump power dissipated as heat and $s(r)$ is the fraction of pump power contained within a disc of radius r given by:

$$s(r) = \frac{2\pi}{P_p}\int_0^r r' I_p(r')\mathrm{d}r'. \tag{2.19}$$

In general, equation (2.18) predicts a thermal lens with a radially varying focal length for a pump beam which has a radially varying intensity. For most realistic pump beam profiles, which have strong radial intensity variation, this

implies a highly aberrated thermal lens which will cause severe degradation of laser beam quality.

More detailed discussions of the influence of the pump beam profile on the thermal lensing and thermal lens induced aberration and strategies for coping with it will follow later in this thesis.

2.5.3 Thermally-Induced Stress Fracture

Due to the high stresses that are produced by intense diode pumping, thermal stress fracture places an ultimate limit on how much pump power can be absorbed in a laser material. Stress fracture normally occurs when the tensile stress in the laser rod reaches the breaking stress of the material. Table 2.4 includes the fracture limit in (W cm^{-1}) for the three materials discussed. While this provides a useful comparison for the materials under approximately the same conditions, several factors other than pump intensity need to be considered to reduce the likelihood of stress fracture. These include the total pump power; the size and shape of the laser material; the doping concentration; the optical quality of the crystal and its dielectric coatings; the efficiency of the cooling mechanism and the temperature to which it is cooled. In practice, it can be difficult to account for all these factors but various techniques can be adopted to maximise the pump power that can be absorbed before thermal fracture occurs and thereby reduce other undesirable thermal effects as well.

2.6 Tackling Thermal Effects

There are three main approaches to tackling detrimental thermal effects in solid-state laser materials. The first is to reduce the thermal loading itself by reducing the quantum defect and minimising concentration quenching by the choice of laser material and wavelengths used. The second is to reduce the temperature of the laser medium by improving the cooling mechanism and changing the heat sinking geometry or architecture of the laser system. The third is to adjust the parameters of the system and employ compensating schemes to reduce the impact of thermal effects on the system performance.

2.6.1 Laser Architecture Alternatives

There have been a wide variety of laser architectures developed, aimed at extending the power and brightness scalability of solid state lasers. One of the principal strategies for reducing thermal effects is to increase the ratio of cooling surface to pumped volume. Another approach that can be applied to a range of laser geometries is cryogenic cooling of the active medium [20]. The thermal properties of most laser materials have been shown to improve dramatically at very low temperatures, such as that of liquid nitrogen. For example the thermal conductivity becomes much larger, making removal of heat much more efficient. Temperature gradients and therefore thermal effects can be made very small. The disadvantage however, is that the complexity becomes prohibitively large for most laser systems. Not only does the cooling system itself add complexity, but also all components which are cooled to low temperature need to be placed in a partial vacuum to avoid problems with condensation. Some of the more popular architectures which can all be used in both laser and amplifier configurations are summarised as follows.

2.6.1.1 Side-Pumped Slab Lasers

The side-pumped slab laser uses a slab of the active medium which is cooled via its top and bottom surfaces which have the largest area. In this scheme, shown in 2.9, one or two of the remaining faces are pumped and the laser radiation is approximately orthogonal to the pump radiation. One particular advantage of side-pumping slabs like this is that the high aspect ratio of the pumping faces of the slab are ideally suited for pumping with high power diode bars which have a similarly high aspect ratio, as discussed in Section 2.7.2. This simplifies the design and means that very high efficiency of incident pump power to available pump power can be achieved. One drawback of this technique, is that the pumped volume is generally not well matched to the laser mode. This implies that it can be difficult to achieve high extraction of stored energy. When a gain medium with a high absorption coefficient such as Nd:YVO_4 is used, the inversion density is localised in the region closest to the pumping face. By utilising a grazing incidence laser beam with a total internal reflection at the pump face, as shown in Figure 2.10 (a), the spatial overlap of

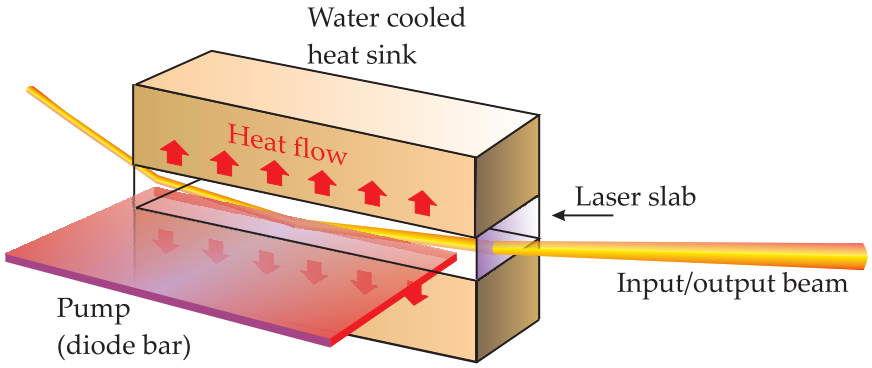

Figure 2.9: Single-bounce slab laser configuration with diode bar side-pumping

the laser and pump volumes is higher and hence the efficiency can be increased compared to a simple beam transit through the material. Moreover, one of the main attractions of this geometry is that the laser beam is inverted horizontally on reflection at the pumped face which means that the distortions, which result from the horizontal gain and temperature gradients, are equal and opposite for each half of the transit through the material. This implies very good compensation for beam quality degradation since the horizontal distortions acquired on the input section of the transit are almost completely reversed on the output section. Another common technique for improving the extraction efficiency is to allow the laser beam to make multiple passes through the material, each one accessing a different region of the slab, as shown in Figure 2.10 (b). From a thermal point of view, slab lasers have some favourable properties such as large cooling area to pump volume ratio, and the pump distribution is more uniform than in end-pumped systems leading to reduced thermal lensing. However, due to the lack of cylindrical symmetry, the thermal lensing effects, when they do occur, can be more problematic with the strong astigmatism of the thermal lens being one example.

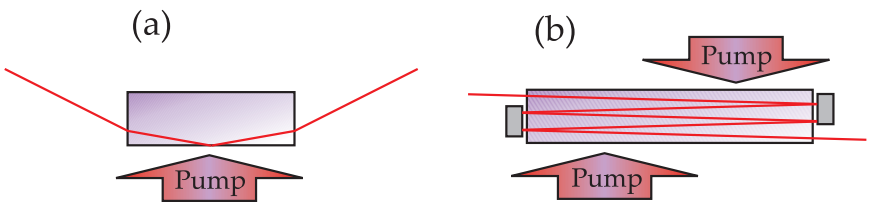

Figure 2.10: Side-pumped slab configurations. (a) Grazing-incidence bounce geometry; (b) Multiple-pass geometry.

2.6.1.2 End-Pumped Rod Lasers

The laser and amplifier systems described later in this thesis are all based on end-pumped rod geometries. In this scheme the pump and laser beams are collinear and the heat removal is through the sides of the rod, as shown in Figure 2.11.

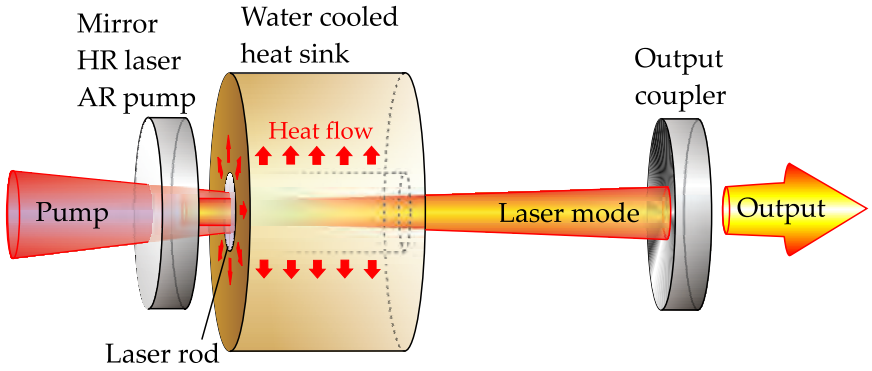

Figure 2.11: End-pumped rod laser configuration

The advantage of this scheme, compared to side pumping for example, is that the pump and laser beams can be very well matched spatially to allow efficient extraction of the stored energy and easy selection of TEM_{00} modes in a resonator. The absorption efficiency can also be made large by choosing a rod of the appropriate length. The cylindrical symmetry of the system, compared to side pumped systems, also implies that the thermal effects are well defined so some of the associated problems can be reduced by simple adjustment of system parameters such as the beam spot sizes. Additionally, the cylindrical symmetry of the system implies that thermal lensing can be compensated for, to some extent, by simple optics. End-pumped rods do, however, suffer from particularly strong thermal lensing effects due the high pump deposition density which leads to strong aberrations in the wings of the pump distribution. One of the most simple techniques for reducing the temperature rise in end-pumped laser materials, is to choose lower doping concentration in the material and longer length. This spreads the thermal load over a larger volume and therefore allows the heat to be removed more efficiently. The main disadvantage is that this requires a pump beam with a better beam quality in order to confine the beam to a small volume in the gain medium. In effect, the pump beam quality limits the maximum length of the rod. Some recent

systems have incorporated undoped end-caps on the laser rods [16, 21]. This implies that pump radiation is only absorbed in the doped region away from the surface. The main advantage of this is to eliminate end-face bulging by minimising the temperature rise at the surface.

2.6.1.3 Thin-Disc Lasers

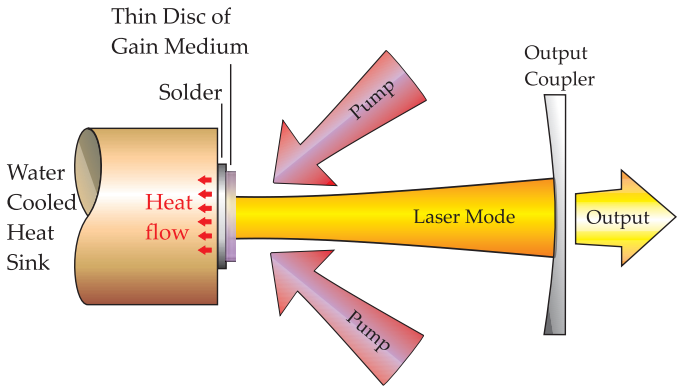

Figure 2.12: An example of a thin-disc laser set-up

One laser geometry, which has been proved to be very successful for power scaling, is the thin-disc laser. In this scheme, shown in Figure 2.12, a thin disc of the gain medium, of a few hundred μm thickness, which is HR coated on the back surface for pump and laser radiation and AR coated on the front surface, is bonded to a water cooled heat sink. A laser resonator is formed between a curved output coupler and the HR surface of the disc. In this scheme, the cooling surface is large compared to the pumped volume so high output power can be extracted from a small volume. Since the back surface of the disc is cooled, the heat flux and the laser beam axis are collinear to each other. As a consequence, thermal lensing effects are dramatically reduced. Due to the very short interaction length in the gain medium, large doping concentrations are required as well as multiple passes of the pump radiation in order to achieve high absorption efficiency. Using this kind of system with Yb:YAG as the gain medium, cw laser powers of up to 1kW have been achieved [22]. Nd^{3+} based lasers materials have a larger quantum defect so thermal loading is typically almost three times higher than in Yb:YAG. One of the highest reported output powers for a thin disc laser based on Nd^{3+} was a Nd:$GdVO_4$ thin-disc laser with 202W of output power [23]. Thin-disc lasers are still ultimately limited by

thermal effects in the gain medium which degrade the beam quality. Thermal distortions stem mainly from the bending of the crystal due to the difference in expansion of its front and back surfaces with additional aberrations resulting from a radial temperature gradient at the edge of the pumped area.

2.6.1.4 Fiber Lasers

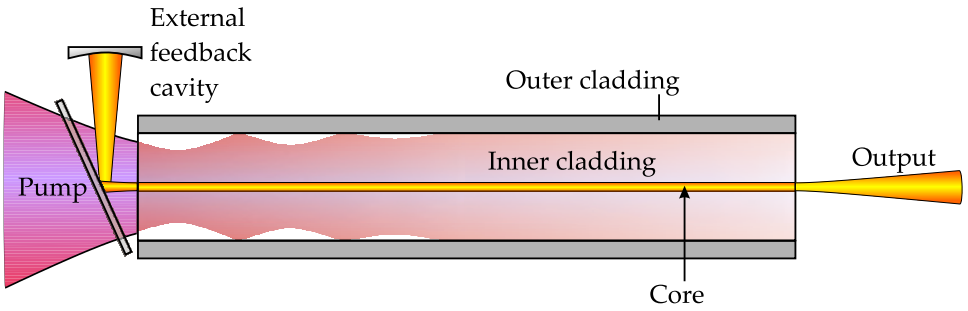

Figure 2.13: Double-clad fibre laser

Power scaling of fibre lasers is a field attracting much attention in recent years. In many applications, fibre lasers are replacing bulk solid-state lasers as cheaper, more efficient and less cumbersome alternatives, often with better performance characteristics. As shown in Figure 2.13, a typical fibre laser consists of a double clad, fused silica optical fibre with a rare-earth doped core. The inner cladding is used to guide the pump radiation which is absorbed in the core over typically several metres. The core can be made single mode for the lasing wavelength so that the output is diffraction limited even at high power. A laser cavity can be set up either externally, as shown in the Figure, or internally using Fibre Bragg Gratings (FBGs). The very high surface to volume ratio of fibres allows for very high pump powers to be absorbed without excessive heating. Thermal effects most commonly take the form of damage to the fibre end facets, or the outer polymer coating, caused by intense diode pumping. The glass host for the active medium gives broader absorption and emission bandwidths than crystal based lasers which allows broad wavelength tunability or potentially ultrashort pulse generation. Compared to bulk solid-state lasers, fibre lasers and amplifiers have superior thermal properties and potentially higher extraction efficiencies, however they suffer from a number of disadvantages. Many applications require polarised output and fibres do

not, in general, maintain the polarisation state of ingoing light. Additional complexity in fabrication is required to produce polarisation maintaining fibres. Moreover, in pulsed operation, the high laser intensities in the fibre core can lead to a number of undesirable nonlinear effects. The most common are Stimulated-Brillouin-Scattering (SBS) and Stimulated-Raman-Scattering (SRS) whereby some of the power becomes backscattered or forward-scattered by acoustic or optical phonons respectively [24]. Some problems can also arise from self-phase modulation caused by the Kerr nonlinearity. Increasing the core size of the fibre is necessary to reduce the nonlinear effects, but this makes single-mode operation more difficult to achieve.

2.6.2 Phase Conjugation

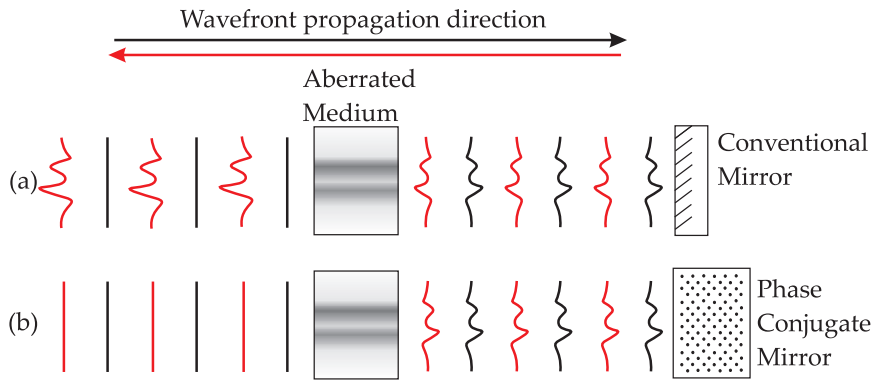

Figure 2.14: Schematic of wavefront distortion through two passes of an aberrated medium with reflection from (a) a conventional mirror and (b) a phase conjugate mirror

One technique, which is a powerful tool for compensating for thermal lens distortion, is phase conjugation. A phase-conjugate-mirror (PCM), unlike a conventional mirror, reverses the phase as well as the direction of an incident beam. This means that a beam which passes through a phase distorting medium can be reflected from a PCM and on return pass through the same distorting medium will have its phase distortions exactly reversed. This is illustrated in Figure 2.14. Various techniques can be used to produce phase conjugate mirrors but the most common is by Stimulated Brillouin Scattering (SBS) [25]. In the latter the laser beam is focused very tightly into a gas or liquid cell in which the SBS takes place. SBS is a nonlinear effect which requires

high intensities to achieve efficient reflection of power but, when achieved, it can produce effective phase conjugation of incoming wavefronts. In principle, lasers incorporating phase conjugators are highly power scalable since thermal distortion problems can be neglected, however in practice they are complex and difficult to implement and the low efficiencies of phase conjugate mirrors often limits their use.

2.7 Diode Pump Sources

Laser diodes are the most efficient pump sources for solid-state lasers. Their electrical to optical efficiency, of around 25 - 50%, is actually lower than a flashlamp pump source which can convert around 70% of electrical power to optical power. However, they can be made to emit all their radiation within the narrow pump band of a selected solid-state laser material, whereas only a small fraction of flashlamp radiation falls within the absorption bands of interest.

The most common types of laser diodes are based on GaAlAs, which emits in the region of 780 - 860 nm and InGaAs, which emits in the region of 940 - 980 nm. The bandgap, or energy difference between the conduction and valence bands, determines the emitted wavelengths. The bandgaps of these semiconductors can be tailored to emit a particular wavelength by changing the relative amount of In or Al in the GaAs and the structure of the diodes. Finer tuning of wavelength can be achieved by temperature tuning the device. In GaAlAs, for example, the wavelength changes by approximately 0.3 nm/$^{\circ}$C.

2.7.1 High Power Diode Bars

Since single emitter laser diodes are limited to a few watts of output power by the relatively low damage threshold of the end facets, pump sources for solid-state lasers are usually based on linear or 2D arrays of single emitters. Each single emitter is actually formed from a sub-array of around 20 single transverse mode emitters on a single chip with an emitting area of around 1 µm $\times$ 200 µm . A diode bar is a linear array of 10 or 20 of these sub-arrays fabricated on a single substrate and equally spaced to produce a 1 cm $\times$ 1 µm emitting

area. With this kind of aspect ratio, the beam divergence angles and M^2 values in the orthogonal directions differ quite dramatically leading to highly elliptical beams. These devices are typically diffraction limited in the fast (1 µm) axis and have M^2 values of around 2000 in the slow (1 cm) axis. In some pumping geometries, for example side pumping laser rods or slabs, the output from diode bars is ideal since the shape of the laser medium matches the shape of the pump beam. By placing the bar very close to the laser medium, the problems caused by the large divergence angles are avoided. For end-pumping however, where a collimated circular beam is required to achieve good mode matching between pump and laser beams, the output beams are less desirable and direct pumping is not normally practical. Several techniques can be used to help reduce this problem and will be discussed in section 2.7.3. Typical output powers of commercially available diode bars are currently around 20 - 100 W [26].

2.7.2 Diode Stacks

In addition to arranging diodes into linear arrays to form bars. These bars can also be arranged in arrays to form 2D diode stacks. Around 5 to 40 bars can be stacked, at separations of around 1.5-2mm, to produce single package devices with up to around 1 kW of output power. The overall dimensions of the emitting area are therefore around 1 cm $\times$ 2 cm.

Achieving these high power levels from single devices with only $\approx$50% electrical to optical efficiency clearly leads to large amounts of heat being generated. Efficient heat removal requires careful engineering of the diode bars and stacks. In most cases diode bars can be conductively cooled by bolting them onto heat sinks, which are either liquid or air cooled, and in some cases a Peltier cooler is used to control the temperature. In diode stacks the cooling mechanism needs to be even more refined to ensure a uniform temperature distribution over the area of the device. Most diode stacks come with a microchanneled heat spreader through which liquid can be forced at high pressure.

2.7.3 Beam Combining and Shaping Techniques

Making use of the highly elliptical beams from diode bars and stacks, often requires several beam shaping techniques. There are many different techniques for beam combining and shaping. A few examples are described here.

2.7.3.1 Microlenses and Microlens Arrays

Cylinder lenses are usually used to match the beam sizes in the orthogonal planes. In many applications, a microlens is attached to each linear bar. These long thin cylindrical lenses extend the length of the bar and have carefully designed cross sections and AR coatings and are used to collimate the beam in the fast axis. Additionally, the slow axis can be collimated by using microlens arrays which consist of many cylindrical sections fabricated along a single glass slab which also extends the length of the diode bar. Each cylindrical section collimates the output from a single emitter and, when the ideal focal length and section spacing is chosen, the array acts to improve the beam quality by a factor of around two in the slow axis by effectively filling in the spaces between emitters. The fast and slow axis collimation of a diode bar using microlenses is shown in Figure 2.15

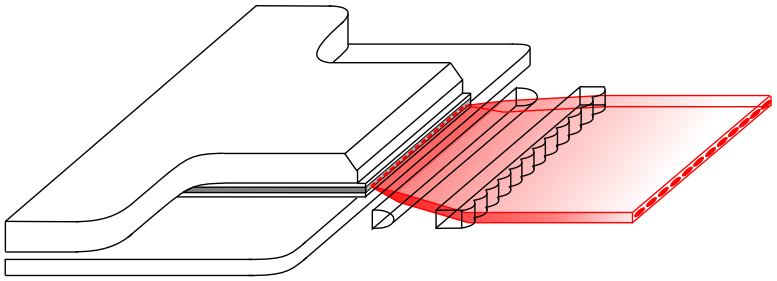

Figure 2.15: Laser diode bar collimation using a microlens and microlens array

2.7.3.2 Polarisation Combining

Laser diodes have highly polarised output and for many solid-state laser materials the pump polarisation is not important. Therefore it is possible to reduce the M^2 value in the slow axis by a factor of two by polarisation combining. In

this scheme, as shown in Figure 2.16, the beam is chopped into two beams using a knife-edge mirror. One of these beams' polarisation is rotated by 90° by a half waveplate (HWP) and the two beams are re-combined by a polarising beam splitter (PBS) such that the beam size in the horizontal plane is reduced by one half. In practice this technique can have transmission efficiencies of around 95 %.

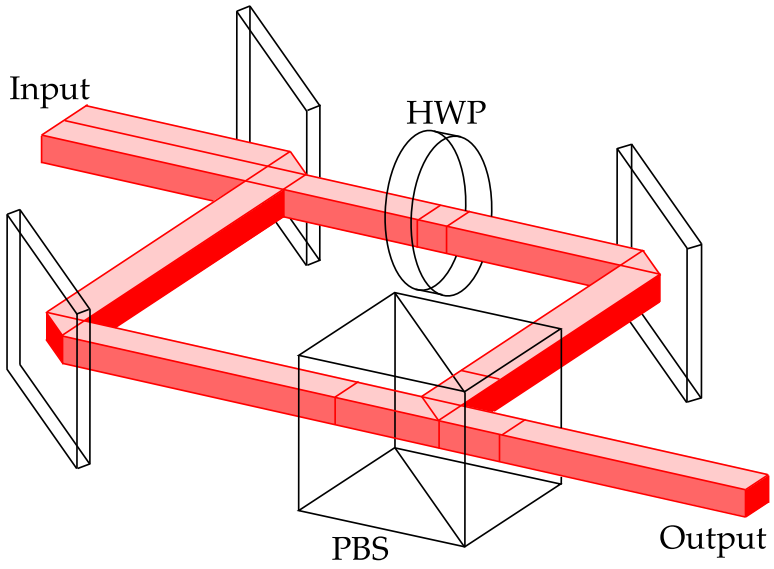

Figure 2.16: Polarisation combining using beam shaping mirrors, a half-waveplate (HWP) and a polarising beam splitter (PBS)

2.7.3.3 Fibre-Bundle Beam Shaping

One technique that can offer equal beam qualities in orthogonal planes is fibre-bundle beam shaping [27]. A bundle of multimode optical fibres, one for each emitter on a diode bar or stack, can collect the emitted light from a microlens-collimated diode bar and the output ends of the fibres can be arranged in a circular formation as shown in Figure 2.17. The multimode nature of the fibres causes the radiation in the fibre to disperse and fill all the available modes, therefore giving an output with equal M^2 values in orthogonal planes. These devices can be used for diode bars and stacks alike. A disadvantage, however, is that the mode coupling whereby imperfections in the fibre cause an increase in the number of modes present in the fibre, leads to an increase in the output divergence and additionally the spaces in between the cores of the fibres

leads to an increase in the effective emitting area. The two effects can cause a significant loss in brightness.

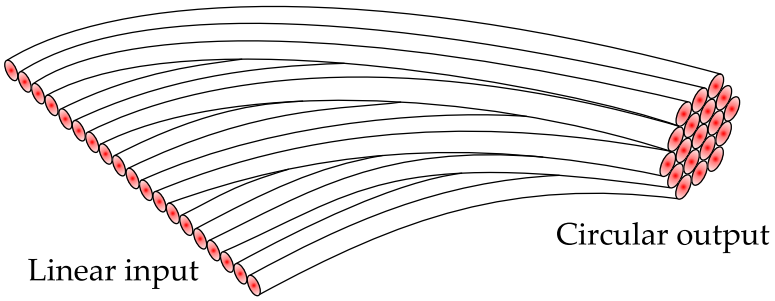

Figure 2.17: A fibre-bundle beam shaper

2.7.3.4 The Two-Mirror Beam-Shaper

Another example of a beam shaping device known as a two-mirror beam-shaper [28], converts the collimated output from a diode bar into a closely packed stack of beams. This allows the beam qualities to be approximately equalised in the orthogonal planes. The device comprises two mirrors facing each other and separated by a small distance. The mirrors are parallel with respect to one another but angled with respect to the incoming beam and the vertical plane, as shown in Figure 2.18. The mirrors allow a small section at the end the beam to emerge on each successive double reflection. Each small section emerges from the beam shaper below the previous one, so the result is a collimated stack of beams. A collimated diode bar with M^2 values of around 1×2000 can be converted into a beam with an M^2 value of around 70 in both planes. An appropriate combination of cylindrical lenses can then be used to produce an approximately circular beam with the same divergence in both planes. Since the beam sections can be stacked very close together this method results in a beam with greater brightness than a fibre-bundle. Figure 2.19 shows a photo of a 40 W diode bar with fast and slow axis microlens-collimation and a two-mirror-beamshaper.

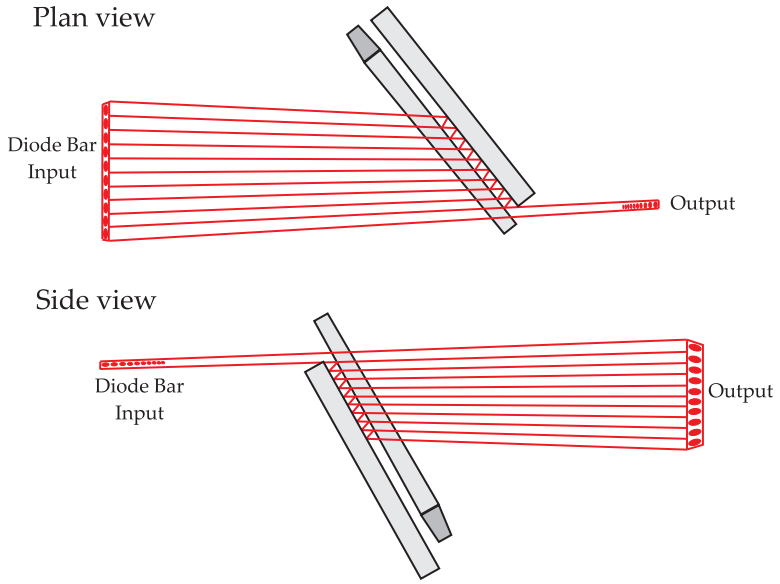

Figure 2.18: Plan and side view of a two-mirror beam-shaper

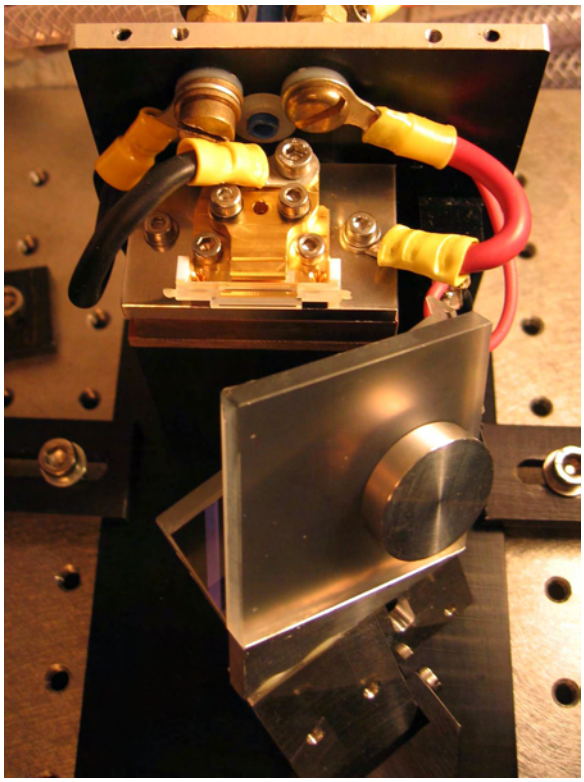

Figure 2.19: Micro-lensed diode bar with two-mirror beam-shaper

2.7.4 Fiber Coupling Diode Bars and Stacks

For end-pumping laser and amplifier configurations there are several advantages to delivering the pump light via a multimode optical fibre. One is simply that the diode apparatus can be kept in a separate location to the laser apparatus and the fibre output can also be easily connectorised and moved around the optical table. Another useful feature is that the mode coupling in the fibre provides a means of smoothing out the irregular beam profiles that are common from beam shaped diode arrays and can lead to serious thermally induced distortions in the gain medium. The output beam from a fibre-coupled diode bar is circular and can be loosely described as 'top-hat' in profile. This is favorable for intense end-pumping because the thermal lens generated in the laser medium is less aberrated than in the case of a Gaussian pump beam for example. This effect will be discussed in detail in Chapter 4.

To efficiently fibre-couple a diode bar or stack, the numerical aperture (NA) of the fibre needs to be slightly larger than the convergence angle of the input beam, as shown in Figure 2.20. A fibre's NA is equal to the sine of the maximum acceptance angle θ_{max} within which rays are guided along the fibre by total internal reflection at the critical angle $\theta_c = \sin^{-1}(n_{cladding}/n_{core})$ [29]. The NA for a fibre with core and cladding refractive indices n_{core} and $n_{cladding}$ is given by:

$$NA = \sin\theta_{max} = (n_{core}^2 - n_{cladding}^2)^{1/2}. \tag{2.20}$$

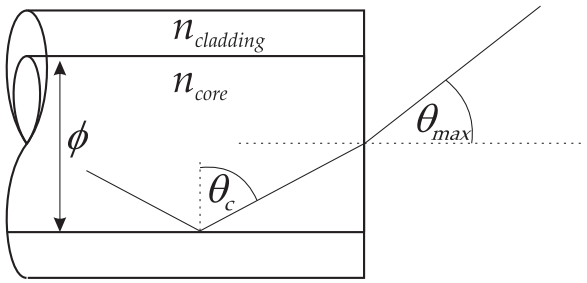

Figure 2.20: Maximum acceptance angle of an optical fibre

All of the fibres used in this work were step-index multimode fibres and had an NA of 0.22. This implies that the beam quality of the diode pump sources sets a lower limit on the fibre core diameter ϕ that can be used to couple the light

efficiently. From equation (2.14) we can see that the minimum core diameter required to couple a given pump beam can be expressed by:

$$\phi_{min} = \frac{2M^2\lambda}{\pi NA}. \tag{2.21}$$

In this situation some loss would arise from the power in the wings of the pump beam not being coupled so one would expect around 95% of the pump power to fall within the fibre core area. Further losses of around 4% due to Fresnel reflection would be expected at the input and output facets of the fibre so 85% transmission efficiency is typical.

2.8 Summary

This chapter has introduced the basic principles required for building lasers and laser amplifiers, and highlighted many of the issues associated with scaling these systems to higher powers. The physical processes involved in laser action were outlined with regard to a 4-level system and the basic equations were introduced for predicting the threshold and slope efficiency in a laser oscillator and the small signal gain in a laser amplifier. The importance of beam quality was discussed and the use of the M^2 parameter to quantify beam quality was described. The main pump power loss mechanisms leading to heat generation in the gain medium were discussed, the main one being the quantum defect but the additional contributions from ETU, ESA and cross relaxation were explained. The energy level structure of Nd:YVO_4 was summarised and the relative merits of using Nd:YVO_4 as a gain medium compared to Nd:YAG and Nd:YLF were discussed. Its main advantages were attributed to its high $\sigma_{21}\tau_f$ product and natural birefringence, however its thermal properties were considered to be more problematic with low thermal conductivity and a high thermo-optical coefficient. The most important detrimental thermal effects were discussed, with particular emphasis on end-pumped rod geometries, with aberrated thermal lensing and stress fracture being the biggest challenges for power scaling in Nd:YVO_4 based lasers. Some of the techniques for reducing or compensating for thermal effects were described and a number of alternative laser architectures were discussed with regard to their power scaling potential. Finally, the technology of pumping laser systems with high

power diode sources was summarised. The advantages and limitations of using high brightness diode bars and diode stacks was described and some of the techniques for coping with their highly elliptical output was discussed. These techniques include beam shaping and combining to equalise the M^2 values in orthogonal planes and also fibre coupling the beams to produce smooth, circular intensity profiles required for end-pumping.

2.9 References

[1] **Kogelnik, H.** and **Li, T.**, *Laser Beams And Resonators*, Applied Optics, Vol. 5, No. 10, pp. 1550–1567, October 1966.

[2] **Ishida, T., Togawa, T., Morita, H., Suzuki, Y., Okino, K.** and **Kubota, K.**, *A 10kW high-power lamp pumped MOPA Nd:YAG laser system*, NEC Research and Development, Vol. 41, No. 2, pp. 178–182, 2000.

[3] **Koechner, W.**, Solid-State Laser Engineering, Springer, 5th edn., 1999.

[4] **Clarkson, W. A.** and **Hanna, D. C.**, Optical Resonators – Science and Engineering,327-361:*Resonator Design Considerations for Efficient Operation of Solid-State Lasers End-Pumped by High-Power Diode Bars*, pp. pp. 327–361, Kluwar Academic Publishers, 1998.

[5] **Siegman, A. E.**, *How to (maybe) measure laser beam quality*, OSA TOPS proceedings, Vol. 19, 1998.

[6] **Chapple, P. B.**, *Beam waist and M^2 measurement using a finite slit*, Optical Engineering, Vol. 33, No. 7, pp. 2461–2466, 1994.

[7] **Petit, J., Vianda, B., Goldner, P., Vivien, D., Louiseau, P.** and **Ferrand, B.**, *Laser oscillation with low quantum defect in Yb : $GdVO_4$, a crystal with high thermal conductivity*, Optics Letters, Vol. 29, No. 8, pp. 833–835, 2004.

[8] **Hardman, P. J., Clarkson, W. A., Friel, G. J., Pollnau, M.** and **Hanna, D. C.**, *Energy-transfer upconversion and thermal lensing in high-power end-pumped Nd:YLF laser crystals*, IEEE Journal of Quantum Electronics, Vol. 35, No. 4, pp. 647–655, 1999.

[9] **Fornasiero, L., Kuck, S., Jensen, T., Huber, G.** and **Chai, B. H. T.**, *Excited state absorption and stimulated emission of Nd^{3+} in crystals. Part 2 YVO_4, $GdVO_4$ and $Sr_5(PO_4)_3F$*, Applied Physics B, Vol. 67, pp. 549–553, 1998.

[10] **O'Connor, J. R.**, *Unusual crystal-field energy levels and efficient laser properties of YVO_4:Nd*, Applied Physics Letters, Vol. 9, No. 11, pp. 407–409, 1966.

[11] **Fields, R. A., Birnbaum, M.** and **Fincher, C. L.**, *Highly efficient Nd:YVO_4 diode-laser end-pumped laser*, Applied Physics Letters, Vol. 51, No. 23, pp. 1885–1886, 1987.

[12] **Yao, A. Y., Hou, W., Kong, Y. P., Guo, L., Wu, L. A., Li, R. N., Cui, D. F.** and **Xu, Z. Y.**, *Double-end-pumped 11W Nd:YVO_4 cw laser at 1342nm*, Journal of the Optical Society of America: B, Vol. 22, No. 10, pp. 2129–2133, 2005.

[13] **Kaminskii, A. A.**, Laser Crystals, Vol. 14, Springer Series in Optical Science, 1981.

[14] **Svelto, O.**, Principles of Lasers, Kluwar Academic Publishers, 1998.

[15] **Divall, M.**, *Photo-injector laser development CTF3 Design*, Powerpoint Presentation, CCLRC Rutherford Appleton Laboratory, 2006: `http://www.infn.it/phin/docs_files/PHIN_Coll_Meeting-2004-05-05-pdf/RAL_Divall.pdf`.

[16] **Xiong, Z., Li, Z. G., Huang, W. L.** and **Lim, G. C.**, *Detailed Investigation of Thermal Effects in Longitudinally Diode-Pumped Nd:YVO_4 Lasers*, IEEE Journal of Quantum Electronics, Vol. 39, No. 8, pp. 979–986, 2003.

[17] **Fluck, R., Hermann, M. R.** and **Hackel, L. A.**, *Birefringence compensation in single solid-state rods*, Applied Physics Letters, Vol. 76, No. 12, pp. 1513–1515, 2000.

[18] **Inncenzi, M. E., Yura, H. T., Fincher, C. L.** and **Fields, R. A.**, *Thermal modelling of continuous-wave end-pumped solid-state lasers*, Applied Physics Letters, Vol. 56, No. 19, pp. 1831–1833, 1990.

[19] **Clarkson, W. A.**, *Thermal effects and their mitigation in end-pumped solid state lasers*, Journal of Physics D: Applied Physics, Vol. 34, pp. 2381–2395, August 2001.

[20] **Brown, D. C.**, *The Promise of Cryogenic Solid-State Lasers*, IEEE Journal of Selected Topics in Quantum Electronics, Vol. 11, No. 3, pp. 587–599, 2005.

[21] **Tsunekane, M., Taguchi, N.** and **Inaba, H.**, *Improvement of thermal effects in a diode-end-pumped, composite Tm: YAG rod with undoped ends*, Applied Optics, Vol. 38, No. 9, pp. 1788–1791, 1999.

[22] **Stewen, C., Contag, K., Larionov, M., Giesen, A.** and **Hugel, H.**, *A 1-kW cw thin disc laser*, IEEE Journal of Selected Topics in Quantum Electronics, Vol. 6, No. 4, pp. 650– 657, 2000.

[23] **Kemp, A. J., Valentine, G. A.** and **Burns, D.**, *Progress towards high-power, high-brightness neodymium-based thin-disk lasers*, Progress in Quantum Electronics, Vol. 28, pp. 305–344, 2004.

[24] **Jaouën, Y., Canat, G., Grot, S.** and **Bordais, S.**, *Power limitation induced by nonlinear effects in pulsed high-power fiber amplifiers*, Comptes Rendus Physique, Vol. 7, No. 2, pp. 163–169, 2006.

[25] **Ostermeyer, M., Heuer, A., Menzel, R.** and **Wulfmeyer, V.**, *27-W average output power with 1.2*DL beam quality from a single-rod Nd : YAG laser with phase-conjugating SBS mirror*, IEEE Journal of Quantum Electronics, Vol. 34, No. 2, pp. 372–377, 1998.

[26] *DILAS diodenlaser GmbH. Single-bar-devices*, Website:`http://www.dilas.de/products/single-bar-drvices/mseries.html`.

[27] **Morris, P. J., Lthy, W.** and **Weber, H. P.**, *High-intensity rectangular fiber-coupled diode laser array for solid-state laser pumping*, Applied Optics, Vol. 32, No. 27, pp. 5274–5279, 1993.

[28] **Clarkson, W. A.** and **Hanna, D. C.**, *Two-mirror beam-shaping technique for high-power diode bars*, Optics Letters, Vol. 21, No. 6, pp. 375–377, March 1996.

[29] **Hecht, E.**, Optics, Addison-Wesley, 3rd edn., 1998.

Chapter 3

Development of a Mode-Locked Nd:YVO_4 Oscillator

3.1 Introduction

The previous chapter discussed many of the issues relevant for scaling the output power of laser sources with particular emphasis on heat generation and management of thermal effects. One strategy that was not mentioned was operating laser oscillators in pulsed mode to increase the peak power while maintaining the same or similar average power. Many laser applications require high peak power for a short duration and the average power is less important. One important example is for achieving efficient nonlinear frequency conversion to wavelengths not attainable from conventional lasers. Exploiting the nonlinear optical response from the materials used for frequency conversion requires a source with high intensity. In nonlinear second-harmonic-generation (SHG) for example, the power conversion efficiency is proportional to the square of the intensity of the laser field. Another example is in processing of materials where high pulse energies, over short timescales, are required to cause laser ablation where the surface of a material is vaporised in the locality of the laser beam. The two main techniques for generating high peak power pulses from a laser oscillator are Q-switching and mode-locking. In the first case an intra-cavity element (usually an electro-optic/acousto-optic modulator or a saturable absorber) varies the loss in the cavity so that under high loss conditions there is no laser output and stored energy builds up in the gain

medium. The loss is then switched to a low level and radiation builds up over several hundred round trips of the cavity and is emitted in a large pulse of the order of ns in duration. To achieve the maximum pulse energy, the repetition rate needs to be comparable to the inverse of the upper state lifetime $(1/\tau_f)$, but higher repetition rates up to ∼100kHz are common and generally result in higher average power [1]. Mode-locked lasers use a similar mechanism (passive or active) to periodically vary the loss in the cavity however, the repetition rate of the low-loss condition in the cavity is made to exactly match the inverse of the cavity round trip time. Therefore the circulating field builds up in narrow pulses for times when the loss is at its lowest point. Compared to Q-switching, mode-locking produces much shorter pulses at much higher repetition rates, of the order of 100 MHz. Due to the high repetition rates of mode-locked lasers, thermal effects over the time scale of the pulse cycle can be neglected and the laser can be considered essentially cw for the purpose of laser design and thermal management. One reason in particular for developing a mode-locked oscillator was to produce a high power source with short pulses and high repetition rate, suitable for synchronously pumping an optical parametric oscillator (OPO). This means that, like the mode-locked oscillator, the OPO is designed to have a cavity round-trip time equal to the inverse of the pump pulse repetition rate. Fine tuning of the cavity length allows each new pump pulse to arrive synchronously with the resonating pulse, thereby adding to its intensity and allowing more efficient frequency conversion.

In the work presented here, we have developed an actively mode-locked, end-pumped Nd:YVO_4 laser oscillator, used as a seed laser for a MOPA system offering high peak power pulses at high repetition rates. The requirements of the master-oscillator in this MOPA system are to provide reliable and efficient TEM_{00} radiation of moderate average power in both mode-locked and cw modes of operation with good stability over a range of output powers. This implies good tolerance to thermal lensing of the gain medium such that efficiency, beam quality and output beam radius should not change much for a wide range of pump powers. In this chapter, the constraints that active-mode-locking places on cavity design and the influence of thermal lensing in the gain medium on resonator stability and mode size are considered. The design strategy and the experimental results obtained for an oscillator which was built and

subsequently used to seed the amplifier chain described in this thesis is also summarised.

3.2 Oscillator Design Considerations

The oscillator design, used in this work, emerged based on a number of constraining factors relating to the pumping scheme, the mode-locking scheme, the available components and the requirements of stable and efficient TEM_{00} operation. Before an effective design was found, a number of resonator designs were realised utilising single and double-end-pumping, Brewster cut and normal incidence Nd:YVO_4 rods, as well as a range of crystals with different doping concentrations. While the use of double-end-pumping provides a more uniform longitudinal distribution of population inversion and potentially higher gain, the added complexity required in the resonator design and the availability of a sufficiently high brightness diode source for single-end-pumping made double-end-pumping unnecessary. Additionally, the use of Brewster-cut crystals which offer lower losses compared to normal incidence AR coated alternatives, was found to be more detrimental to the output beam quality of the oscillator for high pump intensity. This was thought to be due to the radial asymmetry and astigmatism of the thermal lens in Brewster gain media [2] causing more severe aberrations for Brewster incidence compared to normal incidence of the laser mode.

3.2.1 Influence of Nd^{3+} Doping Concentration

A number of authors have studied the influence of neodymium doping concentration in Nd:YVO_4 crystals on laser performance [3, 4]. While higher doping concentration reduces absorption length and therefore leads to higher inversion density and potentially higher gain, the effect of ETU can become high which causes a reduction in efficiency [5, 6]. However, in the cw and mode-locked oscillator described here, the effect of ETU was found to be negligible since the gain was highly saturated and the pump power relatively low. A more important consideration is that the higher pump absorption density

leads to greater thermal gradients and therefore stronger thermal lensing and a greater chance of thermal fracture. Conversely, if the doping concentration is too low then either the absorption efficiency will be reduced or the crystal length required to absorb all the pump light will be too long to effectively focus the pump beam through it, without significant divergence [7]. Another important consideration is the influence of the laser mode size in the gain medium on the stability of the resonator and its tolerance to thermal lensing. In the case where the cavity design constrains the mode size and hence the pump beam size in the laser rod, the Nd^{3+} concentration needs to be high enough to absorb most of the pump radiation within the focal region of the pump beam.

3.2.2 Pumping Scheme

End-pumping of the Nd:YVO_4 rods was chosen because it ensures good spatial overlap between the pump beam and laser mode and thus a high pumping rate density only in the lasing region. This helps to prevent higher order modes from oscillating, by reducing the amount of population inversion outside the TEM_{00} region, and minimizes wastage of pump power implying greater overall efficiency.

An 808nm laser diode bar from Jenoptik Laser Diode GmbH, with a nominal output power of 40W, was set up to pump the oscillator. The diode bar was bolted to a water cooled copper heat sink. The water temperature was controlled to within $\pm 0.1℃$ to fine tune the wavelength to maximise absorption in the laser rod. The output was first collimated in both planes using a cylindrical microlens in the fast axis and a microlens array in the slow axis, as shown in Figure 2.15. The beam was then reshaped using a two-mirror beam-shaper, as described in Section 2.7.3.4, and shown in Figure 2.19. The beam was recollimated in the slow axis using a cylindrical lens and then focused down using a 30mm focal length graded index lens to couple the light into an all silica optical fibre of 365µm core diameter and $NA = 0.22$. The total loss, caused by diffraction and clipping by the beam collimating and shaping optics and fresnel losses from the two fibre facets, was around 19%. This led to a maximum output power from the fibre of 23.5W, for a diode drive current of 40A, as shown in Figure 3.1.

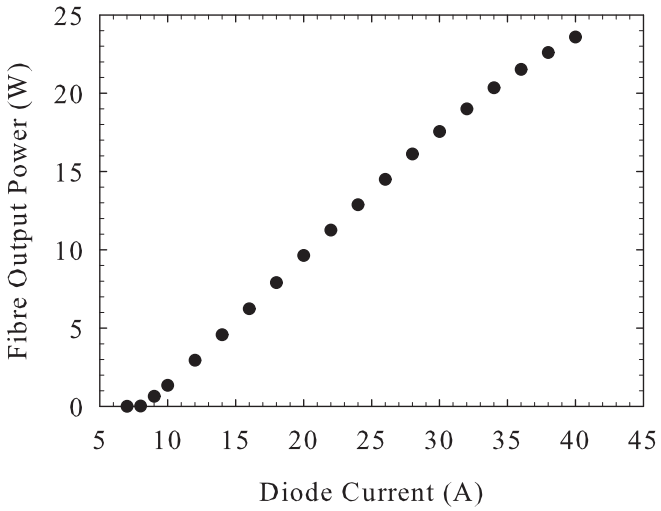

Figure 3.1: The pump fibre output power versus the diode drive current.

In order to end-pump the Nd:YVO_4 rod, the fibre output had to be collimated then focused down to a small spot size in the crystal. The main considerations were to ensure good spatial overlap between the pump beam and the laser mode yet, with as small a spot size as possible, to minimise threshold and also to reduce sensitivity of the cavity to thermal lensing. The latter is because a laser mode with a smaller spot size will have greater divergence and therefore the relative change in divergence caused by a thermal lens will be less.

For a diffraction limited laser mode ie. $M^2 = 1$, its divergence is much less than that of the pump. Therefore the M^2 parameter of the pump sets a lower limit on the spot size of pump and laser if a good overlap is to be maintained over the pump absorption length within the crystal. To calculate the optimum sizes of the pump (ie. the spot size giving minimum pumping volume in the rod), a good approximation is to set the confocal parameter of the pump equal to the rod length. In the case where the length of the rod is longer than the length over which most of the pump is absorbed, the confocal parameter can be reduced to approximately three pump absorption lengths ($3l_{\alpha_p}$) (ie. the length in which 95% of the pump is absorbed). This allows a smaller corresponding beam waist to be used and hence higher gain to be achieved. In this case w_0

can be given by the following expression.

$$w_0 = \sqrt{\frac{3l_{\alpha_p} M^2 \lambda_p}{2\pi n}}, \tag{3.1}$$

where $l_{\alpha_p} = 1/\alpha_p$ and n is the index of refraction in the rod, which has a value of 2.186 in Nd:YVO_4 at 808nm. This technique is similar to confocal focusing, where the confocal parameter is set to the length of the crystal but is modified to take into account the absorption length of the pump radiation. Figure 3.2 shows an end-pumped laser where the pump is confocally focused over length $3l_{\alpha_p}$ in the laser rod where the mode size is slightly smaller than the pump beam waist and is approximately constant over the length of the rod.

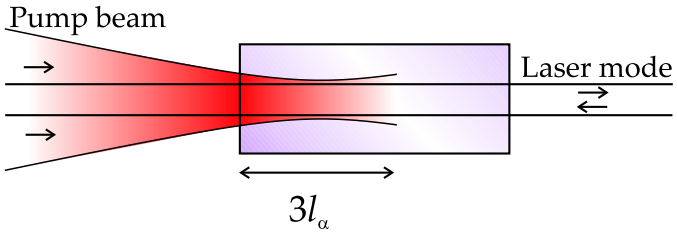

Figure 3.2: Confocal focussing of pump beam in an end-pumped laser rod

3.2.3 Mode-Locking

Standing-wave laser resonators define a set of longitudinal (axial) modes which have an integer number of half-wavelengths within the length of the cavity. The frequency difference between neighbouring axial modes, the *axial mode spacing* was given by equation (2.1) in Chapter 2. In homogeneously broadened gain media, the different axial modes compete for gain so typically only a few modes oscillate near the maximum gain frequency. By introducing an appropriate modulation of the signal within the cavity, it is possible to fix the phase relationship between axial modes so that energy is transferred from the stronger modes in the centre of the gain bandwidth to the weaker modes in the wings. Under ideal conditions all the modes within the gain bandwidth oscillate and are locked in phase to one another. In the time domain this translates to a situation where all the energy circulating in the cavity builds up into a narrow pulse which *sees* the minimum loss in the modulator. There are two

main types of mode-locking: passive and active. In the former, a non-linear optical element, which acts as a saturable absorber, provides an intensity dependent loss which is lower for higher intensity pulses. In this technique, once the mode-locking is established, the pulse becomes shorter and more intense until it becomes balanced by the pulse broadening caused by the limited gain bandwidth of the gain medium and other broadening mechanisms such as etalon effects and, in the case of ultrashort pulses, dispersion and self-phase modulation [8].

Passive mode-locking can potentially produce gain bandwidth limited pulse durations for many solid-state laser materials (tens of fs to a few ps). The most common types of passive mode-lockers consist of either Semiconductor-Saturable-Absorber-Mirrors (SESAMs) [9] or Kerr-lens mode-lockers. SESAMs are typically based on Bragg mirrors which have a layer of semiconductor such as InGaAs on the surface which acts as a quantum-well absorber. Kerr-lens mode-locking is achieved by placing a Kerr medium (or in some cases the laser medium itself) in the cavity which acts as a lens with intensity dependent focal length. This modifies the mode profile so that, when combined with an aperture (hard or soft) placed in an appropriate location in the cavity, this can lead to a loss which is lower for higher intensity pulses [10].

Whereas with passive mode-locking, the laser pulse itself activates the modulator to reduce the loss, with active mode-locking the modulator is activated by an external rf signal, which causes either a phase or amplitude modulation of the laser field. In this case the modulation frequency f_m and the cavity length must be matched so that the circulating pulse is synchronised with the modulator's low loss condition. This implies that

$$f_m = \frac{c}{2l_c}, \tag{3.2}$$

where l_c is the cavity length. From equation (2.1) we can see that this is the same as the axial mode spacing of the resonator which leads to coupling of axial modes. There are two distinct types of active mode-locking, utilising either phase modulation, which alters the frequency (FM), or amplitude modulation (AM). In the FM case an electro-optic phase modulator (EOM) is normally used which introduces a time varying doppler shift in frequency caused by rapidly varying the phase of light passing through the modulator. If this frequency

shift is enough to push the radiation away from the peak of the gain bandwidth of the laser material then this causes a time varying loss in the cavity which gives rise to mode-locking when equation (3.2) is satisfied. Since the phase shift varies approximately quadratically about the pulse arrival time, a frequency 'chirp' over the duration of the output pulse is introduced. While this causes a small amount of broadening of the pulse duration it can be advantageous in systems where even shorter pulse durations are required because it allows pulse compression using dispersive elements such as prism or grating pairs. By this technique, the pulse duration can, in principle, be made bandwidth limited.

AM active mode-locking, which is used in this work, is normally achieved using an acousto-optic modulator (AOM) which is normally comprised of a piezoelectric transducer bonded to a transparent medium like glass or quartz. An acoustic standing wave is set up in the modulator which modifies the local refractive index and causes time varying diffraction of radiation out of the cavity. The resulting amplitude modulation results in side-bands developing at $\pm f_m$ about the carrier frequency of the laser radiation. When the axial mode spacing matches the modulation frequency these side-bands become amplified and in turn develop new side-bands until all the axial modes in the gain bandwidth are coupled. However, compared to passive mode-locking, in practice the maximum achievable bandwidth is normally less due to external conditions which cause minor changes in cavity length. This, combined with lower modulation depths achievable with AOMs compared to SESAMs for example, results in longer pulse durations for most actively mode-locked systems. The pulse durations achievable using active mode-locking, with acousto-optic or electro-optic modulators, is typically tens to several hundred ps [11]. One advantage of active mode-locking, over passive mode-locking, is that mode-locked operation is often easier to initiate. Some passively mode-locked systems require additional active modulators to initiate mode-locking which adds considerable complexity. For (AM) mode-locking, Kuizenga [12] used the boundary condition that, for steady-state operation, the pulse shape is unchanged after one cavity round trip to derive a pulse duration (t_p) of

$$t_p = \gamma \frac{(g l_g)^{1/4}}{(\delta_m f_m \Delta\nu)^{1/2}}, \tag{3.3}$$

where γ is a constant equal to 0.53 for Bragg diffraction, g is the saturated gain coefficient of the laser, l_g is the length of the gain medium, δ_m the modulation depth and $\Delta\nu$ the gain bandwidth of the laser medium ($\sim$250GHz for Nd:YVO_4). The saturated gain coefficient is described in more detail in Chapter 4. It depends on the material parameters of the laser medium, the pump power and also the circulating power in the resonator, which in turn depends on the output coupler transmission T. We know that under lasing conditions the gain equals the loss in the cavity, so the approximation that $2gl_g \approx T + L$ [8] can be used. The AOM used in this work was based on a quartz crystal with Brewster angled faces to give low loss transmission. By placing the AOM as close as possible to one of the end mirrors in the cavity, it was possible to double pass the circulating pulse through the AOM within the low loss region of the modulation cycle. The AOM drive frequency, required to set up a suitable diffractive acoustic standing-wave, was set at 50MHz. The condition for low loss in the modulator occurs twice every rf cycle which means the corresponding modulation frequency was 100MHz. From equation (3.2) this leads to a required cavity length of 1.5m. This rather long cavity length constraint demands careful design of the resonator to accomplish stable diffraction limited operation.

3.3 Resonator Modelling

In Chapter 2 the basic principles of laser oscillation were introduced and expressions were given for the threshold pump power $P_{p,th}$ and slope efficiency η_s for an end-pumped laser. This section focuses on the design of laser resonators based on Gaussian beam optics. A laser mode in a resonator is determined by considering the diffraction of the radiation and the boundary conditions imposed by the cavity mirrors and any other intra-cavity optical elements. By considering the propagation of a TEM_{00} Gaussian beam and its interaction with the mirrors and optics of a resonator, one can predict the modes that the resonator can support. In 1966 Kogelnik [13] summarised most of the theory for predicting laser modes in resonators. The basic theory uses the description of a Gaussian beam given by the complex beam parameter q, where in terms of the radius of curvature of the beam wavefronts R and the radius of

the beam at $1/e^2$ intensity points w,

$$\frac{1}{q} = \frac{1}{R} - j\frac{\lambda}{\pi w^2}. \tag{3.4}$$

Using the following standard ray transfer matrices, assuming paraxial beams for spherical mirrors of radius of curvature R, $(M(R))$, thin lenses of focal length f, $(L(f))$ and free space propagation over distance d, $(S(d))$ given by

$$M(R) = \begin{pmatrix} 1 & 0 \\ \frac{-2}{R} & 1 \end{pmatrix}, L(f) = \begin{pmatrix} 1 & 0 \\ \frac{-1}{f} & 1 \end{pmatrix}, S(d) = \begin{pmatrix} 1 & d \\ 0 & 1 \end{pmatrix}, \tag{3.5}$$

the ABCD matrix for one cavity round trip can be found. By calculating the initial complex beam parameter q_i, based on the boundary condition that the beam parameter is the same after one cavity round trip, hence

$$\begin{pmatrix} A & B \\ C & D \end{pmatrix}_{cavity} \begin{pmatrix} w_i \\ w_i' \end{pmatrix} = \begin{pmatrix} w_i \\ w_i' \end{pmatrix}, \tag{3.6}$$

for a ray of initial radius w_i and slope $w_i' = w_i/R_i$, it can be shown that, if the cavity is stable, the solution is given by

$$\frac{1}{q_i} = \frac{D-A}{2B}(\mp)\frac{j}{2B}\sqrt{4-(A+D)^2}, \tag{3.7}$$

and hence the initial values of w and R are given by

$${w_i}^2 = \left(\frac{2\lambda B}{\pi}\right)\left(\sqrt{4-(A+D)^2}\right)^{-1} \tag{3.8}$$

and

$$R_i = \frac{2B}{D-A}. \tag{3.9}$$

An unstable cavity is one where the radiation field becomes increasingly dispersed at is circulates, rather than being refocused and confined. Light quickly escapes from an unstable cavity which makes it very difficult to achieve lasing. If the cavity is unstable it can be shown that

$$|A+D| \leq 2, \tag{3.10}$$

which is know as the stability criterion. Based on the initial values of the spot size and radius of curvature of the mode from equations (3.8) and (3.9), equations (2.11) and (2.12), given in Chapter 2, can be used to calculate the spot size profile $w(z)$ over the cavity length.

3.4 Mode-locked Oscillator Design

Using the above equations a program was written in Matlab to calculate the mode sizes in the cavity for various cavity designs. The program was set up so that various parameters could be varied and the effect on the cavity beam profile and spot sizes, in the gain medium and at the output coupler, could be monitored. The parameters that were varied were the focal length of a thin lens embedded in the gain medium to simulate thermal lensing; the angles of curved mirrors in the system to ensure low astigmatism and circular output and axial separations of the mirrors to find the best spot sizes. A thin lens approximation was considered a reasonable first approximation for a thermal lens where the focal length is much longer than the crystal length. However a more realistic approach for very short focal lengths could be modelled using using a thick graded index lens approximation. One of the features of real thermal lenses is their radially dependent focal length, which was mentioned in Section 2.5.2. This leads to strong aberrations particularly in the wings of the pump distribution [14]. One technique for reducing the impact of these thermal aberrations, which will be discussed in more detail in Chapter 4, is to use a laser beam which is slightly smaller than ($\sim$ 80-90%) the pump beam size which therefore avoids the most aberrated regions in the wings of the pump distribution. The main design criteria for the resonator were therefore to produce a mode spot size in the gain medium which was a little less than the pump spot size, whilst maintaining a relatively long cavity length of 1.5m to match the round trip time to the mode-locker modulation frequency. Additionally the mode spot size in the mode-locker had to kept below the active aperture of the device which was around 1000µm in diameter. Within these constraints the resonator was also required to have good tolerance to thermal lensing in the gain medium with little change in the mode size for a wide range of thermal lens focal lengths.

The design used was based on a symmetric Z folded cavity but an additional thin substrate dichroic folding mirror at 45° was included near the center point to allow single-end-pumping of the crystal through the mirror. The resulting cavity formed a cross shape with two plane mirrors at normal incidence forming the ends of the cavity, two curved folding mirrors at nearly normal inci-

dence and a 45° pump transmitting mirror at the centre. The experimental layout is shown in Figure 3.3 and a photo of the oscillator is shown in Figure 3.4 .

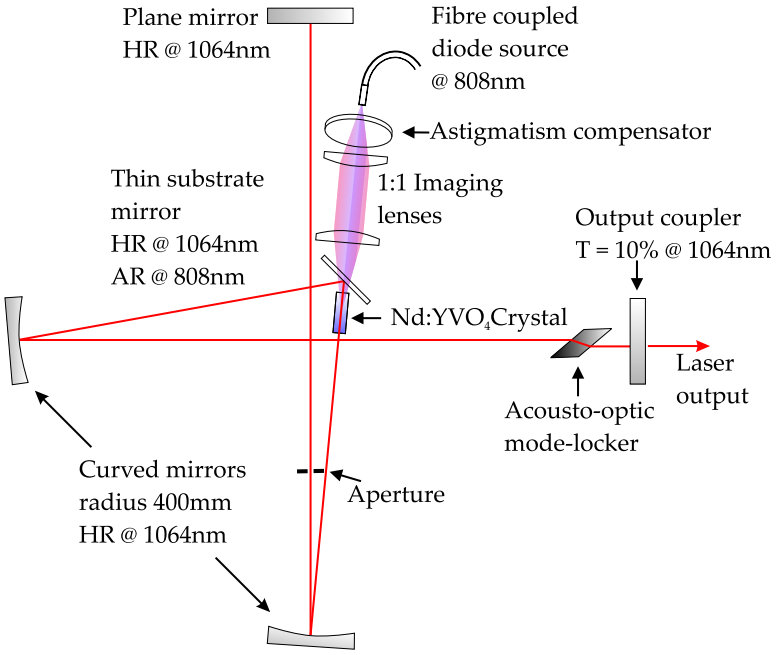

Figure 3.3: Layout of master-oscillator.

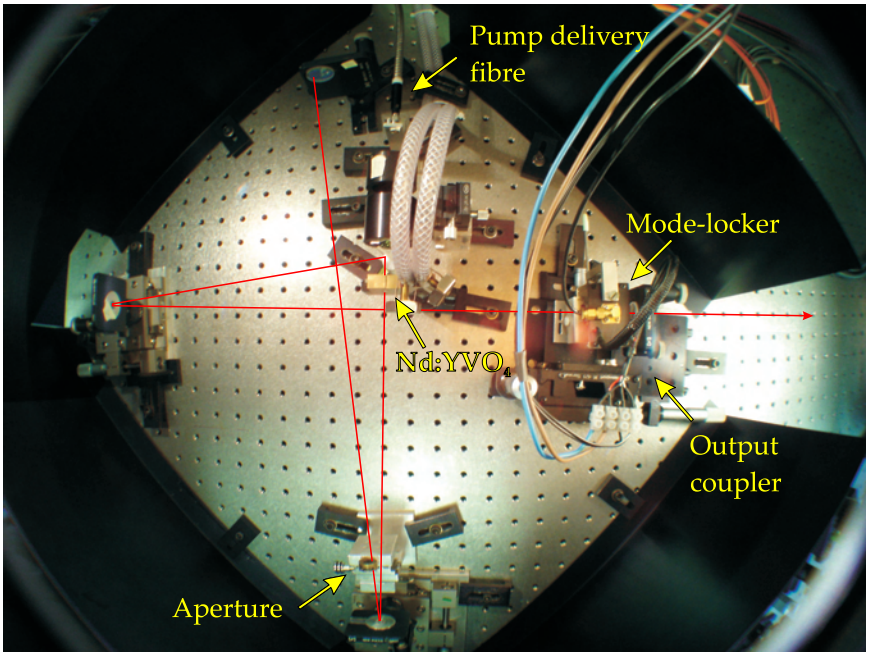

Figure 3.4: Photo of master-oscillator.

A normal incidence c-cut, 0.3 at.% doped, Nd:YVO_4 crystal was used as the gain medium and positioned at the center of the cavity. The crystal, of dimensions $3 \times 3 \times 10$mm, was coated for high transmission at pumping and lasing wavelengths and a small wedge angle of one of the end faces was included to reduce undesirable etalon effects. This doping concentration was chosen because it allows effective absorption over the focal region of the pump beam for a pump beam spot size well matched to the cavity mode size in the crystal. The absorption coefficient α_p, for 0.3 at.% doped Nd:YVO_4 , was estimated to be around 900m^{-1} which implies that the length over which $\sim$95% of pump power is absorbed (ie. $3l_{\alpha_p}$) is around 3mm. Equation (2.14) was used to predict the M^2 value of 156 for the pump beam from the 365µm diameter, 0.22 NA fiber. From equation (3.1), to produce a Rayleigh range of $\sim$3mm inside the crystal required a spot size of $\sim$173µm . This was approximately achieved by simple 1:1 re-imaging of the fibre output to the crystal using two f = 30mm graded index lenses. The pump beam was launched into the cavity through a 45° mirror coated for high transmission at 808nm and high reflectivity at 1064nm. A thin mirror thickness of 2mm was chosen to reduce astigmatism of the pump beam by minimising the path difference between orthogonal planes. However an improvement in beam quality and circular symmetry of the oscillator output was measured after introducing an astigmatism compensating element, in the form of a similar 2mm thick pump transmitting plate, placed between the fibre and collimating lens angled at 45° to the vertical plane. This acted to equalise the path differences in orthogonal planes between the fibre output and the crystal, thereby minimising the astigmatism.

Ignoring the plane folding mirror at the centre, the main cavity was formed by two plane mirrors at the ends and two 400mm radius of curvature folding mirrors. One of the plane mirrors was used as the output coupler with 90% reflectivity. By maintaining a cavity length of 1.5m and keeping the cavity symmetrical about the centre point, the mode size at the centre and at the output coupler was modelled as a function of the distance of the curved mirrors from the plane mirrors. The results are shown in Figure 3.5. From the figure an arm length of 470mm was chosen which resulted in a spot sizes of $\sim$160µm and $\sim$290µm in the rod and output respectively. From the model the mode size versus distance inside the cavity is shown in Figure 3.6.

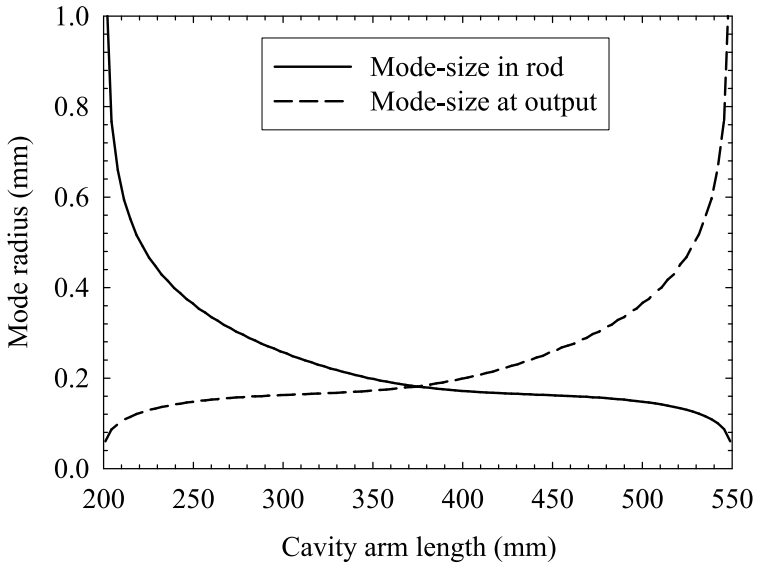

Figure 3.5: Mode radii at output coupler and in the laser rod as a function of plane mirror to curved mirror distances for a symmetric 1.5m long cavity

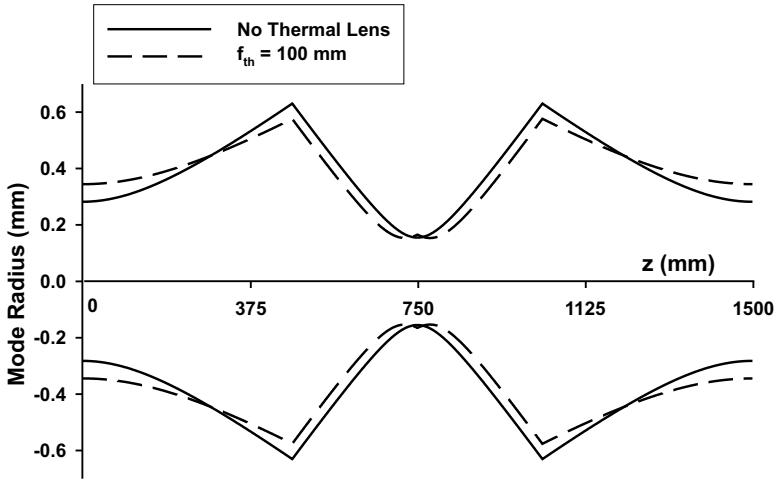

Figure 3.6: Mode size versus distance in master-oscillator without thermal lensing (solid line) and with a 100 mm thermal lens in crystal position (dashed line).

The Figure shows that mode size in the crystal (ie. at z = 750mm) rises by around 10µm for an example thermal lens of focal length 100mm and the output rises by around 60µm . Mode sizes as a function of thermal lens strength were also modelled, to further support this, and the result is shown in Figure 3.7.

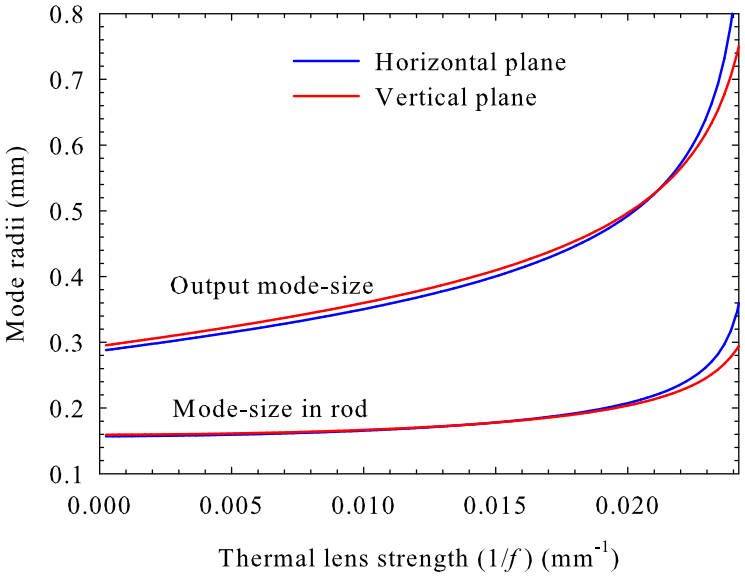

Figure 3.7: Rod and output cavity mode radii in both planes as a function of thermal lens strength in the rod.

The model predicts that the relevant mode sizes begin to increase rapidly for thermal focal lengths shorter than around 50mm and the cavity becomes unstable at a focal length of 42 mm. This is significantly stronger than the expected thermal lens strength based on the measured values by Musgrave *et al.* [15]. This therefore indicates good thermal lens tolerance, particularly in the crystal where the laser performance is more sensitive to mode size.

The difference in mode sizes in orthogonal planes is a result of the astigmatism introduced by the small angle of incidence of the laser beam on the curved mirrors. This was included in the above model, with a value of 0.1rad. for each curved mirror. The effect on the mode sizes, of changing this angle, was modelled to ensure sufficient circular symmetry of the mode. This result is shown in Figure 3.8. The model predicted negligible astigmatism effects provided that the angles were kept below ∼0.1rad. which was achievable in practice.

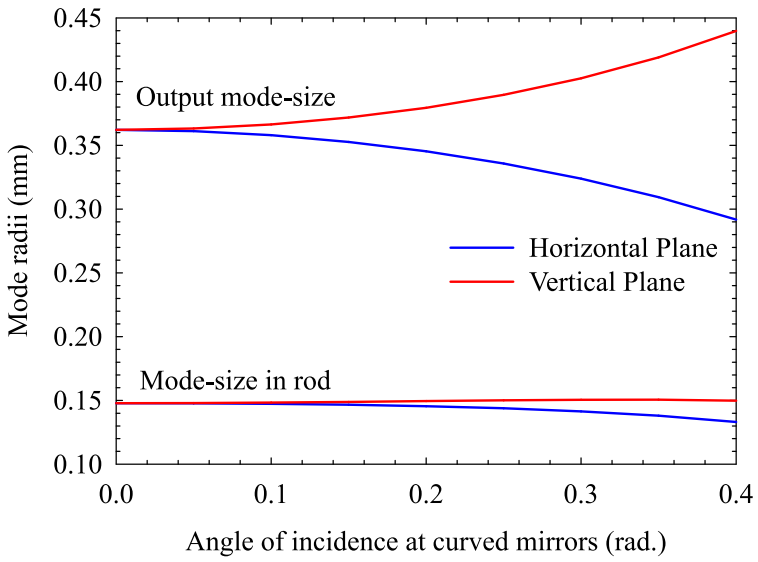

Figure 3.8: Change in rod and crystal mode radii with changing incidence angle at curved mirrors.

It was found, by measuring the beam quality in initial experiments, that the cavity supported higher order modes. This was likely to be a result of gain in the wings of the pump distribution since the laser mode was smaller than the pump beam. To suppress these higher order modes, an aperture in the form of an iris was used. The position of the aperture, between crystal and curved mirror, was chosen where there was predicted (from the model) to be a large difference in spot size between the TEM_{00} mode and a mode with a higher M^2 value. The result of an aperture in such a position is to introduce a high loss for the higher order modes while loss to the fundamental mode is kept to a minimum. The aperture size and position was optimized for high power and TEM_{00} beam quality while the oscillator was running with a pump power of 22W.

3.5 Experimental Results

Figure 3.9 shows the power output as a function of incident pump power. As expected, almost all the pump power (>99%) was absorbed over the length of the crystal. The dashed line represents a linear best fit to the data and the

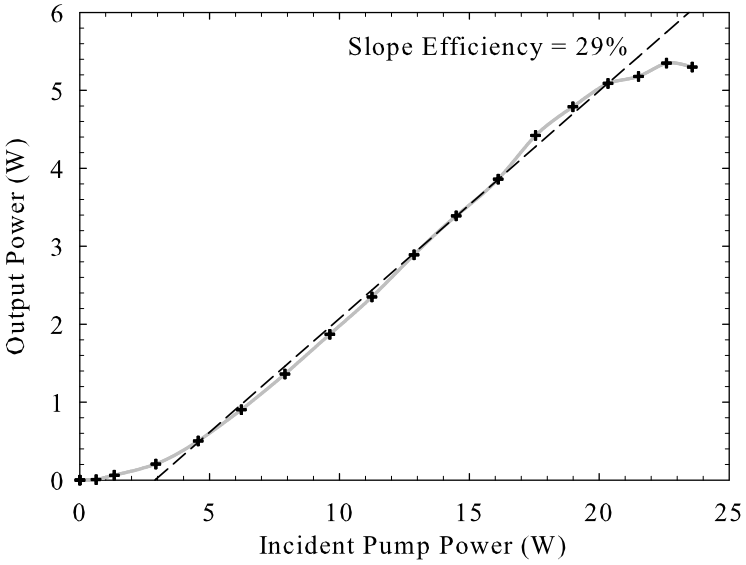

Figure 3.9: The power output as a function of absorbed power in the master-oscillator.

corresponding slope efficiency was 29% and the maximum output power was 5.3W. The threshold pump power was only just above the pump diode threshold, so limited control over pump power made the measurement difficult. The beam was also found to be circular and the ellipticity of the output was less than 5%. Based on the output coupler transmission of 10% and equation (2.3), the cavity loss was predicted to be around 7%. In the absence of the aperture the output power was 6.5W and the slope efficiency was 34%. This implied that the aperture loss was around 2.5% while the losses from the other optics amounted to around 4.5% which is rather high but not unreasonable considering the number of components in the cavity. The total number of surfaces in a round trip (reflections and transmissions) of 17 corresponds to an average loss of less than 0.3% per surface which is close to expectations. Without the aperture, the M^2 was measured as a function of incident pump power and the results are shown in Figure 3.10.

Unusually, the M^2 value rose sharply at low pump power which was thought to be a result of a small misalignment, or instability of the laser, which was rectified by the presence of a thermal lens when the pump power was increased. Conversely, re-aligning the laser for good beam quality at low power resulted

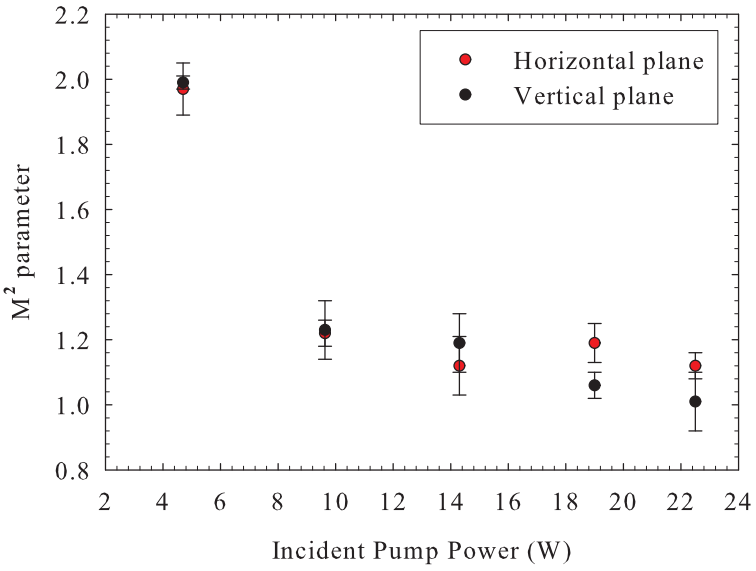

Figure 3.10: The beam quality factor M^2 of the oscillator output with aperture included as a function of incident pump power

in poor beam quality at high power levels. The best beam qualities of 1.01 and 1.12 were actually measured at a maximum pump power of 22W however the aperture was still necessary to achieve even better beam quality over a large range of output powers. Figure 3.11 shows the corresponding beam quality measurements with the aperture included. It can be seen that M^2 values below 1.05 were measured in the pump power range 14 to 23W which corresponds to the output power range 3.3 to 5.3W.

Using equation (1.1) for the brightness and the fact that the solid-angle divergence of the beam is proportional to the product of the orthogonal M^2 values, the brightness of the output was plotted as a function of pump power, as shown in Figure 3.12. This shows that the small degradation in beam quality and small rollover in output power at the maximum pump power causes a significant rollover in brightness suggesting that operating at a slightly lower power of 21W gives the maximum brightness output.

The above results were gathered while operating the oscillator in cw mode. By simply switching on the rf signal to the mode-locker it was possible to select mode-locked operation. This led to a reduction in output power of less than 5% due to additional loss in the AOM. The mode-locked pulse duration was

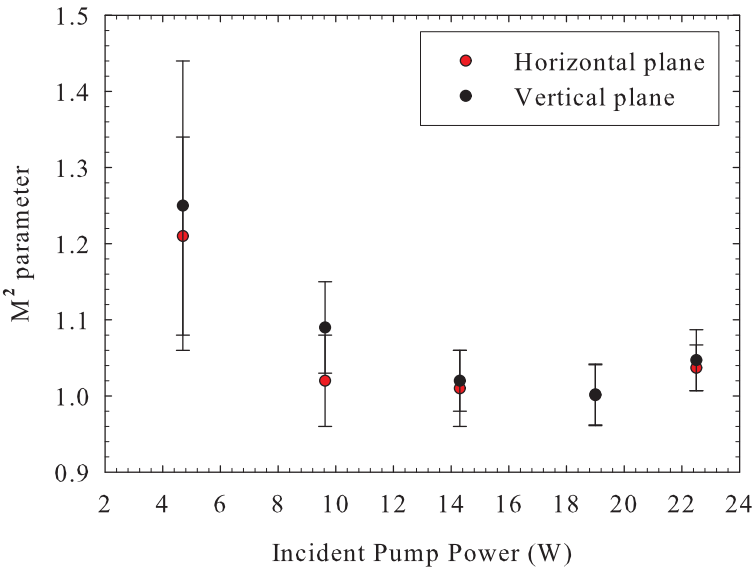

Figure 3.11: The beam quality factor M^2 of the oscillator output, with aperture included, as a function of incident pump power

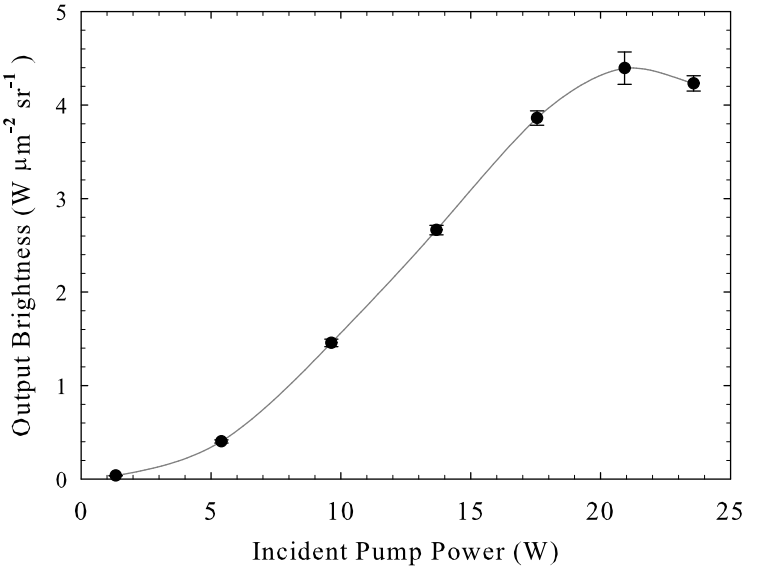

Figure 3.12: Output brightness as a function of incident pump power

measured using a 30GHz, fibre coupled, Digital Communications Analyzer (DCA). The output coupler was mounted on a translation stage so that the cavity length could be fine tuned to match the modulation frequency and at maximum power the pulse was measured to be Gaussian in profile with a FWHM duration of ~358ps, as shown in Figure 3.13.

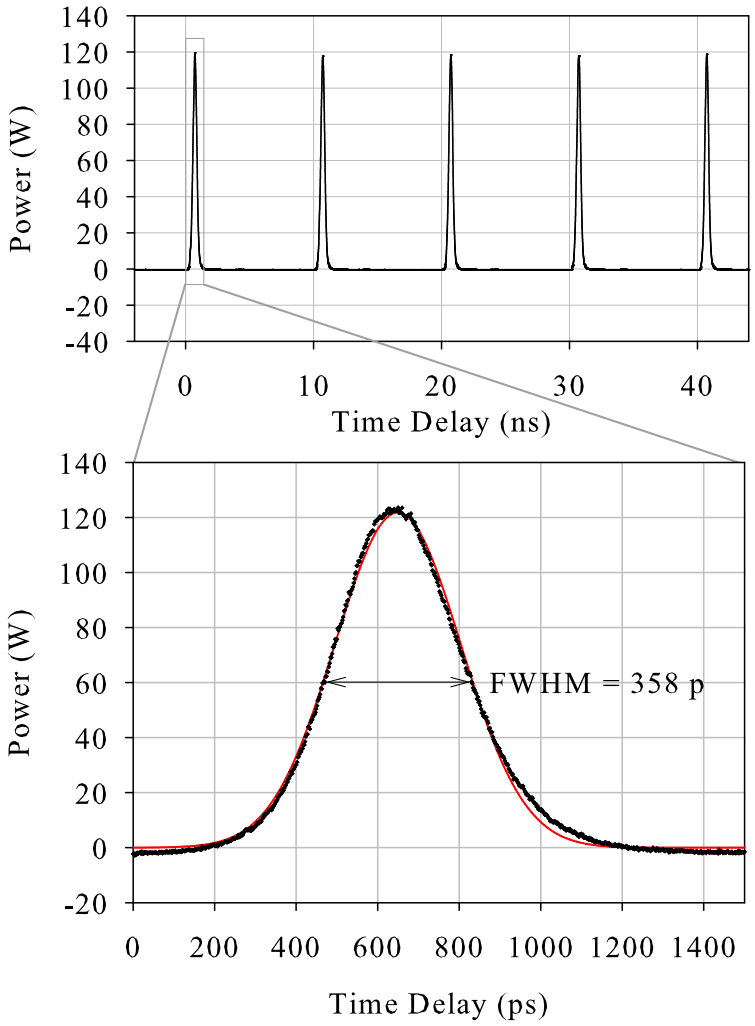

Figure 3.13: DCA trace of mode-locked pulses at 100MHz repetition rate and single pulse with 358ps FWHM duration. Red line shows Gaussian fitting curve.

The graphs show stable mode-locked pulses of well defined FWHM pulse durations of ~360ps and a Gaussian temporal shape shown by a good fit to the Gaussian curve in red. The vertical axis was re-scaled to show the power, by integrating the data numerically and fitting the area to the known pulse energy

given by the average power divided by the repetition rate.

Using equation (3.3) with a measured modulation depth of the mode-locker of 0.6, a modulation frequency of 100MHz, a gain bandwidth of 250GHz for Nd:YVO_4 and a round trip gain $2gl$ equal to the round trip loss of $L+T=0.17$ gives a predicted pulse duration of 88ps. The rather long pulse duration, compared to theory, was not fully investigated but it was thought that it could be attributed to the increase in the mode-size in the mode-locker in the presence of a thermal lens in the gain medium. Since the active aperture of the mode-locker is around 1mm in diameter, a mode diameter similar to or greater than this (which was predicted to occur for strong thermal lensing, $f_{th} < 50\text{mm}^{-1}$), could lead to a reduction in modulation depth or ineffective Bragg diffraction. It was thought that an improved cavity design, with reduced mode size in the modulator, could be adopted to significantly reduce the pulse duration.

Another factor which could influence the mode-locked pulse duration is the effect of spatial hole burning. Braun *et al.* [16] and Kärtner *et al.* [17] studied the effect of spatial hole burning on the optical gain of multiple longitudinal modes in an end-pumped cavity. They found that laser cavities with the gain at the end were subject to enhanced spatial hole burning which gave rise to a flatter spectral gain profile and hence larger bandwidth and shorter mode-locked pulses. In contrast, cavities with the gain at the center (as the oscillator described in this chapter has) were found to have negligible spatial hole burning and hence showed more ideal homogenous line broadening which reduces the bandwidth and hence increases the pulse duration. Cavities with the gain at the center were measured to have pulse durations approximately three times those of similar cavities with the gain at the end. This effect could partly explain the longer than expected pulse durations in the oscillator described in this thesis. Further experiments using a different cavity design with the gain medium at the end would therefore be expected to yield shorter pulses and higher peak powers.

3.6 Summary

In this chapter the design process of a Nd:YVO_4 master-oscillator was described. The rationale for developing a mode-locked oscillator as a seed laser for a power-amplifier was discussed. The application of mode-locked sources for non-linear frequency conversion was discussed with regard to their potential as a pump source for synchronously pumped OPOs. The main design considerations for the oscillator were outlined, including the influences that the choice of Nd^{3+} doping concentration may have on the design and performance, as well as the requirements of the pump source and the constraints that the pumping scheme places on the design. The main principles of mode-locking were described and the relative merits of active mode-locking, compared to passive mode-locking, were summarised. The use of active mode-locking, with an acousto-optic amplitude modulator, was justified as a robust and stable scheme to use in the oscillator and a simple method for predicting the likely pulse durations was introduced. Using a simple ABCD matrix analysis, the principles of resonator modelling were introduced and, using the constraints placed on the design by the pumping scheme and mode-locking scheme, a suitable cavity design was presented. The cavity model was modified to demonstrate its tolerance to changes in various parameters such as mirror spacings, thermal lens strength in the gain medium and the angles of the curved mirrors. In each case the chosen design was deemed to have favourable properties. The experimental results for the oscillator were presented. Its was shown to be reasonably efficient, with excellent beam quality and stable reliable operation, in both cw and mode-locked mode. With a slope efficiency of 29% and cavity losses less than 10% the oscillator achieved a maximum diffraction limited output power of 5.3W for 22W of incident pump power which corresponds to a total optical efficiency of 24%. The power rolled over for higher pump powers due to the increased loss from the aperture for stronger thermal lensing and hence larger mode size. This rollover could be prevented by increasing the aperture size by a small amount, however the measured M^2 value was increased as a result of the thermal lens aberration, even when higher order modes were suppressed. The beam quality as a function of pump power was measured with and without the aperture in place and it was found that, al-

though good beam quality (<1.2) could be achieved at high power without the aperture, by including it, the beam quality was further improved with an M^2 less than 1.05 in both planes over a much wider range of output powers from 3.3 to 5.3W. The peak brightness of the output was shown to occur at a pump power of 21W before rolling over due to thermal lens aberrations and loss at the aperture. In mode-locked mode of operation the output power was only slightly lower and mode-locked pulse durations were measured to be ∼360ps with near perfect Gaussian profiles. This implies peak powers of the output greater than 150W.

3.7 References

[1] **Liu, J., Yang, J.** and **He, J.**, *High Repetition Rate Passively Q-Switched Diode-Pumped Nd:YVO_4 Laser*, Optics and Laser Technology, Vol. 35, pp. 431–434, 2003.

[2] **Rimington, N. W., Schieffer, S. L.** and **Schroeder, W. A.**, *Thermal lens shaping in Brewster gain media:A high-power, diode-pumped Nd:$GdVO_4$ laser*, Optics Express, Vol. 12, No. 7, pp. 1426–1436, 2004.

[3] **Sennaroglu, A.**, *Influence of neodymium concentration on the strength of thermal effects in continuous-wave diode-pumped Nd:YVO_4 laser at 1064nm*, Optical and Quantum Electronics, Vol. 32, pp. 1307–1317, 2000.

[4] **Chen, Y. F.**, *Design criteria for concentration optimization in scaling diode end-pumped lasers to high powers: influence of thermal fracture*, IEEE Journal of Selected Topics in Quantum Electronics, Vol. 35, No. 2, pp. 234–239, 1999.

[5] **Chen, Y. F., Lan, Y. P.** and **Wang, S.**, *Modelling of Diode-End-Pumped Q-Switched Solid-State Lasers: Influence of Energy-Transfer Upconversion*, Journal of the Optical Society of America B, Vol. 19, No. 7, pp. 1558–1563, 2002.

[6] **Musgrave, I. O.**, Study of the Physics of Power Scaling of End-Pumped Solid-State Laser Sources based on Nd:YVO_4 , Ph.D. thesis, Optoelectronics Research Centre, University of Southampton, 2003.

[7] **Chen, Y. F., Liao, T. S., Kao, C. F., Huang, T. M., Lin, K. H.** and **Wang, S. C.**, *Optimization of Fibre-Coupled Laser-Diode End-Pumped Lasers: Influence of Pump-Beam Quality*, IEEE Journal of Quantum Electronics, Vol. 32, No. 11, pp. 2010–2016, 1996.

[8] **Koechner, W.**, Solid-State Laser Engineering, Springer, 5th edn., 1999.

[9] **Fluck, R., Zhang, G.** and **Keller, U.**, *Diode-pumped passively mode-locked 1.3μm Nd:YVO_4 and Nd:YLF lasers by use of semiconductor saturable absorbers*, Optics Letters, Vol. 21, No. 17, pp. 1378–1380, 1996.

[10] **Lagatsky, A. A., Saramani, A. R., Brown, C. T. A., Sibbett, W., Kisel, V. E., Selivanov, A. G., Denisov, I. A., Troshin, A. E., Yumashev, K. V., Kuleshov, N. V., Matrosov, V. N., Matrosova, T. A.** and **Kupchenko, M. I.**, *Yb^{3+}-doped YVO_4 crystal for efficient Kerr-lens mode locking in solid-state lasers*, Optics Letters, Vol. 30, No. 23, pp. 3234–3236, 2005.

[11] **Bai, J. T., Qiao, X. C.** and **Wang, S. C.**, *Acousto-optic actively mode-locked frequency-doubled continuous-wave Nd:YAG laser*, Journal of Applied Physics, Vol. 75, No. 2, pp. 734–736, 1994.

[12] **Kuizenga, D. J.** and **Siegman, A. E.**, *FM and AM Mode Locking of the Homogeneous Laser – Part I: Theory*, IEEE Journal of Quantum Electronics, Vol. 6, No. 11, pp. 694–708, November 1970.

[13] **Kogelnik, H.** and **Li, T.**, *Laser Beams And Resonators*, Applied Optics, Vol. 5, No. 10, pp. 1550–1567, October 1966.

[14] **Clarkson, W. A.**, *Thermal effects and their mitigation in end-pumped solid state lasers*, Journal of Physics D: Applied Physics, Vol. 34, pp. 2381–2395, August 2001.

[15] **Musgrave, I. O., Clarkson, W. A.** and **Hanna, D. C.**, *Detailed study of thermal lensing in Nd:YVO4 under intense diode end-pumping*, CLEO '01. Technical Digest: Summaries of papers presented at the Conference on 6-11 May 2001, pp. 171–172.

[16] **Braun, B., Weingarten, K. J., Kärtner, F. X.** and **Keller, U.**, *Continuous-wave mode-locked solid-state lasers with enhanced spatial hole burning. Part I:*

Experiments, Applied Physics B: Lasers and Optics, Vol. 61, No. 5, pp. 429–437, 1995.

[17] **Kärtner, F. X., Braun, B.** and **Keller, U.**, *Continuous-wave mode-locked solid-state lasers with enhanced spatial hole burning. Part II: Theory*, Applied Physics B: Lasers and Optics, Vol. 61, No. 5, pp. 569–579, 1995.

Chapter 4

Power and Brightness Scaling in End-Pumped Amplifiers

4.1 Introduction

This chapter discusses in detail, the theory of laser amplification and the design considerations for power scaling in an end-pumped amplifier. Many of the challenges in amplifier design lie in optimisation of the various trade-offs involved. For example, with end-pumping, the overlap between the signal beam and pump beam is critical. To reduce distortion of the amplified signal, the signal beam radius is usually chosen to be smaller than the pump beam radius. If the signal radius is too small, the gain in the wings is lost by spontaneous emission, however, if it is too large, the thermally induced lens aberrations in the wings of the pump distribution can significantly reduce the beam quality. Similarly, the pump beam size needs to be optimised: If it is too small then stress fracture of the crystal may occur and thermal lensing may become strong, if it is too large then the extraction efficiency of gain in the crystal will be reduced due to a lower inversion density. Also, with the relatively large M^2 values of fibre-coupled high-power diode-bars, the focused pump beam needs to be large enough not to diverge too much over the length of the rod, so that the pumped volume is minimised. Another problem in designing amplifiers is ensuring that the signal intensity is high enough to efficiently extract the stored energy in the amplifier. Multiple pass amplifiers are often used to increase the signal intensity in the gain medium and, in effect, the amplifier operates more

like a laser. However, for high power operation, using multiple passes, and indeed multiple amplifier stages, will cause the various thermal effects to be compounded. We will see that, although a a range of factors can ultimately limit the power scaling potential of an amplifier, it is of greater concern that the thermally induced degradation in beam quality can cause a reduction in the output brightness. Eventually a brightness scaling limit can be reached, where the degradation in beam quality, caused by thermally induced aberrations, will reduce the brightness more than the potential increase in brightness due to power amplification. The following chapter investigates some of these issues from a theoretical view point, with the aim of formulating a general design strategy for end-pumped power-amplifier systems but with particular regard to developing an amplifier used to amplify the output from the mode-locked oscillator described in Chapter 3.

4.2 Single-Pass Amplifier Theory

4.2.1 Small Signal Gain

The basic principle of small signal gain was introduced in Chapter 2. The total small signal gain G_0, for a single pass through an amplifier, for a signal intensity small enough not to significantly deplete the upper state population was given by the expression:

$$G_0 = \exp(g_0 l), \tag{4.1}$$

where l is the length of active medium traversed. Assuming a four-level system with a population inversion density $n_2(r, z)$, which varies radially and longitudinally, as is the situation in an end-pumped rod, the small signal gain per unit length $g_0(r, z)$ is given by

$$g_0(r, z) = \sigma_{21} n_2(r, z), \tag{4.2}$$

where σ_{21} is the stimulated emission cross section. At low pump power, where the effects of lifetime quenching are negligible, $n_2(r, z)$ is simply related to the pump rate per unit volume $R(r, z)$ and the upper state lifetime τ_f by [1]

$$n_2(r, z) = R(r, z)\tau_f. \tag{4.3}$$

$R(r,z)$ is proportional to the pump power deposition density which, in turn, is a function of the incident pump intensity distribution $I_p(r)$ and the absorption coefficient of the material at the pump wavelength α_p, hence

$$R(r,z) = \frac{\alpha_p I_p(r)}{h\nu_p} \exp(-\alpha_p z), \tag{4.4}$$

where ν_p is the optical frequency of the pump and h is the Planck constant. Now, assuming that the normalised pump intensity profile does not change over the length of the gain medium, we can integrate $R(r,z)$ over length l of the gain medium to give an expression for $g_0(r)l$:

$$g_0(r)l = \frac{I_p(r)\eta_{abs}\sigma_{21}\tau_f}{h\nu_p}, \tag{4.5}$$

where η_{abs}, the pump power absorption efficiency, is given by

$$\eta_{abs} = \int_0^l \alpha_p \exp(-\alpha_p z)\mathrm{d}z = 1 - \exp(\alpha_p l), \tag{4.6}$$

and hence the small signal gain $G_0(r)$ for a 'ray' of co-ordinate r is given by

$$G_0(r) = \exp\left(\frac{I_p(r)\eta_{abs}\sigma_{21}\tau_f}{h\nu_p}\right). \tag{4.7}$$

4.2.1.1 The Importance of Pump Beam Profile and M^2

There are some important simplifying assumptions which are used in the modelling in this chapter, which relate to the properties of the pump beam. In this analysis, we consider end-pumped laser rods with circular pump beams, focused to produce a waist position at the centre of the rod. The first assumption, already mentioned, is that the divergence of the pump beam is neglected over the length of the gain medium and hence the pump beam radius, w_p, is constant. This assumption is a valid approximation, provided that the pump beam waist size is greater than a minimum value, $w_{p,min}$, which depends on the beam quality factor M^2 and the length l_g of the rod:

$$w_{p,min} \approx \sqrt{\frac{l_g M^2 \lambda_p}{2\pi n}}, \tag{4.8}$$

where n is the refractive index of the gain medium. Under this condition called confocal focusing, the beam is $\sqrt{2}$ times larger at the end faces of the rod than

in the centre. Since, in practice, the beam quality of the signal beam is much better than the beam quality of the pump, it is always desirable to use a pump beam with $w_p \geq w_{p,min}$ to ensure sufficiently good overlap of pump and signal beam, so the assumption is valid in most practical situations. Furthermore, using a pump waist size of $w_{p,min}$, gives a volume of the Gaussian pump beam in the gain medium which is very close to the theoretical minimum, shown by Clarkson *et al.* [2] to be

$$w_{min} \approx \sqrt{\frac{l_g M^2 \lambda}{\sqrt{3}\pi n}}. \tag{4.9}$$

Assuming a uniform axial pump deposition density, which is reasonable if $l_g \sim 1/\alpha_p$, this minimum pump waist implies that the overall pump deposition density is maximised and therefore the highest overall small signal gain is reached.

The second assumption relates to the pump beam profile $I_p(r)$. The most convenient way to produce a smooth circular beam profile from a high power diode bar, is to couple the radiation via a multimode optical fibre. The beam profile in the focal region of a beam from a typical multimode fibre looks similar to the solid line in Figure 4.1. In order to produce simple analytical models for the physics of a laser amplifier it is normally necessary to make simplifying approximations for this complicated beam profile. The most simple approximations, which are shown in Figure 4.1, are a 'top-hat' profile where

$$I_p(r) = \frac{P_p}{\pi w_p^2}, \quad \text{for} \quad r \leq w_p, \tag{4.10}$$

and

$$I_p(r) = 0, \quad \text{for} \quad r > w_p, \tag{4.11}$$

and a Gaussian profile where

$$I_p(r) = \frac{2P_p}{\pi w_p^2} \exp\left(\frac{-2r^2}{{w_p}^2}\right), \tag{4.12}$$

where P_p is the pump power in each case. It is clear from the graph, that neither of these approximations provides a very accurate description of the real pump beam profile which could potentially limit the value of the model. In this chapter, the implications on amplifier performance for each of these pump profile approximations is considered and their validity is assessed.

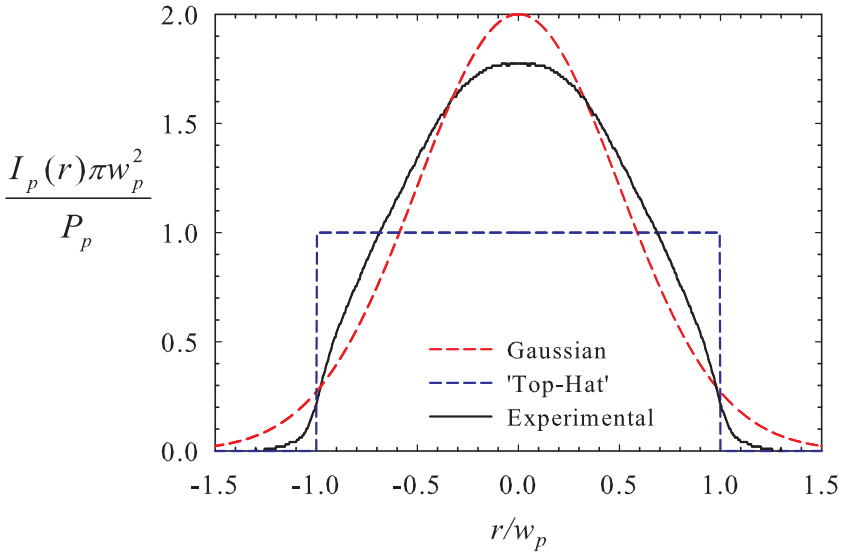

Figure 4.1: Experimental multimode fibre-coupled pump beam profile compared to Gaussian and 'top-hat' approximations with the same output power, assuming cylindrical symmetry.

4.2.1.2 Dependence of Small Signal Gain on Pump and Signal Beam Sizes

For the 'top-hat' case the small signal gain coefficient is zero outside the pump beam radius and constant inside the pump beam radius, with a value given by

$$g_0(r) = \left(\frac{P_p \eta_{abs} \sigma_{21} \tau_f}{l h \nu_p \pi {w_p}^2} \right), \quad \text{for} \quad r \leq w_p, \tag{4.13}$$

and

$$g_0(r) = 0, \quad \text{for} \quad r > w_p. \tag{4.14}$$

For the Gaussian approximation the radially dependent small signal gain coefficient is given by

$$g_0(r) = \left(\frac{2 P_p \eta_{abs} \sigma_{21} \tau_f}{l h \nu_p \pi {w_p}^2} \exp\left(\frac{-2r^2}{{w_p}^2} \right) \right). \tag{4.15}$$

To remove the r dependence an effective value of the small signal gain coefficient per unit length, g_{eff}, can be estimated by integrating $g_0(r)$ over the pumped radius and also by taking into account the radial profile of the signal $I_l(r)$ [3]:

$$g_{eff} = \frac{\int g_0(r) I_l(r) 2\pi r \mathrm{d}r}{\int I_l(r) 2\pi r \mathrm{d}r}. \tag{4.16}$$

g_{eff} represents an average of the small signal gain with respect to area, weighted with respect to the signal intensity. In the case where the signal beam is larger than the pump beam, the effective small signal gain is reduced since a proportion of the signal 'sees' little or no gain. In this analysis we only consider signal beams with Gaussian radial intensity distributions given by

$$I_l(r) = \frac{2P_l}{\pi {w_l}^2} \exp\left(\frac{-2r^2}{{w_l}^2}\right), \tag{4.17}$$

where w_l is the $1/e^2$ signal spot size, assumed to be constant over the length of the rod and centered with respect to the pump, and P_l is the input signal power.

In the first example of a 'top-hat' pump beam g_{eff} in equation (4.16) can be evaluated as

$$g_{eff} = g_0(r)\frac{\int_0^{w_p} I_l(r)2\pi r \mathrm{d}r}{\int_0^{\infty} I_l(r)2\pi r \mathrm{d}r}, \quad \text{for} \quad r \leq w_p, \tag{4.18}$$

and

$$g_{eff} = 0, \quad \text{for} \quad r > w_p, \tag{4.19}$$

which gives an approximate expression for the total small signal gain for a 'top-hat' pump, $G_{0,T}$, given by

$$\ln G_{0,T} = \frac{P_p \eta_{abs} \sigma_{21} \tau_f}{h\nu_p \pi {w_p}^2}\left[1 - \exp\left(\frac{-2{w_p}^2}{{w_l}^2}\right)\right]. \tag{4.20}$$

Using equations (4.16) in the case of a Gaussian pump beam it follows that

$$g_{eff} = \frac{2P_p \eta_{abs} \sigma_{21} \tau_f}{lh\nu_p \pi {w_p}^2}\left(\frac{{w_p}^2}{{w_p}^2 + {w_l}^2}\right), \tag{4.21}$$

and therefore the approximate total small signal gain for a Gaussian pump, $G_{0,G}$, is given by the expression:

$$\ln G_{0,G} = \frac{2P_p \eta_{abs} \tau_f \sigma_{21}}{h\nu_p \pi({w_p}^2 + {w_l}^2)}. \tag{4.22}$$

Figure 4.2 shows a comparison of $\ln(G_{0,T})$ and $\ln(G_{0,G})$, plotted as a function of the signal-pump overlap ratio w_l/w_p. While in the 'top-hat' case the small signal gain becomes constant for $w_l/w_p < 1$, in the Gaussian case the small signal gain increases due to the pump intensity being greatest at the centre.

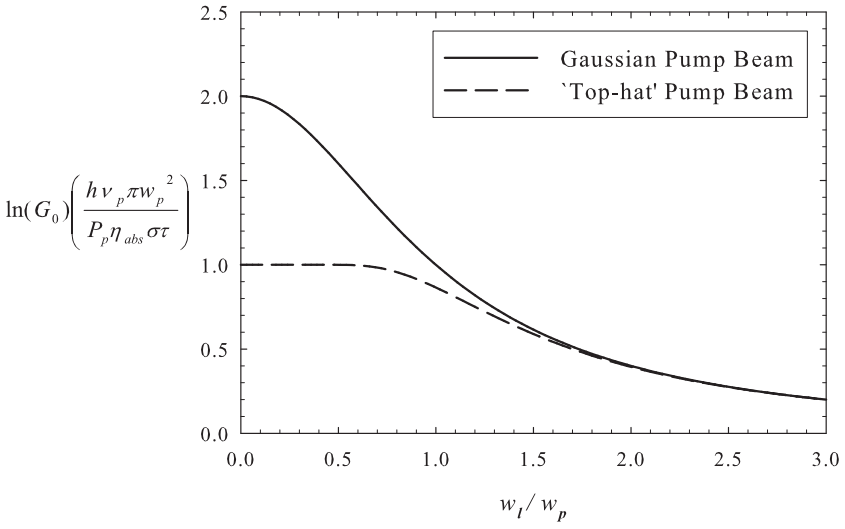

Figure 4.2: Comparison of signal-pump overlap dependence of the total small signal gain for 'top-hat' and Gaussian pump beam approximations

4.2.2 Effect of Energy Transfer Upconversion

At higher pump powers the effect of energy transfer upconversion (ETU) can become significant particularly in an amplifier that is not highly saturated and therefore the inversion density is higher. This leads to a shortening of the effective decay lifetime and reduces the potential gain of the amplifier. With ETU accounted for and in the case of low signal powers, the upper state population n_2 under steady-state conditions becomes [1]:

$$n_2(r,z) = \frac{-1 + \sqrt{1 + 4R(r,z)W\tau_f^2}}{2W\tau_f}, \tag{4.23}$$

where W is the upconversion parameter [cm^3/s]. Using a similar analysis to Musgrave [4] and repeating the derivation for small signal gain above, using equation (4.23) and a 'top-hat' pump beam profile for simplicity, it follows that

$$R(r,z) = \frac{\alpha_p P_p}{h\nu_p \pi {w_p}^2} e^{-\alpha_p z}, \quad \text{for} \quad r \leq w_p, \tag{4.24}$$

and

$$R(r,z) = 0, \quad \text{for} \quad r > w_p. \tag{4.25}$$

The effective small signal gain coefficient can be expressed using (4.16) and integrating over the 'top-hat' pump area and a Gaussian signal area:

$$\begin{aligned} g_{eff}(z) =& \frac{\sigma_{21}}{2W\tau_f}\left(1-\exp\left(\frac{-2w_p^2}{w_l^2}\right)\right) \\ &\times\left(-1+\sqrt{1+\frac{4\alpha_p P_p W\tau_f^2}{h\nu_p\pi {w_p}^2}e^{-\alpha_p z}}\right). \end{aligned} \tag{4.26}$$

To find the total small signal gain coefficient, in the presence of ETU and hence the unsaturated gain $g_{0,ETU}l = \ln G_{0,ETU}$, equation (4.26) can be integrated over the length of the crystal l so that

$$\begin{aligned} \ln G_{0,ETU} =& \frac{\sigma_{21}}{2W\tau_f}\left(1-\exp\left(\frac{-2w_p^2}{w_l^2}\right)\right) \\ &\times\left(-\int_0^l \mathrm{d}z+\int_0^l\sqrt{1+\frac{4\alpha_p P_p W\tau_f^2}{h\nu_p\pi {w_p}^2}e^{-\alpha_p z}}\mathrm{d}z\right). \end{aligned} \tag{4.27}$$

Using the following standard integral

$$\int\frac{\sqrt{x^2+1}}{x}\mathrm{d}x=\sqrt{x^2+1}-\ln\left(\frac{1+\sqrt{x^2+1}}{x}\right)+C, \tag{4.28}$$

and the substitution

$$x(z)=\sqrt{\frac{4\alpha_p P_p W\tau_f^2}{h\nu_p\pi w_p^2}e^{-\alpha_p z}}, \tag{4.29}$$

the second integral in (4.27) can be solved between the limits $x(z=0)$ and $x(z=l)$ and, in the simple case where all the pump power is absorbed over the length of the crystal, implying that $\exp(-\alpha_p l)\sim 0$, it can be shown (see Appendix A.) that the approximate small signal gain is given by.

$$\begin{aligned} \ln G_{0,ETU} =& \frac{4P_p\tau_f\sigma_{21}}{\chi h\nu_p\pi w_p^2}\left(1-\exp\left(\frac{-2w_p^2}{w_l^2}\right)\right) \\ &\times\left[\sqrt{1+\chi}-1+\ln\left(\frac{2}{1+\sqrt{1+\chi}}\right)\right], \end{aligned} \tag{4.30}$$

where

$$\chi=\frac{4\alpha_p P_p W\tau_f^2}{h\nu_p\pi {w_p}^2}. \tag{4.31}$$

It can also be shown that, when ETU becomes small (ie. $\chi \ll 1$), a linear approximation of the second line in equation (4.30) (which can be labelled $f(\chi)$)

can be given by calculating

$$\lim_{\chi\to 0} f(\chi) = \chi \left(\lim_{\chi\to 0} \frac{\mathrm{d}f(\chi)}{\mathrm{d}\chi} \right). \tag{4.32}$$

By differentiating $f(\chi)$, it can therefore be shown that

$$\lim_{\chi\to 0} \left[\sqrt{1+\chi} - 1 + \ln\left(\frac{2}{1+\sqrt{1+\chi}} \right) \right] = \frac{\chi}{4}, \tag{4.33}$$

which means that equation (4.30) becomes the same as equation (4.20); the small signal gain without ETU, as expected.

Using equation (4.30) and the value of the upconversion parameter W, measured by Musgrave *et al.* [4] to be approximately $3\times10^{-16}\mathrm{cm}^3\mathrm{s}^{-1}$ in Nd:YVO_4 for 0.3at.% and 1at.% doping concentration, Figure 4.3 was produced showing the variation in the small signal gain with pump intensity. This used the

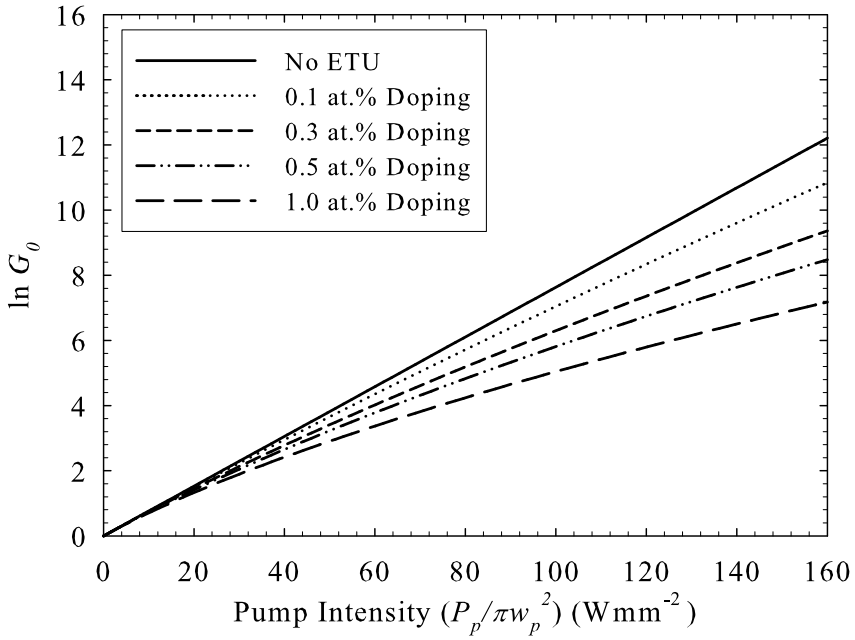

Figure 4.3: Variation in $\ln G_{0,ETU}$ with pump intensity for different Nd^{3+} dopant concentrations in Nd:YVO_4 . For reference, a pump intensity of $100\mathrm{Wmm}^{-2}$ is equivalent to a pump power of 28 W for a pump spotsize of 300µm . This is approaching the damage threshold for a typical 0.5 at.% doped crystal [5]

simplifying assumptions that W, τ_f and σ_{21} are constant with varying doping concentration, with values $3\times10^{-16}\mathrm{cm}^3\mathrm{s}^{-1}$, 90µs , and $25\times10^{19}\mathrm{cm}^2$ respectively,

and that the absorption coefficient α_p and is proportional to the doping concentration with a value of 31.4cm^{-1} and at 1 at.% doping concentration. Additionally, the length of the crystals was assumed to be long enough to absorb all the pump radiation. As can be seen in the graph, the effect of ETU is to reduce the small signal gain an increasing amount for greater pumping intensity. The effect of ETU on crystals with higher doping concentrations is a greater reduction in small signal gain. This is because because they have higher absorption coefficients and hence greater pump rates per unit volume which increases the probability of upconversion events occurring. This highlights the advantage of using lower doping concentrations and longer rods (so that all the pump radiation is absorbed) as a route to power scaling. Not only is the effect of ETU reduced but also the damage threshold of the crystals is increased, allowing higher intensity pump sources to be used. However, the upper limit on the length of rod that can be used is set by the pump beam diffraction, which therefore sets a lower limit on the Nd^{3+} doping concentration that can be used whilst still absorbing a large fraction of the pump light. We can, nevertheless, reduce the impact of ETU to a level sufficiently low that it can be neglected in most regimes described in this thesis.

4.2.3 Continuous-Wave Saturated Gain Operation

In the small signal regime, a continuous laser signal passing through a medium with uniform small signal gain will grow in power exponentially with distance, z, through the medium. However, for a larger signal intensity a significant number of excited ions decay by stimulated emission and since gain is proportional to the number of excited ions, the gain is therefore reduced and the amplifier is said to be saturated. In the heavily saturated regime the signal intensity grows approximately linearly with distance along the gain medium as all the excited atoms are stimulated. Complete saturation, however, is never achievable since the signal intensity required would be infinite. In the following sections the small signal gain analysis is extended to account for signal intensities large enough to cause saturation effects in the gain medium. Siegman [6] analyzed the behavior of a lossless single pass amplifier with continuous pump and signal beams and homogeneous saturation of the gain medium.

The basic differential equation governing the growth rate of a signal with intensity $I_l(z)$ along a lossless amplifier is given by

$$\frac{1}{I_l(z)}\frac{\mathrm{d}I_l(z)}{\mathrm{d}z} = \frac{g_0(z)}{1 + I_l(z)/I_{sat}}, \tag{4.34}$$

where

$$I_{sat} = \frac{h\nu_l}{\sigma_{21}\tau_f}. \tag{4.35}$$

I_{sat} is the signal intensity required to reduce the gain to one half its small signal value. Since the gain coefficient varies with signal intensity and distance z along the amplifier it is not possible to simply express the gain G in terms of G_0 and the input intensity I_{in}. Instead equation (4.34) can be rearranged and integrated over the length of the amplifier and over an input and output intensity I_{in} and I_{out}:

$$\int_{I_{in}}^{I_{out}} \left[\frac{1}{I} + \frac{1}{I_{sat}}\right] \mathrm{d}I = \int_0^l g_0(z)\mathrm{d}z, \tag{4.36}$$

which can be solved to give

$$\ln\left(\frac{I_{out}}{I_{in}}\right) + \frac{I_{out} - I_{in}}{I_{sat}} = g_0 l = \ln G_0. \tag{4.37}$$

By definition, the gain G is given by $G = I_{out}/I_{in}$ and so (4.37) can be rearranged to give the useful formula

$$\frac{I_{in}}{I_{sat}} = \frac{1}{G-1}\ln\left(\frac{G_0}{G}\right). \tag{4.38}$$

Using the knowledge that the maximum gain achievable for an amplifier is G_0, numerical values of G in the range $1 < G < G_0$ can be inserted into equation (4.38) to effectively show the variation in gain with I_{in}.

For a practical amplifier it is normally desirable to operate in a saturated regime so that the maximum power is extracted from the amplifier. This however implies using a higher signal intensity and consequently the gain is lower. Oscillators are generally much better at extracting gain because the laser intensity inside the cavity is much higher due to feedback from the cavity mirrors. The extracted intensity, I_{extr}, of the amplifier can be calculated using (4.38):

$$I_{extr} \equiv I_{out} - I_{in} = \ln\left(\frac{G_0}{G}\right) I_{sat}. \tag{4.39}$$

In the highly saturated regime where the gain approaches one, this equation can be used to show the total available intensity, I_{avail}, that can be extracted from the amplifier assuming 100% extraction efficiency:

$$I_{avail} = \lim_{G \to 1} \ln \left(\frac{G_0}{G} \right) I_{sat} = I_{sat} \ln G_0. \tag{4.40}$$

Substituting equation (4.13), the small signal gain for $r \leq w_p$ with a 'top-hat' pump beam, and equation (4.35) into equation (4.46), and multiplying by the pump beam area ($\pi {w_p}^2$) can yield the simple expression that confirms that, ignoring the effect of ETU, the maximum power available in an amplifier is the pump power absorbed times one minus the quantum defect.

$$P_{avail} = \left(\frac{\nu_l}{\nu_p} \right) P_p \eta_{abs}. \tag{4.41}$$

Equations (4.39) and (4.46) can be combined to form an expression for the power extraction efficiency η_{extr}:

$$\eta_{extr} = \frac{I_{extr}}{I_{avail}} = 1 - \frac{\ln G}{\ln G_0}. \tag{4.42}$$

If we take the simple example of an end-pumped amplifier with a pump power of 10W, Gaussian pump and signal beams of radii 300µm , and we make the simplifying assumptions that all the pump power is absorbed over the length of the gain medium and ETU is negligible, we can make direct comparisons between Nd:YVO_4 , Nd;YAG and Nd:YLF. Using the data in Table 2.4, for 1% doping concentration for each material, and equations (4.35) and (4.22), the small signal gains and saturation intensities were calculated, as shown in Table 4.1.

Material	G_0	I_{sat}
Nd:YVO_4	25.4	8.30 W mm^{-2}
Nd:YAG	2.52	29.0 W mm^{-2}
Nd:YLF	3.42	21.7 W mm^{-2}

Table 4.1: Comparison of small signal gain and saturation intensity for Nd:YVO_4 , Nd:YAG and Nd:YLF

This table clearly shows the significantly higher small signal gains achievable in Nd:YVO_4 compared to Nd:YAG and Nd:YLF under similar conditions. Additionally, the lower saturation intensity in Nd:YVO_4 means that greater extraction efficiencies can be achieved with the same input signal power. Figure

4.4 further justifies the decision to use Nd:YVO_4 , by showing the variation in gain with input signal power, for the examples given above, found by inserting the values from Table 4.1 into equations (4.38) and (4.42).

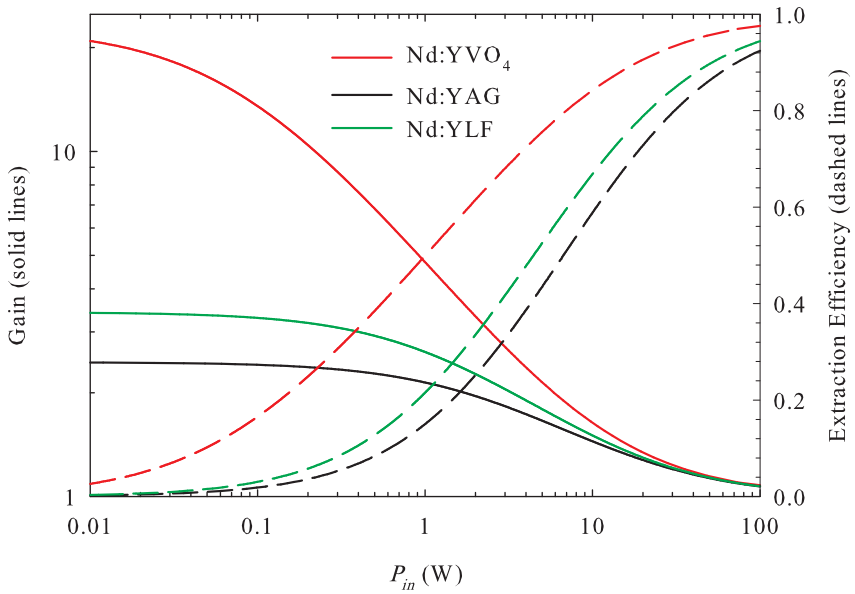

Figure 4.4: The variation in gain (solid lines) and extraction efficiency (dashed lines) with input signal power, for Nd:YVO_4 , Nd:YAG and Nd:YLF amplifiers.

The graph shows that for, all signal powers, the gain and extraction efficiency is significantly higher in Nd:YVO_4 , than in Nd:YAG and Nd:YLF, which have more similar values, although Nd:YLF is shown to have slightly higher gain and extraction efficiency than Nd:YAG. An additional advantage of Nd:YVO_4 is its higher absorption coefficient ($\sim$3 times that of Nd:YAG or Nd:YLF), which has been neglected here, which implies a greater fraction of pump power absorbed.

4.2.4 Pulse Amplification

Due to the non-linearity of equation (4.34) it is difficult to make predictions for amplifier performance in cw mode of operation without resorting to iterative techniques. For an amplifier used to amplify pulses when the pulse duration is small compared to the product of the inverse of the pump rate

and the fluorescence lifetime ($t_p \ll \tau_f {W_p}^{-1}$) the effects of pumping and fluorescence during the amplification process can be neglected and the analysis is simplified. Using the time dependent photon transport equation, Frantz and Nodvik [7] obtained an expression assuming a lossless amplifier, for the gain G of a short signal pulse in a local area of gain medium, in an amplifier with a 4-level transition (quantum efficiency of 1) and an initial signal gain G_i at the time of arrival of the pulse:

$$G = \frac{E_{sat}}{E_{in}} \ln \left\{ 1 + \left[\exp\left(\frac{E_{in}}{E_{sat}} \right) - 1 \right] G_i \right\}, \tag{4.43}$$

where E_{in} is the input pulse fluence (energy per unit area) and E_{sat} is the saturation fluence of the gain medium, given by:

$$E_{sat} = \frac{h\nu_l}{\sigma_{21}}. \tag{4.44}$$

The extraction efficiency η_{extr} of the energy available per unit area E_{avail} in the medium at the arrival of the pulse is given by:

$$\eta_{extr} = \frac{E_{out} - E_{in}}{E_{avail}}, \tag{4.45}$$

where E_{out} is the output pulse energy per unit area and E_{avail} is given by

$$E_{avail} = E_{sat} \ln G_0. \tag{4.46}$$

The above model can be used to predict the total gain and extraction efficiency of an input pulse, however the actual output pulse profile as a function of time is often a very important property to predict as this includes information on the peak intensity which may be much higher than the average intensity over the pulse. According to Siegman [6], the time dependent gain during the pulse is given by:

$$G(t) = 1 + (G_i - 1) exp \left[\frac{-E_{out}(t)}{E_{sat}} \right], \tag{4.47}$$

where $E_{out}(t)$ is the cumulative output pulse energy at time t after the arrival of the pulse, found by inserting the cumulative input energy $E_{in}(t)$ into equation (4.43). Using a step by step numerical technique it is therefore possible to calculate the output pulse shape for a given input pulse shape. If we take the simple example of a rectangular input pulse shape, of pulse duration 100ns,

passing through an amplifier which has an initial gain $G_i = 1000$ at time $t = 0$ when the pulse arrives, the gain as function of time throughout the pulse effectively describes the output pulse shape. Figure 4.5 shows the gain for such a pulse for a range of input pulse energy densities.

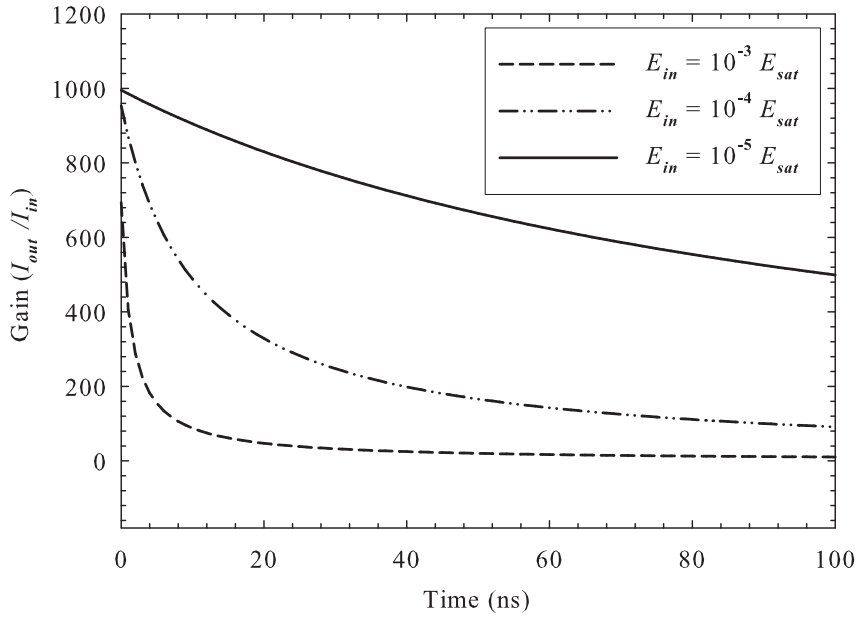

Figure 4.5: Output intensity profile of 100ns pulse from an amplifier with a small signal gain of 1000, for a range of input energy densities

The graph shows the exponential decay in gain over time during the pulse. The rate of decay clearly depends on the input energy, since higher energy density causes faster saturation of the gain. The initial gain G_i also affects the gain decay rate during the pulse, as shown in Figure 4.6. The graph shows the gain as fraction of the initial gain G_i, as a function of time, for a 100ns input pulse of energy density $E_{in} = 10^{-5} E_{sat}$ for a range of values for the initial gain G_i. In this regime, the higher the initial gain, the more rapidly the gain saturates. This is because the high gain systems require lower input signal energies to cause saturation effects. This is slightly misleading because, although the rate of decay of gain is higher in the high G_i case, the gain itself remains higher than in the low G_i case even at the end of the pulse. The main implication is that high gain systems see more pronounced saturation effects and hence stronger pulse re-shaping.

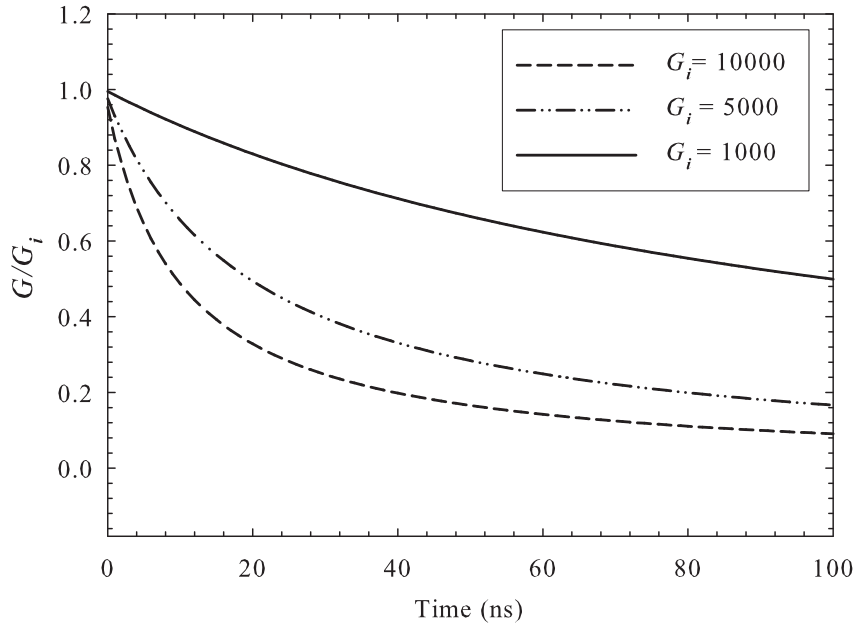

Figure 4.6: The gain as a fraction of initial gain versus time, for a 100ns pulse from an amplifier with input energy density $E_{in} = 10^{-5}E_{sat}$.

In the regime where the pulse repetition frequency f is much less than the inverse of the energy storage lifetime ($f \ll 1/\tau_f$), the initial gain G_i in equation (4.43) can be assumed to be close to the small signal gain G_0, calculated in the previous sections, since the amplifier has time to reach its maximum level of population inversion between pulses. However, when $f \gtrsim 1/\tau_f$ the recovery time between pulses becomes an important factor in determining the value of G_i at the time of arrival of a pulse. Using an iterative approach similar to Pearce [8], it is possible to estimate the steady-state initial amplifier gain G_i after many successive pulses for a range of repetition rates and pulse widths. The gain at the end of the first pulse, G_e, is found by inserting the total output fluence E_{out} into equation (4.47) and using G_0 as the first value of G_i. To find the initial gain G_i for subsequent pulses, assuming constant cw pumping, the gain with respect to the recovery time t_r between pulses is given by [6]:

$$G(t_r) = exp\left(g_0 l\left[1-exp\left(\frac{-t_r}{\tau_f}\right)\right]+lnG_e exp\left(\frac{-t_r}{\tau_f}\right)\right), \tag{4.48}$$

where t_r is given by:

$$t_r = \frac{1}{f} - t_p, \tag{4.49}$$

for pulse duration t_p and repetition frequency f. Applying equations (4.43),(4.47) and (4.48) iteratively and each time replacing the initial gain in equation (4.43) with the new gain from equation (4.48), causes the initial gain G_i to rapidly converge towards its steady-state value, ie. the value after many successive pulses. Figure 4.7 shows how the gain varies over the first few pulse cycles in an amplifier, with a fluorescence lifetime of 100µs and a repetition rate of 20kHz, where the initial gain for the first pulse is 5000 and the input fluence E_{in} is $10^{-5}E_{sat}$. The gain during the pulse cannot be seen in the graph because the pulse duration is short compared to the recovery time of ∼50µs .

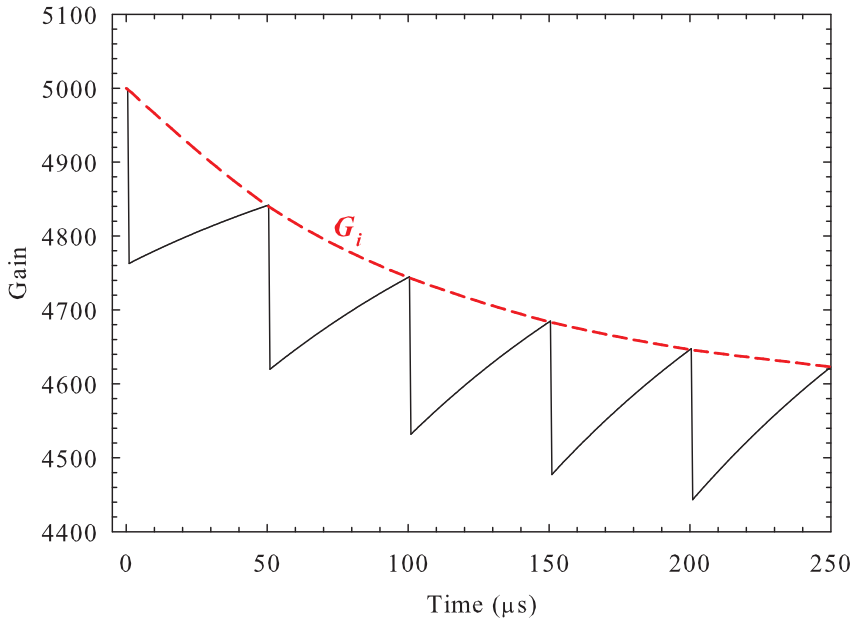

Figure 4.7: Solid line: The gain of an amplifier during the first five pulse cycles where G_i = 5000 for the first pulse and τ_f = 100µs . Dashed line: The decay of G_i to its steady-state value.

The graph shows that the value of G_i is reduced from its initial value and approaches a steady-state value after just a few pulse cycles. Using the steady-state value of G_i, in equation (4.43), it is possible to model the peak and average power gain of the amplifier for arbitrary pulse widths and repetition rates even when the repetition rate is larger than $1/\tau_f$. However the model breaks down when the pulse width approaches the pulse period because equation (4.43) assumes negligible pumping during the pulse. However, this is not a regime of interest for most applications.

In the case where $G_i \approx G_0$ (ie. the repetition rate is $\lesssim 1/\tau_f$), it can also be shown that, if the pulse input energy and saturation energy are replaced by the input intensity and saturation intensity (effectively multiplying them by the pulse repetition rate), equation (4.43) gives a reasonably good approximation to equation (4.38), which applies to a cw amplifier. To show this quantitatively, Figure 4.8 (top) shows the gain curves for a cw signal G_{cw}, calculated by inserting values into equation (4.38), and the corresponding gain curves for a pulsed signal G_P, calculated from equation (4.43), where the pulse separation is longer than the amplifier recovery time. Figure 4.8 (bottom) shows the ratio of G_P over G_{cw} as a function of the input signal intensity (or average intensity in the pulsed case). As can be seen, the ratio is close to one in the small sig-

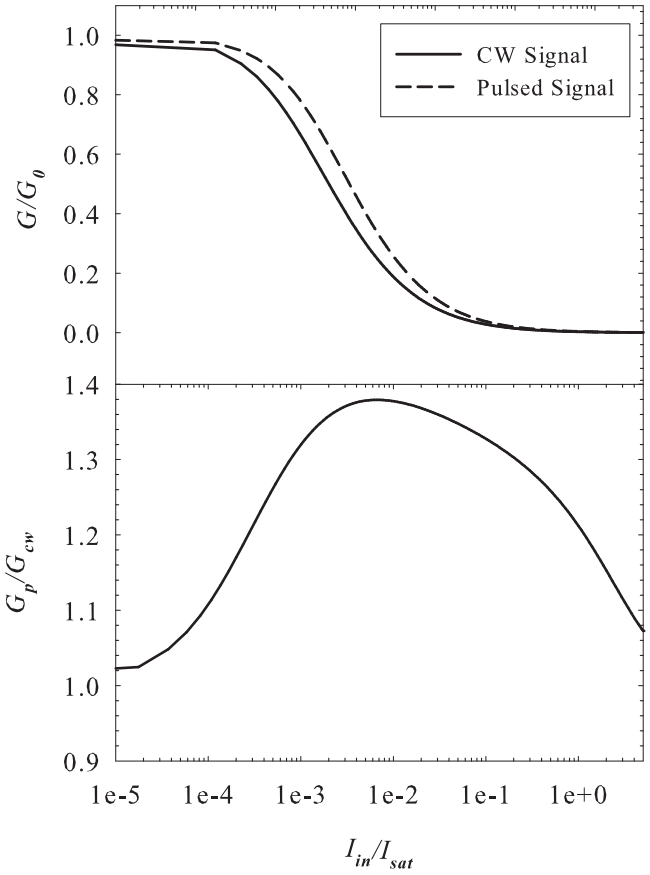

Figure 4.8: a) G/G_0 in (dB) as a function of signal input Intensity I_{in}/I_{sat} for a continuous signal (solid line) and a pulsed signal (dotted line). b) The ratio of pulse gain over cw gain as a function of input intensity, plotted as a logarithm.

nal limit and also in the saturated limit. In the partially saturated regime the

pulse gain is higher by a factor of up to 1.4. This comparison between the two models shows that the pulsed model can be used to achieve a reasonably good estimate of the cw performance of an amplifier using the following expression:

$$G = \frac{I_{sat}}{I_{in}} \ln \left\{ 1 + \left[\exp\left(\frac{I_{in}}{I_{sat}} \right) - 1 \right] G_0 \right\}. \tag{4.50}$$

The higher average gain for the pulsed model arises due to the assumption, that the gain has time to reach its maximum value, G_0, before every pulse and hence the recovery time t_r needs to be much greater than the energy storage time τ_f. However, equation (4.50) assumes that $t_r = \tau_f$ which is a result of converting the input fluence E_{in} and saturation fluence E_{sat} into the average intensities I_{in} and I_{sat}. This leads to an over-estimate of the gain in the pulsed case. In any case, gating the input to amplifiers to achieve pulsed operation yields lower average output power due to a large reduction in input average power caused by switching off the input pulse for a large fraction of the time. This is not always the case for Q-switched or cavity dumped oscillators because they can operate at similar average powers to cw lasers and with repetition rates of the order $1/\tau_f$ [9]. The main advantage of operating in pulsed mode is the access to higher gains during the pulses and therefore higher peak powers rather than higher average power.

4.2.5 Maximum Power Optimisation of Signal-Pump Overlap

Dependence of laser performance on the pump-to-mode size ratio in end-pumped lasers has been studied by Chen *et al.* with regard to the output power optimisation [10] and the thermal loading [11]. However, to the author's knowledge, no studies have been published which address the influence of the signal-to-pump size ratio on the performance of high power, end-pumped, amplifiers. The discussion, in this Chapter, of saturated gain has so far only considered a local area of the gain medium and not the total gain and extraction efficiency over the whole area of the gain medium. While the influence of differing pump and signal beam sizes was taken into account for the small signal gain in Section 4.2.1.2, in the partially saturated regime another effect comes into play when the signal beam size is smaller than the pump beam size. In this situation, only part of the gain distribution in the central region

becomes stimulated by the signal field and the remaining population inversion in the wings is lost by spontaneous emission. In the limit of small signal gain, reducing the signal beam size below the pump beam size has no effect on the gain for a 'top-hat' pump beam and actually increases the gain for a Gaussian pump beam, as shown in Figure 4.2. However, if saturation effects are taken into account, even very low power signals will reach the saturation intensity if the beam size is reduced enough. In this case only a fraction of gain which falls inside the signal beam area will be saturated. The proportion of the population inversion which becomes saturated depends on the spatial distribution of the pump beam and signal beam and on the signal power. Since both the gain and the input intensity and hence the level of saturation depend on the radial position, for circularly symmetric and concentric pump and signal beams, the total gain becomes difficult to model analytically. By employing a numerical integration of the local gain for the cw approximation, from equation (4.50), over the total area of the gain medium and using a plane wave approximation for the signal beam, it was possible to model the total gain G_{tot} for both Gaussian and 'top-hat' pump beam profiles with Gaussian signal beam profiles, where G_{tot} is given by.

$$G_{tot} = \int_0^\infty 2\pi r G(r) I_l(r) \mathrm{d}r. \tag{4.51}$$

Using a specific example of a 0.1 at.% doped, 10mm long Nd:YVO_4 rod pumped by a 300μm radius pump beam, the total gain was modelled as a function of signal-pump spot size ratio for a range of pump powers and signal powers. For this doping concentration the estimated values of τ_f and α_p were 120µs and 170m^{-1} respectively [4]. The total input signal power was set at 5W, which, for a signal beam radius of 300µm has an intensity of nearly 3 times the saturation intensity ($I_{sat} = h\nu_l/\sigma_{21}\tau_f = 6.43$W mm^{-2}). In this regime, it was therefore reasonable to neglect the effect of ETU. Figure 4.9 shows the results of the model as the input signal radius was varied, for a range of pump powers from 5W to 40W.

The graph shows that in each simulation the gain rises from zero at the origin and rolls over to give maximum gain for an overlap ratio in the region from around 0.7 to 0.8. In each case, the peak gain is higher for the 'top-hat' approximation, although, at small values of w_l/w_p the gain is higher for the Gaussian approximation due to higher pump intensity near the centre of the pump dis-

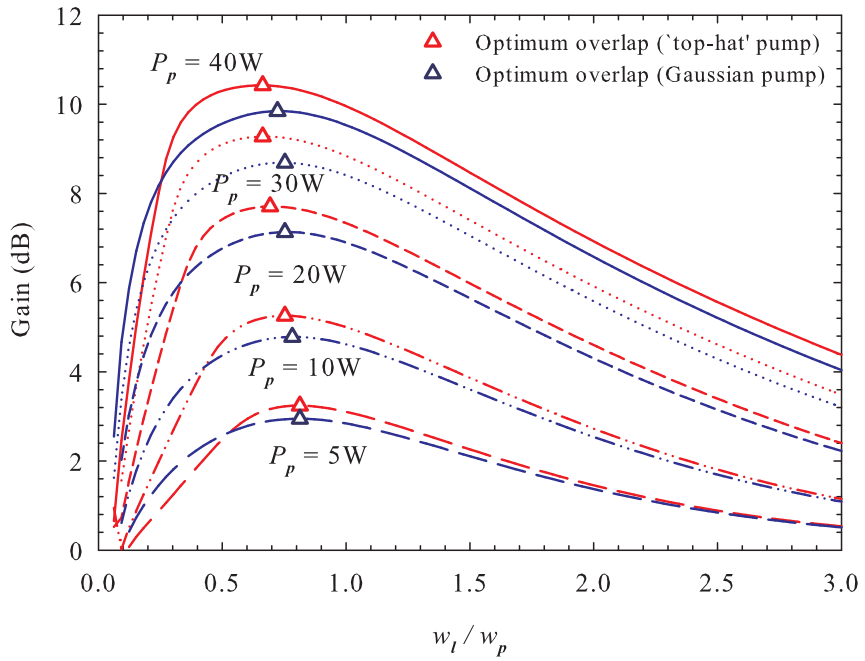

Figure 4.9: Numerical model of saturated gain as a function of signal-pump overlap ratio for Gaussian (blue) and 'top-hat' (red) pump beam profiles for a range of pump powers. Triangles indicate the points of maximum gain showing the optimum overlap ratios.

tribution compared to the 'top-hat' approximation. For larger values of w_l/w_p the gain for the 'top-hat' approximation becomes similar to the gain for the Gaussian approximation.

The non-uniform gain and saturation profile also leads to a reshaping of the signal beam intensity profile as it traverses the gain medium. In very high gain amplifiers where all of the signal distribution becomes saturated, this causes the signal beam to take on the shape of the pump beam. Additionally, even in systems where the pump distribution is approximately uniform across the signal beam area, saturation effects from high intensity signals can cause a flattening of the peak of signal intensity at the centre of the distribution. These effects, and their influence on the output beam quality, are considered in more detail in Chapter 5.

4.3 Aberrated Thermal Lensing

Under a high level of pump power, the effect of thermal lensing alone can conceivably limit the power scaling capabilities of an amplifier by causing the signal beam to be focused out of the gain region or by clipping of the beam by some limiting aperture. However at the high pump intensity required to cause such strong focusing, the additional effect of thermal lens aberration has the much more significant effect of reducing the brightness of the beam due to degradation in beam quality. An analysis of thermal lensing in end-pumped laser rods, with 'top-hat' and Gaussian pump beam profiles, has been summarised by Clarkson [12]. For a 'top-hat' pump beam profile and a thin lens approximation, the thermal lens focal lengths can be expressed as:

$$f_{th}(r) = \frac{2\pi K_c w_p^2}{P_p \gamma \eta_{abs} (\mathrm{d}n/\mathrm{d}T)}, \quad \text{for} \quad r \leq w_p, \tag{4.52}$$

and

$$f_{th}(r) = \frac{2\pi K_c r^2}{P_p \gamma \eta_{abs} (\mathrm{d}n/\mathrm{d}T)}, \quad \text{at} \quad r > w_p, \tag{4.53}$$

where γ is the fraction of absorbed pump power dissipated as heat (equal to $1-\nu_l/\nu_p$ for quantum defect heating), K_c is the thermal conductivity of the gain medium and $(\mathrm{d}n/\mathrm{d}T)$ is the change in refractive index with temperature. This shows that the thermal lens is independent of r inside the pumped region and so has no phase aberration. Outside the pumped region the thermal lens focal length is proportional to r^2 so a laser mode size larger than the pump beam size will be highly aberrated for intense pumping.

For a Gaussian pump beam profile the corresponding expression for thermal lens focal length is

$$f_{th}(r) = \frac{2r^2 f_{th}(0)}{w_p^2[1 - \exp\left(\frac{-2r^2}{w_p^2}\right)]}, \tag{4.54}$$

where $f_{th}(0)$ is the focal length on axis and is given by

$$f_{th}(0) = \frac{\pi K_c w_p^2}{P_p \gamma \eta_{abs} (\mathrm{d}n/\mathrm{d}T)}. \tag{4.55}$$

This implies a factor of two stronger thermal lensing on axis than for the 'top-hat' case, and a highly aberrated thermal lens both when $w_l \leq w_p$ and $w_l > w_p$. Thus, using a pump beam profile similar to a 'top-hat' profile results in

weaker thermal lensing and reduced phase aberration than using a Gaussian pump beam. In reality, it is difficult to control the pump beam profile without reducing the power significantly so for convenience it is often an advantage to use a multimode fibre to deliver the pump radiation and hence produce a beam that is closer in profile to a 'top-hat' than a pure Gaussian, as was shown in Figure 4.1. Due to the r^2 dependence of focal length for a Gaussian pump profile, it is also possible to reduce the impact of aberrations by using the central region of the pump distribution, where the radial variation in pump intensity is small. Siegman [13] used a quartic approximation of the phase aberration of a spherical lens to gain an expression for the M^2 value of a beam after passing through the lens. For an input signal of beam quality M_i^2 the final beam quality M_f^2, after passing through the gain medium, can be expressed as

$$M_f^2 = \sqrt{(M_i^2)^2 + (M_q^2)^2}, \tag{4.56}$$

where M_q^2 is the beam quality degradation factor for a quartic phase aberration. Using this approximation for the phase aberration caused by a thermal lens, Clarkson [12] showed that, for a thermal lens generated by a pump beam with an arbitrary intensity profile given by $I_p(r)$,

$$M_q^2 = \frac{\gamma \eta_{abs} (\mathrm{d}n/\mathrm{d}T) \pi w_l^4}{4\sqrt{2} K_c \lambda_l} \left(\frac{\mathrm{d}^2 I_p(r)}{\mathrm{d}r^2} \right), \quad \text{for} \quad r = 0. \tag{4.57}$$

If we consider the 'top-hat' and Gaussian approximations for the pump beam profile, we find that for a 'top-hat' pump beam; $\mathrm{d}^2 I_p(r)/\mathrm{d}r^2 = 0$ implying that there is no degradation in beam quality, and for a Gaussian approximation $\mathrm{d}^2 I_p(r)/\mathrm{d}r^2 = 8P_p/\pi w_l^4$, for $r = 0$, which implies that

$$M_q^2 = \frac{2 P_{abs} \gamma (\mathrm{d}n/\mathrm{d}T)}{\sqrt{2} K_c \lambda_l} \left(\frac{w_l}{w_p} \right)^4, \tag{4.58}$$

where $P_{abs} = P_p \eta_{abs}$ is the absorbed pump power.

Considering the deviation between the 'top-hat' or Gaussian pump profile approximations and the experimentally measured pump profile for a fibre coupled diode bar, shown in Figure 4.1, the value of $\mathrm{d}^2 I_p(r)/\mathrm{d}r^2$, for $r = 0$, for the experimental pump profile is signifiantly less than that for the Gaussian approximation, yet much higher than that for the 'top-hat' approximation. To improve the accuracy of this model, an additional approximation for the pump

profile was considered which consisted of a truncated Gaussian with intensity falling to zero for $r > w_p$ and a peak intensity of 0.89 times the Gaussian peak intensity (as with the experimental pump profile), such that the total power P_p was the same, as shown in Figure 4.10. In this case $I_p(r)$ is given by

$$I_p(r) = \frac{1.78P_p}{\pi w_p^2} \exp\left(\frac{-1.29r^2}{w_p^2}\right), \quad \text{for} \quad r \leq w_p, \tag{4.59}$$

and

$$I_p(r) = 0, \quad \text{for} \quad r > 0. \tag{4.60}$$

The graph shows that the truncated Gaussian gives a significantly improved

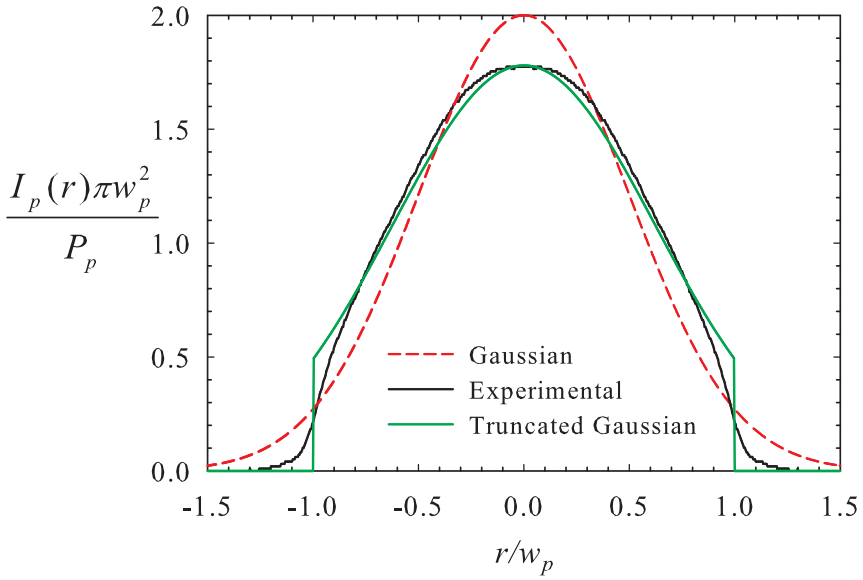

Figure 4.10: Experimental multimode fibre-coupled pump beam profile compared to Gaussian and Truncated Gaussian approximations.

approximation for the experimental pump beam profile compared to the Gaussian. To find the value of M_q^2 for the truncated Gaussian, it can be shown that

$$\frac{\mathrm{d}^2 I_p(r)}{\mathrm{d}r^2} = \frac{4.59P_p}{\pi w_p^4}, \quad \text{at} \quad r = 0, \tag{4.61}$$

which gives

$$M_q^2 = \frac{1.15P_{abs}\gamma(\mathrm{d}n/\mathrm{d}T)}{\sqrt{2}K_c\lambda_l}\left(\frac{w_l}{w_p}\right)^4. \tag{4.62}$$

This implies that, for the truncated Gaussian, M_q^2 is around a factor of two less than for the Gaussian approximation.

In the high power regime, the quartic approximation for the phase aberration is only valid when the signal beam spot size is significantly less than the pump spot size. For fibre coupled pump beams as well as Gaussian pump beams, as the signal beam size approaches the pump beam size, the model breaks down because higher order terms in the phase aberration become significant. However this simple model provides a valuable tool for predicting the pump power required for thermal lensing to cause a significant impact on the beam quality in end-pumped amplifiers.

For amplifiers which are not highly saturated, the fraction of pump power converted to heat γ in equation (4.62) is often more than just the quantum defect heating because amplifiers are generally less efficient at extracting the gain than oscillators and therefore the effects of ETU are greater due to higher inversion densities. It has been shown [12] that the fractional heat generation in the presence of ETU, γ_{ETU}, in Nd-doped laser materials, can be expressed as

$$\gamma_{ETU} = \left\{1 - \frac{2(1-\gamma)}{\beta}\left[2(\sqrt{1+\beta}-1) + \ln\left(\frac{4}{\beta}\frac{\sqrt{1+\beta}-1}{\sqrt{1+\beta}+1}\right)\right]\right\}, \tag{4.63}$$

where γ is the fraction of absorbed pump converted to heat in the absence of ETU and β is a dimensionless parameter given by

$$\beta = \frac{8WP_p\alpha_p\tau_f^2}{\pi w_p^2 h\nu_p}. \tag{4.64}$$

Using γ_{ETU}, instead of γ in equation (4.62), gives an alternative expression for the M^2 value of a beam after one pass of an amplifier rod under intense pumping where the level of saturation is low. Indeed, using γ_{ETU} also leads to modified values for the thermal lens focal lengths in equations (4.52-4.55). From this theory a comparison of the dependence of the output M^2, for a diffraction limited input beam, on the pump power is shown in Figure 4.11 for both a Gaussian pump profile and a truncated Gaussian pump profile. This example is for a 0.1 at.% doped Nd:YVO_4 amplifier with a pump beam radius of 300µm and a signal pump overlap ratio $w_l/w_p = 0.7$. Under high pump powers, the graph shows significant increase in beam quality degradation when ETU is accounted for. The degradation in beam quality is also shown to be significantly less for the, more realistic, truncated Gaussian approximation than for the standard Gaussian approximation for the pump beam profile. Indeed, the increase

in M^2 for the truncated Gaussian pump profile is around 0.3-0.4 times the increase in M^2 for the Gaussian pump profile. As an example, for the truncated Gaussian case here, the pump power required to cause a significant degradation in beam quality, to say $M^2 = 1.1$, is ~25W without ETU and ~17W with ETU, whereas, in the Gaussian case, these power levels are ~14W and ~11W respectively. There are, however, limitations to this analysis because it only accounts for the phase aberrations and not the impact of transversely varying gain on the M^2 parameter. This additional effect is investigated in more detail in Chapter 5.

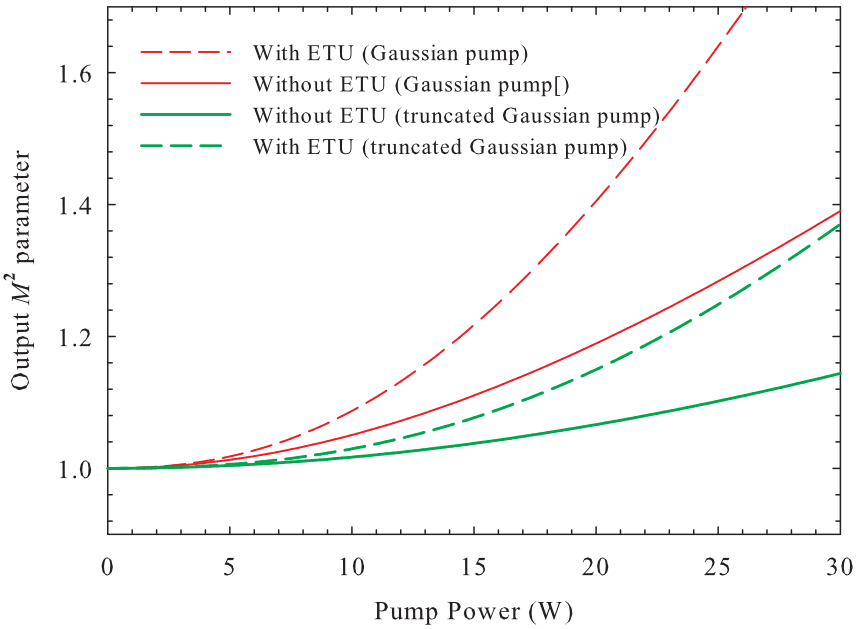

Figure 4.11: Increase in M^2 value of an amplified signal as a function of pump power without ETU (solid lines) and with ETU (dashed lines), for Gaussian and truncated-Gaussian approximations for the pump profile.

It can be seen in equations (4.58) and (4.62) that reducing w_l, compared to w_p, strongly reduces the aberration of the thermal lens. However, for efficient power scaling of the TEM_{00} mode, good overlap of the laser mode and pump beam is required so a compromise is essential. It is worth noting that, while the thermal lens strength is reduced by increasing the pump beam size and keeping the mode-pump overlap (w_l/w_p) constant, the degradation in beam quality remains the same. This is because larger beam radii, with longer radii

of curvature phase fronts, are more strongly affected by phase aberrations than are smaller beam radii with the same phase aberrations. For this reason, the argument to use small pump and signal radii in the gain medium, to obtain high gain and high output power, still holds up to the point where one of a number of other effects becomes dominant. These include the effect of pump beam divergence over the length within which the pump is absorbed, the loss due to ETU and the stress fracture, or damage, of the crystal. An additional limiting effect is the thermal lensing itself which, for very high pump intensities, will be strong enough to cause significant change in the signal beam size over the length of the crystal and hence lead to a reduction in efficiency.

4.4 Scaling Output Brightness

The brightness scaling limit of an amplifier can be defined as the limit where the reduction in brightness (ie. increase in the M^2 value) caused by thermal lens aberration equals the brightness increase due to power amplification of the signal beam. This means that increasing pump power, or adding further amplifier stages beyond this limit, would cause a net reduction in brightness despite the signal power increase.

The brightness B of a beam is defined as the power divided by the product of area and solid angle divergence [3]:

$$B = \frac{P}{A\Omega}. \tag{4.65}$$

Since the divergence of a beam of fixed area is proportional to the M^2 of the beam and hence the solid angle divergence is proportional to $M_x^2 M_y^2$, it follows that the overall fractional change in brightness, the *brightness gain* G_B of a $M_x^2 = M_y^2 = 1$ input beam passing through an amplifier, with aberrated thermal lensing, can be described in terms of the total power gain G_{tot} by:

$$G_B = \frac{G_{tot}}{M_{f,x}^2 M_{f,y}^2}. \tag{4.66}$$

Using the numerical model for the total gain for a Gaussian pump beam approximation and the above analysis for the output M^2 for a truncated Gaussian pump profile, the dependence of brightness gain on factors such as pump

power, and pump-signal overlap can be determined. Using a similar example of a 0.1 at.% doped, 10mm long, Nd:YVO_4 rod pumped by a 300µm radius pump beam and an input signal power of 5W, the brightness gain was modelled for a range of pump powers, as shown in Figure 4.12.

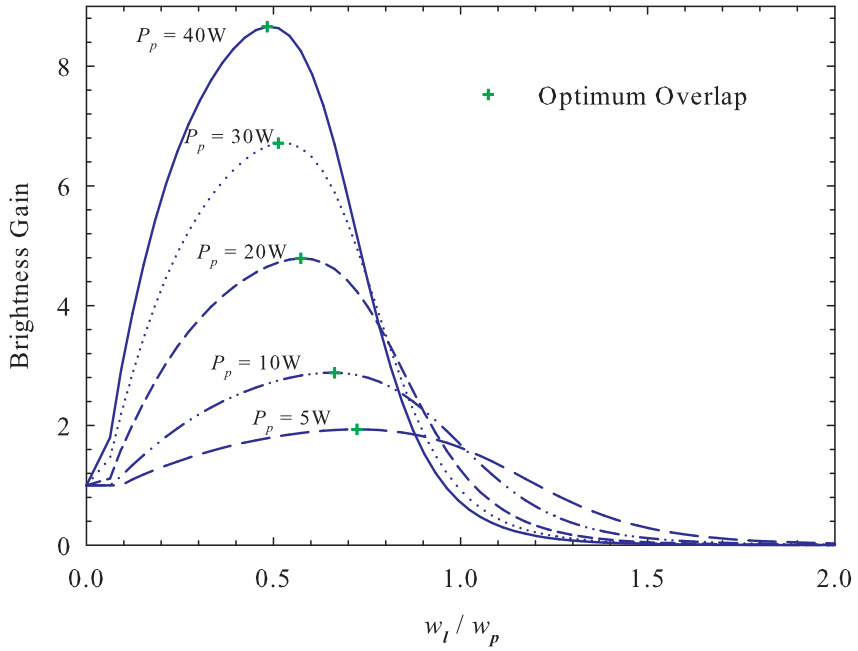

Figure 4.12: Brightness gain as a function of signal-pump overlap for various pump powers

The graph shows that the brightness is greatly reduced when the overlap ratio is increased beyond 1 which is a result of the strong phase aberrations in the wings of the pump distribution. For all pump powers the brightness gain rolls over much more steeply than the power gain which was shown in Figure 4.9. Additionally, the power gain never fell below 1 since there was no loss mechanism included in the analysis whereas, when the beam quality degradation is severe, it can cause a net loss in brightness resulting in $G_B < 1$. The optimum value of w_l/w_p for maximum brightness gain is lower than the value for optimum power gain and it also becomes lower with increasing pump power since, at higher pump power, the beam quality degradation becomes significant at a lower value of w_l/w_p. The optimum overlap ratio reduces from around 0.72 at 5W of pump power to 0.48 for 40W of pump power.

Although the validity of this model is severely limited by the quartic approx-

imation of the phase aberration, which breaks down for values of w_l/w_p approaching and greater than 1, the general trends provide useful information for designing and optimising practical amplifiers. This modelling also provides a strategy for brightness scaling in a multiple rod amplifier chain where the pump power is stepped up in successive amplifier stages. In this scheme, the optimum overlap ratio with respect to brightness therefore reduces with each successive amplifier stage. Using this technique it is possible to scale the brightness further than would be possible using the same overlap ratio for each stage.

4.5 Multiple-Rod and Multiple-Pass Amplification

Most practical amplifiers use multiple laser rods or multiple-pass configurations to increase the gain and extraction efficiency. In multiple-pass amplifiers the signal beam is reflected back through the gain medium after the first pass. In double pass configurations the second pass can take the same path as the first pass and the output can be separated from the input using a Faraday isolator for example [14] . Alternatively two or more passes can be achieved if each pass takes a different path and therefore occupies a different region of gain. In the case where there is no overlap between the passes, the expressions derived for the power or pulse energy gains and extraction efficiencies are still valid but need to be used in sequence where the output from the first pass, or rod, becomes the input to the second pass, or rod. In the case of single pass multiple rod amplifiers, or multiple pass amplifiers, where there is no pulse overlap between passes, this is straightforward although a computer is an advantage in performing the lengthy calculations.

4.5.1 Multiple-Pass Amplification

For double pass amplifiers, where the first pass output is reflected back into the gain medium along the same path as the input beam but there is sufficient delay between passes so that the pulses do not overlap, the reduction in gain caused by the first pass needs to be considered when calculating the gain for

the second pass. Using equation (4.43), the output fluence E_2 from a two pass amplifier can be calculated as follows:

$$E_1 = E_{sat} \ln \left\{ 1 + \left[\exp\left(\frac{E_{in}}{E_{sat}} \right) - 1 \right] G_0 \right\}, \tag{4.67}$$

and

$$E_2 = E_{sat} \ln \left\{ 1 + \left[\exp\left(\frac{E_1}{E_{sat}} \right) - 1 \right] G_0' \right\}, \tag{4.68}$$

where G_0' is the small signal gain for the return pass. If the extraction efficiency of the first pass η_1 is given by equation (4.45) then the energy available E'_{avail} for the return pass can be given by

$$E'_{avail} = (1 - \eta_1) E_{avail}, \tag{4.69}$$

and hence

$$G_0' = \exp\left(\frac{E'_{avail}}{E_{sat}} \right). \tag{4.70}$$

However, if the pulse duration is large compared to the round-trip time in the amplifier, the pulses overlap and the competition for gain between the counter-propagating signals is also an issue and in most cases the second pass steals gain from the first pass. For completely overlapping pulses, Pearce *et al.* [15] modified the analysis by Franz and Nodvik [7] and showed that the gain can be calculated by simply halving the saturation fluence and doubling the gain coefficient g_0, in equation (4.43), as follows:

$$G = \frac{E_{sat}}{2E_{in}} \ln \left\{ 1 + \left[\exp\left(\frac{2E_{in}}{E_{sat}} \right) - 1 \right] \exp(2g_0 l) \right\}. \tag{4.71}$$

The result is in effect equivalent to doubling the stimulated emission cross section, since this halves the saturation fluence and doubles the gain coefficient. Figure 4.13 shows an example of how a signal grows in intensity as it makes two passes through a 10mm long Nd:YVO_4 crystal, assuming uniform gain over the length of the crystal. In this model, the input signal fluence is equal to $0.01E_{sat}$ and the small signal gain coefficient is 10m^{-1}. Each of the lines shows a signal that increases in energy exponentially at first and then becomes linear with distance along the rod as the gain becomes saturated. The blue line shows the signal fluence in an amplifier where the return pass sees the same gain as the first pass. This is physically equivalent to the signal beam passing through a second amplifier rod which has the same parameters as the first or

if a delay is introduced between the out and return pulses which allows time for the population inversion to recover to its initial value. In this case the extracted power is greater for the second pass than for the first. The red line shows the return signal fluence when the pulses do not overlap but the gain for the return pass does not have time to recover from the first pass, as calculated in equation (4.70). Here, the extracted power is lower than that for the first pass. Finally the green line shows the fluence for completely overlapping out and return pulses, calculated from equation (4.71). This is the case in most practical amplifiers where the pulse duration is long compared to the round trip time. In this case the gain for the first pass is reduced by the presence of the returning signal which extracts more of the gain due to its higher intensity.

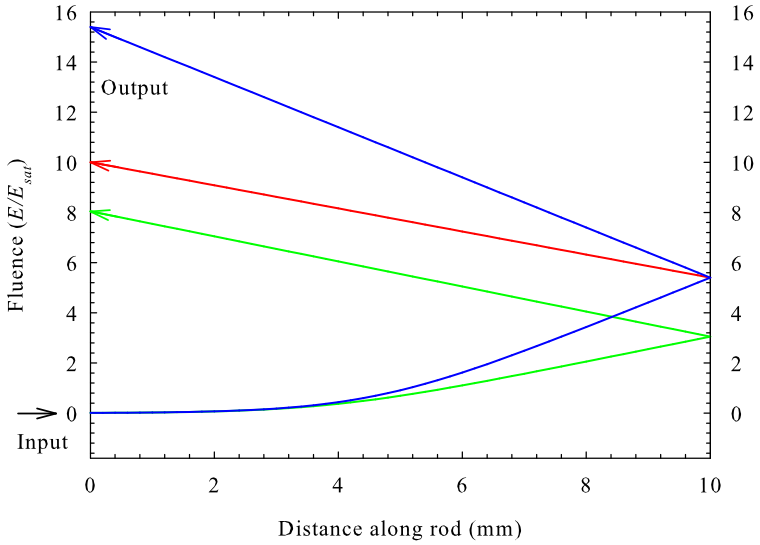

Figure 4.13: The fluence of a signal beam as it makes two passes of an amplifier rod. The blue line is for the case where the return pulse sees the same gain as the input pulse, the red line is when the gain for the return pulse is reduced by the initial pulse but the pulses do not overlap and the green line is where the pulses completely overlap and the counter-propagating signals compete for gain

When the amplifier is reasonably well saturated, as in this example, the amount of power added to the signal, by making it double pass rather than single pass, is relatively small. Indeed, the extracted energy density for this amplifier in a single pass configuration is around $5.5E_{sat}$ and making a second pass only adds another $2.5E_{sat}$. While the gain in power diminishes for multiple passes, the thermally induced aberrations remain just as severe and their effects be-

come compounded. For brightness scaling this often means that it is better to operate amplifiers in single-pass configurations, since the gain in power for multiple passes is offset by the beam quality deterioration.

4.5.2 Multiple-Stage Amplification

While there are benefits of using multiple passes when the extraction efficiency for a single pass is low, the detrimental thermal effects can be severe. Multiple-stage amplifiers, on the other hand, can add much more power than multiple pass configurations because a greater pump power can be distributed over a larger volume of gain medium and therefore offer higher gain, without necessarily causing more severe thermal effects.

Employing a multiple-stage amplifier chain as a route for power scaling, has a number of advantages compared to simply increasing the power of a single-stage amplifier. The most obvious being that thermal effects can be managed more easily because the pump power is distributed over a larger volume of gain medium facilitating more efficient cooling. This reduces the likelihood of thermal fracture and hence allows higher pump powers. Distributing the pump power over many rods with low doping concentrations also reduces the impact of ETU, since the inversion density is reduced. The reduction in ETU leads to an increase in available gain and also reduction in total heat loading in the gain medium. This, in turn, leads to a reduction in thermal lens strength and also a reduction in thermal lens induced aberration of the signal beam. However, the thermal lensing and thermal lens aberrations are still accumulated over a number of amplifier stages such that they are dependent on the total heat deposited in all the amplifier stages as well on the material properties and the geometric parameters of each amplifier stage. With regard to thermal lensing, amplifiers have an advantage over oscillators in that dynamic stability is not such an important issue since they remain stable even for very strong thermal lensing. However, when a number of amplifier stages are combined, the thermal lensing effects become compounded and the resulting change in signal beam radius can become an important issue. One technique that can be used to address this problem is relay imaging of the signal beam, from one rod to another, to ensure that a particular spot size is re-imaged several times,

independently of thermal lens strength. This technique and its limitations are discussed in more detail in Chapter 5.

Leaving aside the issues associated with thermal lens focusing and diffraction of the signal beam, and again assuming constant pump and signal spot sizes over the length of the crystal, the beam quality of a signal after passing several aberrated thermal lenses can be calculated by applying equations (4.58) to (4.56) in sequence, where the M_f^2 for the n^{th} lens becomes the M_i^2 for the $(n+1)^{th}$ lens. Or in effect, for N amplifier stages [13]:

$$M_f^2 = \sqrt{(M_i^2)^2 + \sum_{n=1}^{N} (M_{q,n}^2)^2}. \tag{4.72}$$

For a number of amplifier stages with the same beam quality degradation factor M_q^2, the output M^2 for a diffraction limited input beam is shown in Figure 4.14.

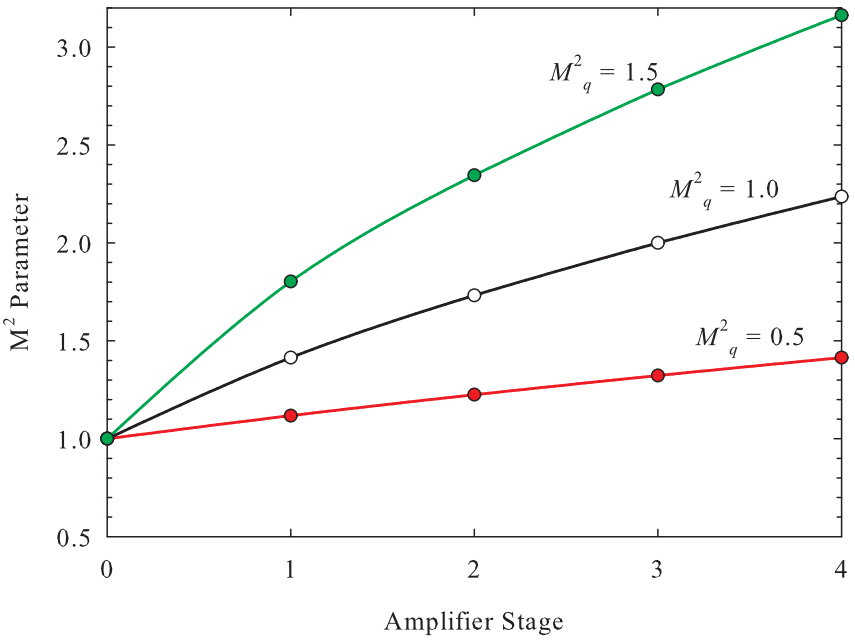

Figure 4.14: Beam quality degradation as a function of the number of amplifier stages

The graph shows that the beam quality degrades to a lesser degree with each successive amplifier stage. Higher values of M_q^2 are shown to lead to more severe beam quality degradation. From equation (4.62) for a truncated Gaussian

pump beam, in the presence of ETU, using the data above for a 0.1 at.% doped Nd:YVO_4 crystal, and for a signal to pump overlap ratio of 0.7, the absorbed pump power required to give M_q^2 values of 0.5, 1.0 and 1.5, as in the graph, are approximately 15W, 27W and 37W respectively, which are similar to the pump powers used in the experimental work described in this thesis. As already mentioned, the validity of equation (4.58) is limited when w_l is close to w_p but, more importantly, the above analysis neglects the effect of the radial gain profile on the beam quality, which is shown in Chapter 5 to play an important role in the degradation in beam quality in a multiple-stage amplifier system.

There are a number of factors which can limit the maximum number of amplifier stages which can be combined, whilst still achieving a net increase in power and brightness. One factor is the transmission losses through each amplifier stage which become significant when the signal power becomes high because the gain becomes comparable to the loss. For example, assuming that a number of amplifier stages in a chain, have the same pump power, the same pump beam radius and the same signal-pump overlap ratio, the output can be modelled, including a transmission loss for each amplifier stage. For a simple example of a 0.1 at.% doped, Nd:YVO_4 amplifier with a pump power P_p of 30W, assumed to be completely absorbed, a pump beam radius w_p of 300µm , assumed to be Gaussian, and a signal-pump overlap ratio w_p/w_l of 0.7, the small signal gain G_0, neglecting ETU, was calculated using equation (4.22). Applying equation (4.50) in sequence for an input power P_{in} for the first amplifier of 5W, Figure 4.15 was produced showing the output power and gain as a function of the number of amplifier stages for the lossless case, and assuming a 5% loss per amplifier stage.

The graph shows that, for an amplifier with loss, for a large number of amplifier stages, the output power reaches a limit at ∼250W, after around 40 amplifier stages, where for the lossless case the power continues to increase linearly with the number of stages, as the gain becomes saturated for each stage. The number of stages before which the limit is reached depends on the input power, the loss per stage and the amount of stored energy. This means that, in order to keep adding a significant amount of power with each stage, the pump power needs to be increased.

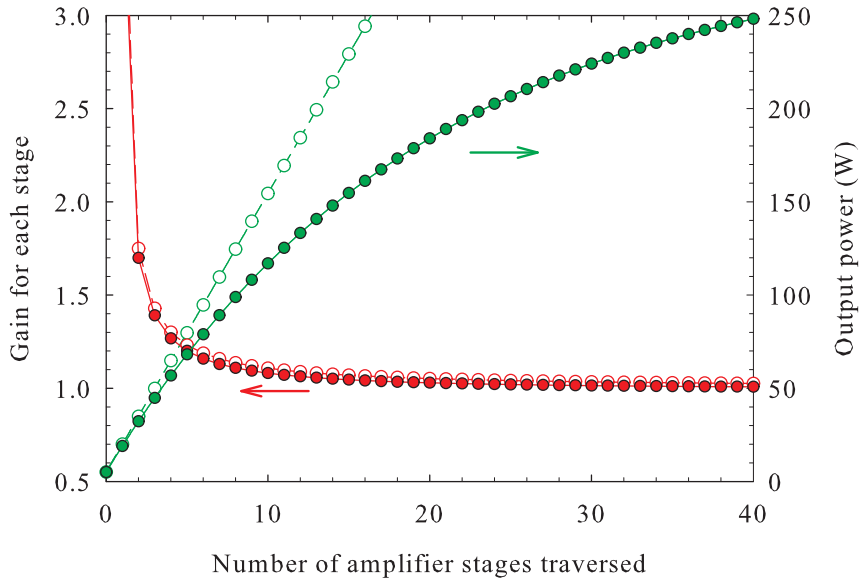

Figure 4.15: Gain (red) and output power (green) as a function of the number of amplifier stages. Dotted line for lossless amplifier, solid line for 5% loss per stage.

Another consideration is the degradation in beam quality for a large number of amplifier stages, which limits the brightness scaling potential of an amplifier chain before the power scaling limit is reached. For the amplifier stages described above, the value of M_q^2, from equation (4.62), for a truncated Gaussian pump beam, is 0.75. By calculating the brightness gain for each amplifier stage and hence the relative output brightness, Figure 4.16 was produced.

For the lossless case, the relative brightness is shown to approach a limit after around 10 amplifier stages due to the cumulative effect of the beam quality degradation. When losses are taken into account (5% loss per stage), the relative brightness rolls over after around 6 amplifier stages, as a result of the brightness gain falling below 1. In this case, increasing the pump power in successive amplifier stage, could be used to increase the maximum brightness, but only up to the limit where the aberrations for a single stage become too severe to cause a net gain in brightness. From Figure 4.12 it can be seen that an increase in pump power should be combined with a reduction in w_l/w_p in order to maximise the brightness gain.

By this theory, increasing the pump power to successive amplifier stages can avoid a power scaling limit being reached. Similarly, if increasing the pump

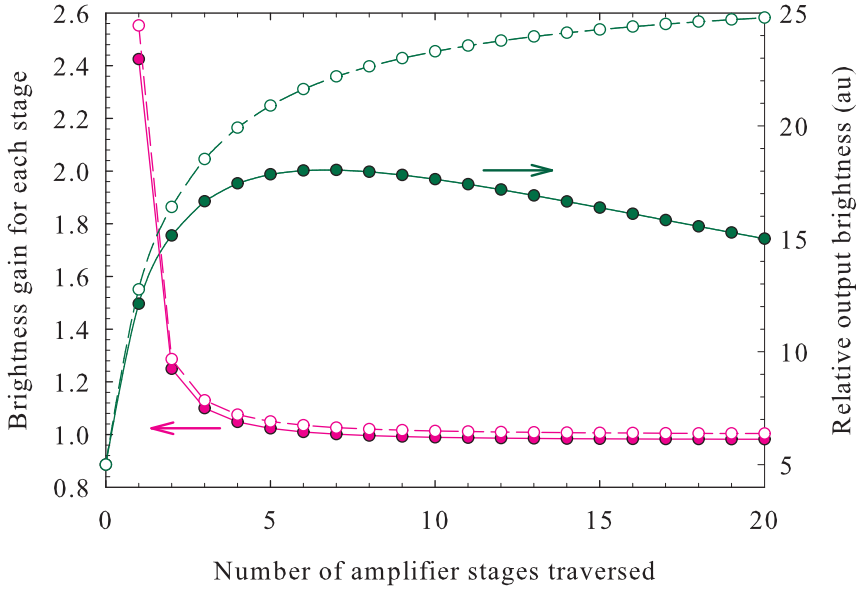

Figure 4.16: Brightness gain (pink) and relative output brightness (green) as a function of the number of amplifier stages. Dotted line for lossless amplifier, solid line for 5% loss per stage.

power is combined with reducing the signal-pump overlap, the brightness scaling limit can be increased. However, this approach is still fundamentally limited by ETU, and thermal damage of the gain medium, which become significant at high pump powers even for crystals of low doping concentration. For this reason, using higher pump powers needs to be combined with using larger pump beam radii, to reduce the impact of ETU, which results a reduced gain. Additionally, if the signal beam radius is also increased to maintain a good spatial overlap, the signal intensity is therefore reduced leading to lower saturation.

4.6 Summary

By starting with a simple analysis of an end-pumped amplifier and building upon it, this chapter has explored the influence of a range of design parameters on the theoretical performance of laser amplifiers and amplifier chains. The total small signal gain for 'top-hat' and Gaussian pump beams was derived for a Gaussian signal beam. Particular emphasis was given to the influence of the signal-pump overlap ratio on the amplifier performance because its opti-

mum value is difficult to determine and depends on a number of parameters. In the small signal limit, the approximation used for the pump beam profile, whether Gaussian or 'top-hat' , makes a large difference to the dependence of the gain on the signal-pump overlap for values of $w_l/w_p < 1$. In the 'top-hat' case, the small signal gain levels off for low values of w_l/w_p where, for Gaussian pump beams, the small signal gain continues to increase as $w_l/w_p \rightarrow 0$. The effect of ETU on the analytical small signal gain was also taken into account and found to significantly reduce the small signal gain for high pump intensities and high doping concentrations. This supports the design strategy of using low doping concentrations and longer crystal lengths to achieve high gain amplification with minimal loss in inversion density due to ETU as well as reducing thermal loading by distributing the absorbed pump power over a greater length of gain medium. The exponential dependence of small signal gain on the population inversion and the interaction length, makes its absolute value very sensitive to upconversion effects as well as the effects of misalignment and loss in population inversion due to amplified spontaneous emission (ASE), which is discussed in the next chapter. These combined effects generally result in a measured small signal gain which is significantly lower than the value predicted from the model. However this analysis still provides useful clues on how to increase the gain for low power signals, such as by controlling the signal-pump overlap.

An analytical model for the saturated gain in a cw amplifier was then presented which accounts for the reduction in gain caused by an intense signal. The gain therefore reaches a steady-state value where the pump rate equals the combined rate of stimulated and spontaneous emission. This model describes the relationship between the input intensity and the gain, in terms of the small signal gain and the saturation intensity, which is a constant for a particular transition in a particular gain medium. This is effectively the signal intensity required to reduce the gain to half its small signal value. The model was used to show how the gain reduces and the extraction efficiency increases as the input intensity is increased. To use this model to make predictions of amplifier performance however, requires iterative techniques which fit a given solution to a set of starting conditions. To simplify the analysis and also to extend it to apply to pulse amplification, a model was described for pulse amplification

where the pumping during the pulse is neglected. From this starting point, Franz and Nodvik's expression for the gain can be derived. This allows the gain or extraction efficiency to be predicted for a set of initial conditions. By considering the change in gain during the pulse, this model was used to predict the output pulse shapes as a function of time, for rectangular input pulses, under a number of operating conditions. The analysis showed the asymmetry of the output pulses, characterised by a sharp peak intensity at the leading edge of the pulse and a decay rate which depends on the initial gain and on the input signal energy. The rate of decay, which corresponds to the rate of gain saturation, was shown to increase with both initial gain and input energy, as one would expect. The model was then extended, using an iterative technique, to account for the build up time of the gain in between pulses which enables the steady-state initial gain after many pulse to be predicted for a known small signal. The main advantage of operating an amplifier in pulsed mode was attributed to the large gain in peak power achievable by allowing the gain to build up between pulses to approach its small signal value.

Having described a model for amplifier gain in both cw and pulsed mode of operation, a comparison was made between the two models to test their compatibility and therefore determine the validity of the more useful pulsed model for making predictions of amplifier performance for cw systems. In general, reasonably good agreement was found between them with slightly higher gain predicted for the pulsed model in the partially saturated regime.

To apply the modelling to practical amplifier systems and to gain insight into the best parameters under which to operate; the model, which so far only considered a local area of the gain medium, was integrated numerically over the gain region to include the whole pump and signal beams. Therefore the influence of the signal-pump overlap and the pump and signal powers on the amplifier performance could be assessed. By first considering only the power gain, the gain as a function of signal-pump overlap was modelled. This showed a peak in gain occurring in the overlap range $0.7 < w_l/w_p < 0.8$ which increased slightly with pump power and showed only small differences between the 'top-hat' and Gaussian pump beam approximations. Greater differences between the two approximations were found to occur for small input energies, as was expected from the small signal gain analysis in Section 4.2.1.2.

The model was then modified to account for degradation in beam quality predicted by a quartic approximation of the phase aberration caused by thermal lensing. This led to an analysis of the brightness gain $G_B = G/(M_x^2 M_y^2)$ as a function of the signal-pump overlap. In contrast to the power gain analysis, the peak brightness gain was shown to reduce with increasing pump power due to the increase thermal aberration. Additionally the optimum overlap, for maximum brightness, was significantly smaller $0.48 < w_l/w_p < 0.72$ than that for maximum power gain.

Finally, the model for saturated pulse amplification was extended to apply to multiple amplifier stages and multiple passes of an amplifier. A step by step approach was proposed for predicting the gain for multiple amplifier stages by simply using the output from one as the input to the next. A similar approach was described for a double-pass amplifier however, in this case, the gain for the second pass is reduced by the first pass. A modification to this analysis was also necessary when there was overlap between the counter-propagating signals since they then compete for gain. By considering the beam quality degradation as well as the diminishing extracted power achievable in multiple-pass configurations, the advantages of single-pass amplifiers were highlighted.

For a multiple-stage amplifier, a simple example was given to illustrate the advantages and limitations of combining a large number of amplifiers in series. By introducing a transmission loss for each amplifier stage it was shown that a power scaling limit can be reached where the loss equals the gain. Additionally the brightness of such an amplifier, which is limited by the thermal aberrations for a lossless amplifier, was shown to roll over when a loss was introduced. The use of multiple amplifier stages has been shown, in principle, to be an effective route to power and brightness scaling, provided that system parameters are carefully controlled. However, limitations still ultimately arise due to ETU, thermal lens focusing and thermal damage to the gain medium.

4.7 References

[1] **Hardman, P. J., Clarkson, W. A., Friel, G. J., Pollnau, M.** and **Hanna, D. C.**, *Energy-transfer upconversion and thermal lensing in high-power end-*

pumped Nd:YLF laser crystals, IEEE Journal of Quantum Electronics, Vol. 35, No. 4, pp. 647–655, 1999.

[2] **Clarkson, W. A.** and **Hanna, D. C.**, Optical Resonators – Science and Engineering,327-361:*Resonator Design Considerations for Efficient Operation of Solid-State Lasers End-Pumped by High-Power Diode Bars*, pp. pp. 327–361, Kluwar Academic Publishers, 1998.

[3] **Koechner, W.**, Solid-State Laser Engineering, Springer, 5th edn., 1999.

[4] **Musgrave, I. O., Yarrow, M. J., Clarkson, W. A.** and **Hanna, D. C.**, *Energy-transfer upconversion in Nd:YVO_4 and its effect on laser performance*, article awaiting submission.

[5] **Peng, X., Xu, L.** and **Asundi, A.**, *Power Scaling of Diode Pumped Nd:YVO_4 Lasers*, IEEE Journal of Quantum Electronics, Vol. 38, No. 9, pp. 1291–1299, 2002.

[6] **Siegman, A. E.**, Lasers, University Science Books, 1986.

[7] **Frantz, L. E.** and **Nodvik, J. S.**, *Theory of Pulse Propagation in a Laser Amplifier*, Journal of Applied Physics, Vol. 34, No. 8, pp. 2346–2349, August 1963.

[8] **Pearce, S.** and **Ireland, C. L. M.**, *Performance of a cw pumped Nd:YVO_4 amplifier with kHz pulses*, Optics and Laser Technology, Vol. 35, pp. 375–379, 2003.

[9] **Wall, K. F., Jaspan, M., Dergachev, A., Szpak, A., Flint, J. H.** and **Moulton, P. F.**, *A 40W single-frequency, Nd:YLF master oscillator/power amplifier system*, OSA Trends in Optics and Photonics, Vol. 26 Advanced Solid State Photonics, pp. 216–221, 1999.

[10] **Chen, Y. F., Kao, C. F., Huang, T. M., Wang, C. L.** and **Wang, S. C.**, *Influence of Thermal Effect on Output Power Optimization in Fibre-Coupled Laser-Diode End-Pumped Lasers*, IEEE Journal of Selected Topics in Quantum Electronics, Vol. 3, No. 1, pp. 29–34, 1997.

[11] **Chen, Y. F.**, *Pump-to-mode size ratio dependence of thermal loading in diode-end-pumped solid-state lasers*, Journal of the Optical Society of America B, Vol. 19, No. 7, pp. 1558–1563, 2002.

[12] **Clarkson, W. A.**, *Thermal effects and their mitigation in end-pumped solid state lasers*, Journal of Physics D: Applied Physics, Vol. 34, pp. 2381–2395, August 2001.

[13] **Siegman, A. E.**, *Analysis of laser beam quality degradation caused by quartic phase aberrations*, Applied Optics, Vol. 32, No. 30, pp. 5893–5901, 1993.

[14] **Kendall, T. M. J.**, Power scaling and nonlinear frequency conversion of single-frequency lasers based on Nd:YLF, Ph.D. thesis, Optoelectronics Research Centre, University of Southampton, 2004.

[15] **Pearce, S., Ireland, C. L. M.** and **Dyer, P. E.**, *Simplified analysis of double-pass amplification with pulse overlap and application to Nd:YVO_4* , Optics and Laser Technology, Vol. 35, pp. 375–379, 2003.

Chapter 5

Realising a High Power Mode-Locked Nd:YVO_4 MOPA System

5.1 Introduction

Many laser applications require a combination of high peak power and high average power as well as good beam quality. In materials-processing, high peak powers or pulse energies are often essential for producing a desired thermo-mechanical, optical or chemical change in the target material, however processing of large volumes of materials at high speed for industrial applications is also dependent on average power. Additionally, for the application of non-linear frequency conversion, while high peak power and good beam quality are important for efficient frequency conversion, high output power requires a high average power pump source. One application of particular interest is synchronous pumping of a singly-resonant OPO to produce efficient frequency conversion with tunable output. This technique requires that the OPO cavity round-trip frequency is matched to the pump pulse repetition rate. The pump pulses therefore add power synchronously to the resonating pulse in the OPO allowing a low threshold and hence high conversion efficiency to be achieved [1].

A solid-state, diode-pumped MOPA system with a mode-locked master oscillator is a very convenient method for producing TEM_{00} output with high

average power and high peak power because the problems of achieving stable mode-locked TEM_{00} operation is largely decoupled from the problem of power scaling. The use of Nd:YVO_4 in high power pulsed lasers and MOPA systems has been demonstrated by several authors [2–4]. In 1993 Plaessmann *et al.* [5] demonstrated a single rod Nd:YVO_4 amplifier in an end-pumped multipass configuration and achieved >50dB small signal gain and 4.3 W of output power. In 2002 Forget *et al.* [6] used a 6 pass configuration Nd:YVO_4 amplifier to achieve small signal gains of 56dB and average powers of 57 W output for 150 W of pump power.

The use of diode-pumped solid-state MOPA systems to synchronously pump OPOs based on nonlinear materials such as KTA, PPLN and LBO have been explored by several authors. These have included cw mode-locked pumping [7,8] and pulsed mode-locked pumping [9,10]. In oscillators, Q-switching is the most common technique for achieving long trains ($\sim$10ns) of mode-locked pulses of high peak power. In a MOPA system however, pulse gating (or slicing) of the output from the oscillator, before it enters the amplifier, can be used to achieve even longer trains ($\sim\mu$s) of mode-locked pulses. In this scheme, the gain in the amplifier reaches much higher levels than under cw conditions when the gain recovery time between pulses is comparable to the inverse of the lifetime of the gain medium. This allows higher power levels to be achieved without the thermal problems associated with cw generation at such high power. Furthermore the long pulse durations achievable (μs), which would be difficult to achieve with conventional Q-switched oscillators, implies that the source retains many of the attractions of cw operation for the application of OPO pumping, notably good beam quality and effective wavelength selection in the OPO.

In this chapter, the strategy of using a multiple stage, end-pumped, power-amplifier to amplify the output from the mode-locked oscillator, described in Chapter 3, is explained. The use of an acousto-optic modulator to gate the input to the amplifier is also discussed as a means to generate pulsed operation and thereby adjust the level of saturation and hence the gain of the amplifier. This technique provides a simple and flexible way to increase the peak power of the output but at the inevitable cost of reduced average power. The design of an amplifier scheme which incorporates multiple laser crystals, with low dop-

ing concentration, to spread the thermal load over a large cooling volume and reduce the impact of ETU, is presented. The choice of design parameters for the amplifier is investigated with particular regard to the power scaling issues and theory discussed in Chapter 4. Finally the experimental techniques for realising the amplifier system are described and the results and performance characteristics are presented.

5.2 Amplifier Design Considerations

The design criteria for the amplifier system discussed here was to achieve efficient extraction of stored energy, minimal degradation in beam quality and stable operation at high peak and high average power in cw, mode-locked and gated mode-locked modes of operation. While the previous chapter discussed many of the theoretical considerations which apply to this amplifier, this section describes the main experimental design considerations and strategies that were adopted for achieving these criteria. Additionally, some of the factors limiting performance of amplifiers are discussed.

5.2.1 Thermal Management

To allow for high pump powers to be absorbed by end-pumping Nd:YVO_4 laser crystals without risk of thermal fracture, a low doping concentration was chosen which implies that the pump power is absorbed over a long length of crystal since the absorption coefficient is approximately proportional to the doping concentration. This low doping concentration reduces the thermal loading density, therefore increasing the damage threshold. This also reduces the total thermal loading by reducing the impact of ETU, as described in Section 4.2.2. There is, however, a trade-off because a sufficiently high doping concentration is required to absorb a large fraction of the pump light over the length of the crystal and a sufficiently short length of crystal is required to achieve a small pumped volume thus achieving high gain.

In the amplifier systems described in this thesis, 0.1 at.% doping concentration Nd:YVO_4 crystals of length 10mm were chosen. These provided a measured

absorption efficiency of 82% of incident pump light at 808nm corresponding to an absorption coefficient of 170m^{-1}. While these provided rather low absorption efficiency for a single pass, allowing the pump light to pass through two crystals, as discussed in the next section, enables ∼96% absorption efficiency, without such severe problems associated with ETU as is expected if higher doping concentration were used.

To illustrate the impact of ETU on an amplifier rod under low signal power conditions, the reduction in small signal gain coefficient and the extra heating, as a result of ETU, can be considered. From equation (4.30), assuming that all the incident pump power is absorbed, and that the pump beam has a 'top-hat' profile, the fraction by which the small signal gain coefficient g_0 is reduced by ETU is given by

$$\frac{g_{0,ETU}}{g_0} = \frac{4}{\chi}\left(\sqrt{1+\chi} - 1 + \ln\left(\frac{2}{1+\sqrt{1+\chi}}\right)\right), \tag{5.1}$$

where, for a pump intensity $I_p = P_p/\pi w_p^2$,

$$\chi = \frac{4\alpha_p I_p W \tau_f^2}{h\nu_p}. \tag{5.2}$$

In addition, the fraction of pump power converted to heat in the presence of ETU was given in equation (4.63) by

$$\gamma_{ETU} = \left\{1 - \frac{2(1-\gamma)}{\beta}\left[2(\sqrt{1+\beta}-1) + \ln\left(\frac{4}{\beta}\frac{\sqrt{1+\beta}-1}{\sqrt{1+\beta}+1}\right)\right]\right\}, \tag{5.3}$$

where γ is the fraction of absorbed pump converted to heat in the absence of ETU (given by $1 - \nu_l/\nu_p$) and β is a dimensionless parameter given by

$$\beta = \frac{8 W I_p \alpha_p \tau_f^2}{h\nu_p}. \tag{5.4}$$

This allows the fraction of pump power converted to heat due to ETU to be calculated by evaluating $\gamma_{ETU} - \gamma$. Using the value of W of 3×10^{-22}cm^{3}s^{-1} from [11], assumed to be constant with varying doping concentration, values for α_p of 170m^{-1} for 0.1 at.% concentration and three times this (510m^{-1}) for 0.3 at.% concentration, and estimated values of τ_f of 120µs and 110µs for 0.1 at.% and 0.3 at.% concentration respectively, Figure 5.1 was produced. The figure shows the large increase in heating due to ETU and also the significantly

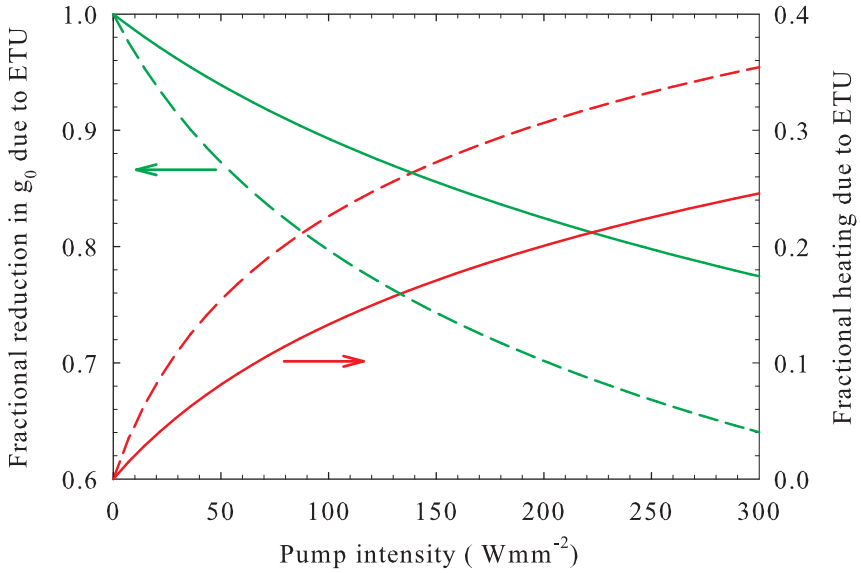

Figure 5.1: The fractional reduction in small signal gain coefficient g_0 due to ETU and the fraction of pump power converted to heat due to ETU, as a function of pump intensity, for 0.3 at.% (dashed lines) and 0.1 at.% (solid lines) doping concentrations.

larger reduction in g_0 for the higher doping concentration. If we take a typical fibre-coupled diode-bar with an output intensity of 240Wmm^{-2} from a $NA = 0.22$ fibre (eg. 30W from a 400µm core diameter fibre), the pump intensity when the pump is confocally focused through a 10mm long Nd:YVO_4 crystal is around 90Wmm^{-2}. For the 1 at.% doping concentration, from the graph, this implies an additional heating of around 13% of the pump power due to ETU and a reduction in small signal gain coefficient of around 10% due to ETU. For the 0.3% doping concentration, these losses are more significant, with an additional heating of 22% and a 20% reduction in small signal gain coefficient. By reducing the doping concentration below 0.1 at.% it would be possible to further reduce these losses due to ETU, however the reduction in absorbed pump power would become more significant. Availability of crystals with lower doping concentration was also limited.

Increasing the volume over which the pump power is deposited, by using low doping concentration crystals also permits more effective cooling of the crystal by increasing the effective area over which the heat can be removed. However, the cooling mechanism itself is also a critical factor in achieving efficient removal of heat from the gain medium. In an end-pumped configu-

ration, cooling crystals from their side faces is responsible for producing the transverse thermal gradients and high stresses associated with thermal lensing and stress fracture. However, in this geometry, this usually remains the only option for removing the large amounts of heat generated and ultimately preventing melting or fracture of the crystal or damage to the AR coatings if the heat was not removed. In this work, all the Nd:YVO_4 crystals used were square in cross section, with dimensions 3×3×10mm. To side-cool the crystals they were first wrapped in indium foil, of thickness 100μm , to achieve efficient thermal contact between the crystal surface and the heat sink. The crystals were then placed in a custom built aluminium mounts ensuring good contact on all four sides. The mounts were bolted to water-cooled copper heat sinks through which cooling water, at a temperature of ∼15℃, was pumped. A photo of the crystal mounting arrangement is shown in Figure 5.2.

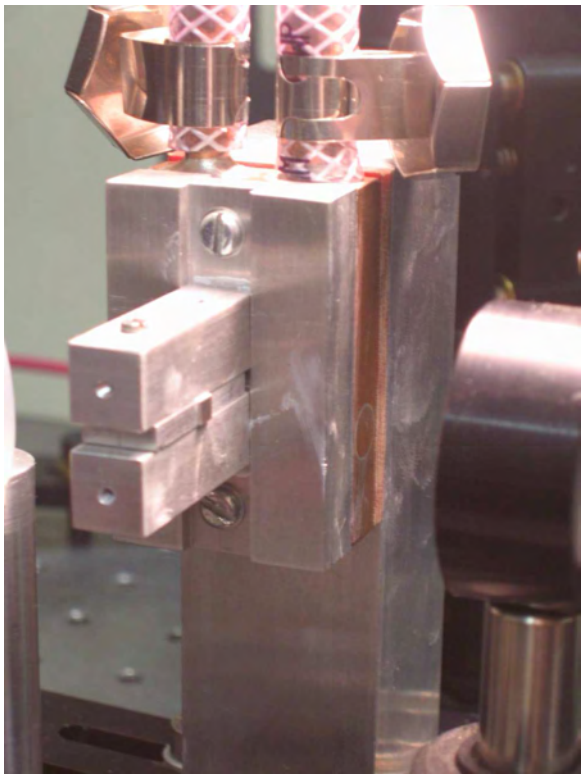

Figure 5.2: Photo of a Nd:YVO_4 crystal in a heat sinking mount.

5.2.2 Relay-Imaging

Multiple-rod amplifier architectures require the signal beam to be imaged through each rod with carefully controlled beam sizes. In the presence of thermal lenses in the rods, which do not have constant or easy to predict focal lengths, this can cause difficulty. Relay-imaging the signal beam from one rod to another can ensure that a particular spot size is re-imaged or magnified by a fixed ratio several times, independently of thermal lens strength. The condition for relay-imaging, using two thin lenses, is that the lenses are separated by the sum of their focal lengths and the relay-imaging planes lie at each end of this lens arrangement at a distance equal to the focal length of the adjacent lens. This can be shown using ray matrix notation:

$$\begin{aligned}\begin{bmatrix} A & B \\ C & D \end{bmatrix} &= \begin{bmatrix} 1 & f_2 \\ 0 & 1 \end{bmatrix} \begin{bmatrix} 1 & 0 \\ -1/f_2 & 1 \end{bmatrix} \begin{bmatrix} 1 & f_1+f_2 \\ 0 & 1 \end{bmatrix} \begin{bmatrix} 1 & 0 \\ -1/f_1 & 1 \end{bmatrix} \begin{bmatrix} 1 & f_1 \\ 0 & 1 \end{bmatrix} \\ &= \begin{bmatrix} -f_2/f_1 & 0 \\ 0 & -f_1/f_2 \end{bmatrix}. \end{aligned} \tag{5.5}$$

Using the initial complex radius of curvature $q_1(z)$, defined by

$$\frac{1}{q_1(z)} = \frac{1}{R_1(z)} - j\frac{\lambda M^2}{\pi w_1(z)^2}, \tag{5.6}$$

where R_1 is the initial wavefront radius of curvature and w_1 is the initial $1/e^2$ beam radius, and the ABCD law for Gaussian like beams given by

$$q_2 = \frac{Aq_1 + B}{Cq_1 + D}, \tag{5.7}$$

it can be shown that

$$R_2 = \left(\frac{f_2}{f_1}\right)^2 R_1, \tag{5.8}$$

and

$$w_2 = -\left(\frac{f_2}{f_1}\right) w_1, \tag{5.9}$$

where the minus sign indicates that the beam is inverted.

From one relay-image plane to the next, the ratio of the radii, w_2/w_1, of any near-paraxial ray is a constant equal to the ratio of the second lens focal length to the first lens focal length. Similarly the ratio of divergence angles w_2'/w_1'

of the ray from one relay image plane to the next is equal to the inverse of this ratio, where $w' = w/R$. These relationships are shown to be independent of both the wavelength, λ, and the beam quality factor, M^2. For 1:1 relay-imaging, this ratio is simply equal to one and the radius and divergence angles are the same in both image planes. If thermal lenses are positioned in the relay-imaging planes this result still holds for the beam radius, but the beam divergence angles are modified on passing through the thermal lenses. This concept is shown in Figure 5.3. The figure shows how the lenses re-produce

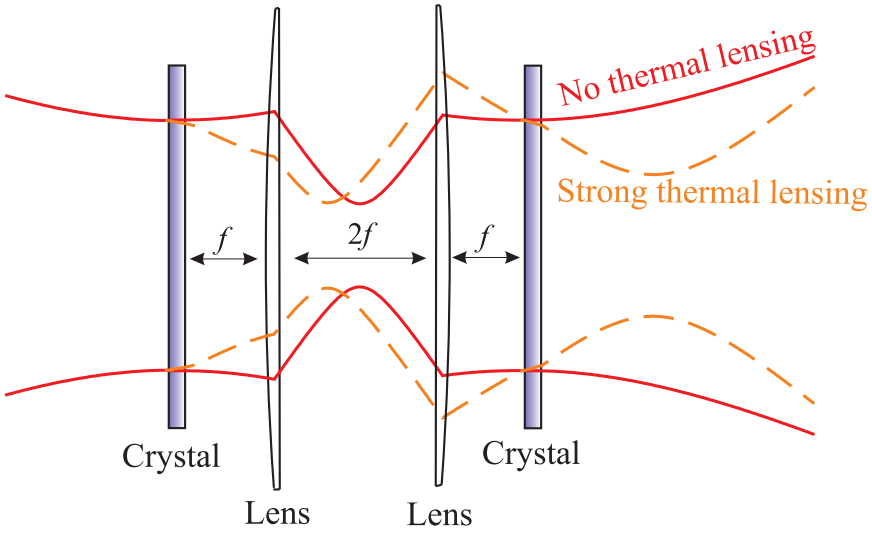

Figure 5.3: 1:1 relay imaging in a multiple rod amplifier for signal propagation from left to right. The two lenses of focal length f are set up with separation $2f$ and the crystals are in the focal planes. The solid line is the signal profile with no thermal lens and the dotted line is with strong thermal lensing. The vertical scale is exaggerated.

the same beam radius in the center of the second crystal as in the first crystal both with and without the thermal lensing. The divergence angle of the beam when it exits the crystal does change due to the thermal lens, so in the case of strong thermal lensing the beam converges out of each crystal and focuses to a smaller waist after passing through it. In this lens arrangement the effect of passing through two lenses of strength $1/f_{th}$ is equivalent to passing through a single lens of strength $2/f_{th}$. In fact, using a thin lens approximation for a perfectly relay-imaged amplifier, the overall effect of n thermal lenses of focal lengths f_i for the i^{th} lens is to produce a focusing power equivalent to a single

lens of focal length f_{eff} where

$$\frac{1}{f_{eff}} = \sum_{i=1}^{n} \frac{1}{f_i}. \tag{5.10}$$

The modification of the wavefront radius of curvature, as the signal beam passes through a thermal lens, is also effected by the degradation in beam quality. However, the relationship given in equation (5.5) still holds, but results in an increase in the far field divergence of the beam.

In the same way as the signal beam, the pump beam spot size of any pump radiation not absorbed in the first crystal is re-imaged and absorbed in the second crystal. This technique is very useful when, as in an end-pumped amplifier, controlling the spot sizes of beams is critical, especially since thermal lens strengths are difficult to predict precisely and change with pump power. Using the simple expression, in equation (4.52), for the thermal lens focal length, for a 'top-hat' approximation for the pump beam profile, Figure 5.4 was produced, showing the predicted thermal lens strength in Nd:YVO_4 with 0.1 at.% doping concentration, with and without the presence of ETU, as a function of pump intensity. The values of K_c and $\mathrm{d}n/\mathrm{d}T$ were taken from Table 2.4 and an upconversion parameter of 3×10^{-22}cm^{3}s^{-1} was used. The graph shows that, for the amplifier rods in this thesis, which are all pumped with intensities $\lesssim$100Wmm^{-2}, the thermal lens strengths predicted using this model are $<$6m^{-1} ($f_{th} > 170$mm) under saturated conditions, where ETU can be neglected, and $<$8m^{-1} ($f_{th} > 125$mm) under unsaturated conditions, where the effect of ETU contributes around an extra 13% more heat at this pump intensity. In practice the pump beam is not 'top-hat' in profile so the effective thermal lens strength is expected to be higher than for the 'top-hat' approximation. For a pure Gaussian pump profile the thermal lens strength is twice as high as for the 'top-hat' profile, on the optic axis and reduces as a function of the distance from the optic axis.

If we consider a multiple-stage amplifier, comprising a number of Nd:YVO_4 crystals of length l, each one having the same pump intensity and the same signal beam radius, a relay imaging scheme will ensure that the signal spot sizes in each crystal will remain approximately constant up to the limit where the effective thermal lens focal length of the whole amplifier becomes compa-

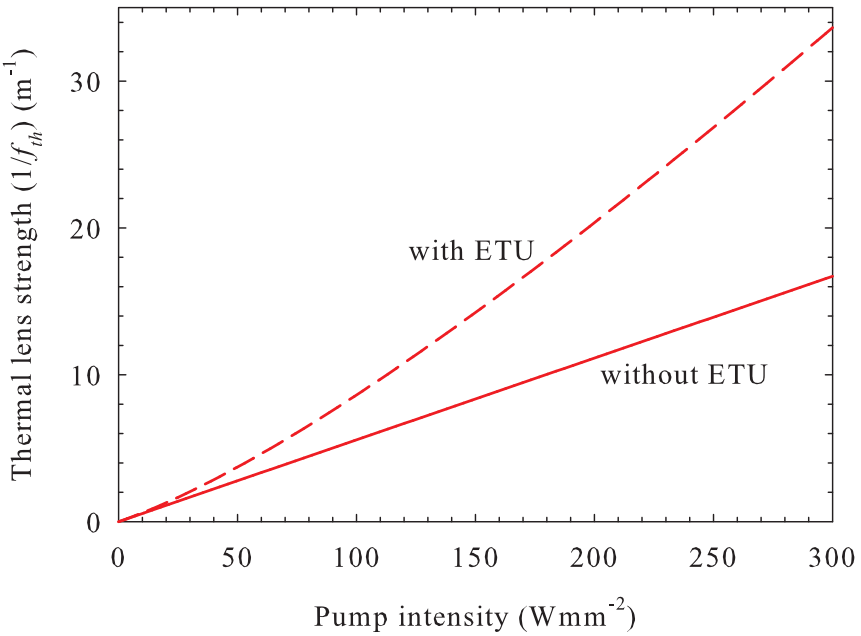

Figure 5.4: Predicted thermal lens strength in a Nd:YVO_4 amplifier rod with 0.1 at.% doping concentrating and a 'top-hat' pump beam profile.

rable to the length of the crystals. This can be considered the limit where the signal beam size varies significantly over the length of the crystal and therefore the spatial overlap between the pump beam and the signal beam becomes reduced. For a thermal lens focal length f_{th}, the approximate number of amplifier stages, n_{max}, required to produce an effective thermal lens focal length, l, is given by

$$n_{max} \approx \frac{f_{th}}{l}. \tag{5.11}$$

For the predicted thermal lens focal length, of 170mm, for a 'top-hat' pump beam without the effect of ETU and for a 10mm long crystal, this corresponds to a maximum number of amplifier stages of 17 before thermal lens focusing significantly reduces the gain. In a worst case scenario, this thermal lens focal length could be reduced to around 125mm in the presence of ETU and reduced by a further factor of two, to 63mm, on axis, due to a more Gaussian pump beam profile. In this case n_{max} becomes ~6. A further problem is the potential for clipping of the signal beam through optics, of limited aperture, such as isolators, outside of the amplifier rods. This may cause the amplifier gain to be limited, before n_{max} is reached. It is also of note, that when the thermal lens

focal length becomes comparable to the crystal length, the thin lens approximation, used to derive equation (4.52), breaks down and a thick, graded index, lens description should be used to accurately predict the thermal lensing. For this reason the predicted limit on the number of amplifier stages, above, can only be used as a rough guide.

Using a crude approximation of completely saturated amplifiers, where all the pump power is absorbed and neglecting ETU and transmission loss, such that the gain $G(n)$ for n amplifier stages is given by one plus the total number of inverted ions for a pump intensity per amplifier of I_p, hence

$$G(n) = 1 + n\left(\frac{I_p \sigma_{21} \tau_f}{h\nu_p}\right), \tag{5.12}$$

and the approximate thermal lens focal length for a 'top-hat' pump profile, given by

$$f_{th} = \frac{2K_c}{I_p \gamma \mathrm{d}n/\mathrm{d}T}, \tag{5.13}$$

it is possible to use the maximum number of amplifier stages, n_{max}, to find the maximum saturated gain, G_{max}, where a crystal of length l is required to absorb all the pump power. By substituting equation (5.11) into equation (5.12), and assuming $G_{max} \gg 1$, $G(n)$ for n_{max} amplifier stages can be given by

$$G_{max} \approx \frac{2\sigma_{21}\tau_f K_c}{l h \nu_p \gamma \mathrm{d}n/\mathrm{d}T}. \tag{5.14}$$

As can be seen, G_{max} is independent of I_p and therefore provides a simple figure of merit, based only on material parameters, for the power scaling potential of different gain mediums, which accounts for the limit imposed by thermal lens focusing. Table 5.1 shows the values of G_{max} for the three materials discussed previously, using the data in Table 2.4 and a crystal length l of 10mm:

Material	G_{max}
Nd:YVO_4	42.8
Nd:YAG	39.9
Nd:YLF	44.2

Table 5.1: Comparison of maximum gain figure of merit for Nd:YVO_4 , Nd:YAG and Nd:YLF

The table shows remarkably similar values for each material, considering the large differences in their properties. While in Section 4.2.3, we saw that the high $\sigma_{21}\tau_f$ product of Nd:YVO_4 led to much higher gain and extraction efficiency in a saturated cw amplifier, these results show that these advantages are offset by the poorer thermal properties of Nd:YVO_4 compared to Nd:YAG and Nd:YLF. Indeed, Nd:YLF is shown to have a slightly higher value of G_{max} due to its relatively weak thermal lensing. Physically this means that although the gain for each amplifier stage may be lower for Nd:YLF than that for a similar Nd:YVO_4 amplifier stage, a greater number of stages can be combined before the thermal lensing becomes a limiting factor, resulting in higher overall gain. Nevertheless, when other factors such as transmission losses, ETU, damage threshold and absorption efficiency are considered, as well as the saturation intensity required to extract the gain, the advantages of Nd:YVO_4 for achieving efficient amplification in relatively few amplifier stages are still very favorable.

5.2.3 Feedback and Parasitic Lasing

In practical amplifier systems which incorporate many optical components, feedback from any of the component's AR coatings can cause problems such as parasitic lasing. Additionally, feedback from the amplifier to the oscillator can cause instability or damage to the oscillator. Parasitic lasing arises when the reflections between two or more optical surfaces in the amplifier system partially or wholly feedback through the gain medium to make multiple passes and effectively form a laser cavity. If the amount of feedback is high enough, then the lasing threshold becomes lower than the available pump power and the cavity oscillates. In high gain amplifiers, where the round trip small signal gain may be several thousand or higher, then the level of feedback required to cause lasing may be very small. For feedback between the end faces of a laser rod for example, where the end faces are parallel and flat with reflectivities r_1 and r_2, the threshold condition for parasitic lasing to occur, assuming complete overlap of the reflected signal with the gain region and neglecting ASE and saturation, is

$$r_1 r_2 \exp(2g_0 l) > 1, \tag{5.15}$$

where l is the length of the gain medium and g_0 is the small signal gain coefficient. The pump intensity required to cause parasitic lasing in a Nd:YVO_4 crystal with 0.1% doping concentration and AR coating reflectivity 0.2% on each face, assuming all the pump power is absorbed and allowing for the effect of ETU was estimated. The value of $g_0 l$ was calculated as a function of pump intensity from equation (4.30) and found to reach the threshold ($0.5\ln(1/r_1 r_2)$) at a value of $\sim$82Wmm^2 which is similar to the average pump intensity used to pump the amplifiers described in this thesis. In practice however, the small signal gain coefficients are much lower than those predicted by this theory. Additionally, diffraction of the reflected signal reduces the fraction of reflected light contributing to parasitic lasing. The small signal gain for a multiple-stage amplifier is much higher (by a power of n for n identical stages), making the threshold gain quite relatively easy to reach. Furthermore, back-reflections from a number of surfaces are possible, potentially reducing the threshold gain somewhat.

Parasitic lasing modes normally occupy the same region as the signal beam so that it normally only presents a problem when the input signal intensity is low (ie. when the gain is high). When a strong signal is present it extracts the gain required for parasitic lasing thereby reducing or eliminating it. However, in some cases the parasitic modes occupy regions of population inversion outside the region occupied by the signal beam, which means they can sometimes oscillate even when the signal power is high. Reflections from any surface in the amplifier, including the side faces of the rods or even metal surfaces near the signal path, can cause stable parasitic lasing.

Several techniques can be adopted to reduce or eliminate parasitic lasing. Ensuring that the AR coatings have very low reflectivity is essential. Another technique, which is adopted in the amplifier system described here, is to tilt the optical components slightly away from normal incidence to prevent the back reflections from mapping back onto the signal beam. Similarly, using laser rods with roughened side faces and slightly wedged end-faces prevents internal parasitic modes and reflections back along the signal path. Another technique is to use spatial filters in the form of an aperture in a suitable location in the amplifier. These can prevent parasitic lasing by blocking the paths of parasitic modes. The problem with the above techniques is that, in a relay-

imaged system, the tilt angles required to stop feedback can be quite large particularly for components near the relay-image planes. Also, finding suitable locations for spatial filters is difficult in the presence of thermal lensing because the beam sizes generally change with pump power. In the amplifier system described here, the only effective way to eliminate parasitic lasing was found to be by inserting Faraday isolators between each amplifier stage.

Another potential effect of unwanted back reflections is feedback from the amplifier into the master-oscillator, this generally causes oscillation of unwanted higher order modes and prevents effective mode-locking of the oscillator by placing additional constraints on the allowable axial modes. This feedback can sometimes be prevented by tilting the amplifier components by a small angle from the normal, however when there are many components, as in this amplifier system, it is usually necessary to introduce a Faraday isolator between the oscillator and the amplifier.

5.2.4 Amplified Spontaneous Emission

Even if loss of population inversion due to the feedback mechanisms described above can be eliminated, the maximum small signal gain achievable from an amplifier is ultimately limited by amplified spontaneous emission (ASE). ASE (sometimes called superfluorescence), occurs when the radiation from spontaneous emission in the inverted gain medium acts as a signal and becomes amplified along the length of the gain medium. Like a small signal to the amplifier, the power of an ASE signal grows rapidly along the length of the amplifier so for a long length of gain medium this can cause significant depletion of the upper state population and therefore reduce the gain. Unlike parasitic lasing, ASE has no threshold and does not require optical feedback. ASE also occurs in both directions along the amplifier, although the preferential signal polarisation in the higher emission cross section direction in Nd:YVO_4 means that isolators between amplifier stages can be used to reduce ASE in the backwards direction. In an end-pumped rod, the signal intensity due to ASE can be predicted by considering the solid angle subtended by the spatial extent of the gain region at one end of the rod, as seen from a point on the optic axis on the other end of the rod, as shown in Figure 5.5. For a confocally-focused pump

beam of minimum waist radius w_p, this solid angle Ω, which defines the region of highest ASE gain, can be expressed as

$$\Omega = \frac{2\pi {w_p}^2}{l^2}, \tag{5.16}$$

where l is the length of the rod. Svelto *et al.* [12] showed that for a rod with uniform gain, the ASE intensity I_{ASE} from a laser rod with small signal gain G_0 can be expressed as

$$I_{ASE} = \varphi I_{sat} \frac{\Omega}{4\pi} \frac{(G_0 - 1)^{3/2}}{(G_0 \ln G_0)^{1/2}}, \tag{5.17}$$

where I_{sat} is the saturation intensity given by equation (4.35) and φ is the fluorescence quantum yield ($\varphi = \tau_f A_{21}$, where τ_f is the upper state lifetime and A_{21} is the rate of spontaneous emission). For high gain amplifiers where $G \gg 1$, the ASE intensity can be approximated by [13]:

$$I_{ASE} = \varphi I_{sat} \frac{\Omega}{4\pi} \frac{G_0}{(\ln G_0)^{1/2}}. \tag{5.18}$$

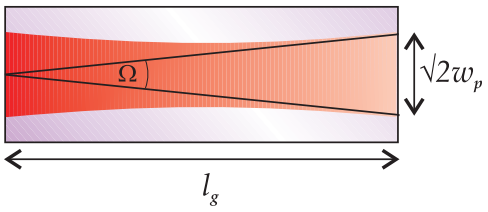

Figure 5.5: The parameters for ASE in a confocally pumped laser rod

From equation (4.35), 0.1 at.% doped Nd:YVO_4 has a saturation intensity of 6.43Wmm^{-2}. For a single stage, single pass Nd:YVO_4 amplifier of length 10mm, with an absorbed pump power of 30W and a pump waist radius of 300µm , the ASE output power from equation (5.18), using equation (4.30) for the small signal gain is 2.5mW, assuming a fluorescence quantum yield of 1.

For a multiple-stage amplifier which adopts a relay-imaging technique to image the output from one rod into the next, the ASE signal is also relay imaged and therefore amplified further. In a perfectly relay-imaged multiple-stage amplifier, the system can effectively be viewed as a single laser rod of

the same length but with a small signal gain calculated using the sum of the pump power to all the amplifier stages. Ω will therefore be the same, assuming that each amplifier has the same value of w_p. In practice however, imperfect relay imaging and diffraction of the ASE signal will reduce the effective value of Ω. Additionally, saturation effects come into play at pump powers of several tens of watts so the above model breaks down. While ASE occurs even when there are no back reflections in the system, feedback from optical components can increase the ASE gain by increasing the effective interaction length, even if there is no closed cavity condition.

5.3 Multiple-Stage Nd:YVO_4 Amplifier Design

5.3.1 Pumping Schemes

The three-stage amplifier, employed in our experiments, was pumped by a combination of fibre-coupled 808nm diode sources. The first stage was pumped by two 30W output fibre-coupled diode bars purchased from LIMO, Lissotschenko Mikrooptik GmbH. These, single-package devices, couple the output from a diode bar into a 400µm core diameter fibre with NA=0.22. The maximum measured fibre output powers of the two devices were 28.3W and 31.5W. The devices were bolted to water cooled heat sinks through which water was pumped from chillers. By connecting each heat sink to a different water chiller, the water temperature and hence the temperature of each diode could be controlled independently to $\pm$0.5℃ to tune the diode wavelengths to the peak absorption wavelength in Nd:YVO_4 at $\sim$808nm, using the tuning slope of $\sim$0.3nm/℃. The cooling water temperatures giving maximum absorption for the two diodes were 18.5℃and 21℃.

5.3.1.1 Four-Fiber Coupled Diode Stack

The second and third amplifier stages were pumped by a single diode stack, of nominal output power 500W, coupled to four delivery fibres. The diode-stack, purchased from Dilas Diodenlaser GmbH, was based on a vertical stack of twelve $\sim$40W bars, which produced a total emitting area of 1cm across by 2cm

high. The device incorporated a water cooled heat sink, with micro-channels for the water, to achieve efficient heat removal and low thermal gradients across the device area. A chiller controlled the water temperature and pressure and the diode wavelength was temperature tuned for maximum absorption in Nd:YVO_4 . An array of 12 vertical cylindrical microlenses was mounted on the device (one for each bar). These microlenses collimated the radiation from each bar in the fast axis. Two cylindrical lens telescopes, one for each axis, were then used to expand and collimate the radiation in the horizontal plane and to reduce the size of the beam in the vertical plane. The resulting collimated beam had dimensions 4cm horizontally by 1cm vertically. The beam was then polarisation combined to halve the M^2 value in the horizontal plane. This was achieved by a similar technique to that described in Section 2.7.3.2, but using a thin-film polariser instead of a polarising beam splitter cube. The only difference here was that the angles of the beam steering mirrors needed to be selected such that the reflected and transmitted beams both met the thin-film polariser at Brewster's angle. The beam steering mirrors used here had coatings which produced high reflectivity in the incidence range 45°-60°, so the appropriate angles were calculated and set-up as shown in Figure 5.6. The figure shows that the output beam was then expanded and collimated once again in the horizontal plane, with two cylindrical lenses, before the output was sliced into 4 approximately equal size beams each having approximate dimensions 1cm$\times$1cm. Figure 5.7 shows a photo of the optical set-up for shaping and fibre coupling the beam from the diode stack which is seen enclosed in a box at the bottom of the photo. The box was purged with nitrogen to keep the stack and the collimating optics free from moisture and dust.

This technique provides an effective way to convert the output from the diode stack, which has roughly 8 times higher M^2 value in the horizonal plane than in the vertical plane, into four beams with roughly equal orthogonal M^2 values and equal orthogonal beam sizes suitable for fibre coupling. The estimated M^2 values of the diode stacks, after fast-axis collimation, was approximately 1500 horizontally by approximately 200 vertically. After polarization combining and slicing into four beams this led to approximately equal M^2 values close to 200 in orthogonal planes for all four beams. Using 30mm focal length aspheric lenses to focus the beams for fibre coupling, the spotsizes and M^2 val-

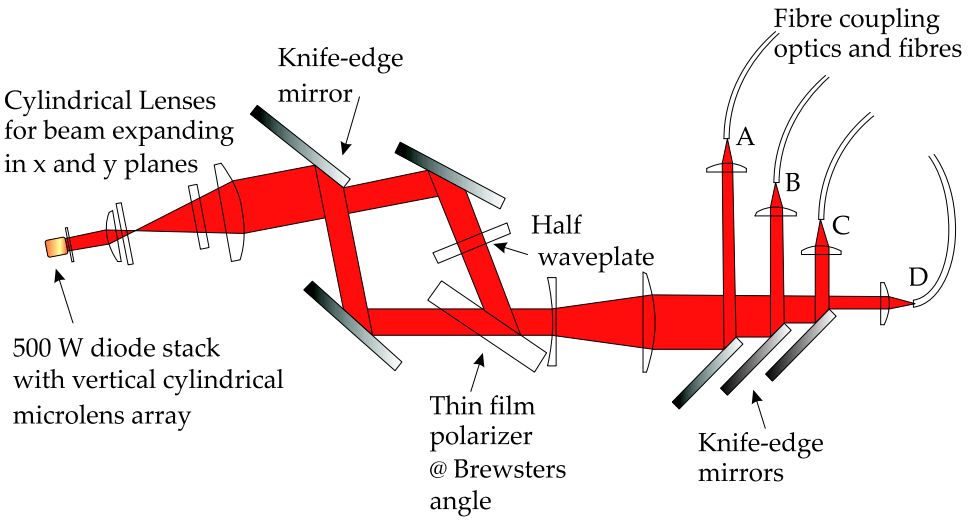

Figure 5.6: Beam shaping and fibre coupling scheme for high power diode stack.

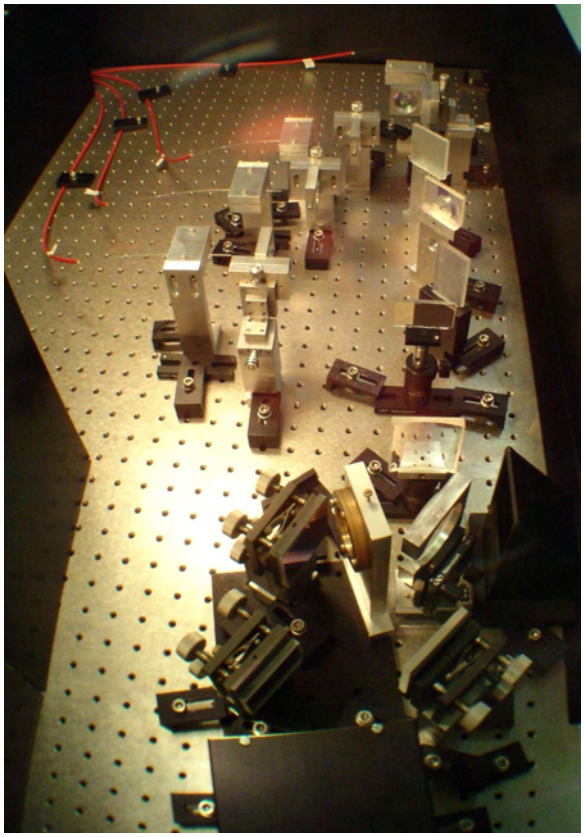

Figure 5.7: Photo of diode stack, beam shaping and fibre coupling optical set-up

ues were measured for each beam. The results for the four beams, labelled A-D as shown in Figure 5.6, are shown in Table 5.2. The table also shows the measured maximum beam powers before the fibre P_{in}, after the fibre P_{out} and the associated coupling efficiency η_c for the fibre of NA = 0.22 and core diameter 600µm . This fibre core size was chosen based on the beam quality of the input beams and the low NA required for collimating the fibre output, as described in Section 2.7.4. Even larger core size fibres would have improved the coupling efficiency, however the choice and availability of such fibre was limited so the resulting coupling efficiency was rather low.

Beam	axis	w_0 (µm)	M^2	P_{in} (W)	P_{out} (W)	η_c
A	x	340	256	79.5	55.3	70%
	y	320	215			
B	x	343	258	103.0	66.3	64%
	y	269	194			
C	x	301	219	96.6	73.9	77%
	y	275	206			
D	x	334	219	79.3	62.7	79%
	y	267	206			
Total				358	258	72%

Table 5.2: Comparison of beam properties and fibre coupling efficiencies of the 4 diode-stack output beams.

The total diode stack output power was measured after the micro-lenses were mounted and found to be 488W at the maximum drive current of 50A. The power before and after entering the polarisation combining stage was 462W and 411W respectively, giving a polarisation combining efficiency of 89%. The following beam expanding, slicing and focusing stage resulted in another 87% transmission, giving a total power in the four beams of 358W. Lastly the overall coupling efficiency of 72% in the four fibres resulted in a total delivered power of 258W. While this amounts to a rather low overall efficiency of ∼53% through the whole set-up, shown in Figure 5.6, the result is a set of four high brightness fibre sources providing the smooth circular beam profiles required for end-pumping and the versatility offered by having the source fibre-coupled. This means that the output could be delivered to anywhere on the optical table and moved very easily. Fibre coupling the diode sources also allowed them all to be set-up and operated on a separate optical table away from the main MOPA sys-

tem thereby isolating them from disturbances and making more space available for the MOPA set-up and peripheral experiments.

There were a number of hazards associated with these high power diode sources as well as the high power solid-state laser sources which they were used to pump. A number of experimental methods and safety precautions were adopted when working with these lasers at high power levels. A summary of these is described in Appendix B.

5.3.2 Double-Rod Geometry

Each amplifier stage employed the same basic design, comprising two 10mm long 0.1% doped Nd:YVO_4 crystals, each end-pumped by a single fibre-coupled pump and mounted in a water-cooled heat-sink, as described in Section 5.2.1. This amplifier scheme, employing low Nd^{3+} doping concentration and the use of multiple crystals, facilitates power scaling by spreading the heat loading over a long total crystal length. This, in turn, leads to a reduction in the thermal lens aberrations, lower loss due to ETU and reduces the likelihood of thermal fracture in the crystals. Furthermore, using two crystals instead of one long crystal, and relay imaging from one to the other, allows the use of smaller pump spot-sizes and therefore higher gain can be achieved. The amplifier was set up using a relay-imaged double rod configuration, as shown in Figure 5.8.

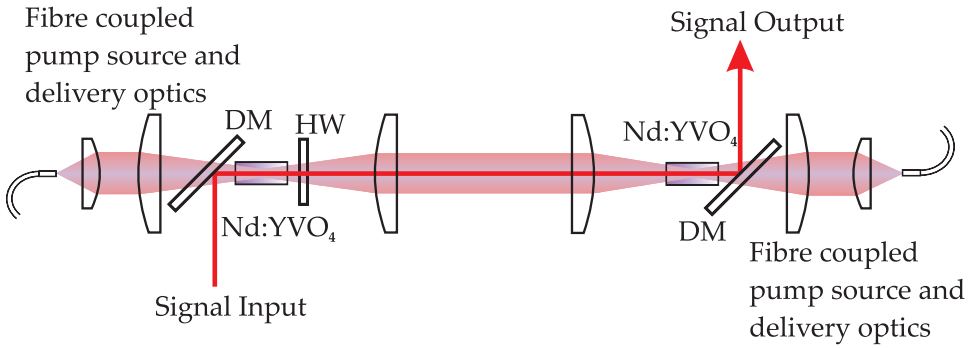

Figure 5.8: Relay-imaged double-rod double-end-pumped amplifier configuration. HW: Half-wave plate, DM: Dichroic mirror.

Two 50mm focal length lenses, separated by 100mm, were positioned in between the crystals with 50mm between each lens and the centre of the crystals.

This configuration, where the lenses are separated by the sum of their focal lengths and their focal points are at the centers of the crystals, satisfies the condition for relay-imaging of both pump and signal beams from one crystal to the next and indeed from one amplifier stage to the next. The two crystals were arranged end-to-end so that the unabsorbed pump radiation from each one was absorbed in the other. This increased the overall absorption efficiency and also created a more uniform distribution of absorbed pump power over the length of each crystal.

The two crystals were orientated with their c-axes orthogonal for two reasons. The first was to maximise absorbed pump power by taking advantage of the polarisation dependent absorption in Nd:YVO_4 . Since the pump absorption coefficient is much higher for π polarised pump light (see Table 2.4), the first rod acts as a partial polariser for the unpolarised pump radiation. By orientating the second rod with an orthogonal c-axis to the first, the absorption is maximised for the partially polarised pump from the first rod. The second reason for this crystal orientation is that it compensates for the astigmatic thermal lens generated due to the anisotropic thermal properties of Nd:YVO_4 , in particular, the thermal expansion coefficient which is more than twice as high in the c-direction ($11\times10^{-}6\mathrm{K}^{-1}$), than in the a-direction ($4.4\times10^{-}6\mathrm{K}^{-1}$). Combining two equally astigmatic lenses at 90° to one another, in this relay-imaging scheme, results in a non-stigmatic compound lens. To ensure that the signal polarisation direction always matched the high emission cross-section direction, a multi-order waveplate was placed between the two crystals. This acted as a half-waveplate for the signal at 1064nm and a full waveplate for the pump at 808nm, the pump beam therefore emerged with no change in polarisation and the signal beam with 90° polarisation rotation.

5.3.3 Optimising Signal-Pump Overlap

In the first amplifier stage, the pump beam spot size was chosen based on confocal focussing of the beam through the crystals to achieve approximately constant pump size over the crystal length. For the 400µm core diameter, 0.22 NA fibre used for pump delivery in the first amplifier, the corresponding pump beam M^2 value was ∼170. This implied a pump waist radius of 330µm for

confocal focusing of the pump through a 10mm long Nd:YVO_4 crystal. To determine the optimum size of the signal beam in the amplifier crystals and also to test the validity of the numerical model, described in Chapter 4, an experiment was conducted to vary the signal size while keeping the pump size constant. The experimental layout is shown in Figure 5.9. The output from the oscillator, while operating in cw mode with the mode-locker switched off, was first passed through an isolator to eliminate feedback from the amplifier. The beam was then passed through a lens, which produced a slowly converging beam which slowly reduced in size, so that the amplifier position could be adjusted to give access to a range of signal spot sizes. This gave beam radii in the crystals in the range 1000-200µm over a distance change of 15cm. This implied that the beam remained approximately constant over the crystal length to within ±25µm and the relay imaging ensured that both crystals had the same signal and pump beam sizes.

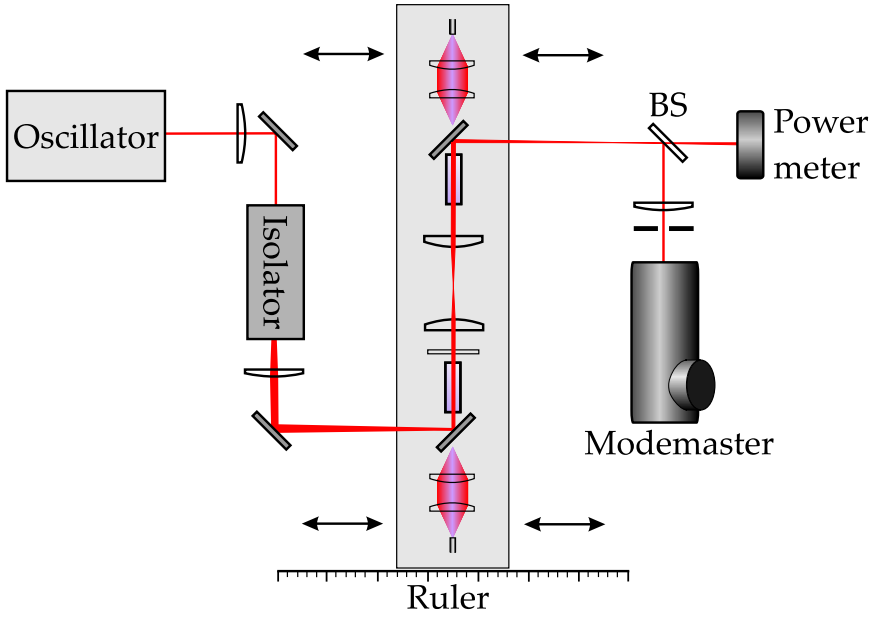

Figure 5.9: Experimental layout used to determine the influence of signal-pump overlap on power and beam quality of the amplifier output. BS: 1% reflectivity beam splitter

The amplifier was pumped from both ends by the two 30W fibre coupled diode bars giving a total incident pump power of ~60W. The output from the amplifier was passed through a beam-splitter so that a small fraction of the power could be analysed using a Coherent Modemaster to measure the M^2 value of

the beam. The remaining power was simultaneously measured using a Gentec thermal power meter. The resulting power gain, as a function of signal-pump ratio, is shown in Figure 5.10. The graph also includes the predicted gain from the numerical model, in Section 4.2.5, where the saturation fluence and input fluence is replaced by the saturation intensity and input intensity in equation (4.43). The measured total input power was 4.66W and the input beam had an M^2 value of 1.08. The total small signal gain used in the models was determined experimentally to be 18 (12.6dB) when the overlap ratio was 1.

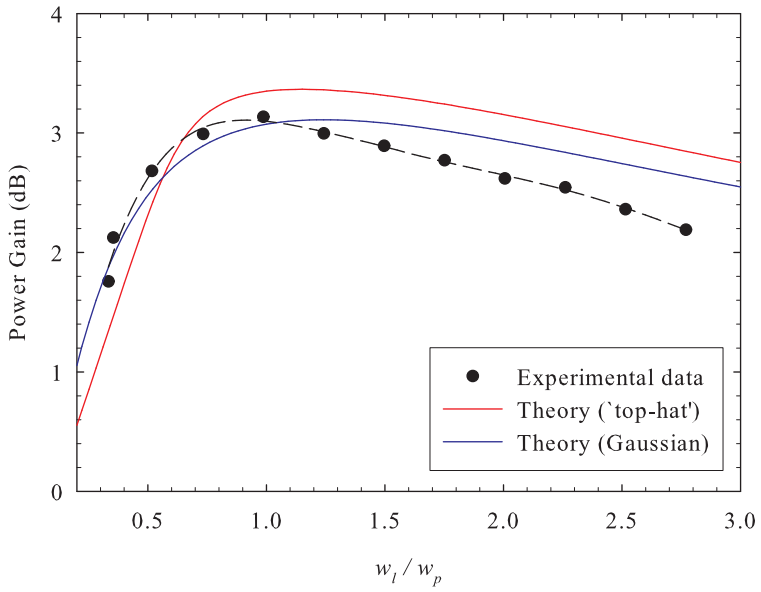

Figure 5.10: Power gain as a function of signal-pump overlap compared to theory.

Good agreement between the models and the experimental results can be seen and in this regime there is little difference between the 'top-hat' and Gaussian pump beam approximations. There is a slight increase in the rate at which the power gain reduces at larger values of w_l/w_p, which it is thought, could be due to losses caused by the thermal lens aberrations which are particularly severe in the wings of the pump distribution. The M^2 value of the output beam, averaged over the two orthogonal directions, as a function of the signal-pump overlap is shown in figure 5.11.

In this case there is a large discrepancy between theory and experiment. The measured M^2 parameter is at a minimum when the overlap ratio is approximately equal to 1 and rises slowly on either side of this minimum approaching

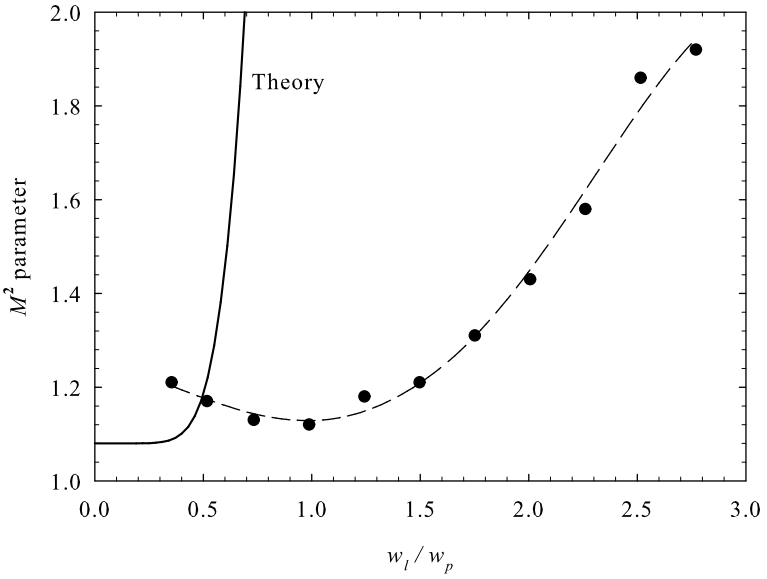

Figure 5.11: Output M^2 parameter as a function of signal-pump overlap for an $M^2 = 1.08$ input beam.

2 for $w_l/w_p = 3$. The theory from Section 4.3, using a truncated Gaussian approximation for the pump beam profile, predicts no increase in M^2 for low values of $w_l/w_p < 0.3$ but a very sharp increase when the overlap ratio is increased further. For w_l/w_p approaching and greater than 1 the predicted M^2 value is much higher than the measured value which was also observed by Clarkson [14]. In this regime, the degradation in beam quality caused by thermal lensing is clearly much less than that predicted by the theory because the quartic phase aberration approximation is no longer valid and higher order terms become dominant. Additionally the truncated Gaussian pump beam profile used to predict the thermal aberration deviates, somewhat, from the actual pump beam profile, limiting the accuracy of the model. Another feature of the experimental results which is not predicted by this theory is an increase in M^2 as w_l/w_p is reduced below 1. This is not thought to be a result of the aberrated thermal lens since this becomes less aberrated as w_l/w_p is reduced, but is instead an effect caused by re-shaping of the signal profile, due to transversely varying gain, which leads to a less Gaussian amplitude profile and therefore a reduction in beam quality. For low values of w_l/w_p, the gain is higher in the wings of the signal distribution than in the centre because the central portion of the signal causes greater gain saturation and yet the gain in the wings remains high. This could lead to flattening of the output signal profile and therefore

a reduced beam quality is likely. This effect was not fully investigated and a significant change in signal profile was not confirmed. However, the effect of the radial gain profile on the beam quality degradation is discussed further in Section 5.5.

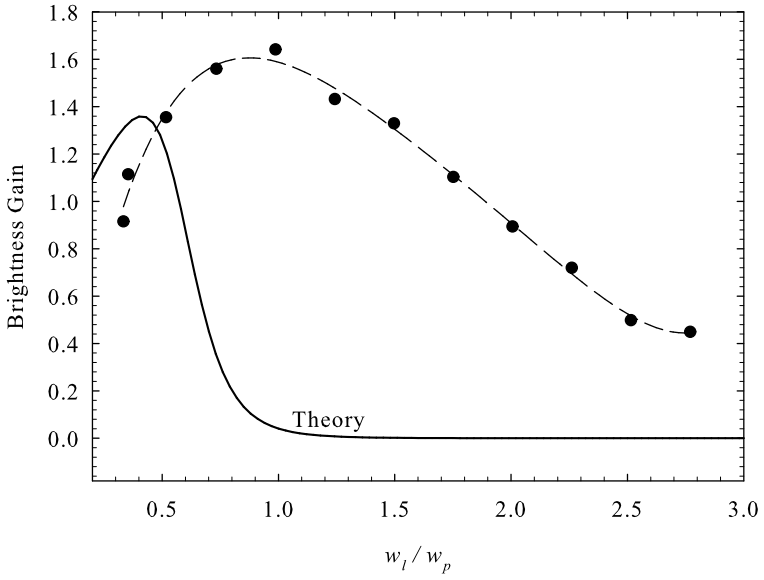

Figure 5.12: Brightness gain ($G/M_x^2 M_y^2$) as a function of signal pump overlap.

The brightness gain, calculated from equation (4.66) as a function of signal-pump overlap, is shown in Figure 5.12. As expected from the limitations of the quartic phase aberration theory, the experimental results are quite different from the theory from Section 4.4. The graph shows an optimum experimental overlap ratio $\sim$1 which falls off more steeply at higher w_l/w_p values than the power gain in Figure 5.10. This indicates that the overlap ratio is more critical for achieving high brightness gain than simply high power gain, as expected.

5.3.4 Three Stage Amplifier

Three amplifier stages, based on the same basic double rod geometry as described in Section 5.3.2, were employed with each stage pumped by two of the fibre-coupled diode sources. The 1st stage used the two fibre-coupled 30W diode-bars from LIMO GmbH., and the 2nd and 3rd stages used the four fibres from the diode stack arrangement, described in Section 5.3.1.1, each de-

livering approximately 60W. The experimental layout of the MOPA system is shown in Figure 5.13. The output from the oscillator was first passed through an acousto-optic modulator (AOM), which is described later in this chapter, as a means to operate the amplifier in pulsed mode. The signal beam was then passed through a Faraday isolator and focused to the desired beam size in the first amplifier. Relay imaging optics within each amplifier and between each amplifier ensured a fixed relationship between signal and pump beam sizes in each amplifier crystal. Additional isolators were used in some of the experiments in between each amplifier stage to eliminate parasitic lasing.

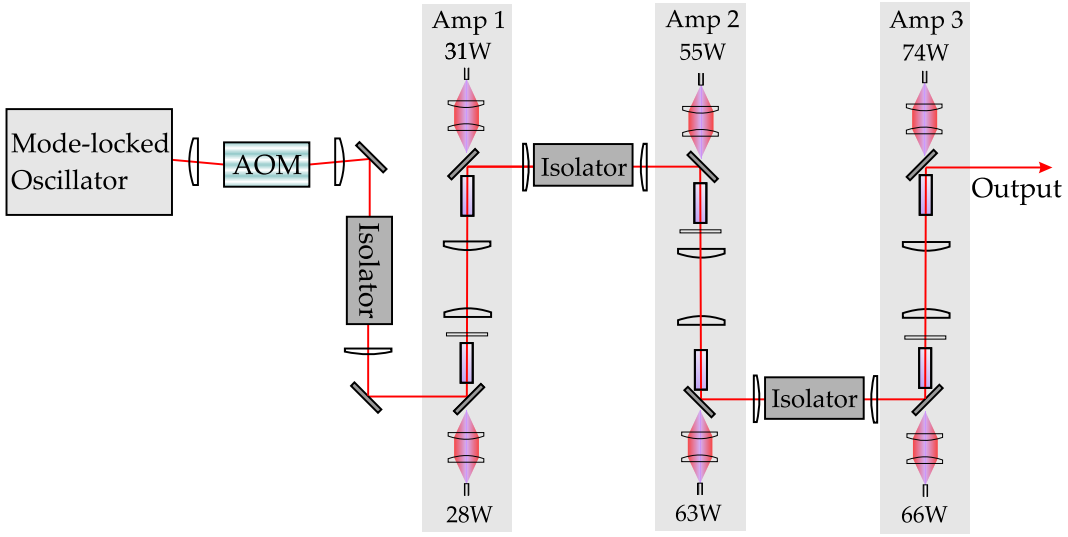

Figure 5.13: Schematic of MOPA set-up showing pump powers at each amplifier stage.

Due to differences in pump delivery fibre diameter, pump power and input signal power for each amplifier stage, it was necessary to use different amplifier parameters for each stage. The larger fibre core diameters of 600µm in the second and third amplifiers, compared to 400µm in the first, meant that a larger pump beam radius in the crystals was necessary in the second and third amplifiers and consequently a proportionately larger signal beam radius was required. These larger pump beam sizes also helped to reduce thermal effects such as thermal lens strength and the likelihood of thermal fracture, which become more important at higher power levels. In addition, according to the theory in Chapter 4, the ratio of signal beam to pump beam size should be reduced for higher pump powers for optimum brightness scaling. Another consideration was that the maximum overall output power should be achieved

when the pump sources are ordered with increasing power along the amplifier chain. This is because the higher the signal intensity, the higher the extraction efficiency. By putting the highest power pump source at the end of the chain, where the signal power is highest, the amplifier stage with the highest extraction efficiency is combined with the stage with the highest power. For this reason the lower power 30W diode bars were used in the first amplifier stage and the four-fibre coupled stack was used in the second and third stages. The different output powers of each of the four fibres, shown in Table 5.2, were also taken into account and they were therefore arranged so that the two lowest power fibres (A and D) were used in the second amplifier and the highest power fibres (B and C) were used in the third stage. This implied that an additional pump power of $\sim$20W was input to the third amplifier stage compared to the second. Confocal focusing of the pump beams through the crystals in the first amplifier implied an approximate pump beam radius of 330µm in each rod, as in Section 5.3.3 which was achieved experimentally using 20mm graded index collimating lenses and 30mm graded index focusing lenses for each fibre output. In the second and third amplifiers the confocal focused beam radius corresponding to the estimated M^2 value of 257 was 406µm . This beam size was increased somewhat in the experiment to $\sim$500µm in the second amplifier and $\sim$550µm in the third amplifier, to reduce the thermally induced stress in the crystal and hence avoid associated thermal fracture. The small increase in size in the third amplifier, compared to the second, was chosen to account for the slightly higher pump power, to further reduce the thermal stress and also to help reduce the signal-pump overlap ratio a little whilst allowing 1:1 relay imaging of the signal beam between the second and third stages. The available graded index lenses were combined as best as possible to achieve the desired pump beam sizes. The second amplifier used lenses of focal lengths 15mm for collimating and 25mm for focusing to achieve the desired 500µm spot sizes and the third amplifier used a similar lens combination of 20mm and 40mm to achieve the 550µm spot sizes. In order to relay image the signal beam from the first to the second amplifier, an appropriate magnification factor of 1.5 was introduced using 100mm and 150mm focal length lenses respectively at a separation of 250mm and with relay imaging planes centred on the amplifier crystals. Similarly the 1:1 imaging from the second to the third

amplifier was achieved using two 150mm lens at 300mm separation. Using a Gaussian beam optics program, written using Matlab, the signal beam radius was modelled as it propagates through the amplifier chain. The program was used to simulate the effect of thermal lenses in the positions of the crystals. By varying the thermal lens focal lengths the effect on the divergence of the output beam could be seen. Figure 5.14 shows the simulated laser beam size through the amplifier chain for various thermal lens focal lengths in the crystals. As can be seen, changing the thermal lens focal lengths affects the spot

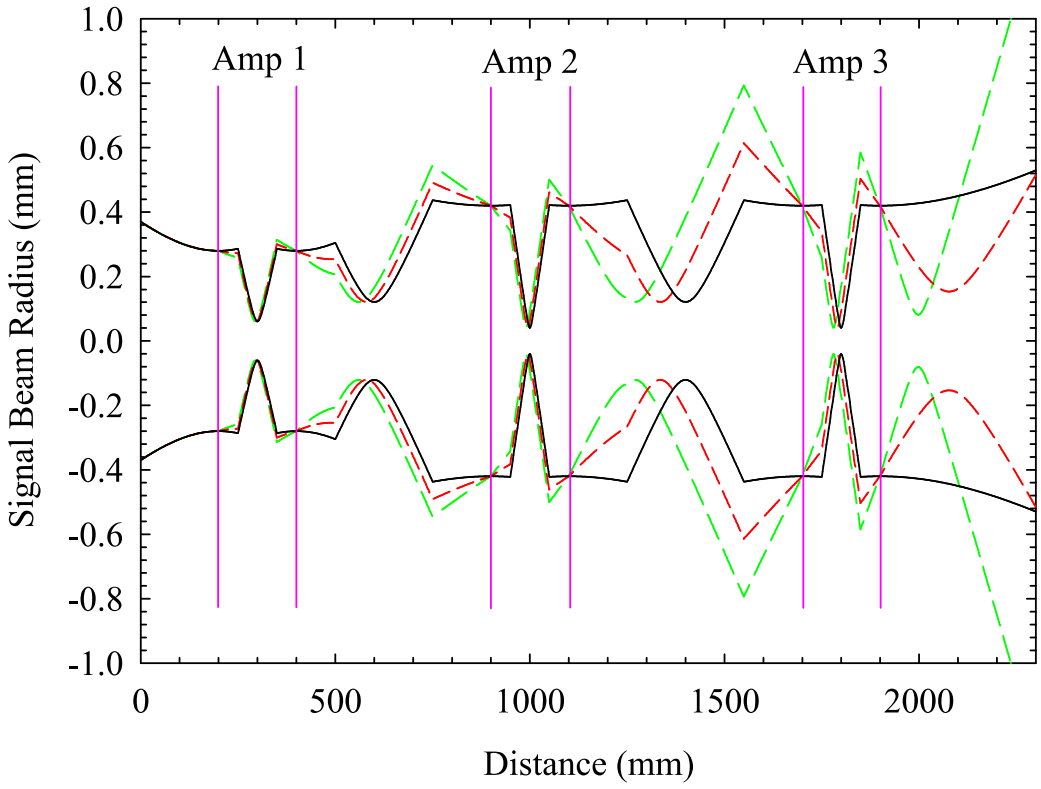

Figure 5.14: Simulated signal beam size through the amplifier chain. The solid black line is for no thermal lensing; the red line is for a thermal lens focal length of 1m in each crystal and the green line is for thermal lens focal length of 500mm in each crystal. The pink lines indicate the positions of the 6 Nd:YVO_4 crystals.

sizes and beam divergence angles outside the laser crystals but the spot sizes in the relay-imaged planes inside the crystals remain the same. However, it is clear that even relatively long thermal lens focal lengths produce high beam divergence angles out of the amplifier.

5.4 Continuous Wave Operation of Amplifier Chain

In the initial amplifier experiments, the mode-locker was switched off so that the oscillator operated in cw mode. Additionally the AOM was driven with a continuous signal to provide cw output with no modulation. It was also found that the isolators between the first and second and between the third and fourth amplifier stages were not required in cw mode, since the reduction in gain caused by the saturating signal beam was sufficient to remove parasitic lasing and any significant ASE. A photo of the amplifier chain, without the isolators, is shown in Figure 5.15.

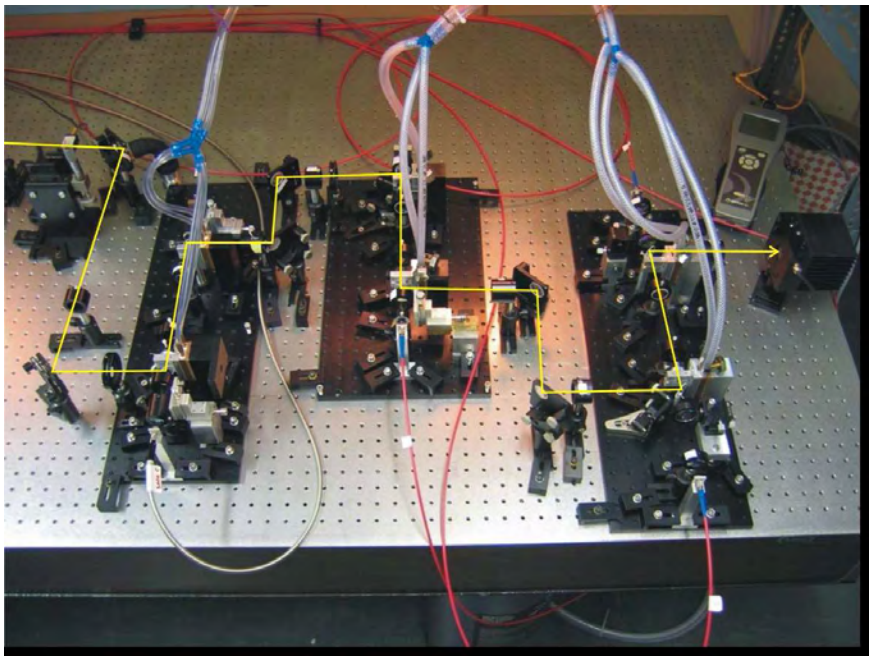

Figure 5.15: Photo of the three amplifier stages with yellow line showing the beam path.

The signal beam sizes in the second and third amplifiers were the same, due to the 1:1 imaging, and were related to the beam size in the first amplifier by a magnification factor of 1.5. This meant that using the measured values of the pump beam radii of ∼311µm , ∼510µm and ∼560µm in the three amplifiers respectively, the overlap ratios of signal beam size to pump beam size were reduced by a factor of approximately 0.9 between the first and second stage and again between the second and third stages. By using a signal beam radius of 300µm , which corresponded to $w_l/w_p \approx 1$, offering the highest brightness

in the first amplifier from Figure 5.12, the corresponding overlap ratios in the three amplifier stages were 0.96, 0.88 and 0.80 respectively. The system was aligned by monitoring the output power and the output beam profile simultaneously to achieve maximum power while keeping the beam profile symmetrical and circular. Misalignment was indicated by a drop in power or by a beam profile skewed to one side due to non-concentric positioning of the signal beam relative to the pump beam.

The fraction of incident pump power absorbed, was measured for one of the crystals to be 82% for 58.8W of pump power. By combining this with a measured transmission of 89% through the two lenses and the dichroic mirror between the fibre output and the crystal, this implied a total fraction of fibre output power absorbed in the first crystal of 72%. Assuming that each crystal had the same absorption efficiency and each pump beam passed through two crystals in series, the total fraction of pump power available from the fibre, which was absorbed, was 86%.

Notably, for the highest power pump fibre in the third amplifier stage, thermal fracture of one of the crystals occurred when the signal path was blocked. The conditions under which this occurred were believed to be at an incident pump power of $\sim$66W with intensity $\sim$67Wmm^{-2} in a 560μm beam radius and an absorbed power (including pump power incident of both ends) of 63W. While there are a number of factors which may reduce the thermal fracture limit, such as the presence of dust on the pump input face of the crystal, poor heat sinking or defects in the crystal, these conditions were considered to be approaching the fracture limit and the the pump power was therefore reduced by a small amount after the crystal was replaced.

Due to the large number of components, the transmission losses for the signal beam were quite significant. Each amplifier stage is composed of 7 optical components which constitutes 10 AR coated surfaces and two HR reflections from the input and output mirrors. Including the additional two lenses between the amplifier stages (but not the isolators) this implies a total number of surfaces of 16 for each amplifier stage and therefore 48 for the entire amplifier chain. The measured loss for the signal beam was $\sim$10% through each amplifier and $\sim$27% for the whole amplifier chain. Hence, an average loss per surface of

around 0.6% can be estimated, which is reasonably consistent with values for typical AR or HR coatings. When the isolators are included between each amplifier stage an additional loss of ∼10% per isolator is added which brings the total loss through the amplifier chain to nearly 40%. This high loss represents one of the limiting factors on the power achievable from this kind of amplifier system, since it ultimately limits the number of amplifier stages that can be added before the loss exceeds the gain. In the case of this amplifier system however, the operating parameters are such that the gain still far exceeds the loss in all the amplifier stages.

Initial experiments, which did not include the AOM and the isolator between the oscillator and the first amplifier stage, nor any isolators in between amplifier stages, yielded a maximum output power of 94W for an input power of 5.5W and a total absorbed pump power of 237W. This corresponds to an extraction efficiency, with respect to absorbed pump power, of 37% and, with respect to incident pump power, of 32%. The output powers from the first, second and third amplifier stages, as a function of total absorbed pump power, is shown in Figure 5.16.

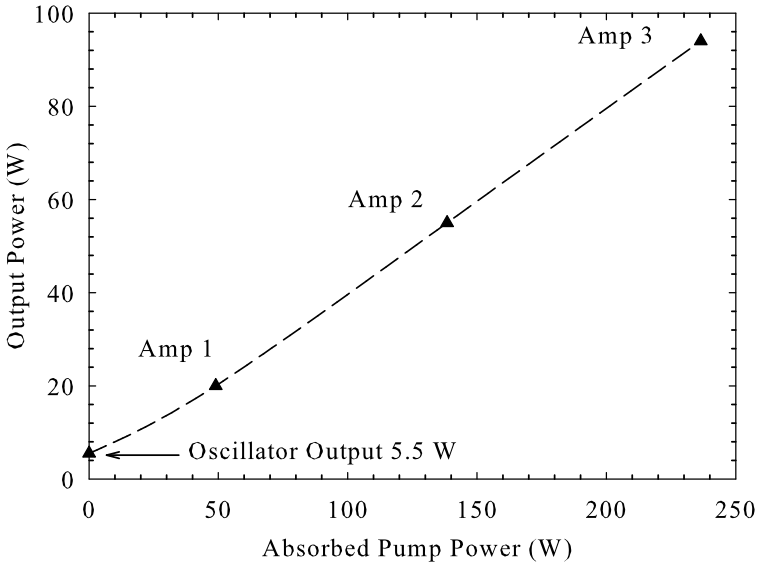

Figure 5.16: Output power versus absorbed pump power for the three amplifier stages with no isolators in the system.

In subsequent experiments the AOM and isolator were included and the oscillator output was ∼4.0W. The input signal power was therefore reduced to

2.68W. The output power, as a function of absorbed pump power, is shown in Figure 5.17. In this case the extraction efficiency, with respect to absorbed pump power, was 34% and with respect to incident pump power was 29% and the power gain was 29 (14.7dB) to give 79W of output power. Figures 5.16 and

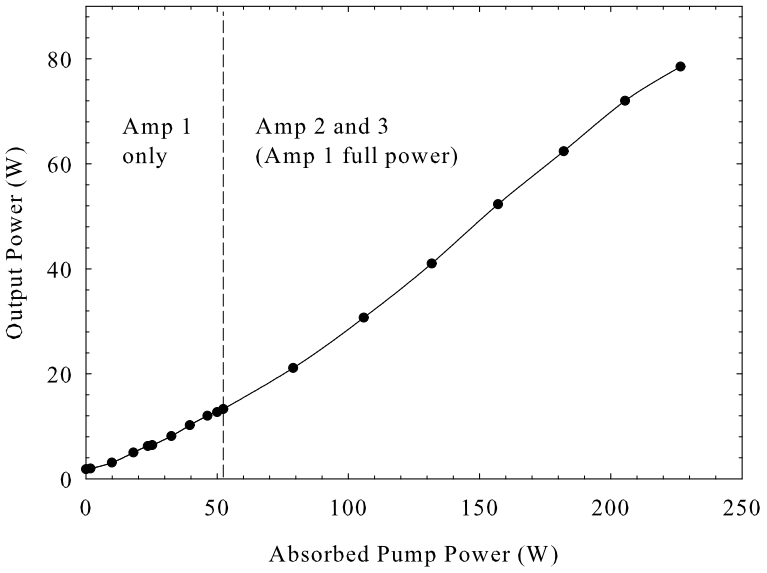

Figure 5.17: Output power versus absorbed pump power for the three stage amplifier chain.

5.17 show the high power levels that can be achieved in this system. There is a small reduction in the slope in Figure 5.17 at the highest power level suggesting that the power is approaching a limiting value.

The significant reduction in output power and extraction efficiency, caused by reducing the input power, is a result of the level of gain saturation which depends on I_{in}/I_{sat}. This increase in extraction efficiency with increasing input power is apparent in Figure 5.18 which shows the output power as a function of input power under maximum pump power conditions. In this case the isolators were included between each amplifier stage because parasitic lasing became a problem for very low signal powers. The input signal power was varied by rotating the half waveplate between the oscillator and the first isolator, as well as by reducing the drive voltage to the AOM, to achieve sufficient attenuation of the oscillator output. The oscillator itself was running at maximum output power because reducing the pump power led to a change in the signal beam size in the amplifier.

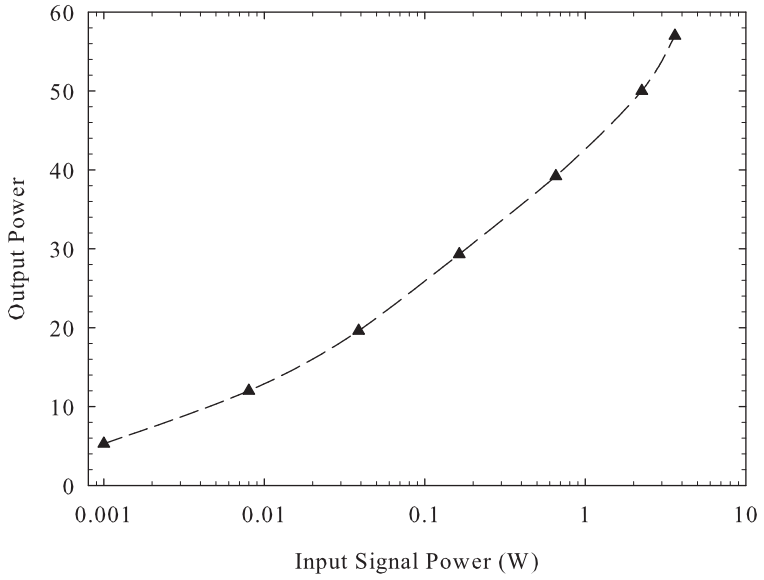

Figure 5.18: Input power versus output power for the amplifier chain.

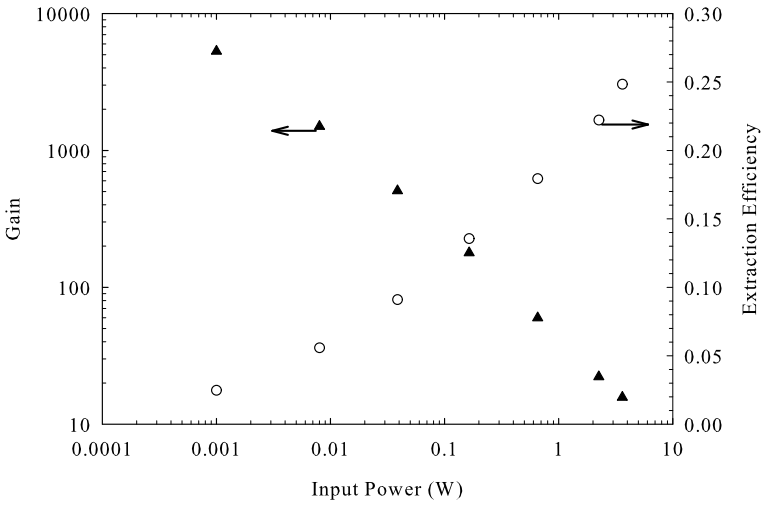

Figure 5.19: Gain and extraction efficiency as a function of input signal power.

The data in Figure 5.18 corresponds to a gain and extraction efficiency shown in Figure 5.19, which resembles the theoretical gain and extraction efficiency shown in Figure 4.4. Further reduction in input signal power made it difficult to distinguish between amplified signal and ASE but the graph indicates a small signal gain approaching 10,000 (40dB). The maximum small signal gain was later measured to be ∼7000 while operating in pulsed mode. The measured small signal gain was many orders of magnitude less than the predicted values from the analytical expressions in Sections 4.2.1.2 and 4.2.2. The reason for this was that the exponential nature of the small signal gain means that, for high pump intensities, its value becomes highly sensitive to loss mechanisms such as ETU, ASE, misalignment or mismatch of signal and pump beams as well as parasitic lasing if it is not suppressed. Additionally, variations in material properties of the gain medium, such as σ_{21}, τ_f and α_p, from the estimated values can lead to large discrepancies between theoretical and experimental small signal gains. The most significant effect limiting the measured small signal gain in this amplifier system is ASE which sets a limit on the maximum small signal gain achievable. Without using isolators between the amplifier stages, the output power from the amplifier with the master-oscillator switched off was measured to be ∼13W in the forward direction and ∼4W in the reverse direction. This represented significant saturation of the amplifier of which the main contribution was parasitic lasing. By inserting the isolators between each stage is was possible to eliminate parasitic lasing and produce an output which was almost all in the forward direction and had an output power ∼2W. This was identified as ASE rather than parasitic lasing due to the absence of a threshold pump power, which was clearly observed when parasitic lasing occurred. While this ASE power was relatively low, it was still enough to cause significant saturation of the amplifier and therefore reduce the small signal gain by a large amount.

Nevertheless, to estimate the impact of ETU on the small signal gain and thermal lens focal lengths of each crystal in the amplifier chain, Table 5.3 was produced. This shows the pump intensity times the absorption efficiency and the predicted small signal gain coefficients, assuming a Gaussian pump beam profile both with and without ETU. The ratio $g_0/g_{0,ETU}$ indicates the factor by which the small signal gain coefficient is likely to be reduced by the effect of

ETU. This is shown to be less than 10% for each crystal. The fraction of pump power converted to heat due to ETU, given by $\gamma_{ETU} - \gamma$, is also shown to be ∼10% for each crystal. These low values are a result of the carefully controlled pump beam sizes and low Nd^{3+} doping concentration. The table also shows

Amplifier crystal	$I_p\eta_{abs}$ (Wmm^{-2})	$g_0 l$	$g_{0,ETU} l$	$g_0/g_{0,ETU}$	$\gamma_{ETU} - \gamma$	f_{th} (mm)	$f_{th,ETU}$ (mm)
1	79.2	9.66	8.78	0.91	0.11	185	126
2	87.7	10.7	9.66	0.90	0.12	167	111
3	57.9	7.66	7.13	0.93	0.09	253	184
4	66.3	8.77	8.09	0.92	0.10	221	156
5	57.6	8.24	7.67	0.93	0.09	255	185
6	64.6	9.23	8.54	0.92	0.10	227	162

Table 5.3: Predictions from theory of gain, impact of ETU and thermal lens focal lengths for each amplifier crystal

the thermal lens focal lengths, predicted using a 'top-hat' approximation for the pump beam profile. These have an average of ∼220mm without ETU and ∼150 with ETU. Using these values this implies an effective thermal length for the whole amplifier chain of ∼35mm without ETU and ∼24mm with ETU. This is approaching the limit where the signal beam size varies significantly over the length of the crystal suggesting that this could present a problem if further amplifier stages were added. It is also approaching the regime where the thin lens approximation breaks down so further analysis may require a thick, graded index, lens approach. The predicted thermal lens strength for the 1st amplifier stage was also shown to give reasonably good agreement with measured values. To estimate this, the divergence of the signal beam from the first amplifier stage was estimated by relay imaging the output using two 100mm focal length lenses. The beam radius, w, and divergence angle ($w' = \mathrm{d}w/\mathrm{d}z$), both with zero ($w_0'$) and with maximum ($w_1'$) pump power to the amplifier, was measured by translating a beam profiler across the relay imaging plane. Using the simple relation, derived from ray matrices,

$$f_{th} = \frac{w}{w_0' - w_1'}, \tag{5.19}$$

the effective thermal lens focal length was estimated to be 260mm for single end-pumping and 122mm for double end-pumping. This implies that, under double end-pumping conditions, the thermal lens focal lengths for the first and

second crystals in the first amplifier were approximately 260mm and 230mm respectively. These values are approximately 1.4 times the predicted values from Table 5.3. Assuming this ratio is approximately the same for each amplifier stage, the effective thermal lens focal length for the whole amplifier chain was estimated to be ∼50mm. However, this was not verified experimentally.

The beam quality M^2 factors in the orthogonal planes were also measured as a function of incident pump power, using a Dataray Inc. Beamscope profiler which could determine the second-moment beam width as a function of distance in the region of a beam waist created by a focusing lens. The results are shown in Figure 5.20. This shows an approximately linear relationship between pump power and output beam quality as predicted by the theory in Section 4.3.

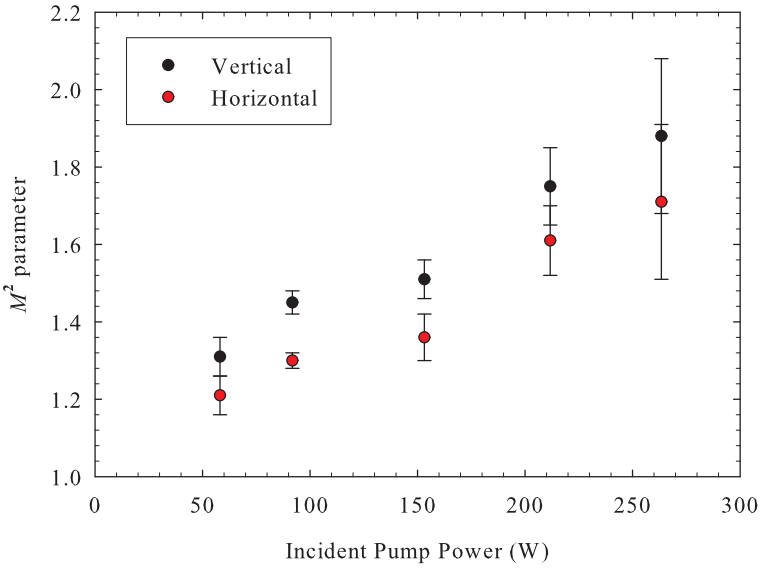

Figure 5.20: Beam quality M^2 factor versus incident pump power.

The phase aberrations caused by thermal lensing caused this degradation in beam quality to reach $M^2 = 1.8$ at the maximum output power. This implies an overall brightness gain G_B of ∼9 for the amplifier. Another effect of these phase aberrations is to change the beam profile of the output, such that focusing the output beam to a waist produces an interference pattern, as shown in Figure 5.21. This plot shows the normalised intensity distribution as the beam passes through the focal region measured with a Dataray Inc. Beamscope. The profile is approximately Gaussian until it reaches the focal plane where side

lobes appear. These side lobes increase in intensity until they become larger than the central lobe, to produce a double peak. As the beam propagates further, additional side lobes appear, to produce profiles with two, three and four peaks and so on.

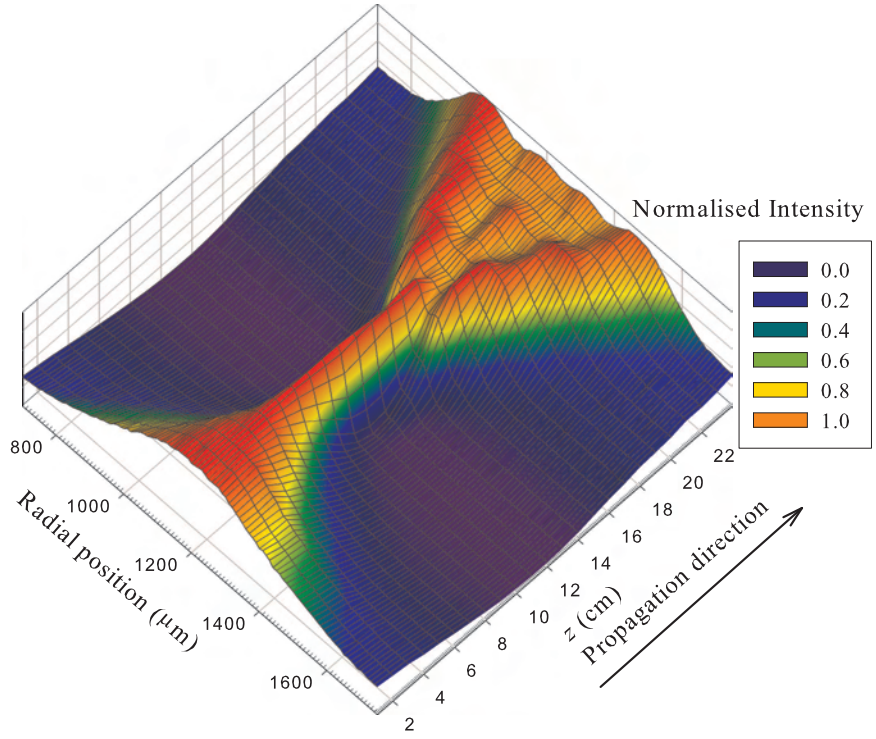

Figure 5.21: Normalised output beam profile as a function of propagation distance in the focal region showing interference pattern caused by thermal lens aberrations.

This interference effect, caused by thermally induced phase aberrations, appears to be consistent with an analysis by Neubert *et al.* [15]. This analysis uses a Wigner distribution function to describe the mutual coherence of a Gaussian beam with a cylindrical-spherical aberration. The resulting numerical results for the intensity distribution, as a function of the propagation distance, show a close resemblance to the measured results in Figure 5.21. This consistency indicates that a spherical approximation for the phase aberration in a thermal lens may be valid in this situation. However a full investigation of this theory has not been carried out.

In addition to measuring the degradation in beam quality with respect to pump power, the beam quality M^2 factor was also measured after each amplifier

stage to show the relative influence of each stage on the beam quality degradation. These results, which are shown in Figure 5.22, show a significant increase in the beam quality degradation caused by successive amplifier stages. Indeed the last amplifier stage accounts for around the same beam quality degradation as the first two stages combined. This relationship is in contrast to the theory in the previous chapter which predicted that the increase in the M^2 parameter diminished with successive amplifier stages, as shown in Figure 4.14.

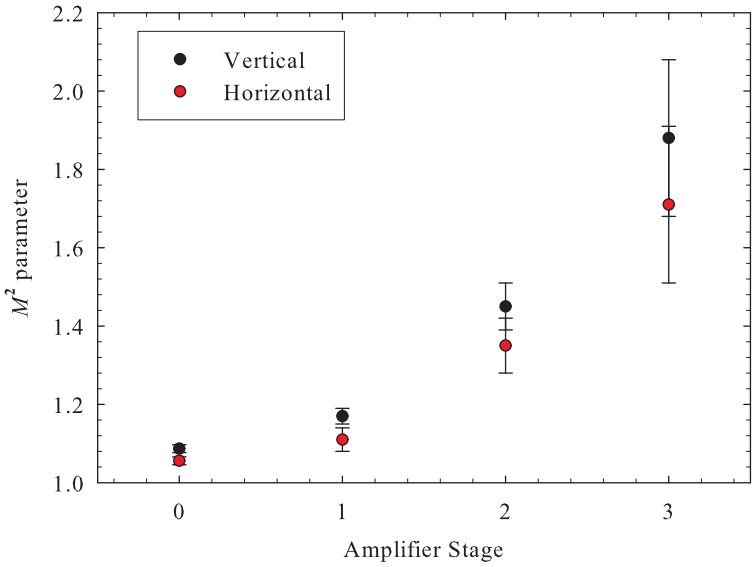

Figure 5.22: Beam quality M^2 factors out of each amplifier stage.

The disparity between the theory and these results was found to be due to an effect, which is discussed in the next section, whereby the gain of the amplifier plays an important part in the influence of its thermal aberrations on the beam quality.

5.5 Influence of Gain-Guiding on Beam Quality

It is well known that the aberrated nature of the thermal lens in the gain medium is largely responsible for degradation in laser beam quality in high power end-pumped laser amplifiers. It has also been discussed that the phase aberrations are most pronounced in the wings of the pump distribution, where the temperature gradients and stresses are highest. In addition, the non-uniform

gain profile, that results from the non-uniform transverse intensity profile for the pump beam and gain saturation, can also play an important role in reshaping the signal beam profile and thereby modifying the beam quality. Gain guiding has previously been demonstrated to provide spatial filtering in end-pumped solid-state laser oscillators, such that large Gaussian modes could be obtained in unstable resonators [16]. Additionally, in side-pumped amplifier configurations with a nearly uniform pump deposition density, it has been reported that gain saturation can play a dominant role in degrading the beam quality [2]. However, to the author's best knowledge, no study has been reported on the effects of gain guiding in end-pumped solid-state amplifiers. In the high gain end-pumped amplifier used in this work, we have found that the gain induced reshaping of the signal beam or gain-guiding effect can partially compensate for the degradation in beam quality caused by thermally-induced phase aberrations. By operating an amplifier in a weakly saturated regime, where the actual gain is higher, we have observed a significant improvement in beam quality compared to the situation where the amplifier is operated in the highly saturated regime, despite the increased thermal loading in the gain medium due to upconversion.

The effect was discovered following the surprising result that the beam quality was found to improve by reducing the input signal power, as shown in Figure 5.23. This was against expectation because the associated lower extraction of stored energy at lower input powers is known to result in higher thermal loading due to ETU which inevitably causes stronger and more aberrated thermal lensing. By considering the gain in Figure 5.19, which reduces as the input power is increased, it can be shown that the M^2 parameter has a strong dependence on the gain in the amplifier such that higher gain results in better beam quality, as shown in Figure 5.24.

To confirm this effect, an end-pumped Nd:YLF probe laser was set up so that the degradation in beam quality could be measured without the effect of gain-guiding since the Nd:YLF lasing wavelength of 1047nm lies outside of the gain bandwidth (0.96nm) for Nd:YVO_4 . The results were compared with the results for a cw beam from a Nd:YVO_4 oscillator which does see the impact of gain-guiding. The Nd:YLF laser beam was measured to have initial M^2 values of 1.01 and 1.03 in the orthogonal planes, whereas the Nd:YVO_4 laser had

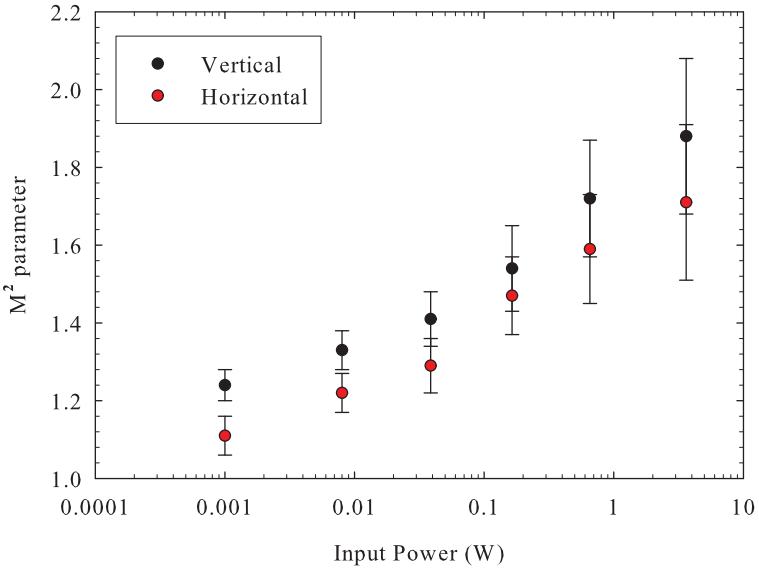

Figure 5.23: Beam quality M^2 parameters as a function of signal input power.

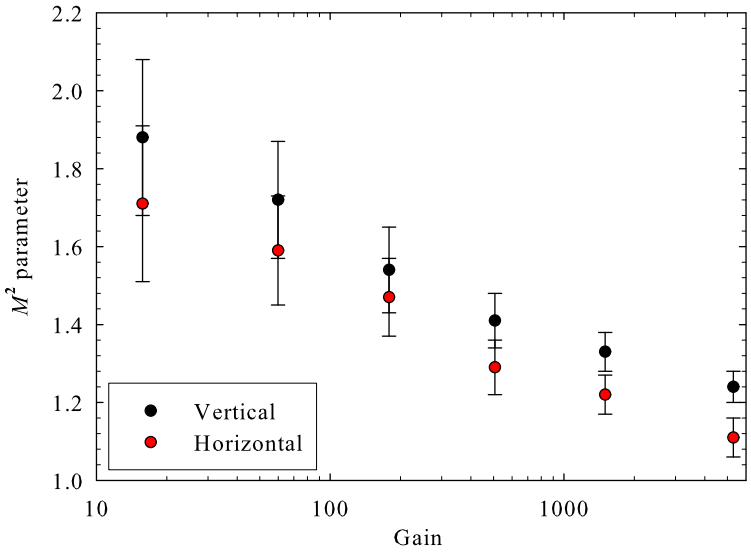

Figure 5.24: Beam quality M^2 parameters as a function of gain measured by adjusting input signal power.

initial M^2 values of 1.04 and 1.02. The input beam radius into the amplifier was matched to the Nd:YVO_4 beam radius so that the probe beam saw the same aberrated thermal lenses but no gain through the amplifier. A polarising beam-splitter and half-waveplate combination was used to align the Nd:YLF laser into the amplifier along exactly the same path as the Nd:YVO_4 signal by matching the output beam positions of the two lasers simultaneously using a Dataray Inc. Beamscope profiler, as shown in Figure 5.25.

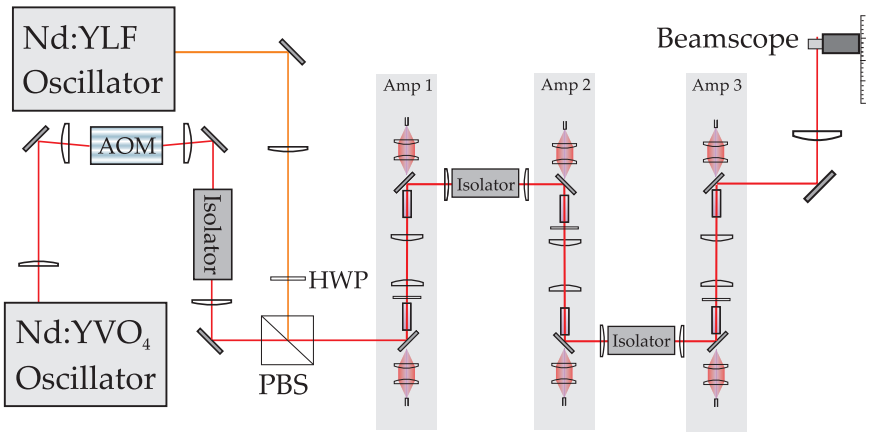

Figure 5.25: Experimental layout used to measure thermal effects without gain with a Nd:YLF probe laser.

The M^2 values were measured, after each amplifier stage, for the two laser sources for a total pump power of ~210W, which was reduced to prevent crystal damage under low saturation conditions. The results, shown in Figure 5.26, demonstrate significantly higher beam quality degradation for the Nd:YLF laser compared to the Nd:YVO_4 laser.

The beam quality of the Nd:YLF output from the amplifier chain was also measured for a range of signal-pump overlap ratios and compared to the results for the Nd:YVO_4 laser. These results are shown in Figure 5.27. This graph clearly demonstrates the much more severe beam quality degradation for the Nd:YLF laser which also increases much more dramatically when the signal size is enlarged compared to the pump size.

The improved beam quality in the high gain regime is attributed to the strong radial dependence of the gain giving relatively low gain in the wings where phase aberrations are more severe, and high gain in central region of the pump

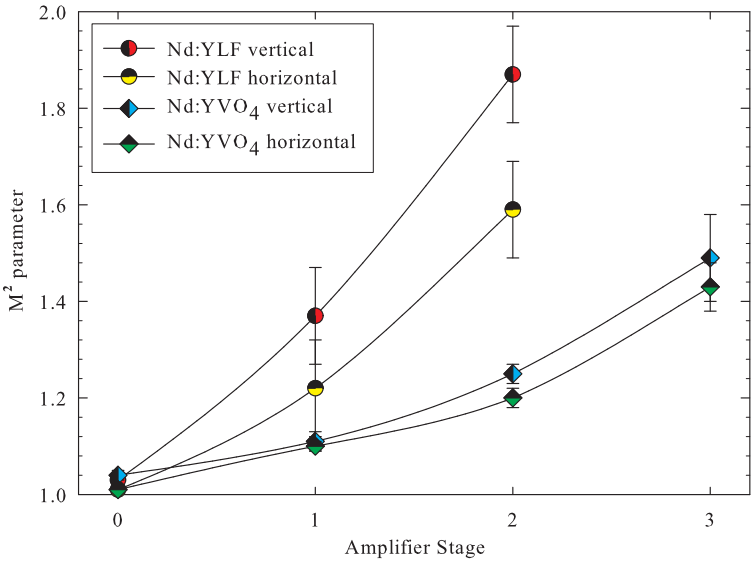

Figure 5.26: Beam quality degradation through amplifier chain for Nd:YVO_4 laser compared to Nd:YLF probe laser.

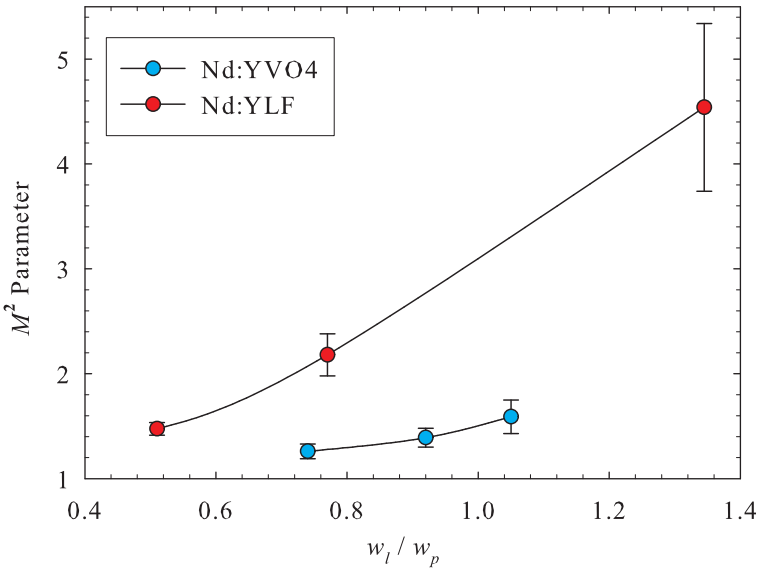

Figure 5.27: Dependence of the beam quality on the signal-pump overlap ratio for Nd:YVO_4 signal for the Nd:YLF probe laser.

distribution where the thermal lens is less aberrated. As the amplifier becomes more saturated, the radial gain gradient decreases and hence thermally-induced phase aberration in the wings becomes more significant. In effect the amplification process re-shapes the beam such that the region with good beam quality, near the centre, becomes amplified much more than the aberrated region in the wings. In the case of the Nd:YLF laser, since there is no gain, the aberrated regions in the wings of the output beam carry the same fraction of power as in the input beam, so that beam quality degradation becomes particularly severe when the signal beam is larger than the pump beam, as shown in Figure 5.27.

In many amplifier systems this gain-guiding effect is of only limited use because high extraction efficiency is a priority, which requires that $I_{in} \gg I_{sat}$ and therefore the amplifier's gain is relatively low. However, this effect is particularly advantageous when operating an amplifier in pulsed mode where the pulse repetition period is comparable to, or longer than, the energy storage time and the amplifier is only weakly saturated. This operating regime is discussed in Section 5.7

5.6 Mode-locked Operation of Amplifier Chain

By operating the master-oscillator in continuous mode-locked mode, it was possible to achieve the same results for average output power and extraction efficiency as in the cw case. The small reduction in input power of the oscillator of $\sim$5% had no significant effect on the output from the amplifier system. Additionally, no significant change in the pulse duration or Gaussian pulse shape was found by measuring the output pulses with a DCA, a trace from which is shown in Figure 5.28.

The vertical scale, in Figure 5.28, was rescaled to give output power by dividing the measured average power of 86W by the duty cycle for the 335ps FWHM, Gaussian pulses with 100MHz repetition rate and multiplying the vertical scale appropriately to give the calculated peak power. This implies peak powers greater than 2.5kW and pulse energies of $\sim$0.9μJ. The negligible change in pulse duration and pulse shape between the input and the output is

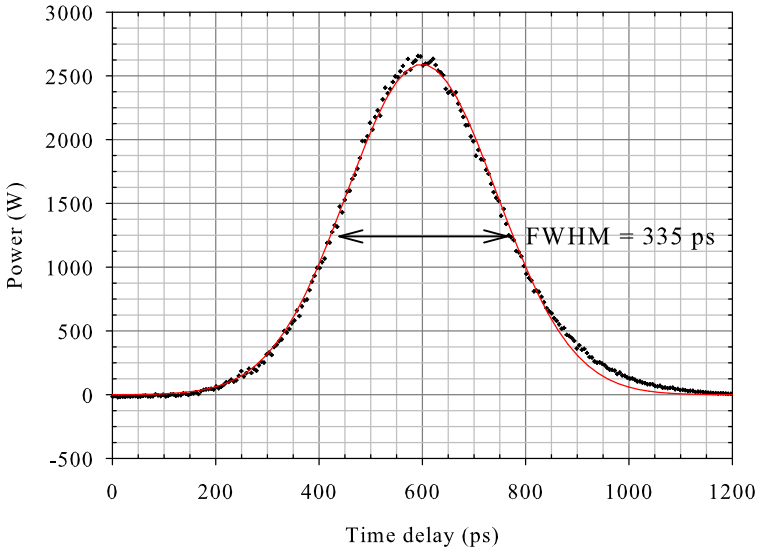

Figure 5.28: Output mode-locked pulse from MOPA systems and Gaussian fit (red).

expected, since the pulses have relatively long pulse widths and a short interaction length in the gain media. Changes in pulse shape and pulse duration through amplifier systems normally only becomes significant for very short pulses (fs) and very long interaction lengths in dispersive media such as in fibre amplifiers for example. The accuracy of the pulse duration measurements and some other measurements made in this work are discussed in Appendix C.

5.7 Gated Mode-locked Amplification

It has been shown that high efficiency amplification of a mode-locked seed, can be achieved using this end-pumped amplifier scheme. This has produced high average power in the tens of watts regime and high peak powers of a few kW. Some applications, however, require a source with higher peak power where average power is less important, for example in high efficiency nonlinear frequency conversion. To generate higher peak powers from the MOPA system, output from the master-oscillator was gated to produce trains of mode-locked pulses with duration from the ns to µs regime, so that the amplifier gain has time in between pulse trains to build up to a level much higher than the steady-

state gain in cw or mode-locked mode of operation. In this way, the high small signal gain of the amplifier can be exploited.

5.7.1 Acousto-Optic Modulation

In between the master-oscillator and the pre-amplifier an additional AOM was used as a pulse-picker (or pulse-train-picker). This used Bragg diffraction of the beam by an acoustic travelling-wave of fixed frequency that is set up in the acousto-optic crystal as shown in figure 5.29.

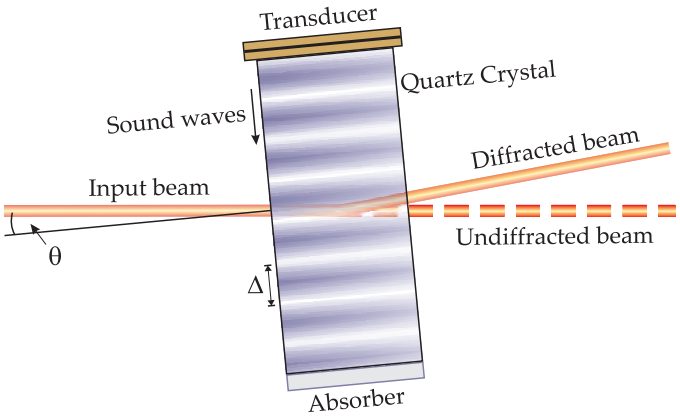

Figure 5.29: Travelling wave acousto-optic modulator.

The beam was approximately 75% diffracted when the crystal was tuned to the Bragg angle θ given by

$$sin\theta = \frac{\lambda}{2\Delta}$$

where Δ is the acoustic wavelength in the crystal [17]. The modulator is driven by an rf generator, up to a maximum rf power of 1W, which produces the travelling acoustic wave and in turn this is switched on and off at much lower repetition rate by a rectangular waveform generator. The resulting diffracted beam, which is selected with an aperture, consists of trains of mode-locked pulses in a pulse envelope with pulse width and repetition rate determined by the waveform generator. The device had a switching time of the order 50ns and the extinction ratio was around 40,000:1 which meant that the background signal power, entering the amplifier during the off-period of the modulator,

was just 35 μW. This small signal leakage represented a potential limiting factor on the small signal gain achievable from the amplifier, however this effect was small compared to amplified spontaneous emission (ASE) in the amplifier which produced an output power of around 2 W at maximum pump power, in the absence of any signal beam. Under saturated conditions however, the ASE power becomes negligible since the saturating signal removes much of the gain.

5.7.2 Peak Power and Average Power Results

In gated pulsed mode, the amplifier performance characteristics became a function of the pulse width and repetition rate that were selected for the waveform generator. A range of operating regimes could be accessed by choosing pulse widths in the range 0.1-50μs and repetition rates in the range 1-100kHz. In general, a reduced repetition rate resulted in a reduce average power but increased peak power. Likewise, increasing the pulse width resulted in reduced peak power but increased average power. In practical terms this means that a trade off between peak power and average power is required for many applications.

5.7.2.1 Varying Pulse Repetition Rate

Initially the oscillator was operated in cw mode with the mode-locker switch off but the results were later found to be effectively the same for mode-locked mode of operation. The peak-power results presented here however, refer to the average power within the pulse envelope and the actual peak power of the individual mode-locked pulses is some ∼30 times greater (30 being the inverse of the duty cycle). The Si photodiode used to measure the pulses had a rise time of ∼30ns so could not resolve the individual mode-locked pulses at 100MHz.

Figure 5.30 shows the output pulse shapes for a fixed rectangular input pulse of pulse width 1μs , for a range of different repetition rates, plotted on a single vertical scale to show the relative peak powers and pulse shapes.

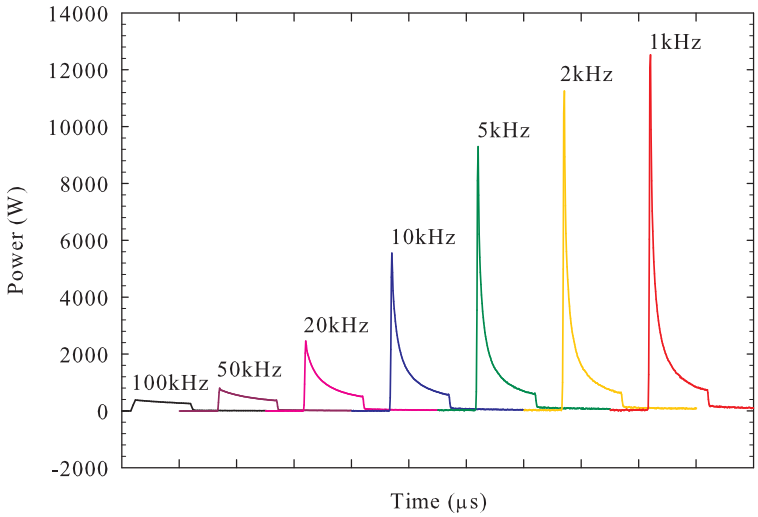

Figure 5.30: Output pulse shapes for 1µs pulse width pulses with a range of repetition rates.

It can be seen from the graph that using lower repetition rates resulted in higher peak powers and also more asymmetric output pulses. This is a result of the higher gain at the time of arrival of the input pulse but also the more rapidly changing gain over the time of the pulse. At very low repetition rates, of $\leq$1kHz, the peak power reached its maximum value and no longer increased which enabled the maximum small signal gain of the amplifier to be measured: The input signal power at the time of maximum peak power output was 1.76W and the output peak power was 12700W which implied a small signal gain of $\sim$7000 (38dB). At high repetition rates the pulse shape became more rectangular, like the input pulse, since this had lower gain and was more similar to the steady-state cw mode of operation. This is in good agreement with predictions from theory in Section 4.2.4. To model the amplifier using this theory, the parameters were simplified so that the amplifier could be described as a single rod with a pump beam of constant radius 500µm , a total absorbed pump power of 215W, a signal-pump overlap ratio of 0.85 and a small signal gain, given by the experimentally measured value, of 7000.

By numerically integrating the area under the pulse profile for each repetition rate and re-scaling the vertical axis so that the pulse energy was equal to the measured pulse energy, given by the average power divided by the the repetition rate, it was possible to show the peak powers of the pulse and therefore produce a plot of peak power and average power versus repetition rate, as

shown in Figure 5.31. At low repetition rates (with output powers $\lesssim 20W$) is was necessary to subtract the ASE power, measured to be about 2W in the absence of a signal beam, from the average power because ASE becomes a significant fraction of the total output power in this regime

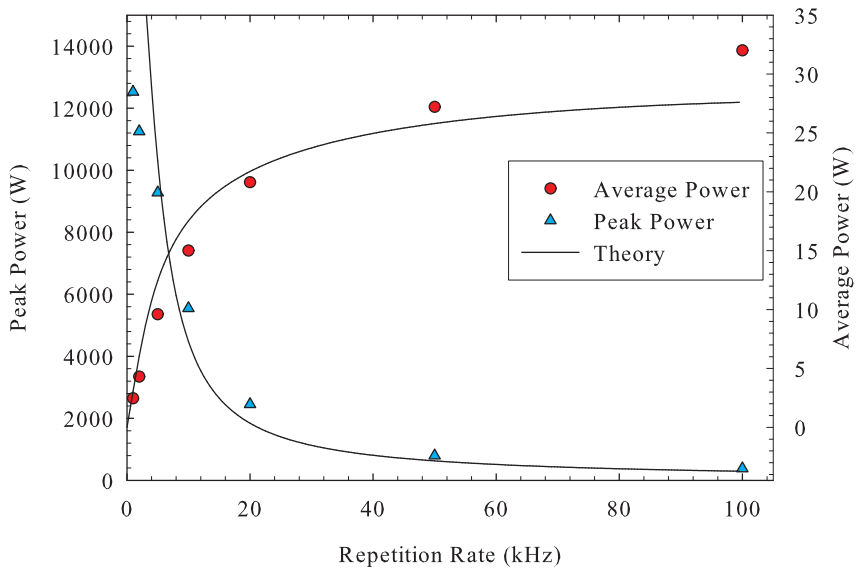

Figure 5.31: Variation of peak power and average power with repetition rate for 1µs pulse width compared to theory (solid line).

Using equations (4.43), (4.47) and (4.47) in the iterative approach, described in Section 4.2.4, the theoretical curves, shown by the solid lines in Figure 5.31, were calculated using the measured small signal gain of 7000 and the experimental results compare very well with the theory. The departure of the average power results from the theory at high repetition rates can be attributed to the pumping during the pulse which is neglected in the theory but becomes significant when the duty cycle becomes large. In general the graph shows clearly the trade-off between average power and peak power and the ability of the amplifier to produce a range of performance characteristics.

By operating the oscillator in mode-locked mode, the above results were found to be apparently the same when a relatively slow 30ns photodiode was used to average the power over a number of mode-locked pulse cycles. The resultant peak powers were therefore a factor of ∼30 higher, as mentioned above. This implies peak powers approaching 400kW in the <1kHz, small signal gain, regime.

5.7.2.2 Varying Pulse Width

A similar approach was used to find the variation in peak power and average power with respect to the pulse width by fixing the repetition rate at 10kHz. The output pulse shapes, for a range of pulse widths, is shown with a constant scale vertical axis and two horizontal axes in Figure 5.32.

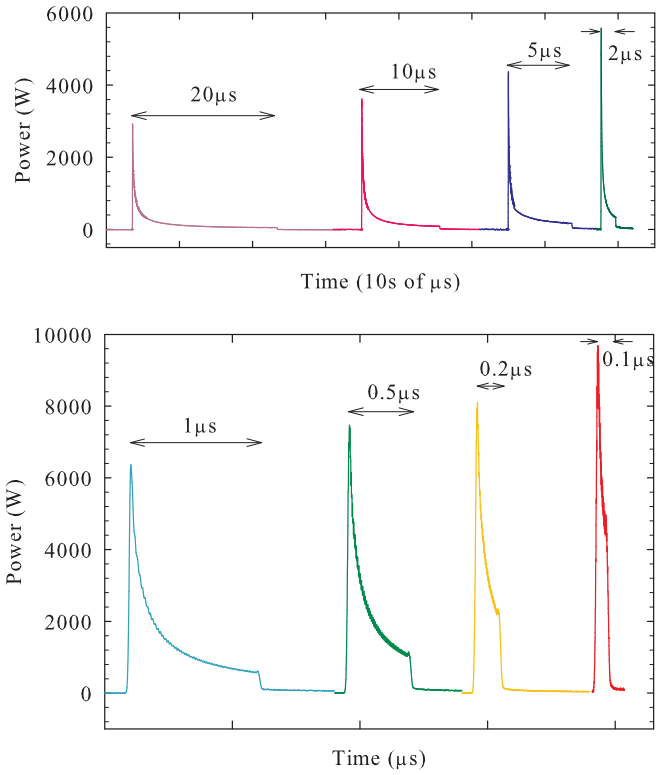

Figure 5.32: Output pulse shapes for 10kHz repetition rate for a range of pulse widths

In this case, the peak power increased as the pulse width was reduced and the asymmetry of the pulses became less severe and more like the input pulse shape for shorter pulse widths. For long pulse widths the peak power was reduced due to the associated reduction in time available for the gain to recover. Additionally, for long pulses, the pulse shapes had long tails with relatively low power because most of the gain became saturated in the first microsecond or so, indicated by a sharp peak at the leading edge of the pulse. By using the same technique as above to calculate the peak power and theoretical curves, Figure 5.33 was produced showing the peak and average power as a function of the pulse width. The discrepancy between theory and results, which

increases with pulse duration, can once again be attributed to the additional gain acquired by the amplifier during the pulse. Since the pulses are generally longer than in the previous experiment, this explains the greater difference between theory and experiment in this case. The longer pulses provide more time for the amplifier to absorb pump power during the pulse, which is not accounted for in the model. The results still show reasonable agreement with the model which therefore provides a useful tool for predicting the performance of the amplifier under a wide range of operating conditions.

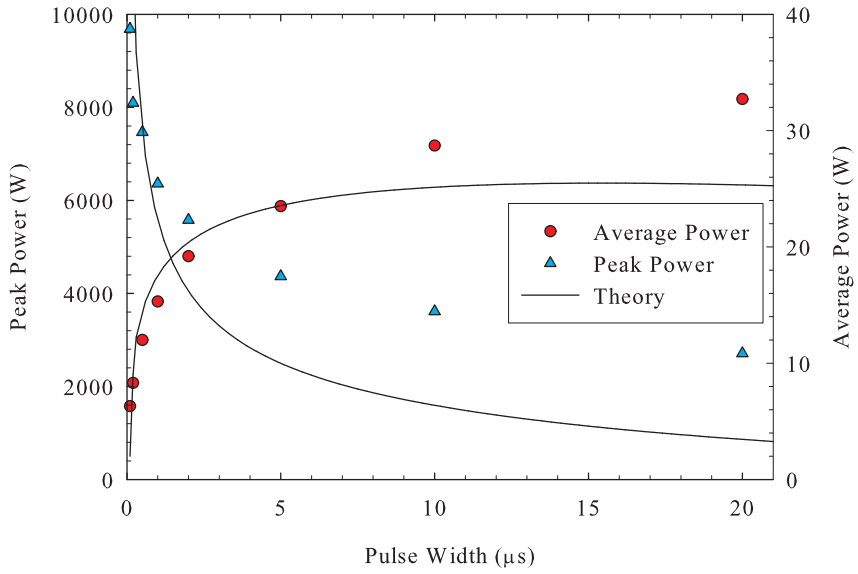

Figure 5.33: Variation of peak power and average power with pulse width for 10kHz repetition rate compared to theory (solid line).

5.7.2.3 A 1μs Pulse Envelope, 10kHz, Mode-Locked Source

We have seen, in the previous sections, that a trade-off is required between peak power and average power in the pulsed regime. The most attractive compromise depends on the application but, for the example of quasi-cw synchronous pumping of an OPO, the following operating conditions are proposed to offer high nonlinear frequency conversion efficiency and high average power operation. By choosing an input pulse width of 1μs and a repetition rate of 10kHz, the MOPA system yielded 15W of average power with a pulse shape shown in Figure 5.34. This regime offers high measured peak powers of ∼6kW corresponding to mode-locked peak powers of ∼180kW and long pulse

trains, as required for effective quasi-cw pumping of OPOs. Each µs pulse train comprising ∼100 mode-locked pulses, had a total pulse energy of 1.5mJ.

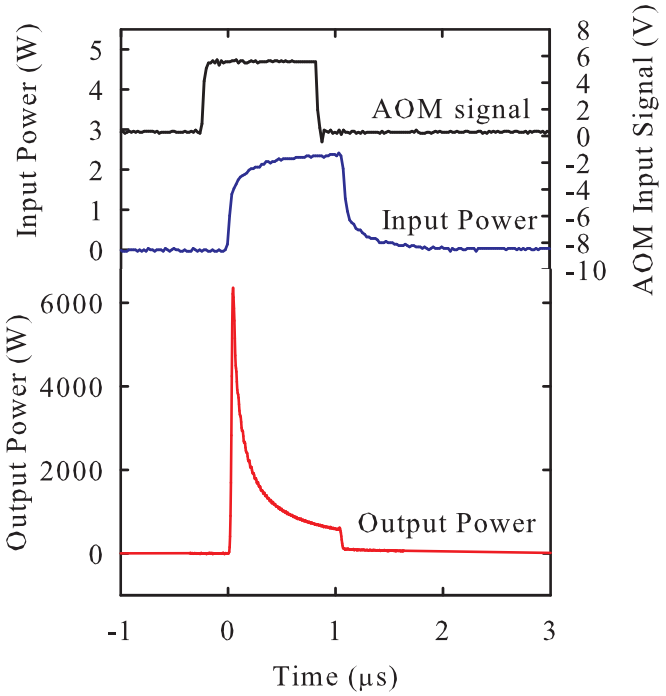

Figure 5.34: An example of a high peak (6kW) high average (13W) power pulse at 10kHz repetition rate and 1µs pulse width.

In addition to this high performance in long-pulse mode, the lower overall saturation of the amplifier and consequent higher average-power gain in this regime, was advantageous from a beam quality point of view, since the gain-guiding effect caused an improvement in beam quality in this regime, compared to the highly saturated regime, where the gain and therefore the gain-gradient is lower. In the 1µs , 10kHz, example above, the M^2 parameters were measured to be 1.3 and 1.4 in orthogonal planes.

One problem of this operating regime, for the intended application, is the temporal pulse distortion resulting from the leading edge of the pulse experiencing a much higher gain than the trailing edge. This causes the skewed nature of the output pulse, shown in Figure 5.34, and hence a reduced effective pulse width. This problem is addressed in detail in Chapter 6.

5.8 Summary

In summary, this chapter has brought together many of the concepts discussed in Chapter 4 and applied them to aid in the design and characterisation of a high power Nd:YVO_4 amplifier system with the mode-locked oscillator described in Chapter 3, as the seed. Some of the more practical design considerations were discussed, such as the thermal management of the amplifier crystals, with regard to their cooling arrangement and the system of relay imaging to ensure good control over the pump and signal beam sizes in the crystals, independently of thermal lens strength. The limitations imposed on the amplifier performance by parasitic oscillation and ASE were also discussed and techniques to eliminate or reduce their impact were highlighted. Parasitic lasing can often be completely eliminated using a number of techniques including angling the optics away from the beam path and using Faraday isolators. However, ASE was identified as potentially being the ultimate limiting factor on the maximum small signal gain that can be achieved in an amplifier since it has no threshold so cannot be completely removed.

The design of the specific three stage amplifier system, which was built, was described as well as the pumping scheme that was employed. The amplifier was pumped by two 30W fibre-coupled diode bars for the first stage and by a single 500W diode stack coupled to four delivery fibres for the second and third stages. The method of beam shaping and fibre-coupling the diode stack was shown which incorporated a combination of cylindrical lenses and a polarisation combining stage to achieve the desired ratio of beam sizes and M^2 values in the orthogonal planes before the beam could be chopped into four smaller beams and fibre coupled. The four fibres, of core diameter 600μm , had a combined output power of 258W.

The generic amplifier configuration used for all three stages was then described and its merits discussed. The strategy of using low Nd^{3+} doping concentration (0.1%) and absorbing the pump radiation over two crystal lengths was described as a means to reduce thermal loading density and to avoid problems with ETU. Additionally, the amplifier crystals were orientated with their c-axes at 90° to one another to maximise absorbed pump power and to com-

pensate for thermal lens astigmatism. An experimental technique was used to find the best signal-pump overlap ratio by moving the amplifier stage relative to a slowly converging input signal beam. This enabled output power and beam quality measurements to be made, for a range of signal beam sizes, with a fixed pump beam size. The results for the power gain, as a function of signal-pump size ratio, compared very well to the theory from Chapter 4 and the optimum ratio was close to 1. In this situation, there was little difference in the theory between the 'top-hat' and Gaussian pump beam approximations, so neither was shown to be more valid than the other when compared to the experimental results. The measured M^2 values were shown to increase significantly for $w_l/w_p > 1$, as expected, however the theory, based on the quartic approximation of the phase aberration, was shown to be invalid for $w_l/w_p > 0.4$, since the measured values increased much more slowly as the signal size was increased. This is not entirely surprising because the quartic approximation is known to break down as w_l/w_p approaches 1, but at such high pump intensity the theory predicts a very rapid increase in M^2 which starts at relatively small values of w_l/w_p. The experimental results also showed an unexpected small increase in M^2 for $w_l/w_p < 1$. This was thought to be a result of distortion of the signal intensity profile caused by the non-uniform radial gain distribution. The brightness gain was shown as a function of the signal-pump ratio and its optimum value was shown to be more critical to w_l/w_p, than in the simple power gain case, due to a more rapid reduction in brightness as w_l/w_p is increased beyond 1. However, the optimum value remained close to 1.

The final design for the three stage amplifier was then described which incorporated relay imaging from one amplifier stage to the next, as well as between the crystals within each amplifier stage. An AOM was also included between the oscillator and the amplifier so that pulsed operation could later be achieved. The pump fibres were used in ascending order of output power so that the maximum extraction efficiency could be achieved and the sizes of the pump and signal beams in each amplifier stage were chosen to account for the different pump powers and therefore the overlap ratios in successive stages were reduced to reduce thermal lens aberration.

The experimental results were presented for cw operation of the amplifier and initially, without the use of isolators or the AOM modulator, the maximum

output power was measured to be 94W. After including the modulator and isolator between the oscillator and amplifier, the maximum power was reduced to around 79W and was shown to be limited by the available pump power. A small decrease in slope efficiency could be seen at higher power levels but power scalability to >100W seems possible. The reduction in gain of the amplifier and the corresponding increase in extraction efficiency with increasing input signal power was shown which explained a steeper increase in output power with signal power at the highest signal power. This suggests that the signal power is not high enough to achieve full saturation, where the output power becomes insensitive to the input power.

The beam quality of the amplifier output was measured as a function of pump power and M^2 values of 1.7 and 1.9 were measured in orthogonal planes, at maximum pump power, in cw mode. This indicates moderate beam quality degradation due to aberrated thermal lensing, but nevertheless represents good overall beam quality, considering the high power level, sufficient for many demanding applications. The aberrated output beam intensity profile was measured as a function of distance propagated near a beam waist and the interference pattern was shown. This pattern was thought to be consistent with predictions from a model by Neubert *et al.* [15] for cylindrical spherical aberrations.

Measurement of the M^2 values out of the amplifier, as a function of signal input power, led to an interesting investigation on the influence of gain, and in particular gain guiding, on the beam quality degradation in the amplifier. The beam quality was shown to improve significantly with increasing gain as measured by reducing the input signal power. This result was confirmed by using a Nd:YLF probe laser which was passed through the amplifier with the same beam size and alignment as the Nd:YVO_4 signal beam. Since the wavelength of the Nd:YLF laser (1047nm) lies outside the Nd:YVO_4 gain bandwidth, the beam experienced the same phase aberration but none of the gain through the amplifier. The much more severe beam quality degradation, measured for the Nd:YLF laser, led to the conclusion that the non-uniform radial gain distribution acts to reduce the impact of thermal lens aberration for the Nd:YVO_4 signal by reshaping the intensity distribution to add extra weight to the unaberrated central portion of the beam.

The results for the amplifier in mode-locked mode of operation were found to be effectively the same as the cw results, with no significant change in average power. The only difference was obviously the high peak powers and short pulses achieved. No significant change in pulse duration was measured so therefore the peak power gain was the same as the average power gain through the amplifier. This implied an output peak power >2.5kW in 335ps pulses. To increase this peak power further, the AOM was used to gate the input to the amplifier. This enabled a range of operating characteristics to be achieved by varying the pulse width and repetition rate for the AOM modulation. The results showed very good agreement with the predictions from the theory in Section 4.2.4. By reducing the repetition rate, or reducing the pulse width, it was possible to achieve higher peak power by taking advantage of the longer recovery time of the amplifier and the resultant higher initial gain. By this technique the maximum small signal gain of the amplifier was measured to be >7000 (38dB). This corresponded to a peak power of 12.7kW, when the oscillator was running in cw mode, and therefore corresponded to peak powers approaching 400kW for mode-locked operation. These operating conditions did however result in low average power of just 3W, so a compromise between peak power and average power is often desirable. By increasing the pulse width or the repetition rate, the average power can be increased and the peak power reduced to suit the intended application. An example is given of a 1μs pulse (or pulse train) of 6kW peak power (180kW in mode-locked mode) at 10kHz repetition rate offering 15W of average power and 1.5mJ pulse energy. Such a source would be an attractive pump source for a quasi-cw, synchronously pumped OPO.

5.9 References

[1] **Ruffing, B., Nebel, A.** and **Wallenstein, R.**, *All-solid-state cw mode-locked picosecond $KTiOAsO_4$ (KTA) optical parametric oscillator*, Applied Physics B: Lasers and Optics, Vol. 67, pp. 537–544, 1998.

[2] **Pearce, S.** and **Ireland, C. L. M.**, *Performance of a cw pumped Nd:YVO_4 amplifier with kHz pulses*, Optics and Laser Technology, Vol. 35, pp. 375–379, 2003.

[3] **Chen, Y. F., Huang, K. F., Tsai, S. W., Lan, Y. P., Wang, S. C.** and **Chen, J.**, *Simultaneous Mode-Locking in a Diode-Pumped passively Q-switched laser with a GaAs Saturable Absorber*, Applied Optics, Vol. 40, No. 33, pp. 6038–6041, 2001.

[4] **Bernard, J. E., McCullough, E.** and **Alcock, A. J.**, *High Gain, Diode-Pumped Nd:YVO_4 Slab Amplifier*, Optics Communications, Vol. 109, pp. 109–114, 1994.

[5] **Plaessmann, H., Ré, S. A., Alonis, J. J., Vecht, D.** and **Grossman, W. M.**, *Multipass Diode-Pumped Solid-State Optical Amplifier*, Optics Letters, Vol. 18, pp. 17, 1993.

[6] **Forget, S., Balembois, F., Georges, P.** and **Devilder, P. J.**, *A New 3D Multipass amplifier Based on Nd:YAG or Nd:YVO_4 crystals*, Applied Physics B, Vol. 75, pp. 481–485, 2002.

[7] **Robertson, A., Klein, M. E., Tremont, M. A., Boller, K. J.** and **Wallenstein, R.**, *2.5GHz repetition-rate singly resonant optical parametric oscillator synchronously pumped by a mode-locked diode oscillator amplifier system*, Optics Letters, Vol. 25, No. 9, pp. 657–659, 2000.

[8] **Butterworth, S. D., Girard, S.** and **Hanna, D. C.**, *High-power, broadly tunable all-solid-state synchronously pumped lithium triborate optical parametric oscillator*, Journal of the Optical Society of America B, Vol. 12, No. 11, pp. 2158–2167, 1995.

[9] **Heinz, P., Seilmeier, A.** and **Piskarskas, A.**, *Picosecond Nd:YLF laser-multipass amplifier source pumped by pulsed diodes for the operation of powerfull OPOs*, Optics Communications, Vol. 136, pp. 433–436, April 1997.

[10] **Butterworth, S. D., Clarkson, W. A., Moore, N., Friel, G. J.** and **Hanna, D. C.**, *High-power quasi-cw laser pulses via high-gain diode-pumped bulk amplifiers*, Optics Communications, Vol. 131, pp. 84–88, 1996.

[11] **Musgrave, I. O., Yarrow, M. J., Clarkson, W. A.** and **Hanna, D. C.**, *Energy-transfer upconversion in Nd:YVO_4 and its effect on laser performance*, article awaiting submission.

[12] **Svelto, O., Taccheo, S.** and **Svelto, C.**, *Analysis of amplified spontaneous emission: some corrections to the Linford formula*, Optics Communications, Vol. 149, pp. 277–282, 1998.

[13] **Smith, G.** and **Damzen, M. J.**, *Spatially-selective amplified spontaneous emission source derived from an ultra-high gain solid-state amplifier*, Optics Express, Vol. 14, No. 8, pp. 3318–3323, 2006.

[14] **Clarkson, W. A.**, *Thermal effects and their mitigation in end-pumped solid state lasers*, Journal of Physics D: Applied Physics, Vol. 34, pp. 2381–2395, August 2001.

[15] **Neubert, B. J.** and **Eppich, B.**, *Influences on the beam propagation ratio M^2*, Optics Communications, Vol. 250, pp. 241–251, 2005.

[16] **Salin, F.** and **Squier, J.**, *Gain-guiding in solid-state lasers*, Optics Letters, Vol. 17, No. 19, pp. 1352–1354, 1992.

[17] **Siegman, A. E.**, Lasers, University Science Books, 1986.

Chapter 6

A Nd:YVO_4 MOPA as a High-Power Single-Frequency Source

6.1 Introduction

High power solid-state sources with good beam quality and a narrow-linewidth output are required for many applications. These include nonlinear frequency conversion, LIDAR [1], spectroscopy [2], metrology and gravitational-wave detection [3]. One demanding application, in terms of output power, is pumping a singly-resonant OPO (SRO) as a route to tunable narrow-linewidth output. Continuous-wave SROs require materials with very high nonlinear coefficients, such as periodically poled lithium niobate (PPLN), to achieve efficient frequency conversion due to their relatively low intensity compared to Q-switched or mode-locked devices. Thresholds for cw pumped SROs based on PPLN are typically at least a few watts [4]. For more complex SRO designs, aimed at extending wavelength flexibility, the threshold pump power can be much higher, and is difficult to obtain from a simple solid-state laser oscillator configuration. Moreover, achieving effective wavelength selection and good beam quality from an SRO requires a cw pump source, or one with pulse durations long enough to allow the signal light to make many round trips of the SRO cavity to establish steady-state oscillation. In the latter, 'quasi-cw', pumping regime, the advantages of pulsed pumping with higher peak power and therefore higher conversion efficiency are combined with the advantages of cw operation for simpler single-longitudinal mode and TEM_{00} selection. Quasi-

cw pumping of SROs is normally achieved with Q-switched oscillators, where pulse durations of the order 10-50ns can make up to around 100 round trips of an SRO cavity of a few cm. In this regime, a significant fraction of the pulse is in the transient phase of the SRO, before steady-state is reached [5]. By operating with longer pulse durations a larger fraction of the pulse energy is in the steady-state phase, which offers improved beam quality and narrower linewidth. For example, Brosnan and Byer [6] showed that, for an SRO utilising a diffraction grating to offer wavelength selection, the linewidth, $\Delta\nu_{SRO}(p)$, of the output, after p cavity round trips can be approximately expressed as:

$$\Delta\nu_{SRO}(p) = \frac{1}{\sqrt{p}}\Delta\nu_{pm}, \tag{6.1}$$

where $\Delta\nu_{pm}$ is the phase matching bandwidth for the nonlinear crystal, given approximately by

$$\Delta\nu_{pm} = \frac{1}{l\Delta n_{si}}, \tag{6.2}$$

where l is the length of the nonlinear medium and Δn_{si} is the refractive index difference for signal and idler wavelengths. Larger numbers of cavity round trips are also an advantage for effective refocusing and hence TEM_{00} mode selection in SRO resonators as discussed by Kogelnik [7]. Obtaining longer pulse durations from Q-switched lasers has been achieved with only limited success [8, 9]. A more flexible approach is offered by a MOPA system which amplifies gated pulses from a cw single-frequency oscillator.

Scaling the output power from single-frequency sources to meet the needs of these and more demanding applications is often very difficult due, in particular, to the problems caused by heat generation in the laser medium including thermal lensing and thermal lens aberration. Moreover, in simple resonator configurations, as power levels increase, changes in resonator length and changes in peak emission wavelength, due to temperature fluctuations become more pronounced leading to mode-hopping and hence multi-axial mode operation. One way to alleviate this problem is to employ a MOPA approach since, in this way, the problems of power scaling and maintenance of robust and reliable single-frequency operation are effectively de-coupled. This approach has proved very popular with fibre-based sources [10, 11], owing to the relative ease with which high gains and high extraction efficiencies can be

achieved in fibre amplifiers. However, achieving high gains and high extraction efficiency, without degrading beam quality, is more challenging in bulk solid-state amplifiers and requires careful consideration of the amplifier design and choice of gain medium. Bulk amplifiers can nevertheless offer some advantages over their fibre-based rivals, particularly in the pulsed regime, owing to higher thresholds for damage and a higher threshold for unwanted nonlinear loss processes, for example stimulated-Brillouin-scattering (SBS) and stimulated-Raman-scattering (SRS) [12], but only if an efficient brightness-scalable amplifier configuration can be realised.

As a result of Nd:YVO_4 's rather poor thermo-mechanical properties, notably its low thermal conductivity ($\sim$5Wm^{-1}K^{-1}) and high temperature dependence of refractive index (dn/dT $\sim$8.5$\times$10^{-6}K^{-1}), and in spite of its advantageous spectroscopic properties, Nd:YVO_4 has so far proved to be rather less popular for power scaling of single-frequency output than Nd:YAG [13] and Nd:YLF [14]. This is mainly due to its stronger thermal lensing and consequent difficulty in achieving TEM_{00} beam quality at high power levels. Nevertheless some success has been reported, for instance, Xi [15] reported 18W of single-frequency output from a Nd:YVO_4 oscillator with a slope efficiency of 48%. The single-frequency Nd:YVO_4 master-oscillator employed in the work described in this thesis, was based on a unidirectional ring cavity which incorporated a frequency doubling crystal to passively suppress axial-mode-hopping, as described in [16].

In this Chapter the use of the amplifier system, described in Chapter 5, to achieve efficient amplification of this 1.06μm single-frequency Nd:YVO_4 laser source is described. Before amplification, the master-oscillator output was incident on an acousto-optic modulator (AOM), the diffracted beam from which was fed into a three stage amplifier. The AOM could select cw or pulsed mode (exploiting the high small-signal gain) with a very large degree of flexibility of the pulse duration and repetition rate. This flexibility offers many advantages over Q-switched oscillators, for example, particularly when long pulses of microsecond order are required. In pulsed mode, a combination of high peak power, high average power and long pulse duration was achieved. To avoid the distorted nature of the output from a rectangular input pulse, temporal pulse shaping was demonstrated by driving the AOM with an arbitrary

waveform generator. The result was a nearly 'top hat' pulse shape with high intensity and an extended effective pulse width. The merits of this source are discussed with regard to the particular application of cw and quasi-cw pumping of SRO's based on quasi-phase-matched nonlinear crystals (e.g. PPLN).

6.2 Single-Frequency Lasers

In contrast to the mode-locked oscillator, described in Chapter 3, where multi-axial mode operation is required to achieve large bandwidth and hence the short pulses; single-frequency oscillators require, by definition, oscillation of just one axial mode. This provides very narrow linewidth output, usually between hundreds of Hz to tens of MHz, much less than the linewidth of the laser transition (hundreds of GHz). The lower limit for the FWHM linewidth $\Delta\nu_l$ of a single-frequency laser depends on the linewidth of the passive resonator and the amount of laser power circulating in the resonator, given by the Schawlow-Townes Limit [17]:

$$\Delta\nu_l = \frac{\Delta\nu_c}{n}, \tag{6.3}$$

where n is the number of laser photons in the cavity given by

$$n = \frac{P_{out}}{L+T}\frac{2l_c}{h\nu_l c}, \tag{6.4}$$

and $\Delta\nu_c$ is the linewidth of axial-modes in the passive resonator, given by the expression

$$\Delta\nu_c = \frac{c(L+T)}{4\pi l_c}, \tag{6.5}$$

where L and T are the round-trip loss and output transmission respectively, P_{out} is the output power, l_c is the cavity length and ν_l is the lasing frequency. In this section a number of methods for achieving single-axial mode operation in laser oscillators are discussed and the single-frequency oscillator used in this work is described. In practice however, the linewidth of a single-axial mode laser is much greater than this theoretical limit. Temperature fluctuations and mechanical vibration can produce rapid changes in the laser frequency which cause linewidth broadening. For this reason, good temperature control and stabilisation of the laser medium can be very important for achieving narrow linewidth output.

6.2.1 Achieving Single-Frequency Oscillation

As was mentioned in Chapter 2, the problem of spatial-hole-burning which occurs in standing-wave laser resonators causes an inhomogeneous spatial gain distribution which normally results in multi-axial mode operation in solid-state lasers. One method which can be employed to prevent multi-axial mode operation is to introduce a strong frequency discriminating element into the laser cavity, such as an etalon, which suppresses oscillation of modes adjacent to the lasing mode. This can reduce but not eliminate spatial-hole-burning, and will also normally result in a loss in efficiency of the oscillator due to unused gain at the nodes of the cavity standing wave [18]. Another approach is to use a micro-cavity laser. In this method a very short ($\sim$1mm) cavity is normally formed by the end faces of the laser rod itself. Such cavities have very large axial-mode spacing which can be comparable to the gain bandwidth of the laser material. For example a transition linewidth of $\sim$250GHz, as in Nd:YVO_4 , would require a cavity length of 1.2mm to ensure that the axial-mode spacing from equation (2.1) is equal to half the linewidth. In this scheme, there is sufficient gain discrimination between axial modes that only one will oscillate. One drawback of such a scheme is that the short cavity length and often monolithic design prohibits the use of intra-cavity elements such as Q-switches, harmonic generators and spatial filters, significantly limiting the design flexibility. One of the most popular techniques for achieving robust single-frequency operation is to use a unidirectional ring-laser. In this scheme, the oscillating mode makes a round trip of a laser resonator in one direction, such that the gain medium can be positioned in a region where there is no counter-propagating beam. The cavity therefore forms a travelling-wave rather than a standing-wave where the round trip cavity length is equal to an integer number of wavelengths. Additional complexity is required in the form of an optical isolator, such as a Faraday element and waveplate combination, to enforce unidirectional operation. However, the result is a very robust single-frequency output. Various different resonator designs can be used as well as different methods for achieving a loss difference between the two propagation directions which only needs to be small, $\sim$0.1%, to ensure unidirectional operation. However, if the loss discrimination is very low ($\ll 0.1\%$) the oscillator becomes very sensitive to feedback from outside the cavity causing bi-directional operation. Some ex-

amples of ring laser configurations are monolithic non-planar ring lasers [19], rhombic and bow-tie ring lasers [20]. The resonator design which was utilised in this work comprised four mirrors in a bow-tie ring-cavity configuration. The main advantages of this design are its compactness and flexibility in the design parameters such that good control over the laser mode characteristics can be achieved. In addition, the angles of incidence on the curved mirrors can be made small to reduce astigmatism.

6.2.2 Mode-Hopping Suppression

Most resonators have cavity lengths greater than several cm which means that there are usually many axial-modes near the peak of the laser line. This means that, in unidirectional ring-cavity configurations which enforce single-axial mode operation, small changes in the optical path length in the resonator due to temperature or pressure fluctuations or mechanical vibration can cause mode-hopping from one axial mode to another. This occurs when the lasing axial-mode frequency changes relative to the laser line centre. This can either occur due to a change in the optical path length in the cavity due to movement of mechanical components or temperature or pressure fluctuations, or a change in the optical frequency of the line centre due to temperature fluctuations, which for Nd:YVO_4 is $\sim$1.6GHz/$^{\circ}$C. In any case, the gain for a neighbouring mode becomes larger than the gain for the lasing mode. The neighbouring mode therefore takes over and begins to lase instead. This is shown in Figure 6.1 where ν_1 and ν_2 are modes close to the line centre. In this case the gain curve (black line) is shifted relative to the axial modes to cause mode-hopping, as is caused by a drift in the temperature of the gain medium. Over longer periods, frequent hops between several axial modes can often be observed.

One common technique for suppressing axial mode-hopping is to employ active stabilisation of the resonator length, for example by mounting one of the mirrors on a piezoelectric transducer (PZT) and forming a negative feedback loop by locking the output to an external Fabry-Pérot cavity [21]. This adds considerable complexity and cost to the system and reduces the compactness of the laser. A more convenient, passive technique, was reported by Martin

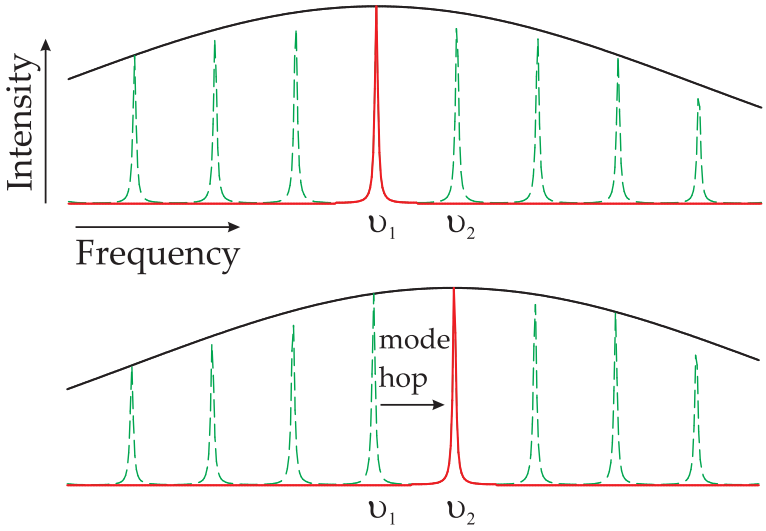

Figure 6.1: Mode-hopping from axial mode ν_1 to ν_2.

et al. [16] which uses an intra-cavity frequency doubling crystal to introduce a loss that is less for the oscillating mode than for neighbouring axial modes. This mechanism can be explained as follows. If we consider two adjacent modes one of frequency ν_1 and intensity $I(\nu_1)$ and the other of frequency ν_2 and intensity $I(\nu_2)$, then each mode has a loss proportional to $[I(\nu)]^2$ due to second harmonic generation and a loss proportional to $I(\nu_1)I(\nu_2)$ due to sum frequency generation. It turn out that the round-trip loss L_1 due to these two components for mode ν_1 is equal to [22]

$$L_1 = k[I(\nu_1)]^2 + 2kI(\nu_1)I(\nu_2), \tag{6.6}$$

where k is constant. This means the fractional loss $L_1/I(\nu_1)$ for mode ν_1 is $kI(\nu_1)+2kI(\nu_2)$ and similarly the fractional loss for mode ν_2 is $kI(\nu_2)+2kI(\nu_1)$. It follows that the ratio of the fractional losses is given by

$$\frac{L_1 I(\nu_2)}{L_2 I(\nu_1)} = \frac{kI(\nu_1) + 2kI(\nu_2)}{kI(\nu_2) + 2kI(\nu_1)}. \tag{6.7}$$

Now if we consider a homogenously broadened laser without spatial-hole-burning, as in a ring cavity, only one mode (eg. ν_1) will be oscillating so it follows that $I(\nu_2) \ll I(\nu_1)$. The above ratio therefore reduces to $1/2$ which implies that the lasing mode has half the fractional nonlinear loss of the non-lasing mode leading to effective suppression of axial mode-hopping. The above result applies to all non-oscillating modes that fall within the phase-matching

bandwidth of the frequency doubler. This technique has been demonstrated in a Nd:YAG laser operating with ∼1W at 532nm [16] where the loss difference was sufficient to allow tuning of the output over 80 axial mode-spacings without mode-hopping and also in a Nd:YLF laser operating with ∼5W output at 1053nm [23]. In the latter, the mirrors were coated to transmit the second harmonic and reflect the fundamental wavelength which resulted in the power lost by second harmonic generation at 527nm amounting to $< 3\%$ of the output power at 1053nm. The nonlinear loss was nevertheless sufficient to suppress axial mode hopping over a tuning range of ∼14 axial mode-spacings. In summary, this passive technique provides a robust single-axial-mode output, which remains free from mode hopping over very long time periods without needing active stabilisation of the resonator length.

6.3 Single-Frequency Master-Oscillator

The master-oscillator employed a 0.1% doped Nd:YVO_4 crystal of length 10mm, end-pumped at 808nm by a 30W fibre-coupled diode-bar. The oscillator set-up is shown in Figure 6.2. A simple bow-tie ring cavity configuration was used with a TGG Faraday rotator and two half-waveplates to enforce unidirectional operation and hence eliminate spatial-hole-burning. This technique proved to be successful in achieving single-axial-mode output. The crystal was square in cross-section and was mounted with its c-axis parallel to the plane of the ring cavity with all the side surfaces in contact with a water-cooled aluminum heat-sink to facilitate efficient heat removal. The cavity also included a Brewster-angled lithium triborate (LBO) frequency-doubling crystal of 15mm length, maintained at 148.5°C, for Type I non-critical phase-matching at 1064nm. This acted to suppress axial mode-hopping in the way described in the previous section.

The pump beam entered the cavity through one of the plane mirrors, which was coated for high reflectivity (>99.8%) at the lasing wavelength (1064nm) and high transmission (>95%) at the pump wavelength, and was focused to a spot radius of 250μm to match the calculated TEM_{00} waist size in the crystal. The two curved mirrors both had a radius of curvature of 100mm and

were coated for high reflectivity (>99.8%) at 1064nm and high transmission (>90%) at 532nm. The plane mirror that served as the output coupler had a transmission of 10% at 1064nm. The distance between the two plane mirrors was approximately 150mm and the distance between two curved mirrors was approximately 110mm. The angle of incidence of the intracavity beam on the curved mirrors (∼13°) was selected to compensate for the astigmatism induced by the Brewster-cut LBO crystal. This arrangement resulted in a calculated TEM_{00} beam waist radius in the LBO crystal of approximately 50µm. The oscillator was able to produce TEM_{00} output beam quality without any spatial filtering for a small range of pump powers. However, with the addition of an aperture, to suppress higher order modes, the range over which robust diffraction-limited TEM_{00} output could be achieved, was extended over the full range of pump powers used in our experiments. A photo of the single-frequency oscillator is shown in Figure 6.3.

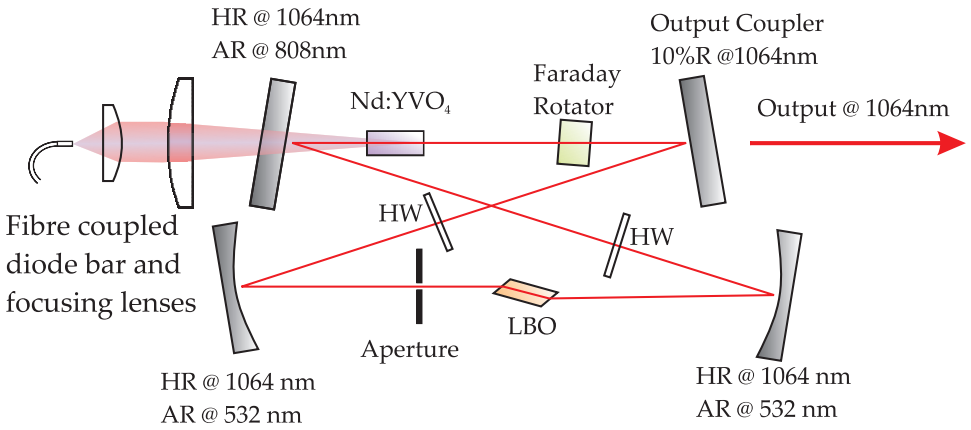

Figure 6.2: Single-Frequency Nd:YVO_4 master-oscillator set-up. HW: Half-waveplate, FR: Faraday-rotator.

6.3.1 Single-Frequency Oscillator Performance

The output power from the master-oscillator as a function of incident pump power is shown in Figure 6.4. The master-oscillator had a threshold pump power of 2.8 W and yielded a maximum output power of 3.8 W for an incident pump power of 24 W (20.4 W absorbed), corresponding to a slope efficiency with respect to absorbed pump power of 22% and an optical efficiency of 16%. The relatively low efficiency can be attributed to non-optimal over-

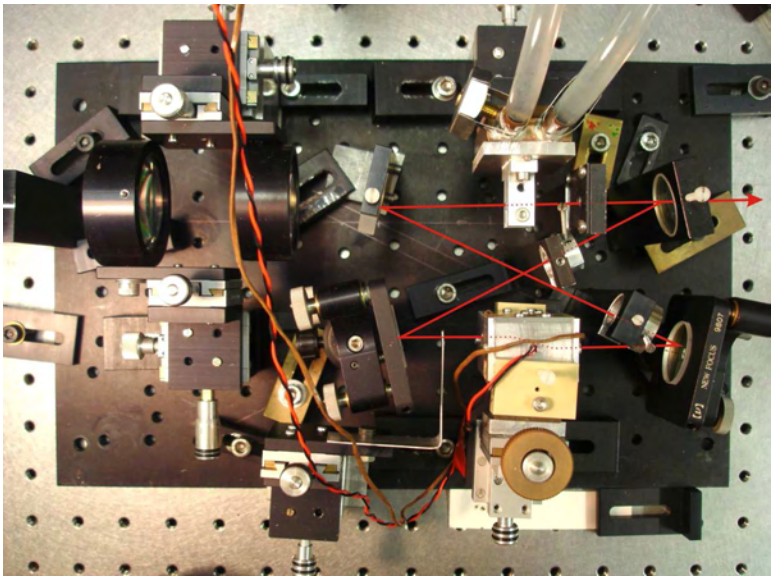

Figure 6.3: Photo of single-frequency Nd:YVO_4 master-oscillator

lap efficiency between pump and laser mode and the significant cavity losses due to the aperture and the total of 14 optical surfaces per round trip. From equation (2.3), the cavity loss was estimated to be ∼13%.

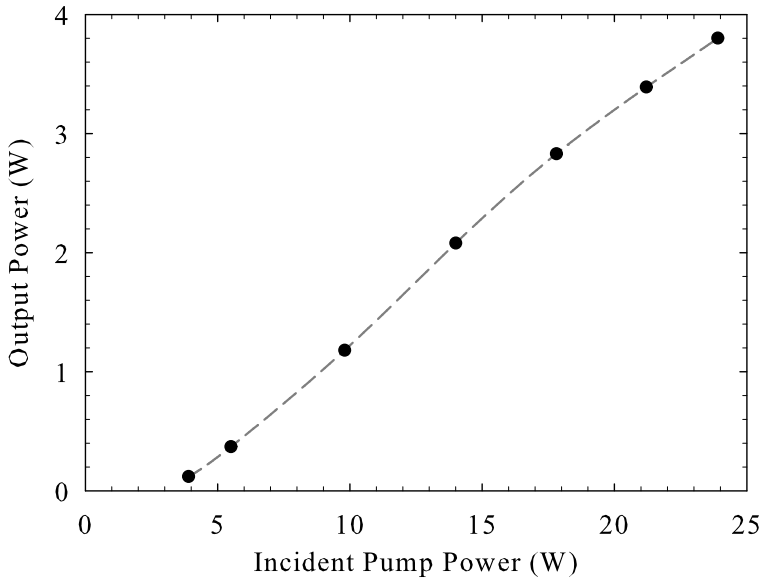

Figure 6.4: Output power versus incident pump power for single-frequency oscillator.

Single-frequency operation up to the maximum output power was confirmed with the aid of a scanning confocal Fabry-Pérot interferometer (FPI) with a free

spectral range (FSR) of 7.5GHz and a finesse of 250. A typical oscilloscope trace from the FPI is shown in Figure 6.5 for the oscillator operating at maximum output power. The trace shows single-frequency operation with linewidth less than the resolution of the interferometer (30MHz). The actual linewidth is expected to be much less than this since the estimated passive cavity linewidth from equation (6.5) is <20MHz for a combined round-trip loss and output coupling of 0.2.

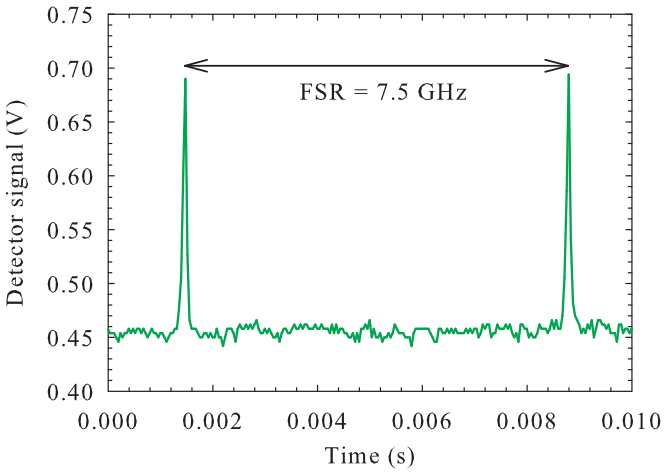

Figure 6.5: Typical oscilloscope trace from Fabry Pérot Interferometer to confirm single axial-mode operation

Mode-hop-free single-frequency operation was observed for long operating times (>30 minutes) without the need for active stabilisation of the cavity length. By comparison, the oscillator mode-hopped frequently (∼every 10 seconds) when the LBO crystal was not included, confirming the benefits of our passive scheme for suppressing mode-hopping. The beam quality of the output beam was investigated with the aid of a Beamscope (Dataray Inc.) and the M^2 parameter was determined to be 1.02 in both planes.

6.4 Single-Frequency Amplification

The single-frequency oscillator was set up next to the mode-locked oscillator so that either of the sources could be used to seed the amplifier chain. Using two 45° HR mirrors and a 200mm focal length lens, the output from the single-frequency laser was aligned to same beam path as the mode-locked laser with

approximately the same beam radius and divergence. A schematic of the system is shown in Figure 6.6. Simple removal of one 45° mirror enabled the system to be transferred back to the mode-locked oscillator with minimal realignment necessary. The Fabry-Pérot Interferometer (FPI), described above, was also used in the set-up to continuously monitor the stability of the output and confirm single-axial mode operation. The small power transmission though one of the HR mirrors was sufficient for monitoring the frequency spectrum using the FPI.

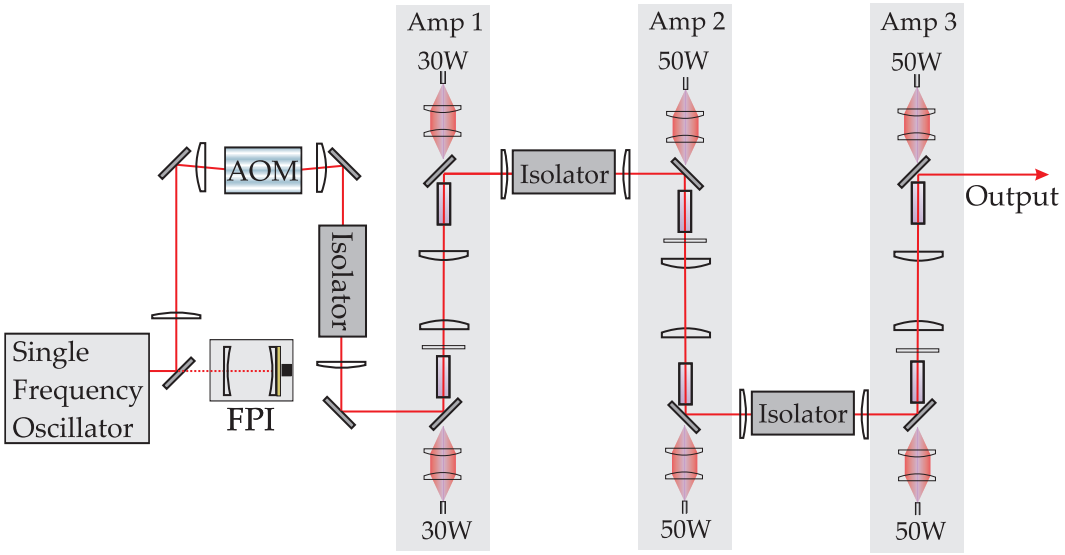

Figure 6.6: Schematic of MOPA set-up showing relay imaging lenses between each crystal and pump powers at each amplifier stage. AOM: Acousto-Optic Modulator, FPI: Fabry-Pérot Interferometer.

The MOPA was initially operated in cw mode by applying a constant rf signal to the AOM. In this regime when the signal power was high enough to cause significant saturation of the gain in the amplifier, the isolators between each amplifier stage, could be removed since the gain was not high enough to cause parasitic lasing. This resulted in a considerable increase in output power owing to the ~10% loss per isolator. In later experiments where the level of saturation was much less due to pulse operation of low cw input powers, parasitic lasing became a problem so the isolators were required to eliminate it.

6.4.1 Single-Frequency cw Operation of the MOPA System

The output power from the three-stage amplifier as a function of incident pump power under these operating conditions and for input signal power from the master-oscillator of 2.4W, is shown in Figure 6.7. The amplifier arrangement yielded a maximum cw output power of 79 W for a combined incident pump of 265W, corresponding to an extraction efficiency of 29% with respect to incident pump power and 34% with respect to the 228W of absorbed pump power. Figure 6.8 shows the amplified output power and gain as a func-

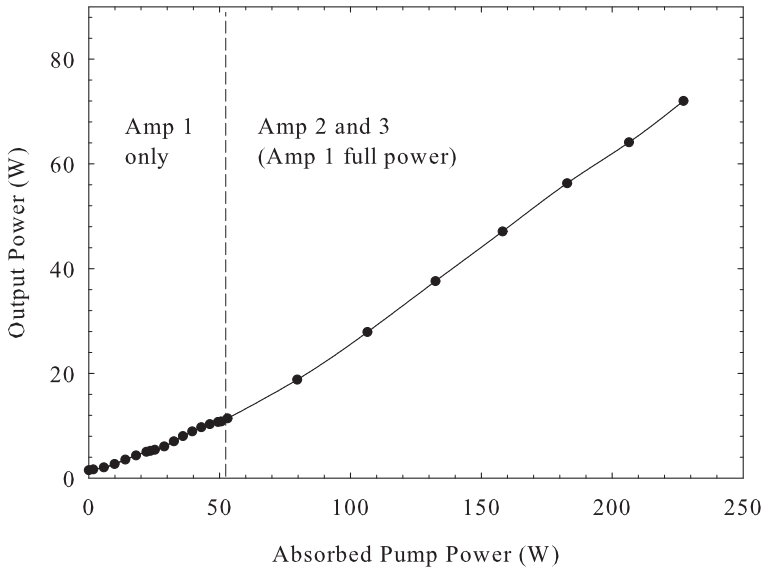

Figure 6.7: Gain and output power of amplifier versus input power.

tion of incident signal power at full pump power. The overall power gain at the maximum output is 15 dB for an input signal power of 2.4W. After the third amplifier the M^2 parameters were 1.43 in the horizontal plane (i.e. the plane of Figure 6.6) and 1.48 in the orthogonal plane. The small difference in the M^2 parameters for orthogonal planes is attributed to the slightly elliptical output beam from the master-oscillator and residual (uncompensated) astigmatism in thermal lensing. At lower pump powers, the M^2 parameters were observed to decrease (as expected) and when the pump power to the amplifier chain was turned off, the M^2 parameter for the output beam was approximately the same as that of the master-oscillator, indicating no significant degradation in beam quality caused by the optical components in the amplifier chain.

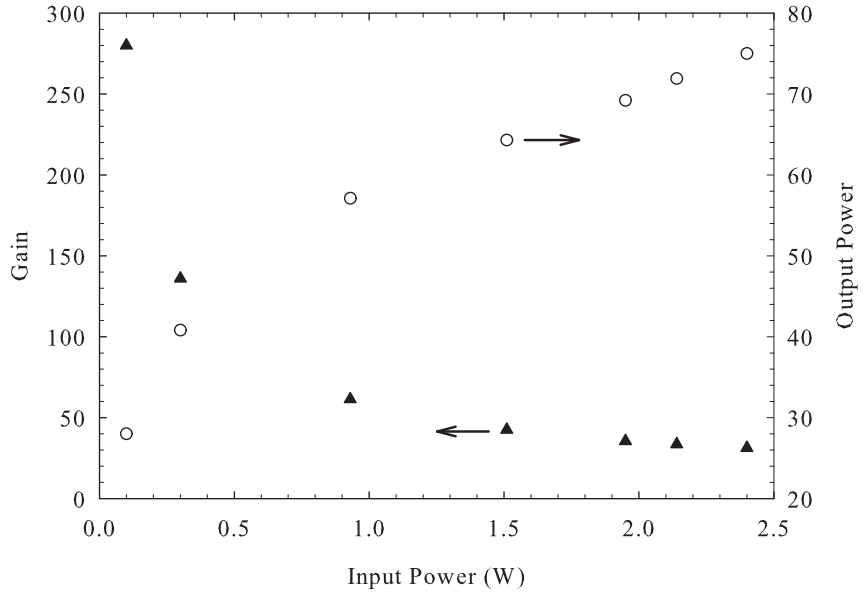

Figure 6.8: Gain and output power of amplifier versus input power.

By adjusting the position of the 200mm focal length lens, which focused the beam into the first amplifier, the degradation in beam quality through the amplifier chain was measured for a range of signal beam sizes. By this technique, signal radii in the range 222μm to 315μm were achievable in the crystals in the first amplifier stage. The M^2 values, measured after each amplifier stage, are shown in Figure 6.9. The best overlap ratio for high output power and high brightness was chosen to be 0.92 (the middle curve in Figure 6.9). The maximum power available from the MOPA could be increased slightly (i.e. by 3-4W) by increasing the signal beam size in the Nd:YVO_4 crystals by ∼20%, but at the expense of a degradation in beam quality ($M^2 \sim 1.6$) and hence a reduction in brightness by ∼20%. Thus, careful selection of pump and signal beam sizes is crucial for maximum power and brightness amplification.

6.4.2 Pulsed Operation of the MOPA System

The MOPA system was operated in pulsed mode using the same technique described for the mode-locked MOPA system in Chapter 5. The AOM was used to gate the signal before amplification with the aim of achieving higher peak powers by allowing the gain to build up to high levels in the time intervals between pulses. In this regime the isolators were required to suppress parasitic

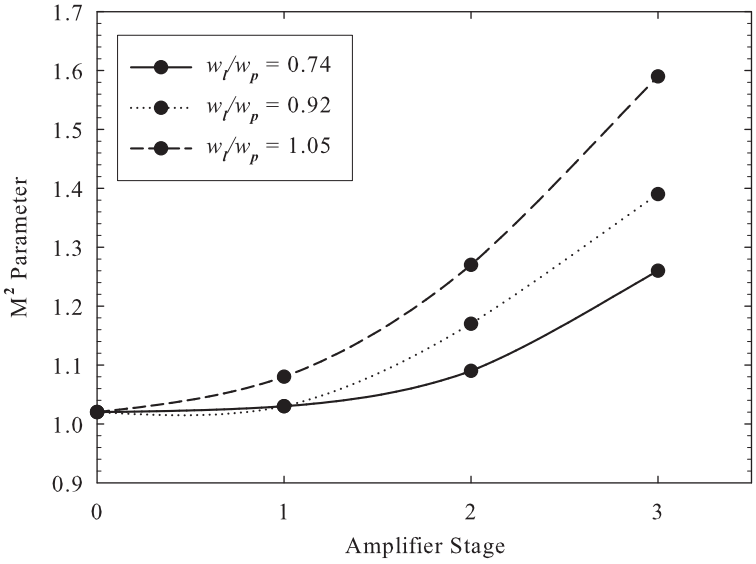

Figure 6.9: Degradation in beam quality through three amplifier stages for a range of overlap ratios given for the first amplifier stage.

lasing by reducing the amount of feedback through the amplifier. In pulsed mode, a range of different performance characteristics could be obtained, depending on the AOM pulse width t_p and the repetition frequency f_r. By reducing the pulse repetition rate to below ~ 1 kHz ($\ll 1/\tau_f$), the peak power of the output pulses was maximised because the population inversion has time to build up to its maximum value and hence the maximum small signal gain was measured. Figure 6.10. shows the input and output pulse shapes in the maximum peak power regime measured by re-scaling the vertical axis such that the integral of the photodetector signal, with respect to time, matches the measured pulse energy given by the average power divided by the repetition rate. In this case, the peak power was 5.6 kW and pulse energy was 2.4 mJ at a repetition rate of 1 kHz. The input power at the time of highest output power was 0.8W which implies that the small signal gain of the amplifier is $\simeq$7000 (38 dB), as measured in Chapter 5. This measured small signal gain was used to predict the amplifier performance under other operating conditions using the theory described in Chapter 4.

In a similar experiment to that described in Section 5.7.2, the variation in average power and peak power of the amplifier output as a function of pulse width and pulse repetition rate was measured and the results are shown in Figures

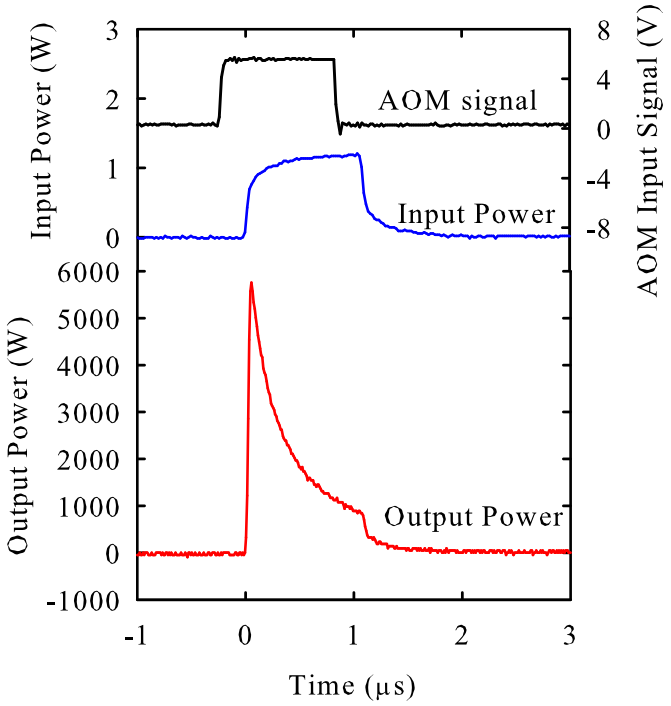

Figure 6.10: Input and output pulse shapes optimised for maximum peak power. Peak power 5.6 kW, Pulse Repetion Rate 1 kHz, Average Power 2.2 W, Pulse Energy 2.4 mJ.

6.11 and 6.12 respectively. In both figures the solid lines represent the theoretical predictions using the theory described in Section 4.2.4 with simplified amplifier parameters. This meant, using the approximation that the amplifier was a single rod with a pump beam of constant radius 500µm , a total absorbed pump power of 215W, a signal-pump overlap ratio of 0.85 and a small signal gain, given by the experimentally measured value, of 7000. As with the results in Chapter 5, the predictions show reasonably good agreement with the experimental results. The larger discrepancy, in Figure 6.11, at long pulse widths (comparable to τ_f) can, again, be attributed to the significant pumping during the pulse, which is not accounted for in the model. Figure 6.11 shows how reducing the pulse width increases the peak power at 10 kHz repetition rate. This is due to the increase in the time between pulses and hence greater population inversion at the time of arrival of each pulse. For the same reason, reducing the pulse repetition rate has the same effect of increasing peak power, as shown in Figure 6.12. However, in both these cases the average output power is reduced because the duty cycle of amplifier input and hence the

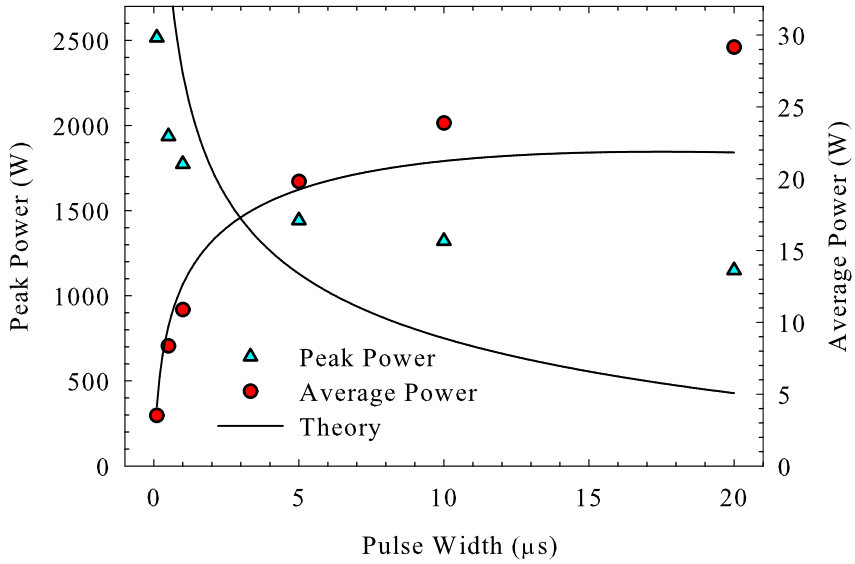

Figure 6.11: Peak power and average power as a function of Pulse Width for 10kHz repetition rate.

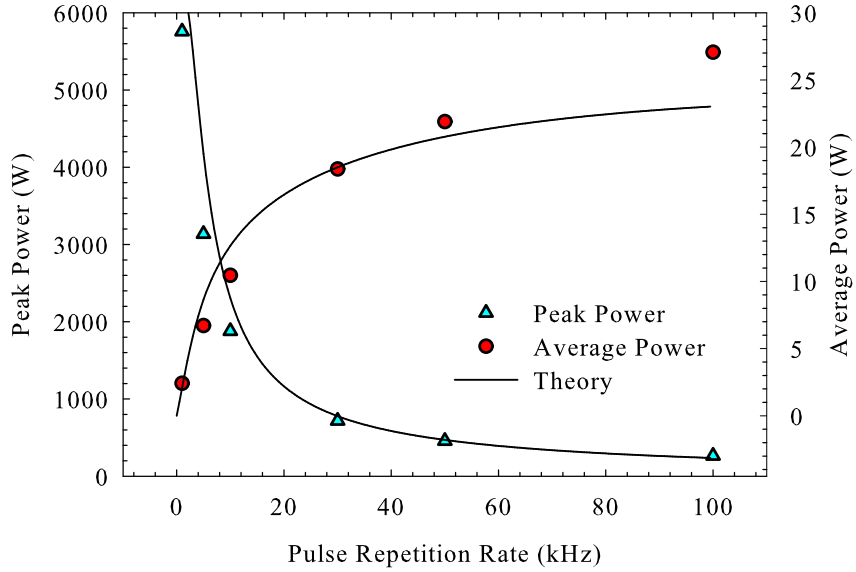

Figure 6.12: Peak power and Average power as a function of Pulse rep. rate for 1 μs pulse width.

input pulse energy becomes small compared to the saturation fluence. Indeed, Figure 6.13 shows the limitation in gain imposed by the average input power which shows little variation between the three modes of operation: Fixed pulse width, variable repetition rate; fixed repetition rate, variable pulse width and continuous wave operation.

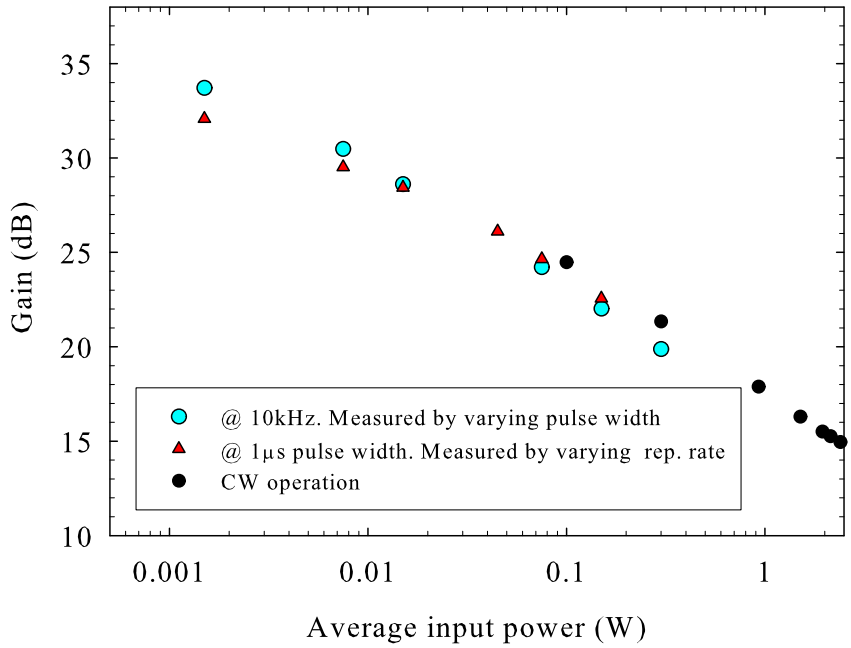

Figure 6.13: Variation in Gain with respect to average input power for three different data sets.

Operating in the maximum peak power regime, as in Figure 6.10, is not necessarily the most effective regime for the application of high power generation in some nonlinear optical devices. Since the repetition rate is so low, the corresponding average power measured just 2.2W which, although potentially useful, represents less than 1% extraction of stored energy in the amplifier. At higher repetition rates (∼11kHz), the master-oscillator power-amplifier arrangement produced lower peak power pulses, but at higher average power. An example of this is shown in Figure 6.14, where a peak power of ∼2kW was obtained in a long pulse of ∼1μs duration, corresponding to a pulse energy of 1mJ and an average power of 11.3W.

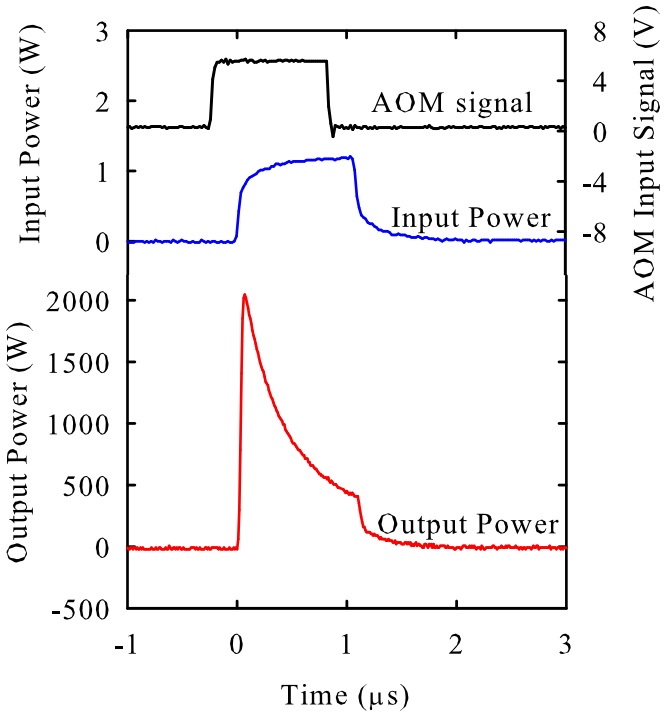

Figure 6.14: Input and output pulse shape at 11 kHz repetition rate. Peak power 2.05 kW, Average Power 11.3 W, Pulse energy 1 mJ.

6.5 Pulse Shaping Techniques

Figures 6.10 and 6.14 show that the pulse shape for rectangular input pulses is characterised by a sharp initial rise in power followed by an exponential decay. This is because the leading edge of the input pulse experiences a higher gain than the trailing edge due to the reduction in population inversion during the pulse amplification process. The energy stored in the upper state is at a maximum at the time of arrival of a pulse and the reduction of stored energy as the pulse passes through the amplifier has a large effect on the gain. This means that, in the case of Figure 6.14, although the input pulse width is greater than 1μs , the output pulse width measured by FWHM method is only 0.38μs . For the application of quasi-cw pumping of a SRO where high intensity is required for a long duration, this distorted pulse shape is undesirable. To address this problem, the AOM was operated in analogue mode to shape the amplifier input pulse to produce a more rectangular output pulse [24]. An arbitrary waveform generator (Hewlett Packard 33120A) was programmed to produce triangular pulses to ramp the AOM from 0 volts up to around the sat-

uration voltage of 4 volts over a period of 1μs and then immediately switch it back to 0 volts. The repetition rate was set at 10kHz. The maximum voltage could be adjusted to change the slope of the leading edge by changing the time taken to reach the saturation voltage. Figure 6.15 shows the waveform generator output as well as the input and output pulse shapes of the amplifier.

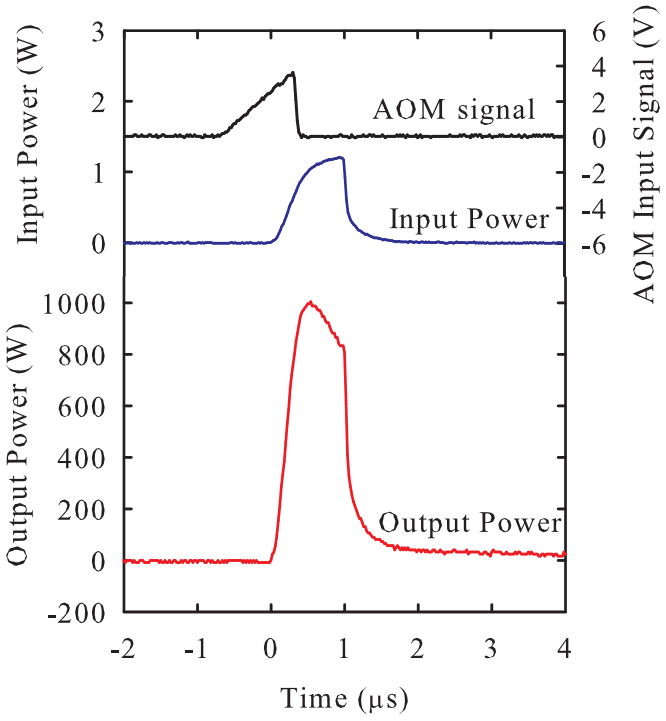

Figure 6.15: Pulse shaping to produce ~symmetric output pulse. Rep.rate 10kHz, pulse energy 0.96mJ, average power 10.6W, peak power 1kW, output pulse FWHM 0.8μs.

It can be see from Fig. 6.15 that the shaped output pulse can be made almost symmetrical in profile using a simple triangular AOM waveform. This pulse has almost the same pulse energy and average power as the pulse in Figure 6.14 despite only having around half the input pulse energy. The peak power is smaller by a factor of two (1kW) and the FWHM is larger by a factor of more than two (0.8µs). Using equation (4.47) from Chapter 4 to find the time dependent gain during the pulse, and hence the output pulse shape for a given input pulse shape, the amplifier output pulse shapes were modelled for a range of input pulse shapes, as shown in Fig. 6.16. The pulse width and repetition rate was maintained at 1µs and 10kHz respectively in all examples.

The pulse shape modelling in Figure 6.16 (a) and (b) predicts the observed be-

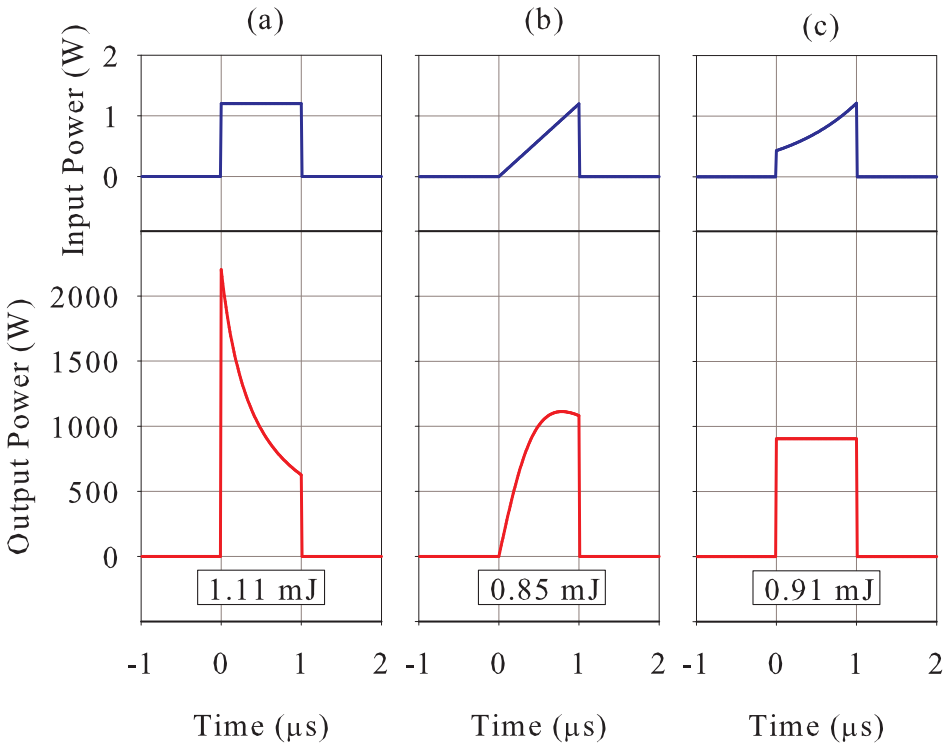

Figure 6.16: Modelling of amplifier output pulse-shapes for different input pulse-shapes.

haviour in Figures 6.14 and 6.15 very well. The model was applied inversely to produce Fig. 6.16 (c) which therefore shows the predicted input pulse shape required to produce a rectangular output pulse. This input pulse was synthesized by programming the waveform generator appropriately and the result is a nearly 'top-hat' pulse shape with only slightly lower peak power (see Figure 6.17). This demonstration shows that a high degree of control over the output pulse shape can be achieved with little change in pulse energy. Furthermore, there is potential for more complex pulse shapes to be realised if required.

6.5.1 Mode-Locked MOPA Pulse Shaping

A further demonstration showed that the same technique could be applied to the mode-locked MOPA system with very similar results. Figure 6.18 shows a similar 1µs pulse achieved from the mode-locked MOPA which has a power in excess of 1kW over the duration of the pulse in a nearly 'top-hat' pulse shape. The average output power was ∼11W. The required input pulse shape

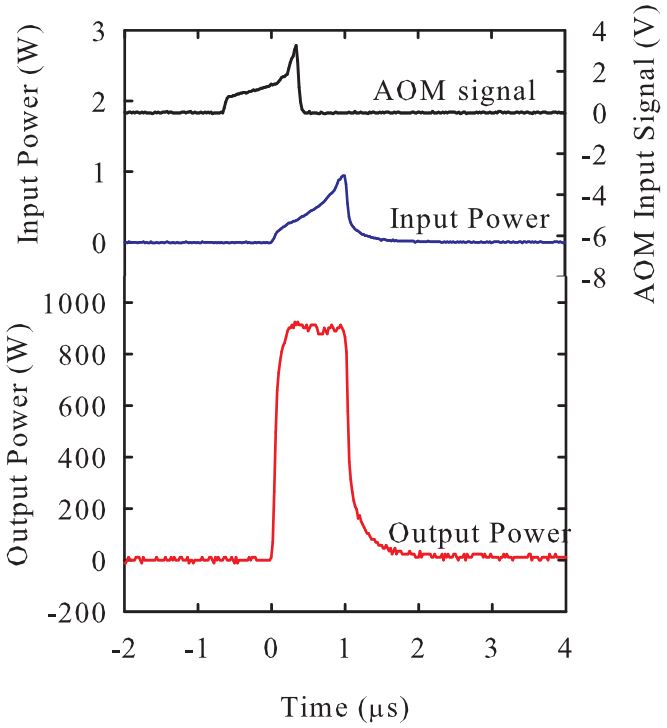

Figure 6.17: Pulse shaping to produce an approximately rectangular output pulse shape. Repetition rate 10kHz, pulse energy 0.91mJ, average power 9.1W, peak power 0.91kW, output pulse FWHM 1.0μs
.

in this case, is less distorted than in the previous case in Figure 6.17. This was attributed to non-optimal alignment of the amplifier resulting in lower small signal gain which caused a reduction in the rate at which the gain is saturated as described in Section 4.2.4.

No change in pulse shape was observed when the mode-locker was activated, as measured by a relatively slow (30ns) detector. This suggested that actual mode-locked peak powers of $\sim 30kW$ were achieved in a 1μs envelope containing approximately 100 mode-locked pulses. This implies a factor of ∼12 increase in peak power compared to the continuous mode-locked output from the amplifier. These output characteristics are equally promising for the application described in Chapter 5 of quasi-cw synchronous pumping of an SRO with long pulse envelopes, as the single-frequency source described in this chapter is, for pumping a narrow linewidth SRO.

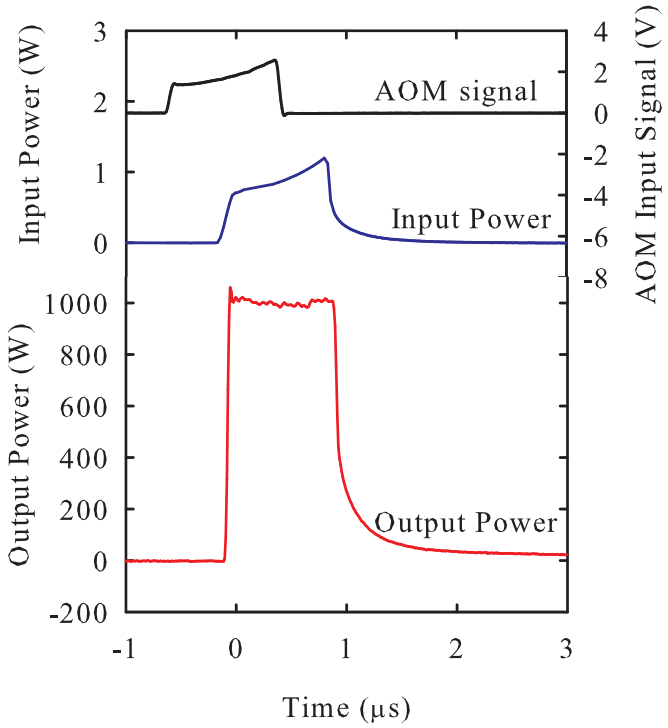

Figure 6.18: Rectangular output pulse shape achieved in the mode-locked MOPA system

6.6 Summary

This chapter has demonstrated the use of the amplifier system, developed for the mode-locked MOPA system described in Chapter 5, as a very effective system for amplifying the output from a single frequency Nd:YVO_4 oscillator in both cw and pulsed mode. Such a system would provide a very attractive pump source for an SRO.

The principle of single-axial-mode operation of solid-state oscillators were explained and some techniques for achieving single-frequency operation were reviewed. The problem of mode-hopping in single-frequency oscillators was highlighted and an effective scheme for suppressing mode-hopping by intracavity second-harmonic-generation was described. The design of a single-frequency Nd:YVO_4 oscillator, end-pumped by a fibre-coupled diode bar, was detailed. The oscillator produced 3.8W of mode-hop-free output at 1064nm.

By seeding the amplifier chain with the single-frequency source, efficient power scaling and brightness scaling was demonstrated. A near diffraction-limited

cw output power of 79W was achieved, limited by the available pump of 265W. Degradation in beam quality due to thermal effects was minimised by optimising the signal-pump beam overlap, with respect to the brightness of the output, resulting in an amplified output beam with M^2 values of 1.42 and 1.48 in orthogonal planes.

The use of an acousto-optic modulator to gate the amplifier input allowed us to operate the amplifier in long pulse mode exploiting the high small signal gain to achieve high peak powers combined with high average powers. Small signal gains in excess of 7000 were measured by operating at low repetition rates. At higher repetition rates, of around 10kHz, 1mJ pulses were measured with peak powers of around 2kW and average power of 11.3W. The input pulse width was around 1μs, however due to the distorted nature of the amplified pulse caused by much higher gain for the pulse leading edge than for the trailing edge, the FWHM of the output pulse was reduced to just 0.38μs. By using a simple triangular waveform to drive the AOM, the input pulse shape was changed to produce a more symmetric output pulse shape, thereby maintaining moderately high peak power over the μs duration of the pulse with no significant change in pulse energy or average power. With further modification of the input pulse shape it was possible to demonstrate almost rectangular output pulse shape, which shows that this technique is a powerful tool for achieving control over the output pulse shape. The high power of $\sim$1kW for μs duration at 10kHz and $\sim$10W average power, is expected to be very useful for quasi-cw pumping of a SRO. Additionally, the gain-guiding effect, which is quite pronounced in this low saturation, high gain, regime caused an improvement in beam quality with measured M^2 values of 1.19 and 1.26 in orthogonal planes at maximum pump power.

6.7 References

[1] **Wulfmeyer, V.**, *Ground-based differential absorption lidar for water-vapor and temperature profiling: development and specifications of a high-performance laser transmitter*, Applied Optics, Vol. 37, No. 18, pp. 3804–3824, 1998.

[2] **Petelski, T., Conroy, R. S., Bencheikh, K., Mlynek, J.** and **Schiller, S.**, *All-*

solid-state, tunable, single-frequency source of yellow light for high-resolution spectroscopy, Optics Letters, Vol. 26, No. 13, pp. 1013–1015, 2001.

[3] **Frede, M., Wilhelm, R.** and **Gau, R.**, *High-power single-frequency Nd:YAG laser for gravitational wave detection*, Classical Quantum Gravity, Vol. 21, pp. 895–901, 2004.

[4] **Bosenberg, W. R., Drobshoff, A., Alexander, J. I., Myers, L. E.** and **Byer, R. L.**, *Continuous-wave singly resonant optical parametric oscillator based on periodically poled $LiNbO_3$*, Optics Letters, Vol. 21, No. 10, pp. 713–715, 1996.

[5] **Elder, I. F.** and **Terry, J. A. C.**, *Efficient conversion into trhe near- and mid-irfrared using a PPLN OPO*, Journal of Optics A: Pure and Applied Optics, Vol. 2, No. 3, pp. L19–L23, 2000.

[6] **Brosnan, S. J.** and **Byer, R. L.**, *Optical Parametric Oscillator Threshold and Linewidth Studies*, IEEE Journal of Quantum Electronics, Vol. 15, No. 6, pp. 415–431, 1979.

[7] **Kogelnik, H.** and **Li, T.**, *Laser Beams And Resonators*, Applied Optics, Vol. 5, No. 10, pp. 1550–1567, October 1966.

[8] **Schmid, W. E.**, *Pulse stretching in a Q-switched Nd:YAG laser*, IEEE Journal of Quantum Electronics, Vol. 16, pp. 790–794, 1980.

[9] **Murray, J. E.** and **Harris, S. E.**, *Pulse Lengthening Via Overcoupled Internal Second-Harmonic Generation*, Journal of Applied Physics, Vol. 41, No. 2, pp. 609–613, 1970.

[10] **Jeong, Y., Nilsson, J., Sahu, J. K., Soh, D. B. S., Alegria, C., Dupriez, P., Codemard, C. A., Payne, D. N., Horley, R., Hickey, L. M. B., Wanzcyk, L., Chryssou, C. E., Alvarez-Chavez, J. A.** and **Turner, P. W.**, *Single-frequency, single-mode, plane-polarized ytterbium-doped fiber master oscillator power amplifier source with 264 W of output power*, Optics Letters, Vol. 30, No. 5, pp. 459–461, 2005.

[11] **Liem, A., Limpert, J., Zellmer, H.** and **Tünnermann, A.**, *100W single-frequency master-oscillator fiber power amplifier*, Optics Letters, Vol. 28, No. 17, pp. 1537–1539, 2003.

[12] **Jaouën, Y., Canat, G., Grot, S.** and **Bordais, S.**, *Power limitation induced by nonlinear effects in pulsed high-power fiber amplifiers*, Comptes Rendus Physique, Vol. 7, No. 2, pp. 163–169, 2006.

[13] **Kracht, D., Wilhelm, R., Frede, M., Fallnich, C., Seifert, F., Willke, B.** and **Danzmann, K.**, *High Power Single-Frequency Laser for Gravitational Wave Detection*, Advanced Solid State Photonics 2006. Technical Digest, WE1.

[14] **Wall, K. F., Jaspan, M., Dergachev, A., Szpak, A., Flint, J. H.** and **Moulton, P. F.**, *A 40W single-frequency, Nd:YLF master oscillator/power amplifier system*, OSA Trends in Optics and Photonics, Vol. 26 Advanced Solid State Photonics, pp. 216–221, 1999.

[15] **Xi, W.-Q., Zhao, J.-Y.** and **Zhang, K.-S.**, *A high-power continuous-wave laser-diode end-pumped Nd:YVO_4 Laser of single-frequency operation*, Chinese Physics Letters, Vol. 22, No. 5, pp. 1144–1147, 2005.

[16] **Martin, K. I., Clarkson, W. A.** and **Hanna, D. C.**, *Self-suppression of axial mode hopping by intracavity second-harmonic generation*, Optics Letters, Vol. 22, No. 6, pp. 375–377, 1997.

[17] **Schawlow, A. L.** and **Townes, C. H.**, *Infrared and Optical Masers*, Physical Review, Vol. 114, No. 6, pp. 1940–1949, 1958.

[18] **Zayhowski, J. J.**, *The effects of spatial hole burning and energy diffusion on the single-mode operation of standing-wave lasers*, IEEE Journal of Quantum Electronics, Vol. 26, No. 12, pp. 2052–2057, 1990.

[19] **Kane, T. J., Nilsson, A. C.** and **Byer, R. L.**, *Frequency stability and offset locking of a laser-diode-pumped Nd:YAG monolithic nonplanar ring oscillator*, Optics Letters, Vol. 12, No. 3, pp. 175–177, 1987.

[20] **Abitan, H.** and **Skettrup, T.**, *Laser resonators with several mirrors and lenses with the bow-tie laser resonator with compensation for astigmatism and thermal lens effects as an example*, Journal of Optics A: Pure and Applied Optics, Vol. 7, No. 1, pp. 7–20, 2005.

[21] **Drever, R. W. P., Hall, J. L., Kowalski, F. V., Hough, J., Ford, G. M., Munley, A. J.** and **Ward, H.**, *Laser phase and frequency stabilization using an optical*

resonator, Applied Physics B: Lasers and Optics, Vol. 31, No. 2, pp. 97–105, 1983.

[22] **Baer, T.**, *Large-amplitude fluctuations due to longitudinal mode coupling in diode-pumped intracavity-doubled Nd:YAG lasers*, Journal of the Optical Society of America B, Vol. 3, No. 9, pp. 1175–1180, 1986.

[23] **Kendall, T. M. J., Clarkson, W. A., Hardman, P. J.** and **Hanna, D. C.**, *High power Nd:YLF master oscillator power amplifier with 15W single frequency output at 1053nm*, CLEO '01. Technical Digest: Summaries of papers presented at the Conference on 6-11 May 2001, pp. 417–418.

[24] **Butterworth, S. D., Clarkson, W. A., Moore, N., Friel, G. J.** and **Hanna, D. C.**, *High-power quasi-cw laser pulses via high-gain diode-pumped bulk amplifiers*, Optics Communications, Vol. 131, pp. 84–88, 1996.

Chapter 7

Conclusions and Future Directions

7.1 Summary of Thesis

The work presented in this thesis, has explored a range of issues relating to the power scaling of oscillators and amplifiers based on Nd:YVO_4 . The power scaling, via a diode-end-pumped MOPA system, of both mode-locked and single-frequency sources operating at 1064nm has been achieved to the $\sim$80W average-power regime with near diffraction-limited, TEM_{00} beam quality. In continuous mode-locked mode of operation this corresponds to peak powers $>$2.5kW at 100MHz repetition rate. The degradation in beam quality in end-pumped Nd:YVO_4 amplifiers, due to thermal effects, was studied and an amplifier design strategy for minimising the influence of thermal effects on performance was developed. In pulsed mode of operation, the MOPA system achieved mode-locked pulse trains with $\sim$30kW peak powers over long durations of $\sim$1μs . Pulsed operation of the single-frequency MOPA yielded long pulse durations of $\sim$1μs at power levels $\sim$1kW. These laser sources have desirable characteristics for a number of applications, notably, frequency conversion via optical parametric oscillators and amplifiers.

7.1.1 Nd:YVO_4 Master-Oscillator

The oscillator described in Chapter 3 was developed to achieve moderately high output power and high efficiency, but with the main priorities being stable, TEM_{00}, mode-locked operation with short pulse durations and minimal

influence from thermal effects. These requirements were key to the successful development of the entire MOPA system since the stability, beam quality and pulse characteristics of the MOPA were largely governed by the master oscillator while the amplifier primarily governed the power. Nevertheless a sufficiently high-power signal beam was required to saturate the amplifier and therefore extract power efficiently from it. The oscillator criteria were achieved with a good degree of success. The maximum output power achieved was 5.3W with a 29% slope efficiency and 24% optical efficiency. The relatively low efficiency, compared to many cw Nd:YVO_4 oscillators, is a result of the significant cavity losses resulting from the relatively large number of optical components required, including an aperture to enforce TEM_{00} mode operation, the mode-locker and the number of mirrors required to achieve the relatively long cavity length of 1.5m for mode-locking at 100MHz. The beam quality of the oscillator was shown to be extremely good in the power range from 3.3W up to maximum power of 5.3W, with the M^2 values at this power level being 1.05 in both orthogonal planes. The oscillator could be operated in both mode-locked and cw mode with very little difference in output power between the two modes of operation. In mode-locked mode, pulse durations of 360ps were measured at 100MHz repetition rate indicating a peak power of $>$2.5kW. While this oscillator provides relatively modest output power and long pulse-durations, compared to many state-of-the-art mode-locked Nd:YVO_4 systems, it nevertheless fulfils the main requirements as a seed for a high power MOPA system. Its stable operation and excellent beam quality made this source very useful for long term operation in the study and development of amplifier systems and its relatively simple and compact architecture enabled relatively easy maintenance and operation.

7.1.2 Mode-locked MOPA system

Using theoretical modelling for the performance of end-pumped amplifiers, which were reviewed and developed in Chapter 4, a design strategy for power scaling in an end-pumped Nd:YVO_4 multiple stage amplifier was proposed. The amplifier system that was developed used a combination of techniques to achieve high gain, high power and minimal degradation in beam quality due

to thermal effects. These included, double-end-pumping of a double-rod amplifier geometry using low Nd^{3+} doping concentration, Nd:YVO_4 crystals to achieve high absorption efficiency, relatively uniform longitudinal distribution of absorbed pump power and low thermal loading density. Additionally, polarisation rotation between the rods was used to compensate for thermal lens astigmatism and relay imaging of the signal and pump beam between the crystals (and of the signal beam between amplifier stages), ensured that the beam sizes in the crystals remained the same independently of thermal lens strength. The overlap between the signal beam and the pump beam in the amplifier crystals was a major focal point of the work on the amplifier. Both theoretical and experimental techniques were adopted to optimise this parameter with respect to the power scaling and more importantly the brightness scaling of the amplifier system. In the latter case, the degradation in beam quality caused by thermal lens aberration was measured and taken into account. Of particular interest, was the observation that the effect of gain-guiding can play an important part in the degradation in beam quality through a high-gain, end-pumped amplifier system. It was shown that the re-shaping of the signal beam due the gain-gradient in high gain end-pumped amplifiers can significantly reduce the degradation in beam quality caused by aberrated thermal lensing because the aberrations primarily affect the wings of the pump distribution where the gain is relatively low.

The MOPA system described in this thesis produced cw output powers as high as 94W and continuous mode-locked average powers as high as 79W which corresponds to peak powers as high as 2.6kW. At maximum pump power the small signal gain was measured to be >7000 (38dB) and the saturated gain at maximum output power was ∼24 (14dB). The output beam quality M^2 factors were measured to be 1.7 and 1.9 in orthogonal planes at maximum power. In pulsed mode of operation, using a AOM to gate the input to the amplifier, the amplifier was able to produce a large increase the output power for long pulse envelopes in the ∼µs regime. By varying the pulse width and repetition rate a large degree of flexibility over the peak powers and average powers was available. The peak powers could be scaled to the ∼13kW level for the oscillator running in continuous-wave mode-locked mode and ∼400kW with the oscillator running in long-pulse mode-locked mode when the pulse repetition rate

was reduced below ∼1kHz, the average power in this regime being ∼2W. Additionally, by controlling the AOM with an arbitrary waveform generator (a technique described in Chapter 6), the temporal pulse shape distortion could be compensated for by shaping the input pulse thereby increasing the effective pulse width of the output. An example of the effectiveness of this technique was used to produce 1µs , rectangular output pulses at 10kHz, with a power of 1kW for cw oscillator-operation and ∼30kW peak powers for mode-locked oscillator operation. The average power in each case was ∼10W. In addition to this high performance in long-pulse mode, the lower overall saturation of the amplifier, and resultant higher average-power gain in this regime, was advantageous from a beam quality point of view, since the gain-guiding effect caused an improvement in beam quality in this regime, compared to the highly saturated regime, where the gain and therefore the gain-gradient is lower. In the 1µs , 10kHz, example above the M^2 parameters were measured to be 1.3 and 1.4 in orthogonal planes which is approximately half the degradation in beam quality for maximum power, cw operation.

7.1.3 Single-Frequency MOPA system

This thesis also described the use of the amplifier chain as an effective route for power scaling of a single-frequency source. An end-pumped, Nd:YVO_4 single-frequency oscillator based on a unidirectional ring cavity was described which had a similar output power to the mode-locked oscillator. The oscillator provided stable and robust single-frequency output at 1064nm, up to a maximum power of 3.8W and with a linewidth less than the resolution limit of the FPI (30MHz). The oscillator also incorporated an intra-cavity LBO crystal, which was phase matched for second harmonic generation. This proved to be very effective for suppressing axial-mode-hopping while loss caused by second harmonic generation was minimal. Mode-hop-free oscillation was observed for long operating times (>30 minutes). When amplified by the amplifier chain described in Chapter 5, the cw single-frequency output was scaled from an input power of 2.4W to a maximum output power of 79W, limited by the available pump power of 265W implying a total gain of 33 (15dB) and an extraction efficiency of 29%. This is thought to be the highest output power

from a single-frequency, Nd:YVO_4 based laser system to date. The beam quality of the output was measured, at maximum power, to be 1.43 and 1.48 in the orthogonal planes indicating minimal degradation in beam quality due to careful control of the amplifier parameters.

The single-frequency MOPA system was also operated in long-pulse mode by gating the amplifier input with an AOM. This enabled higher gains to be accessed with large flexibility over the pulse width and repetition rate. In this regime, pulses as long as 1µs were achievable with powers greater than 1kW at 10kHz repetition rate yielding an average power of >10W. Additionally, the gain-guiding effect, which is quite pronounced in this low saturation, high gain regime caused an improvement in beam quality with measured M^2 values of 1.19 and 1.26 in orthogonal planes at maximum pump power. A good degree of control over the output pulse shape was also achieved by shaping of the input pulse to compensate for temporal pulse distortion in the amplifier. This combination of high peak power, high average power, long pulse duration and good beam quality in single-frequency operation, is considered to offer a unique source, ideal for the application of quasi-cw pumping of singly-resonant OPOs for efficient, high power frequency conversion for use in a range of applications.

7.2 Future Directions

7.2.1 Further Characterisation

There are a number of characteristics of the performance of the MOPA systems described in this thesis which, with more time, would be very useful to investigate. The majority of the work described here, focuses on the average power and peak power of the output of the laser sources as well as the beam quality and hence the brightness. For a number of applications, other characteristics can be very important such as the power fluctuations over short and long timescales and the transience when the systems are switched on or the power levels are changed. From experience in the laboratory, it was observed that when the pump diodes were switched on and operated at moderate out-

put power levels, it took a period of several minutes (∼5-15) where the power fluctuated by ∼10-20%, before the power stabilised. Also when the power was changed, a period of 2 to 5 minutes was required before the output power became relatively stable. After this period the fluctuations were much less but were not measured. It would be possible to measure the transient behaviour of these systems as well as the relative intensity noise under steady state conditions. The reason for these fluctuations was thought to arise from thermal fluctuations in the laser diodes and hence wavelength drift away from the peak absorption wavelength in the Nd:YVO_4 crystals, as well as thermal expansion of mechanical parts and variations in the thermal lensing.

In addition, the thermal influence on the mechanical stability and the thermal lensing would also be expected to influence the pointing stability of the output laser beam: another important characteristic which could be measured with relative ease using the Beamscope beam profiler from Dataray Inc.

For the mode-locked system the spectral content of the output could be investigated indicating the effectiveness of the mode-locking and the bandwidth of the output. Additionally, the bandwidth of the single frequency source and its wavelength stability could be measured with a higher resolution interferometer.

The pulse-to-pulse stability is also a useful characteristic to study, both for the mode-locked pulses and also the modulated pulses from both mode-locked and single frequency sources under a range of conditions. In particular, under low saturation conditions where the gain becomes very high, the pulse-to-pulse stability was observed to be quite poor due to the sensitive nature of the small signal gain. More quantitative information would, however, be useful.

7.2.2 Further Power Scaling

The two oscillator systems described in this thesis could be developed to produce higher output powers, without degrading the beam quality, by using higher brightness pump sources and improving the management of thermal effects. Other authors have achieved higher output powers from both single-frequency [1] and mode-locked Nd:YVO_4 oscillators as well as achieving much

shorter pulse durations, of a few picoseconds, by using passive mode-locking techniques to achieve much higher peak power [2]. These improvements alone could increase the output of the whole MOPA system by increasing the extraction efficiency and also causing some reduction in thermal loading in the amplifier by reducing the effect of ETU. In this particular amplifier, this will however, lead to further degradation in beam quality because the influence of gain guiding will be reduced. Furthermore, when an amplifier becomes more highly saturated, the output power becomes less sensitive to the input power. Therefore, improving the efficiency of the amplification process generally results in greater improvement in performance compared to power scaling of the relatively low power oscillator.

To assess the potential for further power scaling in this amplifier scheme when operating in cw mode, assuming the signal input powers are fixed at 2W and have an signal-pump overlap ratio of 0.9 in each amplifier, the effects of increasing the pump power and adding further amplifier stages are considered. In the first case, the pump power could in principle be increased moderately for the first and second amplifier stages, up to a power similar to that in the third stage since this was considered to be close to the thermal fracture limit of the crystals. In the first amplifier however, the pump spot size would need to be increased to match that of the third, so that the influence of ETU remains low ($<$12% extra heating). For 70W of pump power for each crystal with pump beam radii of 500μm in each case, the predicted output power was $\sim$130W, using equation (4.50), including a loss per crystal of 5%, and an estimate of the small signal gain coefficient of 0.6 times g_0 from equation (4.30) (which gave reasonable agreement with the experimental results for saturated gain). This represents a significant power increase by a factor of around 1.6 compared to the experimental results in proportion to the increase in pump power, hence giving a similar extraction efficiency of $\sim$30%. However, these power levels have been demonstrated, in this work, to have caused thermal fracture of the crystals. In this example, the gain in the first amplifier is much greater than 1 so gain guiding can be expected to minimise the beam quality degradation, however, due to the higher saturation in the second and third amplifiers and greater thermal loading, the thermal aberration is expected to have much more influence, so beam quality degradation is predicted to be worse ($M^2 \gtrsim 2$) than

in the results described in this thesis. Further increase in pump power without causing thermal fracture or greater impact from ETU would require the use of lower Nd^{3+} doping concentration and longer crystals. To maintain pump intensity along the length of such crystals would also require higher brightness pump sources with lower beam divergence. By this strategy further power scaling may be possible but with limitations still imposed by thermal lens focusing of the signal beam out of the gain region and brightness limitations caused by thermal lens aberration.

Another way to increase the output power would be to utilise additional amplifier stages. Using the same performance modelling as used above, and the $\sim$80W output from the MOPA system described, a forth amplifier stage with the same parameters as the third stage ($\sim$65W pump power and 560µm pump beam radius) would yield a predicted output power $\sim$120W and a fifth stage would yield $\sim$150W, with a similar overall extraction efficiency of $\sim$30% in each case. However, the likely impact of thermal lens aberration by simple extrapolation of Figure 6.9 brings the predicted M^2 values to between 2 and 3. Moreover, the reduced impact of gain guiding at even higher levels of saturation, are expected to result in a more rapidly increasing M^2 with increasing number of amplifier stages, as the gain approached 1. An additional problem could be the thermal focusing of the signal beam out of the gain region. Using the estimated experimental values of the thermal lens focal length for each crystal of 220mm. The effective focal lengths for the whole amplifier are $\sim$38mm and $\sim$30mm for 4 and 5 amplifier stages respectively. This is approaching the regime where the signal beam size changes significantly over the crystal length which would result in a reduction in signal-pump overlap efficiency.

Further work in the area of power scaling of diode-pumped Nd:YVO_4 oscillators and amplifiers is likely to continue to achieve TEM_{00} beam quality with higher average output powers in to the hundreds of watts to kilowatts regime with the development of more advanced cooling techniques and laser geometries, notably cryogenic cooling and thin-disk geometries. The latter of which has already been applied to achieve $>$kW power levels in Yb based gain media [3]. The development of high-power fibre lasers has also achieved multi-kW power levels with TEM_{00} beam quality and their operation at narrow linewidth

has superseded most bulk single-frequency lasers for cw output power [4]. In spite of this, bulk solid-state oscillators and amplifiers have some advantages over fibre-based systems when operated in the pulsed regime, with high peak powers, owing to higher thresholds for damage and a higher threshold for unwanted nonlinear loss processes (e.g. SBS, SRS). Availability of new laser materials will also continue to provide more desirable properties and therefore produce improved performance of solid-state lasers. A notable example is Nd:$GdVO_4$, thought by many to have similar spectroscopic properties to Nd:YVO_4 but with improved thermal properties. Nd:$GdVO_4$ has recently been used to achieve >100W TEM_{00} output in an oscillator with single-bounce slab geometry [5]. However some reports suggest very little improvement in performance compared to Nd:YVO_4 [6].

7.2.3 Non-linear Frequency Conversion

The principal applications of the laser systems, presented in this thesis, are for efficient frequency conversion to new wavelengths by nonlinear parametric processes. With more time, a number of different frequency conversion schemes could be explored using the mode-locked MOPA system and also the single-frequency MOPA system, to achieve high power radiation at a range of wavelength regimes from the UV to the mid-IR.

By exploiting the high nonlinear optical response of certain crystals, to high intensity radiation, it is possible to generate higher harmonics of the fundamental pump frequency. The most common (and most efficient) generated frequency is the second harmonic which for a 1064nm pump corresponds to generation of radiation at 532nm. The second harmonic generation (SHG) conversion efficiency depends on the nonlinear crystal used as well as the pump source. High efficiency requires high intensity, good beam quality and narrow spectral linewidth. SHG is often performed inside a laser cavity because the power of the radiation is much higher than the laser output power (by a factor of $1/T$ (in a single direction), where T is the output mirror reflectivity). However, a high power output beam from a MOPA system can also achieve high conversion efficiencies, without the added complexity of a resonator with intra-cavity frequency doubling. Furthermore, the flexility of the MOPA sys-

tem described in this thesis allows for a range of operating condition, from cw to pulsed, with high peak powers, as well as the option to use a single frequency or a mode-locked source. The mode-locked source will generally offer higher conversion efficiency due to the much higher peak powers available. However, in some applications the narrow linewidth of the single-frequency source would be advantageous.

Another frequency conversion scheme which, using the MOPA systems described, has many possibilities, is the optical-parametric-oscillator (OPO). OPOs use parametric amplification to generate signal ω_s and idler ω_i frequencies from a given pump frequency ω_p, where conservation of energy gives

$$\omega_p = \omega_s + \omega_i. \tag{7.1}$$

Many OPOs have been developed, where the cavity mirrors are chosen to resonate both the signal and idler wavelengths (and in some cases the pump wavelength as well). These are known as Doubly (or Triply) Resonant OPOs (DROs) and are attractive mainly because they have low threshold pump powers. However, DROs have very strict design constraints and are intrinsically unstable [7]. A more stable and versatile approach is to resonate just one wavelength (signal or idler) in singly-resonant OPOs (SROs). The disadvantage, however, is that SROs have much higher thresholds so high power pump sources are required. The biggest attractions of OPOs are their ability to access parts of the spectrum unattainable by existing lasers and their wide tunability of wavelengths, which in some cases is only limited by the transparency range of the nonlinear crystals used. Two important examples of OPOs, which could be pumped by the MOPA system described here, are synchronously-pumped OPOs which use picosecond pulses from mode-locked sources and cw or single-frequency OPOs which require narrow linewidth pump sources which operate in the cw or long pulse duration regime.

Some of the most common nonlinear crystals used for frequency conversion of solid-state lasers are Lithium Triborate (LBO), Beta-Barium Borate(BBO), Potassium Titanyl Phosphate (KTP), and Lithium Niobate ($LiNbO_3$). For very high peak intensity pump sources ($>1GW/cm^2$), of these crystals, only BBO and LBO offer high enough damage thresholds to be used, however their nonlinearity is lower than that of KTP and $LiNbO_3$. Other factors are also impor-

tant such as their transparency ranges and the conditions required to achieve phase matching [7].

7.2.4 A Synchronously-Pumped OPO

Since the pulses in the ps regime are too short for most practical OPO cavity lengths to provide enough round trips to produce efficient parametric gain and wavelength selection over the duration of the pulse, the most effective way to utilise the high peak power available from mode-locked sources is to use synchronously-pumped OPOs (SP-OPOs). These generally require that the cavity length of the OPO is the same as the cavity length of the oscillator, such that each pump pulse arrives synchronously with the circulating field in the OPO. Using the mode-locked MOPA system described in Chapter 5 as the pump, a number of possible frequency conversion and SP-OPO schemes could be realised for a range of applications. One example is described here. In continuous mode-locked mode at maximum power, efficient frequency doubling (>30%) would be expected using a non-critically phase matched LBO crystal [8]. If this 532nm source were then used as a pump source for a synchronously-pumped SRO also based on LBO, it would be possible to produce signal and idler output-wavelengths which are tunable from near the pump wavelength to the IR, by temperature tuning of the LBO crystal. The limit on the maximum wavelength, to which the idler wave can be tuned, depends on the limitations on the phase matching wavelength range, the parametric gain for the signal wavelength and on the range of transparency of the LBO crystal as well as the wavelength ranges for the optical coatings in the SRO. For LBO, the maximum idler wavelength is $\sim$2.7μm , limited by the optical transmission of the material [9]. Several authors have demonstrated such SROs, most of which were based on Nd:YLF oscillators or MOPAs [10]. Butterworth *et al.* [11] used a relatively low average power ($\sim$1W at 1047nm) mode-locked Nd:YLF MOPA which yielded up to 72% conversion efficiency to 523.5nm by resonant doubling. The signal-resonant SRO produced tunable output in the range 0.65-2.7μm with signal and idler power of greater than 200mW and 90mW respectively. Scaling this type of system to the power levels available from the mode-locked MOPA in this thesis could provide a

source with several tens of watts of radiation at 532nm by single-stage frequency doubling and several watts of tunable radiation in the visible to IR range. By employing a further frequency doubling stage it would be possible to produce a high power source with a wavelength range extending down to the UV range. The MOPA system could also be operated in pulsed mode to achieve much higher peak powers and potentially increase the efficiency of the SRO. Sources of powerful UV radiation (>100mW) are difficult to achieve with solid-state lasers. Furthermore, tunability in the UV is particularly useful for several applications. One application of interest is UV writing of structures like wave-guides and gratings in germanium doped silica and potentially a range of other glasses which have specific absorbtion bands of interest in the UV region. Such structures are becoming increasingly useful in a wide range of optoelectronic devices.

7.2.5 A Single-Frequency cw or Quasi-cw SRO

While a SP-OPO could potentially provide highly efficient frequency conversion owing to the high peak powers, SP-OPOs are limited to large spectral linewidths similar to the pump laser linewidth. Some application such as spectroscopy and LIDAR require highly coherent narrow linewidth radiation with tunable wavelength. For these applications the single-frequency MOPA system described in Chapter 6 has many attractive features for cw or quasi-cw SROs. Many authors have reported cw SROs pumped by single-frequency Nd based lasers [12–14]. The most attractive nonlinear material for this application is periodically poled $LiNbO_3$ (PPLN) because in its quasi-phase-matched (periodically poled) state, it has a much higher nonlinear coefficient than other popular nonlinear crystals ($\sim$ 17pm/V), which is around fifteen times higher than LBO (1.16pm/V) [7]. It does however have a very low damage threshold (<5% that of LBO) so its use is mainly limited to applications where the intensity is too low for other materials to achieve efficient frequency conversion. In a cw SRO, pumped by a single-frequency source, single-axial mode operation can be achieved by using a travelling-wave ring resonator as the OPO cavity. Tunability of a PPLN, cw SRO, pumped by a 10W 532nm single-frequency solid-state source, has been demonstrated in the range 550-2830nm with out-

put power between 30 and 500mW [12]. With a 1064nm pump source output powers >1.2W have also been achieved in a PPLN, cw SRO [13]. By using the high power cw single-frequency MOPA described in this thesis, the output powers of such an SRO could potentially be scaled to the several Watt regime. Furthermore, operating the MOPA in quasi-cw mode with long pulses of μs order could yield higher output powers while retaining the attractive features of cw SROs, such as single-axial-mode operation. One of the problems with tunable SROs operating on single-axial-modes is that mode-hopping normally occurs very frequently as the wavelength is changed. One approach could be to employ a similar system to that described by Kendall [15], where the same method of suppression of axial modes by SHG, as used in the Nd:YVO_4 single-frequency oscillator, is used in the SRO. Since the phase matching bandwidth of a nonlinear crystal can be made much greater than the gain bandwidth of a laser gain medium by reducing the crystal length or, in the case of PPLN, using a chirped poling period, it follows that successful suppression of axial-mode-hopping by this technique could enable large tuning ranges to be covered without any mode-hopping. Such a source would be valuable for many applications such as narrow linewidth spectroscopy.

7.3 References

[1] **Xi, W.-Q., Zhao, J.-Y.** and **Zhang, K.-S.**, *A high-power continuous-wave laser-diode end-pumped Nd:YVO_4 Laser of single-frequency operation*, Chinese Physics Letters, Vol. 22, No. 5, pp. 1144–1147, 2005.

[2] **Chen, Y. F., Tsai, S. W., Lan, Y. P., Wang, S. C.** and **Huang, K. F.**, *Diode-end-pumped passively mode-locked high-power Nd:YVO4 laser with a relaxed saturable Bragg reflector*, Optics Letters, Vol. 26, No. 4, pp. 199–201, 2001.

[3] **Stewen, C., Contag, K., Larionov, M., Giesen, A.** and **Hugel, H.**, *A 1-kW cw thin disc laser*, IEEE Journal of Selected Topics in Quantum Electronics, Vol. 6, No. 4, pp. 650– 657, 2000.

[4] **Jeong, Y., Nilsson, J., Sahu, J. K., Soh, D. B. S., Alegria, C., Dupriez, P., Codemard, C. A., Payne, D. N., Horley, R., Hickey, L. M. B., Wanz-**

cyk, L., Chryssou, C. E., Alvarez-Chavez, J. A. and **Turner, P. W.**, *Single-frequency, single-mode, plane-polarized ytterbium-doped fiber master oscillator power amplifier source with 264 W of output power*, Optics Letters, Vol. 30, No. 5, pp. 459–461, 2005.

[5] **Minassian, A., Thompson, B., Smith, G.** and **Damzen, M. J.**, *High-power scaling (> 100 W) of a diode-pumped TEM_{00} Nd:$GdVO_4$ laser system*, IEEE Journal of Selected Topics in Quantum Electronics, Vol. 11, No. 3, pp. 621–625, 2005.

[6] **Didierjean, J., Balembois, F., Druon, F.** and **Georges, P.**, *Comparative study of Nd:$GdVO_4$ and Nd:YVO_4 and test of a composite Nd:YVO_4 /YVO_4 rod using a new method of bonding*, Advanced Solid State Photonics 2006, Technical Digest, WB18.

[7] **Koechner, W.**, Solid-State Laser Engineering, Springer, 5th edn., 1999.

[8] **Wall, K. F., Smucz, J. S., Pati, B., Isyanova, Y.** and **Moulton, P. F.**, *A Quasi-Continuous-Wave Deep Ultraviolet Laser Source*, IEEE Journal of Quantum Electronics, pp. 1160–1169, 2003.

[9] **Kafka, J. D., Watts, M. L.** and **Pieterse, J. W.**, *Sychronously pumped optical parametric oscillators with LiB_30_5*, Journal of the Optical Society of America B, Vol. 12, No. 11, 1995.

[10] **Hall, G. J., Ebrahimzadeh, M., Robertson, A., Malcolm, G. P. A.** and **Ferguson, A. I.**, *Synchronously pumped optical parametric oscillators using all-solid-state pump lasers*, Journal of the Optical Society of America B, Vol. 10, No. 11, pp. 2168–2179, 1993.

[11] **Butterworth, S. D., Girard, S.** and **Hanna, D. C.**, *High-power, broadly tunable all-solid-state synchronously pumped lithium triborate optical parametric oscillator*, Journal of the Optical Society of America B, Vol. 12, No. 11, pp. 2158–2167, 1995.

[12] **Strößner, U., Meyn, J. P., Wallenstein, R., Urenski, P., Arie, A., Rosenman, G., Mlynek, J., Schiller, S.** and **Peters, A.**, *Single-frequency continuous-wave optical parametric oscillator system with an ultrawide tuning*

range of 550 to 2830nm, Journal of the Optical Society of America B, Vol. 19, No. 6, pp. 1419–1423, 2002.

[13] **Bosenberg, W. R., Drobshoff, A., Alexander, J. I., Myers, L. E.** and **Byer, R. L.**, *Continuous-wave singly resonant optical parametric oscillator based on periodically poled $LiNbO_3$*, Optics Letters, Vol. 21, No. 10, pp. 713–715, 1996.

[14] **Batchko, R. G., Weise, D. R., Plattner, T., Miller, G. D., Fejer, M. M.** and **Byer, R. L.**, *Continuous-wave 532-nm-pumped singly resonant optical parametric oscillator based on periodically poled lithium niobate*, Optics Letters, Vol. 23, No. 3, pp. 168–170, 1998.

[15] **Kendall, T. M. J.**, Power scaling and nonlinear frequency conversion of single-frequency lasers based on Nd:YLF, Ph.D. thesis, Optoelectronics Research Centre, University of Southampton, 2004.

Appendix A

Small Signal Gain Calculation with ETU

To find the total small signal gain coefficient, in the presence of energy-transfer-upconversion (ETU) and hence the unsaturated gain $g_{0,ETU}l = \ln G_{0,ETU}$, equation (4.26), in Chapter 4, can be integrated over the length of the crystal l so that

$$\begin{aligned}\ln G_{0,ETU} =& \frac{\sigma_{21}}{2W\tau_f}\left(1-\exp\left(\frac{-2w_p^2}{w_l^2}\right)\right) \\ &\times\left(-\int_0^l \mathrm{d}z+\int_0^l\sqrt{1+\frac{4\alpha_p P_p W\tau_f^2}{h\nu_p\pi {w_p}^2}\exp(-\alpha_p z)}\mathrm{d}z\right).\end{aligned} \tag{A.1}$$

The integral in equation (A.1) can be expressed as

$$I=-l+\int_0^l\sqrt{1+\chi\exp(-\alpha_p z)}\mathrm{d}z, \tag{A.2}$$

where

$$\chi=\frac{4\alpha_p P_p W\tau_f^2}{h\nu_p\pi {w_p}^2}. \tag{A.3}$$

Using the substitutions

$$x(z)=\sqrt{\chi\exp(-\alpha_p z)}, \tag{A.4}$$

and

$$\mathrm{d}z=-\frac{2\mathrm{d}x}{\alpha_p x}, \tag{A.5}$$

it follows that

$$I=-l+\int_{x(z=l)}^{x(z=0)}\frac{2\sqrt{x^2+1}}{\alpha_p x}\mathrm{d}x. \tag{A.6}$$

Using the following standard integral

$$\int \frac{\sqrt{x^2+1}}{x}\mathrm{d}x = \sqrt{x^2+1} - \ln\left(\frac{1+\sqrt{x^2+1}}{x}\right) + C, \tag{A.7}$$

integral I can be solved to give

$$\begin{aligned} I = -l + \frac{2}{\alpha_p}\Bigg\{&\left[\sqrt{\chi+1}\right] - \left[\sqrt{\chi\exp(-\alpha_p l)+1}\right] \\ &+ \left[\ln\left(\frac{1+\sqrt{\chi\exp(-\alpha_p l)+1}}{\sqrt{\chi\exp(-\alpha_p l)}}\right)\right] - \left[\ln\left(\frac{1+\sqrt{\chi+1}}{\sqrt{\chi}}\right)\right]\Bigg\}. \end{aligned} \tag{A.8}$$

Equation (A.8) can be simplified to give the following:

$$I = \frac{2}{\alpha_p}\left[\sqrt{\chi+1} - \sqrt{\chi\exp(-\alpha_p l)+1} + \ln\left(\frac{1+\sqrt{\chi\exp(-\alpha_p l)+1}}{1+\sqrt{\chi+1}}\right)\right]. \tag{A.9}$$

In the simple case where all the pump power is absorbed over the length of the crystal, implying that $\exp(-\alpha_p l) \sim 0$, it can be shown that

$$I = \frac{2}{\alpha_p}\left[\sqrt{1+\chi} - 1 + \ln\left(\frac{2}{1+\sqrt{1+\chi}}\right)\right]. \tag{A.10}$$

By rearranging equation (A.3), so that

$$\frac{\sigma_{21}}{2W\tau_f}\frac{2}{\alpha_p} = \frac{4P_p\tau_f\sigma_{21}}{\chi h\nu_p\pi w_p^2}, \tag{A.11}$$

a final expression for the small signal gain $G_{0,ETU}$, can be given as:

$$\begin{aligned} \ln G_{0,ETU} =& \frac{4P_p\tau_f\sigma_{21}}{\chi h\nu_p\pi w_p^2}\left(1-\exp\left(\frac{-2w_p^2}{w_l^2}\right)\right) \\ &\times\left[\sqrt{1+\chi} - 1 + \ln\left(\frac{2}{1+\sqrt{1+\chi}}\right)\right]. \end{aligned} \tag{A.12}$$

Appendix B

Experimental Methods

Working in a laboratory with high power lasers of several tens of Watts average power, requires a number of experimental methods and precautions in order to prevent damage to equipment and to prevent personal injury. High power lasers operating at infrared wavelengths are particularly hazardous because they are invisible to the human eye. This Appendix summarises some of the methods used in the experimental work presented in this thesis to ensure a safe working environment.

All the diode laser power supplies were connected to fail-safe interlocks, which were triggered by a master switch and also connected to the laboratory doors, so that the power to the lasers was cut by opening the doors. To protect the diode lasers themselves from overheating, flow switches, connected to the cooling water pipes, were also connected to the interlock system, so that failure of the chiller also resulted in the diode power being switched off. Appropriate laser safety goggles with all-around protection were worn by all lab users when the lasers were switched on and IR viewers (and not viewing cards) were used to observe the laser beams. Additionally, the diode stack, the diode bar and the beam shaping optics were all housed in anodised metal boxes with nitrogen purges to protect the optics and diodes from dust and condensation and also protect the users from stray scattered radiation. To further protect users from stray radiation and for convenience, the diode lasers were located on a separate optical table away from the main oscillator and amplifier experiments and the entire table was enclosed with protective anodised metal panels.

To avoid excessive heating of components, all the optical mounts which were exposed to scattered radiation from the high power diode sources, were left as bare aluminium, as opposed to using a black anodised finish, so that the absorption of radiation was minimised. This was particularly important for the fibre mounts for the diode stack which, nevertheless, heated up considerably at high power levels.

A range of beam stops were used and bolted to the optical table to terminate stray reflections and high power laser beams during experiments. Some of these, constructed from 3mm thick anodised aluminium, were found to become very hot (too hot to touch) when exposed to $\gtrsim$ 30W of laser power for several minutes. A safer alternative was constructed from a solid block of aluminium of approximately 60×60×140mm, with a hole of ∼30mm diameter bored in one side for the beam to enter and with an anodised finish. These were also mounted on water cooled bases (for even higher power levels) but connecting the cooling water was not required in these experiments.

A mains cooling water system was used to cool the laser and amplifier crystals. This was fixed at a temperature of ∼13 - 16 ℃ which was found, in ambient conditions of high humidity, to cause condensation to form on the crystals causing severe laser beam distortion and increasing the likelihood of damage. This was avoided by increasing the cooling water flow rate as the laser power was increased and reducing the flow rate when the laser crystals were not being pumped.

For safety, most of the alignment of the laser and amplifier systems was carried out at relatively low power levels (pump powers $\lesssim$ 20W for each pump fibre). However, for the final adjustments on the alignment, the maximum power levels were required to achieve maximum output powers, since this allowed for thermal expansion of mounts, as well as alignment variations induced by thermal lensing and gain-guiding. In this case and in general, care was required to prevent passing objects and fingers through the beam path.

Appendix C

Dealing with Errors

This appendix offers some comments regarding the experimental precision and errors associated with many of the measurements which were made in this work. In most cases (excluding the beam quality measurements) the precise, absolute values and uncertainties of the parameters which were measured were not considered to be of great importance since the primary aims of this work were concerned with formulating a robust strategy for achieving efficient power scaling by studying the relative impact of various system parameters on the overall system performance. However, there remains a number of assumptions relating to the experimental apparatus and measurement techniques such that the precision and validity of some results should be explained.

All average power measurements were made with a range of thermopile power meters manufactured by Gentec except for the very low power measurements, used to determine the small signal gain, which was made with a photodiode. The thermal power meters had power ranges of 1mW to 10W, 10mW to 100W and 10mW to 1kW. These all gave power measurements with calibration uncertainty of $\leq$5% and repeatability 0.5%, according to the manufacturers specifications. When more than one power meter was used in the same experiment they were calibrated with respect to one another to ensure consistent results. Likewise, for the low power measurements to determine the small signal gain, a large area silicon photodiode was used which was calibrated with respect to a thermal power meter at around the 5mW level.

The M^2 values were measured to using a Dataray Inc. Beamscope as described

in Section 5.4. The second moment beam width data as function of propagation distance was analysed using Sigmaplot, which found a least squares fit of the data to a gaussian beam propagation function giving a resultant M^2 value and associated error for each measurement. The M^2 error bars shown in the graphs in this thesis were typically between ± 0.02 and ± 0.2.

The mode-locked pulse widths were measured using a Digital Communications Analyser (DCA). This comprised a fast ($\sim$30GHz) silicon photodiode with a delivery fibre and a 30GHz digital storage oscilloscope. This implied a minimum pulse duration of $\sim$30ps which was sufficient for the 100 to 400ps pulse durations which were measured. The experimental error in these measurements was not fully investigated but experimental results showed fluctuations in pulse duration of upto $\sim$10%.

Appendix D

List of Publications

Journal Articles

M. J. Yarrow, J. W. Kim, W. A. Clarkson, *"High power, long pulse duration, single-frequency, Nd:YVO_4 master oscillator power amplifier"*, Optics Communications, Volume 270, Issue 2, 15 February 2007, Pages 361-367

J. W. Kim, M. J. Yarrow, W A Clarkson, *"High power single-frequency continuous-wave Nd:YVO_4 master-oscillator power amplifier"*, Applied Physics B: Lasers and Optics, Volume 85, Number 4, December, 2006, Pages 539-543

I. O. Musgrave, M. J. Yarrow, W. A. Clarkson and D. C. Hanna, *"Energy-transfer upconversion in Nd:YVO_4 and its effect on laser performance"*, Article to be submitted to IEEE Journal of Quantum Electronics.

Conference Papers

M. J. Yarrow, J. W. Kim, W. A. Clarkson, *"Influence of gain-guiding on beam quality in a thermally aberrated end-pumped Nd:YVO_4 amplifier"*, Contributed paper FrB4, EPS-QEOD Europhoton, Pisa, September, 2006.

M. J. Yarrow, J. W. Kim, W. A. Clarkson, *"High power single-frequency continuous wave and pulsed Nd:YVO_4 master oscillator power amplifier"*, Contributed paper MC6, ASSP, Lake Tahoe, January, 2006.

M. J. Yarrow, W. A. Clarkson, *"High average power end-pumped Nd:YVO_4 master oscillator power amplifier"*, Contributed paper MC2, IEEE-LEOS annual meeting, Sydney, October, 2005.